The Greener Alternative: Sustainable Development in Iron Catalysis and Biodegradable Polymers

Simon Velasquez Morales

B.S. Chemical & Petroleum Engineering, The University of Kansas, 2017

Submitted to the graduate degree program in Department of Chemical & Petroleum Engineering and the Graduate Faculty of the University of Kansas in partial fulfillment of the requirements for the degree of Doctor of Philosophy.

Committee members

Dr. Alan M. Allgeier, Chairperson

Dr. Mark B. Shiflett

Dr. Laurence R. Weatherley

Dr. Kevin C. Leonard

Dr. Michael J. Hageman

Date defended: August 2, 2022

The Dissertation Committee for Simon Velasquez Morales certifies
that this is the approved version of the following dissertation :

The Greener Alternative: Sustainable Development in Iron Catalysis and Biodegradable Polymers

Dr. Alan M. Allgeier, Chairperson

Date approved: August 11, 2022

Abstract

The world is 8 years away from reaching the 2030 U.N. deadline requiring the reduction of carbon equivalent emissions by half before reaching a 1.5°C temperature rise that tips the scale of climate change against us. Within the next decade, the world needs to achieve its 17 sustainable development goals to meet the need of the present generation without compromising the ability of future ones to meet their own needs. In the last 37 years since sustainable development was defined, the world has made tremendous progress in shifting away from non-renewable to renewable resources. However, to meet sustainable development goals, the world must come together and bring forth alternatives that foster economic, environmental, and societal pillars.

Scientific research, from both the private and public sectors, is crucial to advancing industrial innovation while protecting terrestrial and aquatic life. From a socioeconomic perspective, every 1% increase in research and development (R&D) spending leads to roughly 120,000 new jobs and approximately $3 billion in earnings.[174] If the world comes together, as it did to repair the ozone layer, to solve the existential threat that is posed by climate change, then, in the remaining 8 years the U.N. sustainable goals will be satisfied.

This dissertation brings forth scientific research centered around the deployment of earth-abundant components (both catalyst and substrates), advancing greener chemistries, and the development of smart manufacturing platforms to leverage sustainable change in the pharmaceutical, plastics, and detergent industries.

Through an in-depth kinetic and mechanistic study of an iron homogeneous pincer complex, we advance the general understanding needed for its industrial adoption. This complex enables a route for the reduction of 45% of substrates commonly reduced in pharmaceutical processes. Dehydrogenations of limited substrates can also be conducted with this complex. In this investigation, we describe the first-order dependence of the reaction rate with respect to hydrogen and catalyst,

an activation energy of 93.6 $\pm$ 9.7 kJ mol^{-1}, and a pre-exponential factor of 1.75 $\times$ 10^{15} M^{-1}s^{-1}. Additionally, transition state energetic insights through Eyring plot theory, describe the Gibbs free energy of 79.5 $\pm$ 26.8 KJ mol^{-1}, an enthalpy of 90.8 $\pm$ 9.6 KJ mol^{-1}, and an entropy of 37 $\pm$ 28 J mol^{-1} K^{-1}. This key evidence supports the findings that the rate-determining step is associated with hydrogen addition and is assisted by a proton shuttle hydrogen bonding network in the catalyst cycle. Also, through in-situ pressure nuclear magnetic resonance (NMR) investigation, we made an unprecedented discovery that has vast implications for the understanding of nitrile hydrogenation mechanisms. We found crucial evidence of two oligomeric intermediate cascades governed by imine self-condensation and benzylamine condensation, respectively. The higher oligomeric intermediates also hold pharmaceutical value, as they are important substrates used in substituted imidazoles in important drug substances and agrochemicals.

Based on the kinetic and mechanistic findings, we design, construct, and pursue the first iteration of a continuous, modular hydrogenation station. Continuous flow reactors are critical to unlocking consistent quality by control (QbC) strategies that reliably make drug products in accordance with FDA regulations. To enable this manufacturing modality, a custom setup was designed and built from the ground up; including enhanced safety elements for the safe use of hydrogen gas, a highly explosive substance. Industrial innovation is key to unlocking efficient operations that lead to more responsible resource utilization. Additionally, we expand the tools behind residence time distributions in the characterization of continuous reactions by implementing an off-line low-field NMR technique that is far superior to commonly used on-line UV-Vis analytics. Included here are new tracer options, previously unavailable for this type of analysis that better resemble substrates used in chemical reactions.

To further the development of smart manufacturing, we deploy conductivity to measure the kinetics in a batch reactor for the nucleophilic substitution between benzylamine (the product of interest in kinetic/mechanistic and continuous reaction platform) and benzyl bromide. Conductivity is an inexpensive, reliable way to measure the concentrations of electrolytes in solution; a necessary and common operation required by pharmaceutical processes. To develop it as a process

analytical technique (PAT), we construct a LabVIEW code for data acquisition. To enable this methodology for smart manufacturing, we couple data acquisition with kinetic simulations that can be utilized for predictive control.

Focused on employing greener chemistry for the production of plastics, we adopt a bioengineered polysaccharide, i.e., α-1,3-glucan, that is naturally present in the plaque produced by mouth microorganisms and plant's cell wall. To add thermoplastic properties to naturally occurring polymers, we perform an esterification with palmitoyl chloride, a moiety of plamitic acid. Through reaction engineering improvements we increase yield, selectivity, recovery, and decrease process mass intensity (PMI) beyond what is known in the literature. Here, we also conduct application testing into the chemical, mechanical, and transport properties of biodegradable polysaccharide thermoplastics for their use in the food packaging industry.

To eliminate the permanence of detergents in nature, we attempt to make a greener non-ionic detergent with the α-1,3-glucan polysaccharide and benzoyl chloride, a moiety of benzoic acid, in a completely aqueous system. The α-1,3-glucan-benzoate (GB) materials are characterized through ^{1}H and DOSY NMR spectroscopy, FTIR, and solubility. We employ sodium hydroxide to activate the polysaccharide and promote solubility in the reaction media. Cation species have a strong influence on activation which follows trends from the Hofmeister series. Throughout this investigation, we inspect conditions to maximize selectivity, yield, and solubility, while minimizing process mass intensity.

Finally, we go a step beyond in the characterization of α-1,3-glucan (microcrystalline and wet cake) with low field NMR and gas adsorption to investigate the specific surface area of "soft-matter" polysaccharides under conditions of use. Gas adsorption, a well-established technique to measure specific surface area, pore volume and diameter of porous media, undergoes a dehydrating pretreatment step that causes soft-matter to shrivel and morphologically change its structure. To measure the true nature of the material under application relevant conditions, we look at low-field NMR; an analytical technique that uses solvents (wet conditions) to measure morphological properties of materials. Additionally, we explore the physics of x-ray illuminated tomography and

its applications in catalysis, geological samples, and electrochemistry under conditions of use.

Acknowledgements

Winston Churchill once said, "Success is not final, failure is not fatal, it is the courage to continue that counts." I find this to be extremely applicable to research, as one often goes through pivotal moments of failure and success that shape our journey. Throughout the last five years, I have found the strength and courage to continue in this journey through the unwavering support of my mentors, colleagues, family, and friends. There is a bit of each one of you in this body of work that I will take with me wherever I go...

Dr. Alan M. Allgeier, as I transition into the next chapter of my life, I look forward to calling you one of my greatest friends, mentors, and pun-enthusiasts. Thank you for telling the most captivating stories, for your help with GEAK5, for giving me the best personal and career advice, and for helping me become a better version of myself.

Dr. Mark B. Shiflett you were one of the first to guide me as I started my journey as a scientist. Since then, you have played an important role as a mentor both in and outside of work. Thank you for always setting a great example of a successful yet balanced lifestyle for me to follow.

Dr. R.V. Chaudhari thank you for always showing me the greatest kindness, going above and beyond to provide constructive feedback, and for always being a positive force in my life. The time I spent in your classroom and engaging in discussion with you are some of my most treasured memories in graduate school.

Dr. Laurence Weatherley it was in your introduction to chemical engineering course where I found my passion. Since day one, you have believed in me and supported my personal growth; for that, I am extremely thankful.

Dr. Kevin Leonard thank you for providing the great fundamentals in reaction engineering and kinetics, but also for sharing your love for nature with me. This is where my interests in biomimicry began and thanks to you, today, it shapes the way I look at the world and at my research.

Dr. Michael Hageman taking your physical chemistry of solids, solutions, and surfaces course strengthened my fundamental knowledge in pharmaceutical manufacturing, which has helped me address some of the most difficult problems in my research. I treasure your expertise and your willingness to share it with me.

Sergio, Mónica los valores que ustedes me inculcaron, los sacrificios que hicieron, y el ejemplo que me dan cada día son unas de las muchas razones por las cuales estoy donde estoy. Gracias por ser los mejores padres, amigos y por crear las fundaciones en las que hoy me sostengo.

Clara, Jaime, no tengo palabras para agradecerles todo el cariño y aprecio que me han dado, pero sobre todo por haberme brindado un hogar durante todos estos años de estudio. Sin sus palabras alentadoras y buena energia se me hubiera hecho una zanja impasable en este largo camino.

Camilo, Santiago, Austin, Samuel, Tomas, you have been part of the most important moments in my life, shared my struggles but also celebrated my accomplishments. Thank you for always being present when needed and for wanting to be there when not. You have been a constant in a world of variables.

Matt, Murilo, Ana, Tess, Victor, Ankit, Kyle, Karim, Tugba, Vyoma, Hannes, Carlos, Raj, John, Samir, Andrew J, Abby, Andrew Y, Dia, Yssa, Dylan, Berlyn, Anoop, Kalin, Nicole, thank you for all the runs, walks, billiard games, golf outings, dinners, pub crawls, "coffice", bike rides, picnics, and all the amazing memories we have shared. Your company throughout the years has meant the world to me.

Jennifer, Priscilla, Brooke, Alysha, Brad, Khanh, you are the best undergraduates researchers in the world! I was able to learn far more from each one of you than I could ever teach you. Thank you for your patience, strong work ethic, curiosity, and willingness to go above and beyond.

Martha Kehr, Nathan Fortner, thank you for always going above and beyond to solve any problem, answer any question, or address any concern I might have. In more ways than one, your constant support facilitated the completion of my work.

Contents

List of Figures

List of Tables

Chapter 1

Introduction

Abstract

This chapter provides a framework for understanding and characterizing sustainable manufacturing and introduces the objectives and outlines of this dissertation.

1.1 Historical Relevance of Sustainability and Development

Historically, sustainability, or at least its definition, is rooted in the German word *Nachhaltigkeit* (meaning lastingness).[79] The word was first used by Hans Carl von Carlowitz in the 1713's *Sylvicultura Oeconomica* to describe the depleting tree harvesting practices that almost left Europe bare of its most important resource at the time.[79,133] The concept of sustainability went beyond harvesting of trees to things like coal and oil as society moved its energy dependence to non-renewable resources. Today, we have the technology to make progress through the use of renewable sources that will not compromise our planet, society, or economy.

Progress has always been a metric of a thriving society; for example, prior to the Industrial Revolution, progress was often tied to the ideology of preparing one's soul for the afterlife by advancing culture and morality.[79] After the linear incorporation of time to the inner workings of society, progress became associated with incremental steps. Then came the Enlightenment, a period where science and technology drove society forward in an unprecedented manner by creating contiguous technological advancements that fuel the beginnings of modern day industrialized societies. This led to the Industrial Revolution where we first see the progression of society measured in terms of economic remuneration[79] and gave importance to supply chains.[217] Throughout this

period of time, the unheard voices of sustainability were present, but their warnings did not resonate with the rest of the world. It was not until after the two Great Wars where we saw a period of unprecedented economic growth at the expense of nature, that we, as a society, realized the harm we were causing to our planet. Major catastrophic events and garnered scientific understanding helped establish the triple bottom line (society, economy, and environment) that govern the manner by which we now measure the development of our globalized society.

Throughout time, we have known of the consequences of our actions and how they impact the environment around us but have failed to take global action to meet the needs of the whole rather than the individual nation. Since the late 1970s and the Brundtland report (1985), we have slowly taken action to curve our negative impact towards a more harmonious exchange with the environment based on criteria scientists and policymakers have developed.

Between now and 2030, we face a pivotal moment on climate change where we need to reduce our carbon emissions by 48% to prevent an increase in global temperatures of 1.5°C. By 2050, the world must reach net-zero carbon emissions to make our society sustainable and prevent further environmental deterioration without compromising our quality of life and protecting those in underdeveloped nations. A global temperature increase of 1.5°C is projected to have catastrophic consequences for animal species (homo-sapiens included) and our environment, Figure 1.1.

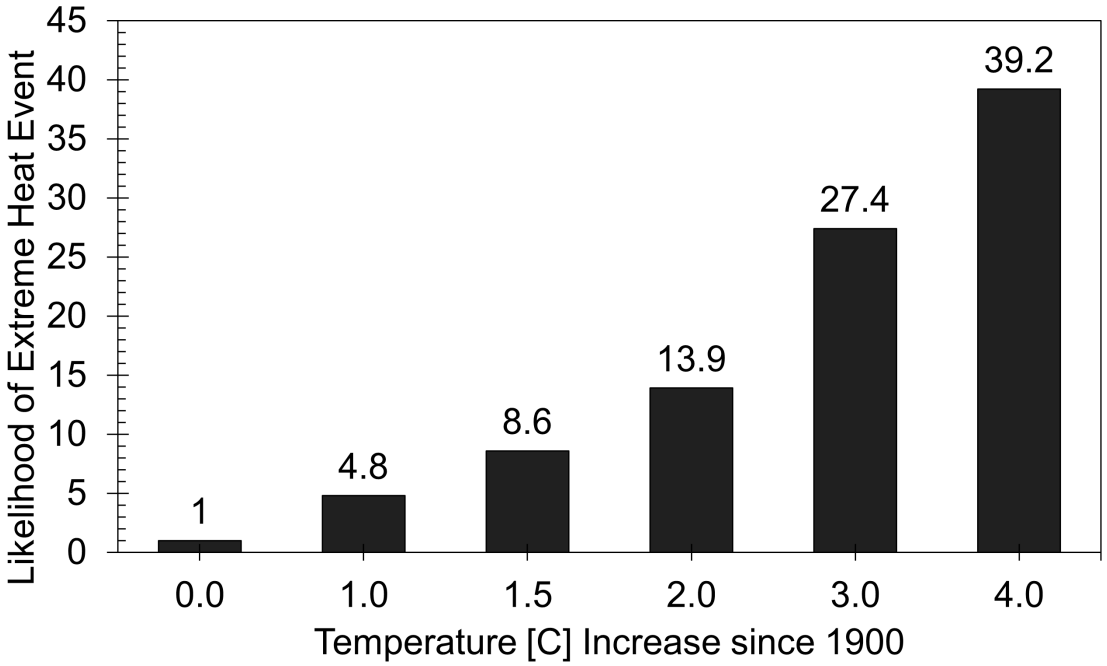

Figure 1.1: IPCC data on global temperature rise correlating to likelihood of extreme weather events. Redrawn from IPCC Report.

1.2 U.N. Sustainable Development in Academia and Research

The 17 Sustainable Development Goals (SDGs), Figure 1.2, are an urgent call for global action by developed and developing countries to ending poverty, improve health and education, reduce inequality, and accelerate economic growth, while addressing climate change issues that threaten terrestrial and aquatic life.[229]

Pursuing sustainable development is both a personal and professional passion of mine that has driven my research and experience through graduate school.

From a graduate student perspective, there are many examples of how academia is affected by lack of sustainable development. Whether it is the rise in inflation that makes it hard for graduate students to purchase groceries,[136] or perhaps, the inequitable cost of learning opportunities, e.g., conferences, seminars, or trainings,[203] or the mental and physical toll that most graduate degrees require.[84] As a personal anecdote, through my time as a graduate student we were able to advance sustainable develop in two of these three issues by creating GEAK5, a mental health run whose

Figure 1.2: U.N. Sustainable Development Goals (SDG) for 2030.

profits were used to promote student learning opportunities, like conferences, through a series of travel awards.[223]

In terms of research, we can transform the dependence on non-renewable resources by devoting our resources to finding sustainable alternatives. Olson *et al.* analyzed the influence of R&D spending on the U.S. economy and their investigation yielded that a 1% increase in research and development (R&D) spending correlates to roughly 120,000 more people employed and $3 billion more earning in metropolitan areas.[174] If all new investments had a sustainable development focus, the world could reach the looming 2030 deadline and meet the U.N. sustainable development goals.

Through our research, we explore the use of naturally abundant components to achieve sustainable consumption and production of goods, the twelfth SDG.[104] Using naturally abundant resources adds flexibility to the 'just-in-time' supply chains by avoiding total control of one resource, e.g., precious metals.

Metal extraction is extremely costly to the environment. Deforestation, animal displacement and fatalities, contamination of freshwater supplies, among other consequences are associated with this practice. Utilizing earth-abundant resources is advantageous because it requires fewer efforts to isolate, which translates to less energy (and less CO_2) required during extraction. Perhaps, by

investing in sustainability research, we can also take climate action, and thus meet the thirteenth SDG.

Plastics and detergents are among the most used products due to their excellent applications in transporting goods and promoting sanitation. However, their permanence in the environment is causing devastating consequences for all animal life.

In this dissertation, we recognize the need to develop technology around earth-abundant components to promote sustainable development, in particular to the pharmaceutical and plastic industries. To measure the overall impact of the technology, we rely on greener chemistry and engineering principles and metrics to guide the innovation of sustainable technology.

1.3 Sustainability Metrics for Greener Chemistry

Table 1.1 depicts the 12 green chemistry[11] and engineering[12] principles that guide scientists to make greener chemicals, processes, and products. These 24 principles align with the 17 U.N. sustainable development goals, but also advance the scientific field by providing metrics to evaluate the degree of sustainability relative to a benchmark. Here we opt to use the world 'greener' rather than 'green' as these metrics are meant to be utilized in an iterative process as new technology and techniques become available rather than a definite solution.

Table 1.1: Greener chemistry and engineering principles guiding the development of greener chemical processes for sustainability.

Chemistry	**Engineering**
Prevention	Inherent Rather Than Circumstantial
Atom Economy	Prevention Instead of Treatment
Less Hazardous Chemical Syntheses	Design for Separation
Designing Safer Chemicals	Maximize Efficiency
Safer Solvents and Auxiliaries	Output-Pulled Versus Input-Pushed
Design for Energy Efficient	Conserve Complexity
Use of Renewable Feedstocks	Durability Rather Than Immortality
Reduce Derivatives	Meet Need, Minimize Excess
Catalysis	Minimize Material Diversity
Design for Degradation	Integrate Material and Energy Flows
Real-time analysis for Pollution Prevention	Design for Commercial Afterlife
Inherently Safer Chemistry for Accident Prevention	Renewable Rather Than Depleting

1.3.1 Traditional Metrics: Conversion, Selectivity, Yield, and Turnover Frequency

On a fundamental level, chemists and engineers have relied on simple metrics, like conversion, yield, selectivity, and turnover frequency to understand reaction performance. These metrics help us understand more efficient conditions but have little to say on the overall sustainability of the process. Conversion, for example, is a metric that tells us how many moles of substrate have reacted, but does not include important factors like catalyst concentration or time, Equation 1.1.

$$\% \text{ Conversion} = \frac{\text{Moles Reacted}}{\text{Initial Moles}} \times 100 \tag{1.1}$$

Turnover Frequency (TOF), unlike conversion, provides perspective on the catalyst influence

on the rate of reaction, Equation 1.2. TOF equates the ratio of the moles of a substrate reacted to the moles of catalyst used and the time. This quantity, like initial rates, is much higher during the beginning of a reaction for positive order of reaction.

$$\text{Turnover Frequency (TOF)} = \frac{\text{Moles of Substrate Reacted}}{\text{Moles of Catalyst} \times \text{Time}} \tag{1.2}$$

Even though this might provide insight into the activity of a catalyst, it fails to show how much of that material is turned into the product. This is described by the selectivity, which is a metric that equates the ratio of the moles of desired product formed to the moles of substrate that reacted, Equation 1.3.

$$\%\ \text{Selectivity} = \frac{\text{Moles Desired Product}}{\text{Initial Moles - Final Moles}} \times 100 \tag{1.3}$$

To understand how much we were able to make during a reaction, we calculate the yield, Equation 1.4. The formula to calculate yield ratios the moles of desired product to theoretical moles of product that could have been formed based on the limiting reagent.

$$\%\ \text{Yield} = \frac{\text{Moles of product}}{\text{Theoretical moles of product based on limiting reactant}} \times 100 \tag{1.4}$$

While all the previously mentioned metrics are necessary to gauge important information on reaction performance, they do not tell us the complete picture. The turnover frequency is great for comparison of catalytic systems as it normalizes the amount of substrate converted to the time of reaction and catalyst concentration. These can then be used to compare and contrast different catalyst in the same reaction, and ideally the same conditions and time. The other metrics do not provide an intuitive comparison for different chemistries; this falls on the shoulders of the trained scientist.

1.3.2 Process Mass Intensity (PMI)

The American Chemical Society (ACS) Green Chemistry Institute (GCI) along with the members of the pharmaceutical round-table created process mass intensity (PMI), a mass-based metric to measure the overall greenness of a reaction, unit operation, or overall process.[210]

$$\text{Process Mass Intensity (PMI)} = \frac{\text{Total Process Mass}}{\text{Mass Isolated Product}} \tag{1.5}$$

This is a metric can be divided into different components so that we can be more inclusive of the literature that does not take sustainability into account.[156]

$$\text{PMI} = \frac{\text{Mass}_{\text{reactants}} + \text{Mass}_{\text{reagents}} + \text{Mass}_{\text{catalyst}} + \text{Mass}_{\text{solvents}}}{\text{Mass Isolated Product}} \tag{1.6}$$

Typically, the preexisting literature includes enough information on reactants, reagents, and catalytic complexes utilized in a process, but often the amount of solvents used in the work-up stage is not reported. Therefore, we can utilize Equation 1.6 to measure each contributing mass index to the total PMI and use those individually for contrast with the preexisting literature.

1.3.3 Atom Economy (AE)

Another useful metric used as a way to address wastefulness in chemical synthesis is atom economy, Equation 1.7. Atom economy is defined by the ratio of the molecular weight of the desired product(s) to the sum of the molecular weights of all reagents involved in the reaction. Reagents that are completely incorporated into the product have higher atom economies.

$$\%\ \text{Atom Economy} = \frac{\text{MW of product(s)}}{\sum \text{MW of all reactants}} \times 100 \tag{1.7}$$

The criteria presented here will be utilized throughout this dissertation as metrics for sustainability and reaction efficiency.

1.4 Life Cycle Inventory and Assessment (LCIA)

Life cycle inventory and assessments on chemical processes are the ultimate green chemistry and sustainability analyses we can perform. These analyses evaluate global warming potential (GWP), eutrophication, toxicity, ozone depletion, acid rain, smog formation, among other indices of interest when evaluating sustainability. These analyses are best applied holistically through a chemical facility and across different chemical lifetimes, i.e., from cradle-to-gate, gate-to-gate, gate-to-grave, cradle-to-gate, cradle-to-grave, or cradle-to-cradle (when upcycling is considered) to evaluate true impacts of the process at relevant scales.[145,184]

While LCIA are best for the evaluation of chemical processes at commercial scales to evaluate realistic environmental impacts, the other mass based metrics are useful during early-stage process development to evaluate efficiency and screen the best chemical and operational practices. However, it is recommended that a full LCIA is conducted during the mid-to-late stages of process development and decisions are taken on the best commercial process based on this analysis.

1.5 Applying Opportunities for Greener Chemical Synthesis in Pharmaceutical and Polymer Manufacturing

This dissertation furthers sustainable development goals through the promotion of greener chemical synthesis in pharmaceuticals and plastics manufacturing. The scope is restricted to reduction of nitriles, nucleophilic substitutions of amines, and acylation of polysaccharides. From a survey conducted by Carey *et al.* on the reactions used in the preparation of drug candidates, reductions, substitutions, and acylations accounted for 9%, 19% and 12%, respectively, of the 1039 chemical transformations.[47]

1.5.1 Reductions

Out of the 500 reductions surveyed by Carey *et al.* and Roughley *et al.*, between 5-15% convert nitriles and imines to amines.[47,200] From their surveys, the list of most common reduced substrates

include nitro groups, alkenes, alkynes, amides, esters, ketones, aryl groups. Additionally, Carey *et al.* determined that 44% of reductions utilize heterogeneous catalyst, 41% use hydrides and boranes, 11% utilize other stoichiometric reductants, and only 4% of the syntheses utilizes homogeneous catalysts.[47]

Hydrides and boranes are highly hazardous and carry excess matter that diminishes atom economy. The most atom economic reductions are conducted by catalyzed hydrogenation. For example, the catalyzed hydrogenation of benzonitrile achieves 100% atom economy, while stoichiometric reduction of benzonitrile with sodium borohydride achieved 42 % atom economy, Table 1.2. In terms of PMI, the use of stoichiometric reagents with unreactive mass leads to lower performance for this metric. We will explore this synthesis further in Chapters 3-4.

Table 1.2: Atom economy assessment of benzonitrile hydrogenation.

Compound Name	Molecular Weight [g/mol]
Benzonitrile	103.04
Hydrogen	2.02
Benzylamine	107.15
Atom Economy	100 %

1.5.2 Nucleophilic Substitutions

Approximately 90% of all drug candidates are N-containing compounds.[47] When coupling drug candidate building blocks, it is common to implement nucleophilic substitutions of N-, O-, and S-containing moieties. Due to the toxicity associated with alkylation agents, these syntheses are discouraged in late stage processes. In Chapter 5, we explore the nucleophilic substitution between benzylamine and benzyl bromide, modelling of reaction data and regression of kinetic rate constants through LabVIEW to enable predictive control strategies that enhance quality by control attributes of these syntheses at any manufacturing state.

From a sustainability perspective, the halide identity in the acylation of amines has a strong

influence on atom economy. To improve atom economy one could exchange benzyl bromide for benzyl chloride, which increases AE from 71%, Table 1.3, to 84%.

Table 1.3: Atom economy assessment of the nucleophilic substitution between benzyl bromide and benzylamine.

Compound Name	Molecular Weight [g/mol]
Benzylamine	107.15
Benzyl bromide	171.04
Dibenzylamine	197.27
Atom Economy	71%

1.5.3 Acylations

Out of 128 acylations, 4% produced esters[47] generally from acid chlorides. Acid chlorides are highly reactive in the presence of water to form acid moieties. These transformations have garnered attention in the modification of polysaccharide polymers.[29,105] In Chapters 6-7, we explore the acylation of α-1,3-glucan with palmitoyl and benzoyl chlorides under organic and aqueous media, respectively.

Acylations of glucan with acid chlorides, just like reductions with stoichiometric reagents, carry excess elements that diminish atom economy of the synthesis. In Table 1.4, we observe that atom economy decreases with increasing number of modifications of the glucan with palmitoyl chloride. This is due to the waste contributions of each chloride ion that is not incorporated into the glucan-palmitate or benzoate materials.

Table 1.4: Atom economy assessment of glucose acylation with palmitoyl chloride.

Compound Name	Molecular Weight [g/mol]
Anhydrous Glucose Unit	162.15
Palmitoyl Chloride	274.87
Glucan-Palmitate (DS 1)	400.57
Glucan-Palmitate (DS 3)	877.41
Atom Economy (DS 1)	92 %
Atom Economy (DS 3)	89 %

1.6 Dissertation Objectives

The objective of this dissertation is to advance the use of abundant materials in pharmaceutical and plastics manufacturing, to further U.N. sustainable development goals that help protect our environment while furthering our quality of life. To do so, we divide the work into the following goals:

1. Characterize the kinetic and mechanistic profile of a homogeneous iron catalyst.
2. Construct a continuous flow hydrogenation station with data acquisition and control.
3. Characterize the residence time distribution to determine viability of quality by design (QbD) paradigm.
4. Commission the reactor and perform a benzonitrile hydrogenation under continuous operation.
5. Develop process analytical tools for data acquisition and enable model predictive control to enable quality by control (QbC) manufacturing modality.
6. Deploy greener synthesis, based on metrics, for biodegradable thermoplastics.
7. Characterize the product's thermoplastic properties and composition.

8. Fabricate films to characterize their viability in the food packaging industry through mechanical, chemical, and transport properties.
9. Deploy greener synthesis, based on metrics, for biodegradable detergents.
10. Characterize product and assess viability as a surfactant, capable of performing as a detergent.

All the work, conclusion, and future perspective associated with this dissertation are organized into the following chapters.

1.7 Outline of Thesis

In Chapter 2 the experimental methods and techniques utilized throughout this dissertation are discussed. Here, we explore the necessary skills needed for the characterization of hydrogenations, substitutions, and acylations and the tools required for the characterization of their products.

In Chapter 3 we explore an atom economic, catalyzed, selective homogeneous hydrogenation of benzonitrile to benzylamine. This chapter explores kinetics and mechanistic considerations that have no literature precedent and provide direct evidence of two oligomeric intermediate cascades, a novelty in homogeneous nitrile hydrogenation literature. The catalytic complex implemented here provides industries, in particular pharmaceuticals, with a high flexibility as this complex can hydrogenate 45 % of all commonly reduced substrates[47] and it can also participate in dehydrogenations. Due to the high abundance of iron, the implementation of this complex reduces the environmental impacts associated with the extraction of noble metals. In this chapter we further develop the U.N. sustainable development goals of innovation (Goal 9), protecting life on earth and below water (Goals 14 and 15), utilizing inherently safe metals (Goal 3), and minimizing resource utilization (Goal 12).

Chapter 4 continues the work established in Chapter 3 by taking the kinetic and mechanistic understanding of homogeneous catalyzed nitrile hydrogenations to design, build, characterize, and test a continuous flow hydrogenation reactor.

In Chapter 5, we explore the nucleophilic substitution of benzylamine, the product of interest

in Chapters 3-4, with benzyl bromide to form secondary amines. To implement this chemistry, we use conductivity as a process analytical tool to monitor reaction progression and investigate reaction kinetics. Additionally, we automate data collection through LabVIEW and incorporate a simulation environment to predict reaction profiles in a variety of conditions. The goal is to build the infrastructure required for smart manufacturing through model predictive controls and in-line monitoring of reaction conditions.

Continuing the theme of sustainable development, Chapter 6 explores the acylation of glucan with palmitoyl chloride in organic media for the development of at-home compostable thermoplastics. Here, we advance sustainability metrics, i.e., process mass intensity (PMI), conversion, selectivity, and yield, for these types of synthesis. Additionally, we produce glucan-palmitate films and characterize is chemical, mechanical, and transport properties for food packaging applications.

In Chapter 7, we explore the acylation of glucan with benzoyl chloride under aqueous conditions for the production of biodegradable, polymeric, non-ionic surfactants for detergent applications. While adopting more benign conditions, we are also launching forward the protection of terrestrial and aquatic life (Goals 14 and 15) by creating products with an end-of-life goal in mind.

Chapter 8 presents a targeted tutorial on materials characterization and our work on furthering fundamental understanding of soft-matter under conditions of use, with respect to the glucan polymer. Here, we contrast low-field nuclear magnetic resonance, a novel technique, to gas adsorption for the determination of specific surface area under wet and dry conditions, respectively. Additionally, we present fundamentals of x-ray computed tomography and a wide range of applications of this technique for the characterization of soft-matter materials that could form part of the future characterization of the materials and reactors disclosed.

Chapter 9 concludes this body of work and provides insights into the future direction of the projects that are discussed through this dissertation.

Chapter 2

Experimental Methods

Abstract

In the makings of this dissertation, a variety of techniques and instruments were used for the synthesis and characterization of organometallic complexes and small and large molecules. This section provides experimental details of the techniques and enough general understanding of the physics behind the instrument to understand results and analysis of their experimental data.

2.1 Nitrogen Schlenk Line

A Schlenk line, an air free technique, is a necessary instrument for dealing with atmospheric (temperature and composition) sensitive reagents, solvents, and catalysts, Figure 2.1. The Schlenk line was invented by Wilhelm Johann Schlenk, a German chemist tasked with handling pyrophoric and air-sensitive radicals during his Ph.D.[206] Flammable, peroxidizable, and inherently toxic solvents with low flash point temperatures and toxic gasses are also suitable for Schlenk line techniques, i.e., tetrahydrofuran (THF), lithium-based compounds, or carbon monoxide.[71,113]

A Schlenk line is a two-chamber glass apparatus that typically possess 4 double oblique stopcocks (or Teflon taps).[34] The first chamber, typically has an inert gas, e.g., nitrogen or argon. The nitrogen gas chamber is connected to an oil-based bubbler to prevent backflow of oxygen into the Schlenk line. Typically, an oil-based blubber is utilized out of convenience, but there are also over-pressure and mercury based bubblers available.[34] Mercury is disadvantageous due to health and waste concerns. The second chamber is typically held under vacuum. There is a solvent trap

Figure 2.1: A depiction of the Ace Glass Schlenk line used for the synthesis of organometallic complexes used in this body of work.

under cryogenic temperatures placed between the vacuum pump and the Schlenk line to prevent solvents from entering the pump and allowing for better longevity of the pump. A Schlenk line with oblique stopcocks, as seen in Figure 2.1, requires greased joints to properly maintain vacuum. Silicone or hydrocarbon based grease are typically used for these purposes. Clear Tygon tubing, or thick rubber hoses are used to connect the Schlenk line to the Schlenk flask.

Schlenk line operations require the cyclic exchanges between vacuum and inert gas, solvent transfer using cannulas, among other specialized procedures depending on the chemistry being utilized. It is important that users be trained from experienced supervisors to understand best practices, even through there are excellent resources available.[34,116] However, Schlenk line operations require an extra level of care. The following section seeks to disseminate the safety Schlenk line considerations every user should take.

2.1.1 Schlenk Line Safety

Safety is paramount for chemistry and engineering fields dealing with complex chemistries, extremely hazardous reagents, and conditions.

2.1.1.1 Cryogenic Temperatures

The solvent trap is normally submerged in a cryogenic liquid, like, liquid nitrogen or argon. Liquid nitrogen has a boiling point temperature of 77K. There are multiple hazards associated with cryogenic temperatures. The most common is associated with unprotected contact of user for long periods of time. Cryogenic gloves, face shield, and sometimes a leather apron are considered required personal protective equipment (PPE) when handling cryogenics.

However, when dealing with Schlenk lines and cryogenics the greatest hazard comes from the condensation of oxygen in the solvent trap. Liquid oxygen, with a pale blue color, is an extreme oxidizer that reacts explosively in the presence of organics. Pressure build up can also occur that yields an explosive event while the trap warms from cryogenic to room temperature.[53]

2.1.1.2 Needles and Cannulas

A cannula is a double-ended needle used to transfer solvents that are air or moisture sensitive during Schlenk line operations. Handling chemically contaminated needles and cannulas requires special attention due to the high risk of punctures and/or tare of personal protective equipment and skin.

Chandra *et al.* recently published a guide for safe handling of cannulas and needles in chemistry laboratories.[54] Chandra *et al.* recommend the use of the one-handed technique to manipulate needles and cannulas to prevent the jerk movement from excessive force that causes most punctures. In addition to the one hand technique, the scooping method is effective at reducing the risk of puncture while dealing with sharps.

2.1.1.3 Glassware

Most commercially available Schlenk (air-free) glassware, including Schlenk lines, does not have pressure ratings from the manufacturer. High and low pressure can lead to breakage of faulty glassware. It is recommended to check for cracks in glassware before use. Also, as an engineering control, it is important to incorporate a pressure relief device set to 5 psig to prevent over pressurization that leads to an explosive event.

The interested readers of this dissertation looking to learn more about Schlenk line techniques, equipment, and good practices, should refer to the Schlenk Line Survival Guide by Dr. Andryj Borys.[34,100]

2.2 Nitrogen Glovebox

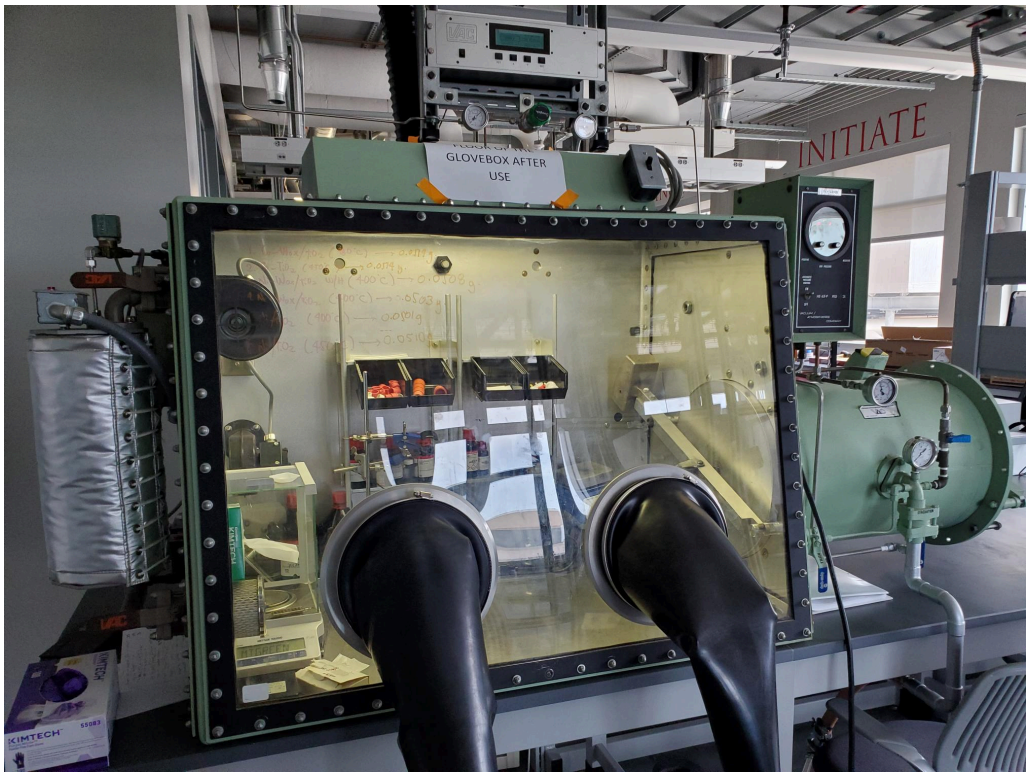

Figure 2.2: Nitrogen glovebox used for the storage of air sensitive compounds, including the iron homogeneous complex utilized in Chapter 3.

A glovebox is an isolated environment that enables operations that are air and moisture sensitive, Figure 2.2. A typical glovebox is composed of an antechamber, vacuum pump, pressure control system, oxygen and/or moisture sensors, gloves, and a circulation and purification system.

To maintain the quality of isolation of the glovebox, strict operating procedures must be followed while introducing, removing, and handling chemicals and materials.

To introduce contents into the glovebox one must first make sure both latch doors of the antechamber are properly closed. Then, open the exterior door and place approved materials under vacuum. Let the vacuum reach -30 in Hg and hold for a minimum of 2 minutes (preferably 7 minutes) before refilling the antechamber with inert gas. Repeat evacuation and refill cycles 3 times prior to introducing the contents of the antechamber into the glovebox. Introducing glassware with septa require a minimum pressure of -20 in Hg to avoid the septum from popping off the flask and spilling of the contents. When following this procedure, the number of cycles has to increase from 3 to 7 before introducing the contents into the antechamber. When not in use, the antechamber should be maintained under vacuum to maintain a well isolated environment.

While operating in the glovebox, the user should be hyperaware of sharps, needles, and open bottles containing liquids and solid as to prevent punctures, spills and contamination of the isolated environment. If compromised, the glovebox atmosphere should be flushed by continuously passing nitrogen until desired conditions are reestablished.

To remove contents from the glovebox make sure the antechamber has been properly inerted through the cycling process previously described. Then, move the contents to the antechamber and make sure the inner door is properly latched prior to opening the exterior door of the antechamber to remove contents. Utilizing appropriate personal protective equipment is emphasized at this point, as all the items removed from the glovebox were exposed to a chemical environment.

2.2.1 Glovebox Safety

When manipulating the glovebox the user should have special consideration with the following:

2.2.1.1 Moisture and Oxygen

All kind of porous materials can hold oxygen and moisture. If porous, the material should be pretreated in a vacuum oven at 100°C for a minimum of 3 hours before transferring hot into the glovebox. For example, one should pretreat paper towels, KimWhipes, notepads, powders, etc.

2.2.1.2 Catalyst Bed

The most expensive and important component to the glovebox is the catalyst that sequesters oxygen, moisture and organics from the environment to maintain the pristine conditions of the glovebox. Due to its importance, the catalyst should always be protected. The following materials should be avoided: amines, halogenated solvents, phosphines, and thiols. If these materials must be utilized inside the glovebox, then the catalyst should isolate and the glovebox atmosphere should be flushed prior to reconnecting the catalyst.

2.3 Semi-Batch 5500 Parr Reactor

Figure 2.3: 5500 high-pressure compact Parr reactor with a 50 mL cup.

The batch 5500 high-pressure compact Parr reactor, with a 50 mL cup, was converted into a semi-batch hydrogenation system via a custom, in-house gas distribution panel capable of measuring hydrogen uptake data. The hydrogenation system offers enhanced safety features that close hydrogen flow when ventilation or power is disconnected. Hydrogen uptake data were collected by monitoring the pressure and temperature of a calibrated-volume feed-reservoir through a high accuracy pressure transducer (Omega Engineering; PX419-1.5KGI) and a type J thermocouple (McMaster Carr; 3856K911).

The reactor was prepared inside the N_2 glovebox with 1g of benzonitrile (Millipore-Sigma, PN: 294098), 4 mg of PNP-Fe(H)(BH_4)CO catalyst, and 25 g of 2-propanol (Millipore-Sigma, PN: 278475). The reactor was connected to the gas manifold, purged with nitrogen and hydrogen

and subsequently heated to 70°C using the 4848 Parr control system. The reaction began when the pressure was increased to the operating pressure and the stirring was initiated simultaneously. Small aliquots were collected throughout the reaction to monitor reaction progress via gas chromatography, while simultaneously collecting H_2 uptake measurements.

2.4 Gas chromatography (GC)

Figure 2.4: A depiction of the Hewlett Packard Gas Chromatography 6890 equipment utilized in the body of work included in this dissertation.

Gas chromatography (Hewlett Packard GC 6890) was used to analyze concentration profiles using a RESTEK RTX-5 Amine (30 m, 0.25 mm ID, 1 μm) column connected to an FID detector. The auto-sampler was set to inject 1 μL aliquots. The inlet was heated and pressurized to 300°C and 38 psig, respectively, and with 57.2 mL/min flowrate of He (with a 10:1 split ratio). The system was operated at constant 5 mL/min flow rate of helium. The oven was heated from 50°C to

100°C at 15°C/min. For 2 minutes, the temperature was held at 100°C before ramping to 210°C at 25°C/min. 210°C was held for 5 minutes before ramping at the same rate to 250°C and holding for 2 minutes. The FID detector was heated to 300°C while flowing hydrogen, air and helium at 40, 450, and 45 mL/min, respectively.

2.5 High-Field Nuclear Magnetic Resonance (NMR)

Figure 2.5: Bruker Avance AVIII 500 MHz spectrometer

NMR characterization was conducted in a Bruker Avance AVIII 500 MHz spectrometer, Figure 2.5, equipped with a multi-nuclear BBFO cryoprobe.

For characterization of the pre-catalytic species **14** and **8** in Chapter 3, the ^{1}H NMR parameters were changed to SW = 50 ppm and transmitter/spectrum center (O1P) = -9 ppm in order to cover the hydrides at -19.5 and -22 ppm in C_6D_6. Data were collected at room temperature. For the ^{31}P NMR, the number of scans was increased to 64.

For characterization of glucan, glucan-palmitate, and glucan benzoate products the ^{1}H NMR parameters were changes to include a delay (d1) of 15 seconds and 32 number of scans at 55°C. deuterated DMSO

2.5.1 In-situ Pressure NMR Characterization

Figure 2.6: Three-channel Bruker DRX 500 MHz spectrometer

In-situ NMR experiments were conducted in a three-channel Bruker DRX 500 MHz spectrometer, Figure 2.6. The instrument also has a MAS controller, a modified BCU-05 temperature bath for low temperature operation and a liquid nitrogen boil off variable temperature controller capable of reaching temperatures well above 70°C. For these experiments a 5 mm Heavy Wall Precision Pressure/Vacuum Valve NMR Sample Tube 7 L (Wilmad-LabGlass; SKU: 522-PV-7) was utilized under a hydrogen atmosphere (180 psig) and deuterated 2-propanol (Millipore Sigma; SKU: 175897-5G). ^{1}H spectra were collected every 5 minutes for 5 hours, and then the frequency

was changed to a spectrum every 15 minutes for the remaining 19 hours. The NMR tube was shaken twice to promote mass transfer at the beginning of the experiment and after 5 hours. After a 24-hour reaction, there was still pressure in the NMR tube.

2.6 Jenway UV-Vis Spectrophotometry

A Jenway UV-Vis spectrophotometer, Figure 2.7, was used with a continuous flow cell for the characterization of residence time distribution in Chapter 5.

Figure 2.7: Jenway UV-Vis Spectrophotometer equipped with a continuous flow cell.

The spectrophotometer is equipped with an ultraviolet (UV) and visible (Vis) light sources that pass through a monochromator to get a single wavelength illumination that passes through the analyte into the detector. The transmittance, I, of the light is measured and correlated to the concentration of the analyte in solution by Beer-Lambert's law, Equation 2.1. Where the absorbance, A, is equal to the logarithm of the ratio of the detected transmittance, I, and the reference value, I_0. Alternatively these expressions are also equivalent to the product of the molar extinction coefficient, ε, the path length, l, and the concentration of the analyte in solution.

$$A = \log\left(\frac{I_0}{I}\right) = \varepsilon l C \tag{2.1}$$

2.7 YSI 3200 Conductivity Meter

A YSI 3200 conductivity meter and a 3252 conductivity cell were utilized to monitor the concentration of dibenzylamine hydrobromide salt in methanol solvent during a reaction between benzyl bromide and benzylamine in Chapter 5.

In order to measure the electrolytic conductivity of a system, we have to measure the resistance in a circuit, Figure 2.8. The circuit is composed by the conductivity meter and conductivity cell and the electrolyte solution that conducts electrical current between the two electrodes.

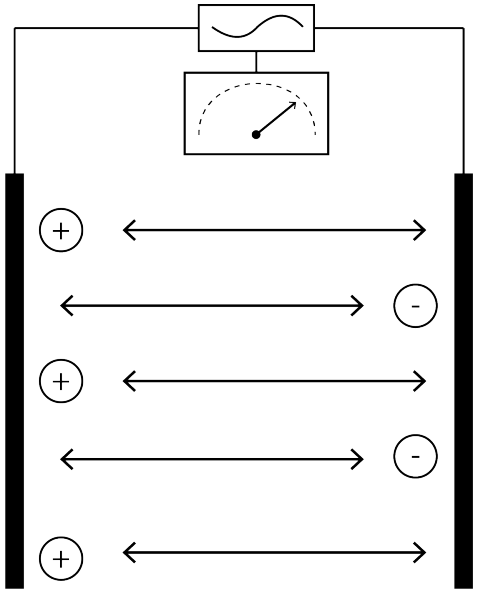

Figure 2.8: A depiction of the circuit involved in the measurement of electrolytic conductivity.

Electrolytic conductivity (S cm^{-1}) is the inverse of electrolytic resistance (Ohms cm), which can be described by Equation 2.2. A Siemens (S) equates to the inverse of an Ohm (Ω).

$$\text{Electrolytic Resistance} = (\text{Circuit Resistance}) \frac{\text{Electrode Area}}{\text{Electrode Distance}} \tag{2.2}$$

The circuit resistance can be calculated through the ratio of the applied voltage and current going through the circuit. An alternating current is used to minimize the potential for electrolysis. Conductivity (C) varies with temperature, concentration, and composition of the media. From a molecular point of view, increasing temperature encourages the diffusion of molecules through

media, which correlates to a higher conductivity measurement. Similarly, increasing the number of ions increases the conductivity of the media. Lastly, ions with higher ionic strength can also increase conductivity. For this we calibrate against concentration under reaction appropriate media and correct temperature differences by reporting conductivity at 25°C, Equation 2.3. α temperature coefficient associated with the electrolyte in appropriate solution media.

$$C = \frac{C_T}{1 + \alpha(T - 25)} \tag{2.3}$$

2.8 Kettle Reactor Configuration

Figure 2.9: 1L kettle reactor with a 5-neck cap utilized in the production of modified α-1,3-glucan materials.

A 1L kettle reactor with a 5-neck cap was placed in a heating mantle controlled by a 1-10 set point dial, Figure 2.9. The reactor utilizes a (100 mm diameter) FEP-Silicone O-ring compatible with reaction conditions. An overhead stirrer equipped with a Teflon shaft and U-shaped blade was utilized to improve mixing criteria. During reactor pretreatment, a distillation apparatus and a round bottom flask were used to collect distilled DMAc/water mixture. During the reaction, a condenser replaced the distillation apparatus to retain dry DMAc in the system. The condenser was connected to a bubbler filled with oil as to prevent oxygen back flow and nitrogen was introduced through one of the five neck-ports. A temperature probe was submerged in the reaction media with

a plastic liner to prevent corrosion.

2.9 Karl Fisher Titration

Figure 2.10: Mettler Toledo C20S Karl Fisher Titrator utilizing CombiCoulomat solution.

An aliquote (0.5-1 mL) of solvent was injected into a Mettler Toledo (C20S) Compact Karl Fischer Titrator capable of measuring water content between 1 ppm 5 %. An Aquastar Combi-Coulomat fritless solution (Millipore Sigma; SKU: 1092570500) was utilized for assay purposes.

2.10 Thermogravimetric Analysis (TGA) and Differential Scanning Calorimeter (DSC)

A TA Instruments SDT Q600 TGA-DSC analyzer was used for thermal characterization of the glucan and glucan-palmitate products in Chapter 6.

Figure 2.11: TA Instruments SDT Q600 TGA-DSC analyzer

The thermogravimetric approach uses two beams, a reference and a sample holder, to monitor changes in mass of the sample throughout the curse of the experiment, as temperature is increased. The heat flux DSC approach measures the temperature difference between the sample and reference cups through the integrated thermocouples in the sample holders. The difference between two temperatures and those of the system equates to the heat flux recorded by the instrument.

A sample contains approximately 20 mg of material in a sample cup. Ideally 2/3 of the cup is filled as to prevent fine materials from being carried out of the cup, but also to have enough sample for accurate measurements. The temperature program used was set to ramp up at a rate of 5°C/minute from room temperature (ca. 23-27°C) to 400°C. At the end, the 400°C would be held for 5 minutes before air cooling would begin, concluding the analysis.

2.11 SPEX 6770 Cryogenic Mill

Figure 2.12: SPEX 6770 Cryogenic Mill used with liquid nitrogen to mill α-1,3-glucan-palmitate thermoplastic polysaccharides.

A SPEX 6770 Cryogenic Mill was used to pulverize glucan-palmitate materials prior to hot press fabrication. The cryomilling instrument shuttles a steel impactor back and forth against two stationary steel end plugs. The sample is pre-cooled for 10 minutes before running 4 cycles; each cycle is 1 minute long with an impactor oscillation rate of 5 cycles per second (CPS). A 1-minute cool time between cycles is placed to maintain the cryogenic environment of the sample.

2.12 Hot Press Fabrication of Thermoplastic Films

Figure 2.13: Hot press equipment utilized in the fabrication of polysaccharide thermoplastic films in Chapter 6.

Cryogrinded glucan-palmitate thermoplastic was placed between 2 non-adhesive Kapton films (Grainger; SKU: 497X97). The material was spread to form a layer ca. 0.5 cm thick. The area of the material was measured (in inches) and used to calculate the applied load (lbs.) of the sample to maintained 100 lb in^{-2}. The temperature was set based upon TGA/DSC, or melting point apparatus studies, i.e., 130°C for the GP materials of interest.

2.13 Contact Angle Measurements

A rame-hart 190 goniometer, Figure 2.14, equipped with a U4 series camera and Halogen fiber optic illuminator was utilized in contact angle measurements that elucidate the surface energy of

glucan palmitate thermoplastics in Chapter 6.

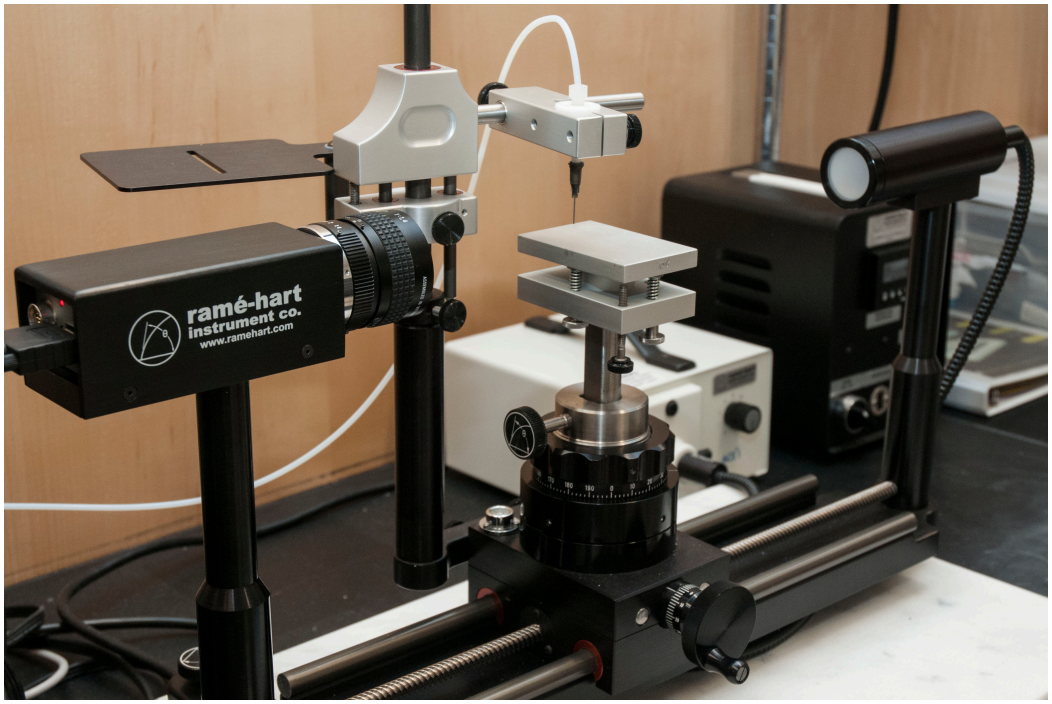

Figure 2.14: A depiction of a rame-hart 190 goniometer used in surface energy analysis.

All contact angles were measured by advancing about 100 μL of hexadecane and/or water onto the surface of the material. The contact angle of both non-polar and polar liquids was used to compute the surface energy of the material (SE) following Equations 2.4-2.5.

Equation 2.4 is used to estimate the solid surface energy (SSE), γ_{SV}, following an Owens-Wendt approach. The SSE is made up of polar (γ_{SV}^{p}) and dispersive (γ_{SV}^{d}) contributions represented by Equations 2.5 and 2.6, respectively.

$$\gamma_{SV} = \gamma_{SV}^{d} + \gamma_{SV}^{p} \tag{2.4}$$

In Equations 2.5 and 2.6, γ_{SV} and γ_{LV} represent the solid surface energy and liquid surface tension, where the superscripts d and p represent dispersive and polar contributions. θ is the contact angle.

$$\gamma_{SV}^{p} = \frac{1}{\gamma_{LV}^{p}} \left(\frac{\gamma_{LV}(1+cos\theta)}{2} - \sqrt{\gamma_{SV}^{d}\gamma_{LV}^{d}} \right)^{2} \tag{2.5}$$

The surface tension of water and hexadecane is 72.1 and 27.5 mN m^{-1}, respectively.[146] The polar and dispersive contributions to the water surface tension are 51.0 and 21.1 mN m^{-1}, respectively.[146]

$$\gamma_{SV}^{d} = \gamma_{LV} \left(\frac{1+cos\theta}{2} \right)^{2} \tag{2.6}$$

Maharjan provides additional insights into the derivation of Equations 2.5 and 2.6. The interested reader is referred to his work for more details.[146]

2.14 Dynamic Mechanical Analyzer (DMA)

Figure 2.15: TA dynamic mechanical analyzer (RSA III) utilized in the mechanical characterization of the polysaccharide thermoplastic films in Chapter 6.

A TA dynamic mechanical analyzer (RSA III) instrument was used to measure the tensile force and strain of a 0.5 cm by 2 cm membrane cutout. The instrument was set to stretch at a rate of 0.05 cm per second until failure was detected.

2.15 Oxygen Permeability (OP)

Figure 2.16: Experimental apparatus utilized in the study of gas permeability for a variety of polymeric films.

Oxygen permeability was characterized using a variable pressure, constant volume membrane apparatus, Figure 2.16, according to Equation 2.7:

$$P = -\frac{V_{DS}\delta}{ARTt}\ln\left(\frac{P_{US}-P_{DS}}{P_{US}}\right) \tag{2.7}$$

where the permeability (P) is in Barrer, V_{DS} (m^3) is the downstream volume, δ (m) is the membrane thickness, A (m^2) is the area of the membrane, R ($\frac{m^3 Pa}{molK}$) is the gas constant, T (K) is the absolute temperature, P_{US} (Pa) is the upstream pressure, and P_{DS} (Pa) is the downstream

pressure.[103] One can easily convert 1 Barrer to $6.48 \cdot 10^{-7}$ $\frac{cm^3_{STP}m}{m^2 dayPa}$ with both units commonly used when reporting permeability. Note that Equation 2.7 is valid for a linear increase in downstream pressure with respect to time when the downstream pressure is less than 1% of the upstream pressure. Additionally, the downstream pressure is taken as 0 at t=0.

Samples were prepared according to previous work[103] by measuring the sample thickness and adhering each sample to a brass disk with a hole of known area (1.28 cm^2) using a quick-setting epoxy glue. Within the apparatus, the brass disk was placed on a macroporous sintered metal support disc with the downstream side of known volume underneath the metal disc. A vacuum/-turbo pump was used to degas the apparatus and sample for a minimum of 12 hours before each experiment. After degassing was complete, oxygen was introduced to the upstream side of the apparatus and maintained at a constant pressure. A LabVIEW Data acquisition program monitored the upstream and downstream pressures and sample temperature using pressure transducers and a thermocouple, respectively. Oxygen permeated through the membrane until a permeation steady state was reached. Equation 2.7 was used to calculate the pure gas steady-state permeability of the polymer/oxygen system at 35°C.

2.16 Water Vapor Permeance (WVP)

Water vapor transmission rate (WVTR) and water vapor permeance (WVP) were measured over a 10-20 day period in which the mass of a water reservoir was monitored along with humidity and room temperature. The reservoir was constructed out of a mason jar and a whole was punched on the lid. The membrane was cut to fit the lid and the container was sealed to prevent water vapor leakage.

2.17 Fourier Transform Infrared (FTIR) Spectroscopy

A Shimadzu IRSpirit FTIR analyzer, Figure 2.17, was used for the characterization of glucan-benzoate detergents in Chapter 7.

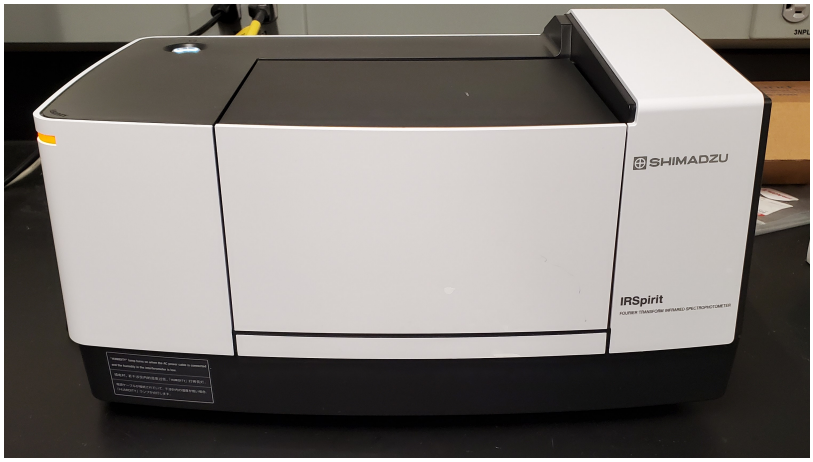

Figure 2.17: Shimadzu IRSpirit FTIR analyzer.

The FTIR analyzer uses a polychromatic light source that passes through a Michelson interferometer to produce the illumination used to probe the analyte. The Michelson interferometer moves a mirror along one axis during the analysis to obtain different wavelengths of illumination. The detector measures the intensity of light at the these positions (in cm) and applied a Fourier transformation to convert the displacement of the mirror into is inverse domain (wavenumber in cm^{-1}).

The samples were analyzed in KBr pellets by grinding and mixing both the analyte and KBr before using a manual press to create a translucent pellet.

2.18 Gas adsorption

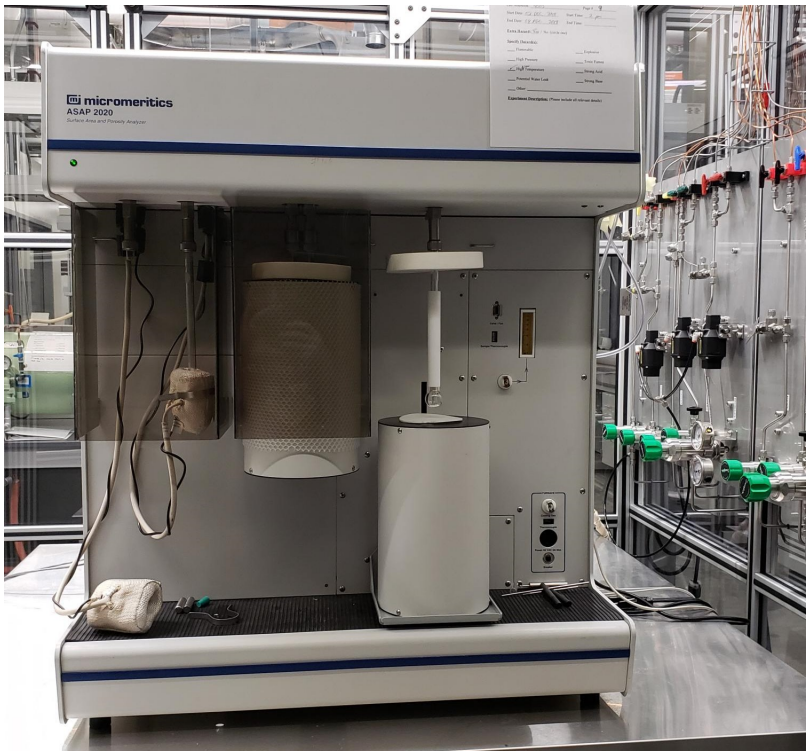

Figure 2.18: Micromeritics ASAP 2020 analyzer

Micromeritics ASAP 2020, Figure 2.18, was utilized in the measurement of specific surface area. The instrument has two degassing stations and one analysis port. The gas manifold, has a variety of gases for use under physisorption and chemisorption capabilities; however, for physisorption, we primarily use helium and nitrogen gas, and vacuum.

Each sample is prepared by placing enough material so that at least 1 m^2 of surface area is present for analysis. Depending on the material, this might vary between tens of milligrams to a gram of material. Once the material is in the bulb, a filler rod is used to minimize the volume of the sample cell. Once prepared, the sample cell is placed in one of the pretreatment stations where the sample is heated under vacuum. For soft matter, we might implement low temperature pretreatment steps, while for hard matter, we can implement temperature up to 350°C for 12-24 hours. Then, the mass of the degassed sample can be measure, while keeping moisture and air from coming into the tube. Then, the sample cell is placed in the analysis port where the free volume

will be measure and the amount of volume of nitrogen.

For surface area analysis, we use a 5 point (BET) analysis described by Equation 2.8. X is the weight of nitrogen adsorbed at a given relative pressure ($\frac{P}{P_0}$). C is a correlation coefficient. V_m is the volume of the monolayer.

$$\frac{1}{X((\frac{P_0}{P})-1)} = \frac{C-1}{V_m C}\left(\frac{P}{P_0}\right) + \frac{1}{V_m C} \tag{2.8}$$

Once we determine a value for a monolayer, we can use Equation 2.9 to calculate the surface area of the material.

$$\mathrm{SA}_{BET} = \frac{V_m \times (0.162\ \mathrm{nm}^2) \times (6.023 \times 10^{23})}{(22414\mathrm{cm}^3\mathrm{STP}) \times (10^{18}\mathrm{nm}^2/\mathrm{m}^2)} \tag{2.9}$$

2.19 Low Field NMR

For an in-depth review on Low Field NMR spectroscopy, including instrumentation and methods, please refer to Section 8.2.

For the purposes of this dissertation, we will be utilizing a Bruker Minispec mq 20 LF-NMR, Figure 2.19, in Chapters 4 and 8 as an analytical tool for residence time distributions and to measure the specific surface area of polymeric materials.

Figure 2.19: Bruker Minispec mq 20 Low Field NMR.

The following equation is utilized throughout this dissertation to provide insights into the NMR

response versus solute concentration (wt. ratios) and the specific surface area of a polysaccharide material.

$$\frac{1}{T_2} = \frac{1}{T_{2b}} + (\rho_2 \times SSA_{BET}) \frac{\text{Mass of solute}}{\text{Mass of Solvent}} \tag{2.10}$$

T_2 is the LF-NMR response, the T_{2b} is the response of the LF-NMR associated with the bulk fluid, ρ_2 is a constant for a material based on its surface chemistry, SSA_{BET} is the specific surface area of a material obtained from gas adsorption, and the wt. ratio is based on the slurry/solution being analyzed.

Chapter 3

Kinetics and Pathway Analysis Reveal an Unprecedented Mechanism for a Homogeneous Iron Catalyzed Nitrile Hydrogenation

Abstract

Nitrile hydrogenation via a PNP-$Fe^{II}(H)_2CO$ catalyst leads to previously inexplicable loss of mass balance. Reaction kinetics, reaction progress analysis, in-situ pressure NMR and X-ray diffraction analyses reveal a mechanism comprising a reversible cascade of imine self-condensation cascade that yield >95% primary amine. Imine self-condensation has never been reported in a nitrile hydrogenation mechanism. The reaction is first order with catalyst and hydrogen and zero order upon benzonitrile in 2-propanol solvent, Equation 3.1. Variable temperature analysis revealed values for $\Delta G^{\ddagger}_{298K}$ (79.6 $\pm$ 26.8 [kJ mol^{-1}]), $\Delta H^{\ddagger}$ (90.7 $\pm$ 9.7 [kJ mol^{-1}]), and $\Delta S^{\ddagger}$ (37 $\pm$ 28 [J mol^{-1} K^{-1}]), consistent with a solvent-mediated proton-shuttled dissociative transition state. This work provides a basis for future catalyst optimization and essential data for design of continuous reactors with earth-abundant catalysts.

$$Rate = [H_2]_S \left[\frac{1}{k[PNP = Fe(H)CO]} + \frac{1}{K_L a_B} \right]^{-1} \tag{3.1}$$

3.1 Introduction

The use of iron (Fe) as a metal catalyst for nitrile hydrogenation has many benefits consistent with green chemistry & engineering principles that help further the U.N. Sustainable Development Goals (SDG).

First, the high natural abundance of iron results in environmental and economic savings as less energy is emitted to extract a given quantity of its mineral forms,[172,251] making better use of our water and land resources (SDG Goals 14 and 15). Second, iron has one of the highest permissible concentration limits in final drug formulations due to its low toxicity,[244] promoting inherent safety and the health and well-being of stakeholders (SDG Goal 3). The tridentate PNP-$Fe^{II}(H)_2CO$ (**1**) catalyst of interest to this investigation has been used in the hydrogenation of nitriles[33], esters[49], amides[197], and alkenes[247] and in the dehydrogenation of alcohols[50], including glycerol[209], formic acid[27] and N-heterocycles.[48] In fact, this complex can hydrogenate 45% of the most common substrates reduced during pharmaceutical processes.[47] This versatility promotes industrial innovation (SDG Goal 9) with minimal material diversity. Furthermore, the use of a tridentate ligand increases the durability of the catalyst, supporting more efficient resource utilization (SDG Goal 12).

Nitrile hydrogenations are atom economic, catalytic transformations that can easily replace stoichiometric reactants, e.g., sodium borohydride in pharmaceutical synthesis. Some primary (1°) and secondary (2°) amines have become common building blocks for many HIV integrase inhibitors, bronchodilators, and antidepressants, e.g., dolutegravir, albuterol, and venlafaxine, respectively, Figure 3.1. Jamison & coworkers utilized a benzylamine moiety in the 7-step continuous synthesis of dolutegravir.[256] Similarly, albuterol is known to utilize tert-butyl benzylamine in one of its syntheses.[232] Kobayashi & coworkers utilized a continuous reactor to synthesize venlafaxine, an antidepressant, relying on a hydrogenation of a phenylacetonitrile derivative.[201] The design of continuous reaction technologies requires understanding of intrinsic kinetics, which is often overlooked in early catalyst development. Based on the previous examples, we utilize benzonitrile as a representative substrate to selectively produce benzylamine, a common pharmaceutical building block.

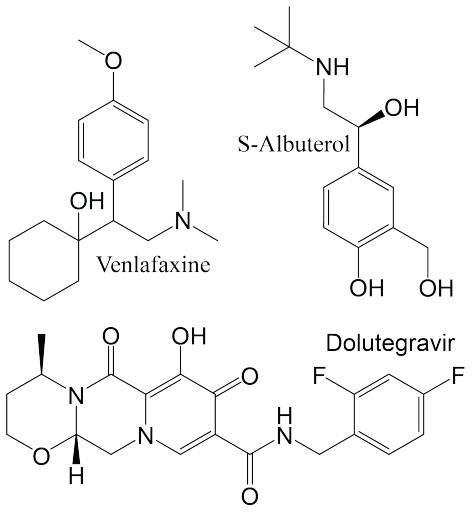

Figure 3.1: Approved drugs synthesized using nitrile hydrogenation. Venlafaxine is an antidepressant used to treat major depression disorders. Albuterol is a bronchodilator used to treat asthmatic patients. Dolutegravir is an HIV integrase inhibitor that decreases viral replication.

Highly selective homogeneous nitrile hydrogenation catalysts have recently appeared in the literature. The first generation of homogeneous complexes used noble metals, i.e., ruthenium (Ru),[20,21,138,195] rhodium (Rh),[2] and osmium (Os).[25] To reduce cost and improve sustainability, the second generation of catalyst used non-noble metals, e.g., iron (Fe),[33,51,135] cobalt (Co),[68,161,227] or manganese (Mn).[83,92,208] While there have been notable advancements in synthetic methodology, there remains insufficient kinetic and mechanistic understanding of these reactions under process relevant conditions. A number of studies have focused on exploring substrate scope, improving catalyst design for specific substrates, and generating a high-level understanding of the respective catalytic cycle via nuclear magnetic resonance (NMR) and idealized density functional theory (DFT) calculations, which may ignore solvation and pressure effects.[25,33,138,195] To our knowledge, there has been no report characterizing the concentration profile of reaction intermediates and exploring the relevant mechanistic implications. Herein, we report the surprising role of imine self-condensation, which challenges the conventional view of the amine formation mechanism. Additionally, using in-situ techniques, we identify reaction intermediates, the rate determining step, reaction kinetics under high pressure and temperature, and characterize the operative transition state for benzonitrile hydrogenation, catalyzed by PNP-$Fe^{II}(H)_2CO$ (**1**) complex.

3.2 Materials & Synthetic Methods

3.2.1 Synthesis of Iron Catalytic Complexes for the Hydrogenation of Benzonitrile

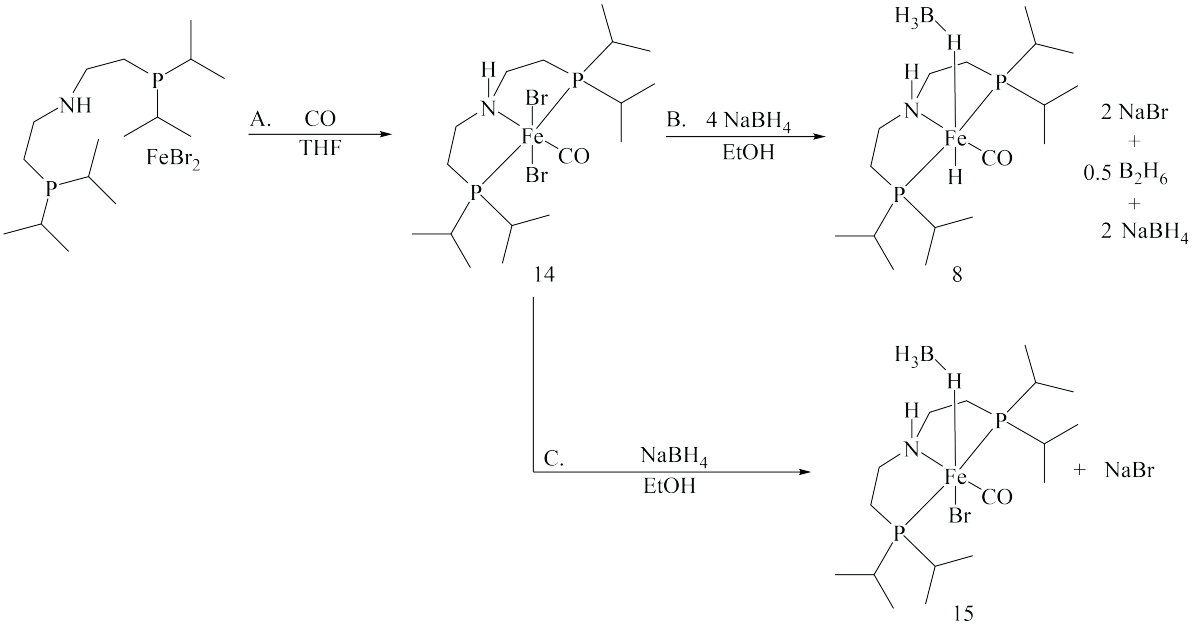

Figure 3.2: Synthesis (steps A and B) of PNP-Fe(H)(BH_4)CO complex (**2**) and competitive reaction (step C) to form PNP-Fe(Br)(BH_4)CO (**3**) complex with respective byproducts.

All chemicals were used as received. Sure seal, anhydrous tetrahydrofuran (SKU: 401757-100ML), ethanol (SKU: 459836-100ML), and toluene (SKU: 244511-100ML) and iron (II) bromide (SKU: 400831-10G) were purchased from Sigma Aldrich. A 10% solution of Bis [(2-di-i-propyl phosphino) ethyl]-amine (SKU: 15-7304) ligand in tetrahydrofuran was purchased from Strem Chemicals, Inc. Carbon monoxide (SKU: SG G1918775) was purchased from Matheson Tri-Gas. Sodium Borohydride (SKU: 213462-25G) was purchased from EMD Millipore.

The syntheses of PNP-Fe($Br)_2$CO (**14**) and PNP-Fe(H)(BH_4)CO (**8**), Figure 3.2, were conducted according to the methodology reported by Guan & coworkers.[49] Further details are provided (vide-infra) in this text. However, it is worth mentioning that there are different synthetic routes available in the literature for the same complex.[33,125]

3.2.1.1 Synthesis of Iron Dibromide Complex (14)

In a N_2 glovebox, 20.945 g of the 10% PNP ligand/THF solution was added slowly to a stirred solution of $FeBr_2$ (1.4072 g, 0.95 equiv.) and THF (75 ml) in a 100 mL Schlenk flask. The slurry changed color from orange/yellow to white with a concomitant increase in viscosity. The Schlenk flask was moved to a N_2 Schlenk line where CO was bubbled (at 10 psig inlet pressure) through the solution for about 30 min, until the solution turned a deep blue color and the viscosity decreased. Excess CO was diluted with N_2 and exhausted to the back of the fume hood. Safety note: CO is an extremely dangerous gas and appropriate safety measures are required, e.g., adequate ventilation and electronic CO monitoring. The solution was evaporated, yielding a blue powder. The powder was washed three times with 25 ml of pentane to remove free ligand and later dried under vacuum. To corroborate quality, a ^{1}H and ^{3}1P NMR in benzene-d6 were obtained, Figures A.1S and A.2S, respectively.

3.2.1.2 Synthesis of Iron Borohydride Complex (8)

In a glovebox, a 100 mL Schlenk flask was charged with 0.967 g of PNP-Fe$(Br)_2$CO- and 0.339 g of $NaBH_4$ (5.1 equiv.). The flask was transferred to the Schlenk line where 60 mL of chilled EtOH was transferred to the flask via a 22 gauge cannula. The blue and white powders slowly dissolves yielding a yellow solution and warming to room temperature over 16 hours. The ethanol was evaporated, yielding a dark yellow powder. The contents of the flasks were extracted with toluene and passed through a sand-Celite-sand plug. The sand and Celite were dried in a vacuum oven at 100°C and 25 in.Hg of vacuum for $>$ 3 h before use. The process removes excess $Fe(Br)_2$, NaBr, among other impurities. Note: These salts and remaining impurities are soluble in THF and therefore this solvent is not useful for the Celite filtration. Toluene has a boiling point of ca. 110 °C; making it hard to evaporate. An NMR in benzene-d6 of the filtered residue compound was taken. It revealed the presence of the by-product Fe(H)(Br)CO and the pre-catalyst Fe$(H)(BH_4)$CO along with phosphine oxide (P-Ox) impurities. A tolune-pentane crystallization was performed and removed free ligand and P-Ox impurities. To increase yield and purity the

residue was dried and treated with an additional 0.0722 g of $NaBH_4$ and reacted in chilled ethanol for 18 hrs to convert Fe(H)(Br)CO to Fe(H)(BH_4)CO. The solution was evaporated, filtered, and crystallized as previously described to yield a pure yellow Fe(H)(BH_4)CO powder with purity >93%, Figures A.3S and A.4S.

It is important to note that to reduce batch variability and therefore reaction performance of the catalyst, the purity was kept at or above 93%.

3.3 Results & Discussion

3.3.1 Reaction Kinetics

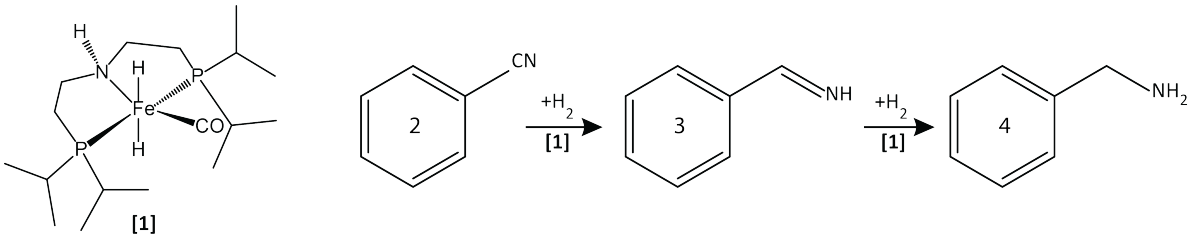

Figure 3.3: Overall benzonitrile hydrogenation catalyzed by PNP-$Fe^{II}(H)_2CO$ (**1**)

A preliminary screening of solvent effects in the hydrogenation of benzonitrile to benzylamine (0.1 mol% catalyst **1**, 30 bar H_2, 70°C, 2 hours) corroborated the preferred performance of 2-propanol solvent with 94% benzonitrile conversion, as observed by Beller & coworkers, Figure S7.[33] Solvent clearly plays a role in catalysis, perhaps modulating the stability of catalytic and reactive intermediates. The reaction rate decreased in tert-butanol which resulted in 48% benzonitrile conversion. Intriguingly, hexafluoro-2-propanol, chosen for its high solubility of hydrogen, did not achieve any percent conversion. Likely, the acidity of this solvent interferes with catalysis. Based on these findings, 2-propanol was selected for kinetic investigations.

The PNP-$Fe^{II}(H)_2CO$ (**1**) catalyzed benzonitrile hydrogenation proceeds rapidly through a series of intermediates, achieving 50% conversion within 15 minutes. H_2 uptake measurements provide high-frequency sampling and were preferred in kinetic studies compared to offline chro-

matographic analyses. The derivation of the H_2 uptake equation (Eq. 3.2) and the propagation of uncertainty through this equation can be found in the Supporting Information.

$$Rate = \frac{1}{\alpha}\frac{dC_a}{dt} = \frac{1}{RT}\frac{dP}{dt}\frac{V_g}{V_L} \tag{3.2}$$

H_2 uptake measurements, collected in the absence of mass transfer influence (Supporting Information) were used to accurately quantitate the intrinsic reaction rate and study the concentration dependence of substrates and catalyst, as described by Eq. 3.3.

$$Rate = k[H_2]_B^x[Fe]^y[BN]^z \tag{3.3}$$

The hydrogenation of benzonitrile with an PNP-$Fe^{II}(H)_2CO$ (**1**) catalyst proceeds efficiently at moderate temperatures and pressures and relatively low catalyst concentrations (ca. 0.01-1 mol%). At 0.1 mol% PNP-$Fe^{II}(H)_2CO$, 70°C, 1000 rpm, 48 bar H_2, and 0.3 M of benzonitrile the reaction achieved complete conversion and excellent yield of primary (1°) amine, >95% within 90 minutes, Figure 3.4A. Intriguingly, there was a momentary loss of % mass balance (%MB) at 50% conversion that had not previously been reported in the literature for a PNP-$Fe^{II}(H)_2CO$ catalyzed benzonitrile hydrogenation. The temporary loss in % mass balance (%MB) is attributed to the formation of higher molecular weight oligomeric intermediates (vide-infra) not detectable via established GC methodology and has been reproduced many times. A conventional view of nitrile hydrogenation invokes secondary and tertiary amine formation via condensation reactions, but is inconsistent with the present data, which show negligible yield to such species at high conversion.[7,235]

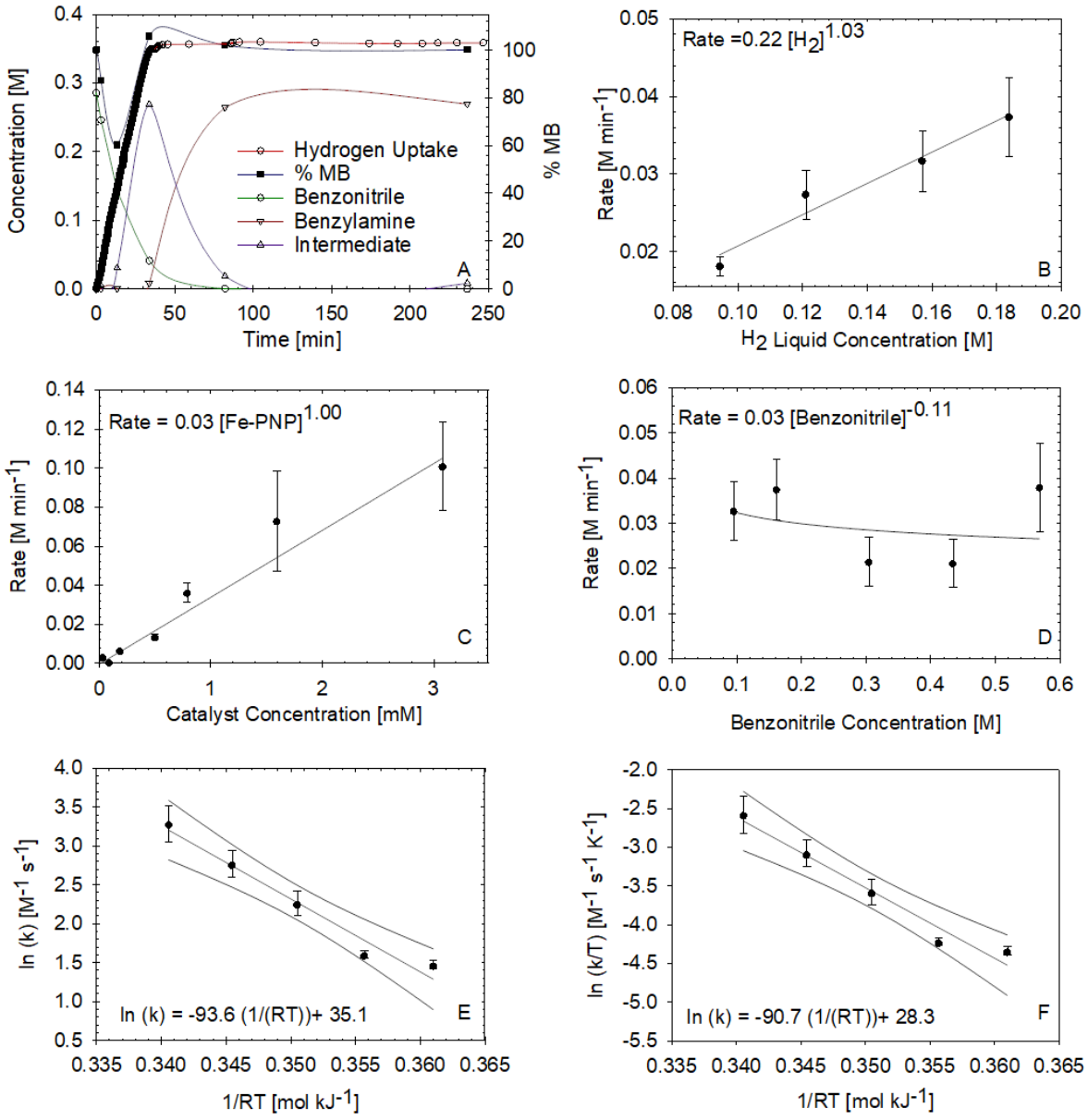

Figure 3.4: A) Concentration-time profile of reaction media evaluated via off-line GC analysis accompanied by H_2 uptake measurements, B) Influence of H_2 liquid concentration on reaction rate, C) Influence of PNP-Fe^{II}(H)$_2$CO catalyst concentration on reaction rate, D) Influence of benzonitrile concentration on reaction rate, E) Arrhenius plot with second order rate constant, and F) Eyring plot yielding reaction energetics based on transition state theory. E and F are plotted with the 95% confidence interval associated with the data.

Figure 3.4B-D plot H_2 uptake derived reaction rates versus H_2, PNP-Fe^{II}(H)$_2$CO (**1**), and benzonitrile concentrations, respectively. Figure 3.4B explores the reaction rate dependence on H_2 concentration between 24 and 48 barg, or 0.09-0.18 M (in 2-propanol at 70°C). The rate of

reaction has a 1^{st} order dependence with H_2 concentration. Figure 3.4C portrays the dependence of the rate of reaction on catalyst concentration between 0.01 to 1 mol%, or 0.03 to 3.1 mM. A higher concentration and, therefore, reaction rate, were avoided as they would lead to mass transfer limitations, masking the intrinsic kinetic regime. The rate of reaction exhibits a 1^{st} order dependence on catalyst concentration. In Figure 3.4D the reaction rate was determined to be independent of benzonitrile concentration. In developing a rate expression, it is appropriate to consider the role of mass transfer rate, which is a function of the overall mass transfer coefficient ($K_L a_B$) and the difference between the equilibrium solubility of the gas in the liquid ($[H_2]_S$) and the bulk liquid hydrogen concentration ($[H_2]_B$), Eq. 3.4.

$$Rate = K_L a_B([H_2]_S - [H_2]_B) \tag{3.4}$$

An overall rate expression combining the intrinsic kinetics and mass transfer contributions into an overall expression yields Eq. 3.5, where PNP=Fe^{II}(H)CO (**6**) is the dominant catalytic species during the rate determining step:

$$Rate = [H_2]_S \left[\frac{1}{k[PNP = Fe(H)CO]} + \frac{1}{K_L a_B} \right]^{-1} \tag{3.5}$$

Through Arrhenius (Figure 3.4E) and Eyring (Figure 3.4F) plots, the activation energy (E_a, 93.6 $\pm$ 9.7 [kJ mol^{-1}]), pre-exponential factor (A, $1.75 \cdot 10^{15} \pm 4.9 \cdot 10^4$ [M^{-1} s^{-1}]) and transition state energetics, i.e., Gibbs free energy, $\Delta G^{\ddagger}_{298K}$ (79.5 $\pm$ 25.1 [kJ mol^{-1}]), enthalpy $\Delta H^{\ddagger}$ (92.0 $\pm$ 8.4 [kJ mol^{-1}]), and entropy $\Delta S^{\ddagger}$ (37.7 $\pm$ 92 [J mol^{-1} K^{-1}]), were regressed. The uncertainty in the pre-exponential factor, and entropy values were determined through the extrapolation of the 95% confidence interval.

The observed kinetic behaviors are characteristic of the rate-determining step being associated with hydrogen addition in the catalyst cycle. Figure 3.6 represents the mechanism, consistent with the above observations. 1) PNP-Fe^{II}(H)(BH_4)CO is activated in-situ by secreting B_2H_6 in the presence of hydrogen. 2) Catalyst species **1** participates in outer-sphere partial hydrogenations

of benzonitrile or benzylimine to yield the Fe^{II} amide complex (**5**). 3) Species **5** is stabilized by 2-propanol to form PNP-Fe^{II}(H)(iPrOH)$_2$CO (**6**). 4) Species **6** proceeds through a rate controlling transition state (**4c**) where hydrogen addition is facilitated by the hydrogen bond network between the N-H ligand backbone and 2-propnaol molecules. 5) 2-propanol is secreted out of the catalyst cycle, regenerating the activated complex, **1**.

Beller & coworkers conducted DFT investigations, ignoring the role of solvent but providing evidence of an outer-sphere mechanism for the partial hydrogenation of benzonitrile to benzylimine, determining an activation energy of 64.4 [kJ mol^{-1}]. The outer sphere mechanism was established based on the energetic penalty for an inner sphere mechanism, specifically for a benzonitrile molecule replacing a CO ligand in the catalyst complex.[33] In the DFT study, the highest energetic barrier, 71.5 [kJ mol^{-1}], was the addition of H_2 to **5**.[33] The experimental $\Delta G^{\ddagger}_{298K}$ value of 79.5 $\pm$ 25.1 [kJ mol^{-1}] and that calculated by Beller & coworkers are in reasonable agreement with one another and fall within the error associated with the experimental data. The assignment of the rate-controlling transition state is supported by reaction energetics retrieved from the Eyring plot (Figure 3.4F). The high $\Delta H^{\ddagger}$ suggests the presence of a hydrogen bond network in the transition state.[212] A positive $\Delta S^{\ddagger}$ suggests the presence of a dissociative mechanism consistent with release of the proton-shuttle, 2-propanol.[95]

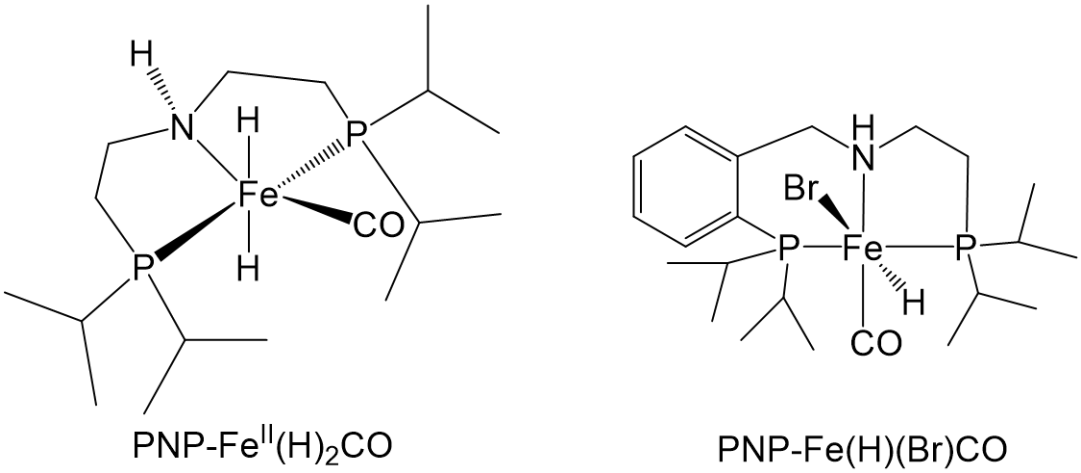

Figure 3.5: A depiction of Beller's PNP-Fe*II*(H)$_2$CO and Milstein's PNP-Fe(H)(Br)CO catalysts.

Wang & coworkers furthered Milstein's investigation into an alternate PNP ligand complex:

PNP-Fe(H)(Br)CO (Figure 3.5) conducting DFT calculations simulating the catalyst cycle.[109] Their DFT investigation included the role of solvation in toluene but not a protic solvent and concluded that the greatest energetic barrier with the PNP-Fe complexes, 97.5 [kJ mol^{-1}], is associated with hydrogen addition. This value falls within the error of the present, experimentally determined $\Delta G^{\ddagger}_{298K}$, but the positive offset of the simulated value could be attributed to the absence of a protic solvent serving as a proton shuttle. Notably, Hazari & coworkers investigated the role of alcohol solvents (tert-butanol in particular) as proton shuttles, suggesting alcohol solvents aid the activation of H_2 by shuttling protons between the amide moiety of the ligand and the iron(II) centered activation of H_2.[214] Recently, Chianese & coworkers conducted an extensive kinetic and density functional theory (DFT) investigation on Milstein's PNN-Ru$(H)_2$CO complex[254] utilized in ester hydrogenations.[183] The N-H moiety in the ligand, also present in PNP ligands, plays a crucial role in the activity of this catalyst and stability of intermediates through hydrogen bonding.

These kinetic studies provide important insights to spur further catalyst design efforts, as well as reactor design for continuous manufacturing. Both are important themes in our research program. Still, they do not directly clarify the temporary loss of mass balance in reaction profile, Figure 3.4A. Most DFT calculations are conducted assuming gas phase conditions (1 atm or below), however, elevated pressures allow for better representation of entropy effects arising from the restrictions in the translation degrees of freedom experienced by liquid phase reactions. Buhl & coworkers calculated the effects of pressure upon entropy calculations; the increased density of the system increased entropic values by nearly 83.7 [J mol^{-1} K^{-1}] in contrast to non-pressurized systems.[211]

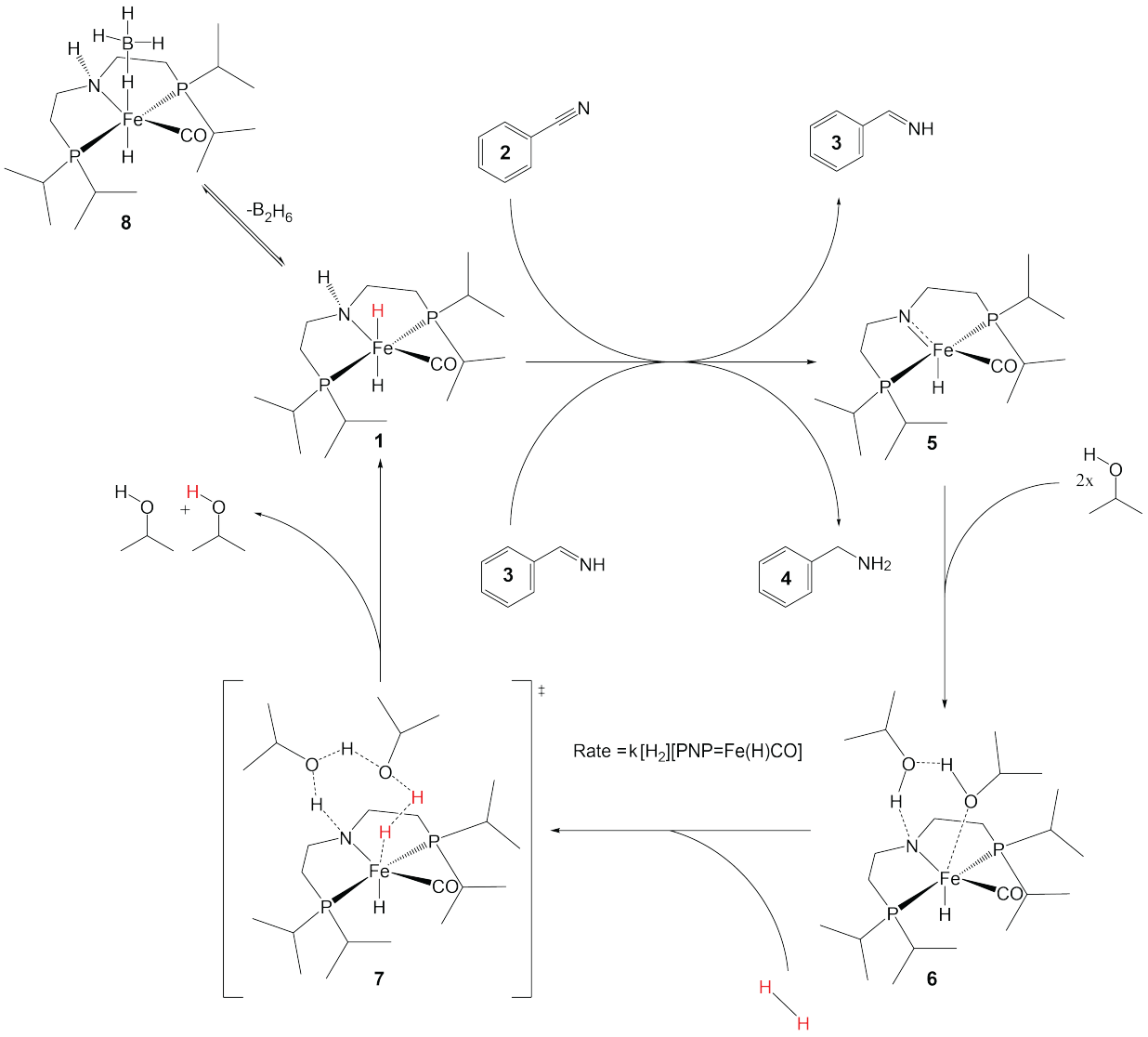

Figure 3.6: Catalytic micro-kinetic steps for the hydrogenation of benzonitrile incorporating shuttling effects of 2-propanol

3.3.2 Reaction Mechanism

To the best of our knowledge, the reaction profile presented in this investigation has not been reported in the literature for the hydrogenation of benzonitrile to benzylamine and is differentiated from those observed in the heterogeneous catalysis. For example, in heterogeneously catalyzed nitrile hydrogenations, the von Braun-Greenfield mechanism is often invoked and ammonia is frequently used as an auxiliary component to drive the equilibrium towards benzylimine to avoid

secondary amine formation.[7] Furthermore, when using heterogeneous catalysts, modern mechanistic investigations clearly describe the role of surface intermediates in amine condensation and the absence of observable primary imine accumulation.[7,64] Indeed, Sachtler & coworkers conclude that primary imine cannot be an intermediate in nitrile hydrogenation over Ru, which favors surface bound nitrene and carbene species. Here, we present a reaction cascade for the hydrogenation of benzonitrile to benzylamine using (**1**) that is consistent with all observed reactivity trends, Figure 3.7. The temporary loss of mass balance in GC analysis, shown in Figure 3.4A, is attributable to oligomeric intermediates formed via two reversible cascades that are governed by the nucleophilicity of benzylimine and benzylamine, respectively. Published density functional theory (DFT) calculations fail to investigate the formation of these intermediates due to a lack of experimental evidence. Leitner & coworkers point out the need to explore all imaginable pathways to form reaction intermediates, as there might be stable energetic minima that can be reached through low-lying transition states.[199] To support the proposed mechanism (Figure 3.7), in-situ pressure NMR investigations were conducted, Figure 3.8.

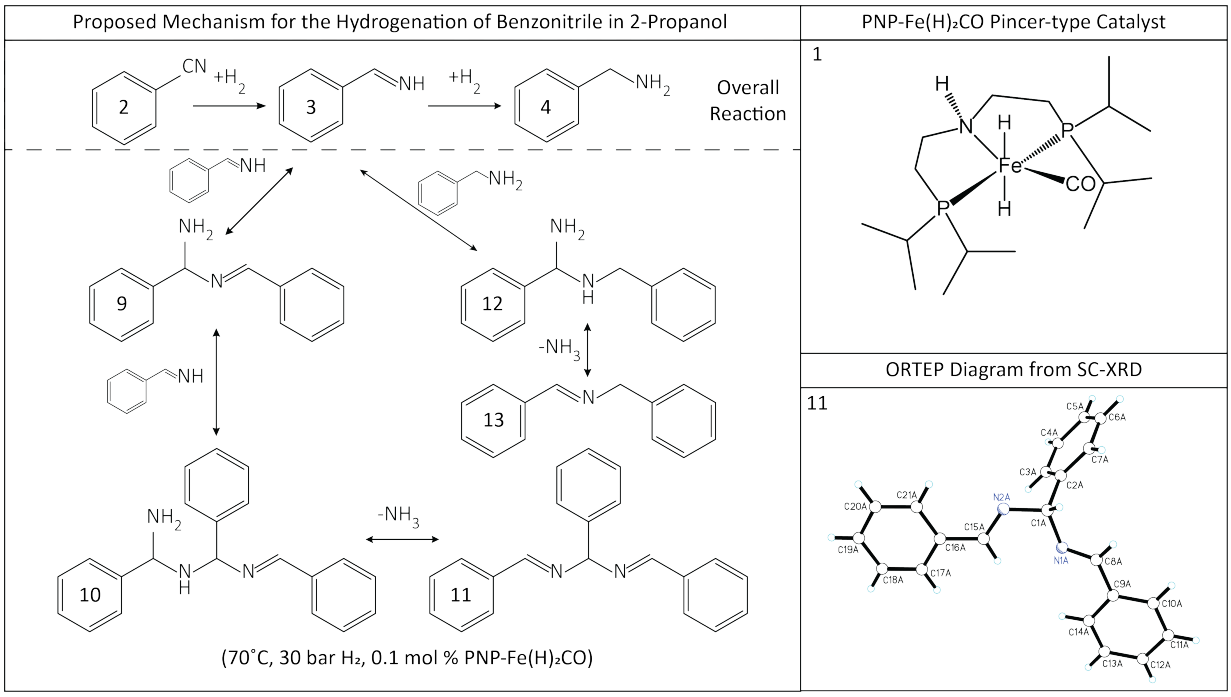

Figure 3.7: Proposed mechanism for the hydrogenation of benzonitrile with an PNP-Fe^{II}(H)$_2$CO catalyst.

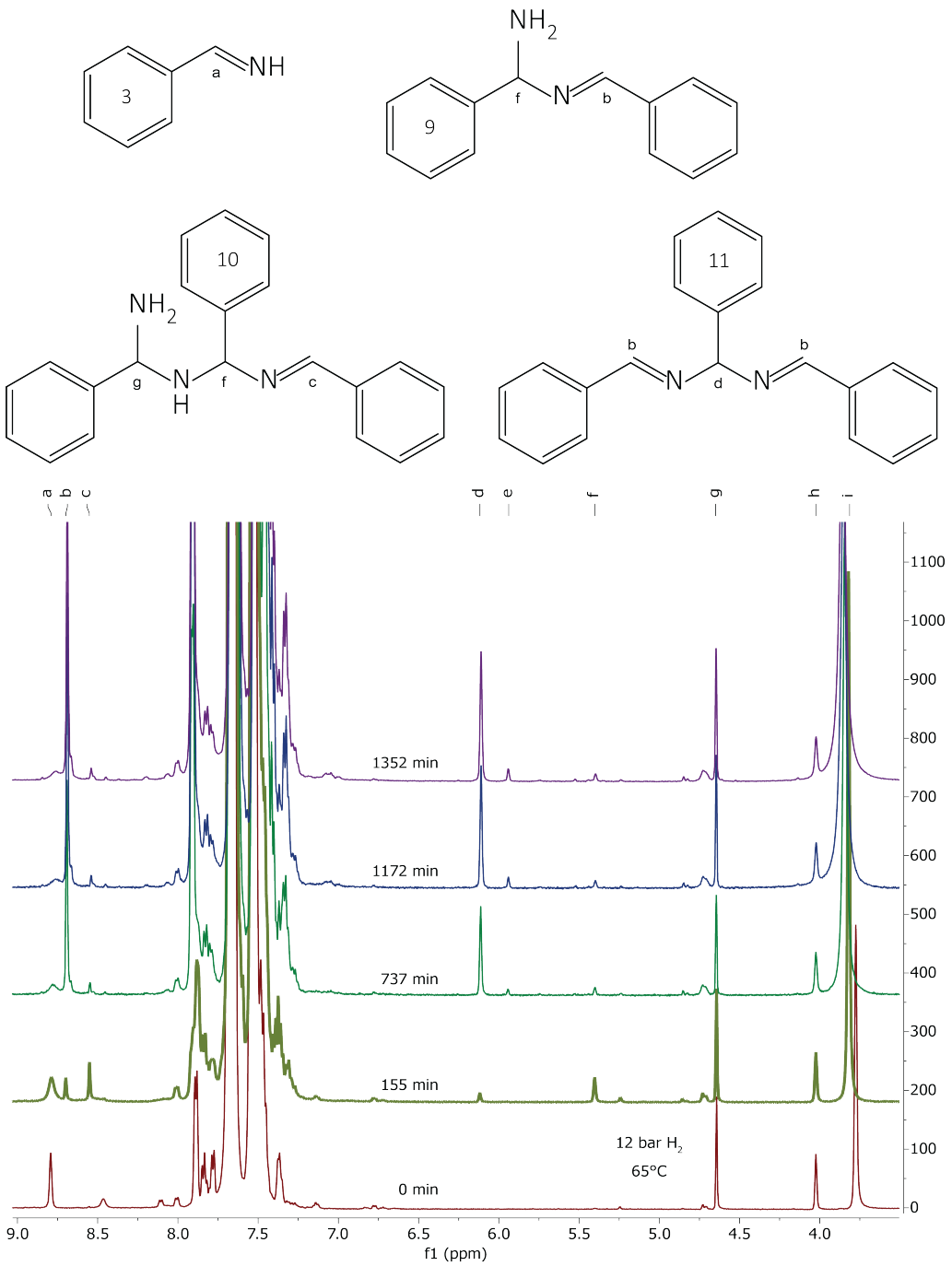

Figure 3.8: In-situ pressure NMR experiments at 12 bar H_2. ^{1}H NMR spectrum are referenced to 1.2 ppm, which correspond to the CH_3 peaks of 2-propanol.

The hydrogenation of benzonitrile at 12 bar and 65°C in deuterated isopropanol, was monitored via in-situ ^{1}H NMR spectroscopy every 5 minutes for the initial 60 samples and then every 15 minutes for the course of the remaining 24 hours, Figure 3.8. The final, top spectrum corresponds to

just 10-20% benzonitrile conversion, prior to the point of minimum %MB in the kinetic investigation (Figure 3.4A). Multiple imine proton resonances are observed in the region 8.5 8.8 ppm. In the first spectrum collected, 8.79 ppm is attributed to benzylimine (**3**), a species which disappears as the reaction progresses. Resonances at 5.94 and 6.12 ppm are consistent with oligomeric species **10**, **11** and similar higher order oligomers. These resonances are not observed early in the reaction but grow simultaneously with imine C-H resonances at 8.55 and 8.70 ppm, respectively. On reaching a certain mass, such oligomers may precipitate from solution or be too large to elute via the standard GC method, explaining the loss in %MB observed in Figure 3.4A. Notably, the formation of **10** and **11** can only be explained by imine acting as a nucleophile in a self-condensation. This reaction has precedent in the literature[57] and the interaction of **3** with the Fe catalyst may promote the condensation. To further support the mechanism, we interrupted a series of reactions at partial conversion when the %MB achieved the local minimum. Through an evaporative crystallization, we obtained triclinic crystals that were characterized through SC-XRD. The ORTEP diagram of N, N'-(phenylmethylene)bis(1-phenylmethanimine) (**11**) is presented in Figure 3.7 and the Supporting Information contains additional data, i.e, crystallographic table, bond length and angle tables. It is evident from the crystallographic data that C(15A)-N(2A) and C(8A)-N(1A) are double bonds with lengths 1.279 and 1.259 Å, respectively. While N(2A)-C(1A) and N(1A)-C(1A) are each single bonds with bond lengths of 1.463 and 1.468 Å, respectively. Furthermore, the bond angles between N(1A)-C(1A)-C(2A) and C(9A)-C(8A)-N(1A) are 110.4° and 118°, indicative of sp^2 and sp^3 hybridization, respectively. In independent experiments, control samples of **11** and **13** are not hydrogenated to **4** nor to secondary amine structures, suggesting steric hindrance impedes reaction for this catalyst. Given the high selectivity (>95%) of the optimized reaction, the removal of NH_3 from aminals like **9** and **11** to form secondary imines is not preferred in-situ. Rather, the oligomeric cascade eventually reverts to monomeric **3** on the path to **4**. The isolation of single crystals of **11** through evaporative crystallization is consistent with slow condensation of NH_3 from structures like **11**. Milstein & coworkers proposed **11** on the basis of GC-MS observations when studying an alternate PNP-Fe(H)(Br)CO pincer complex for secondary imine formation but did

not explain the mechanistic relevance.[52] Wang & coworkers determined the nucleophilic attack between a secondary imine and a nitrile to be unfeasible with an activation barrier greater than 418.4 [kJ mol^{-1}].[109]

During in-situ NMR studies, **4** was observed and may also participate in oligomeric cascades, (Figure 3.7). Experiments that included the addition of benzylamine as an initial condition, Figure 3.9 confirmed the oligomeric cascade controlled by benzylamine. Intriguingly, when sub-stoichiometric amounts of benzylamine were loaded into the reactor, the benzylimine cascade was temporarily eliminated from the reaction pathway delaying the onset of the %MB deficiency but prompting the immediate formation of **11**. In related work, Wang & coworkers concluded that a PNP-Fe(H)(Br)CO complex in toluene facilitated the nucleophilic coupling of benzylamine to benzylimine producing **11**.[109]

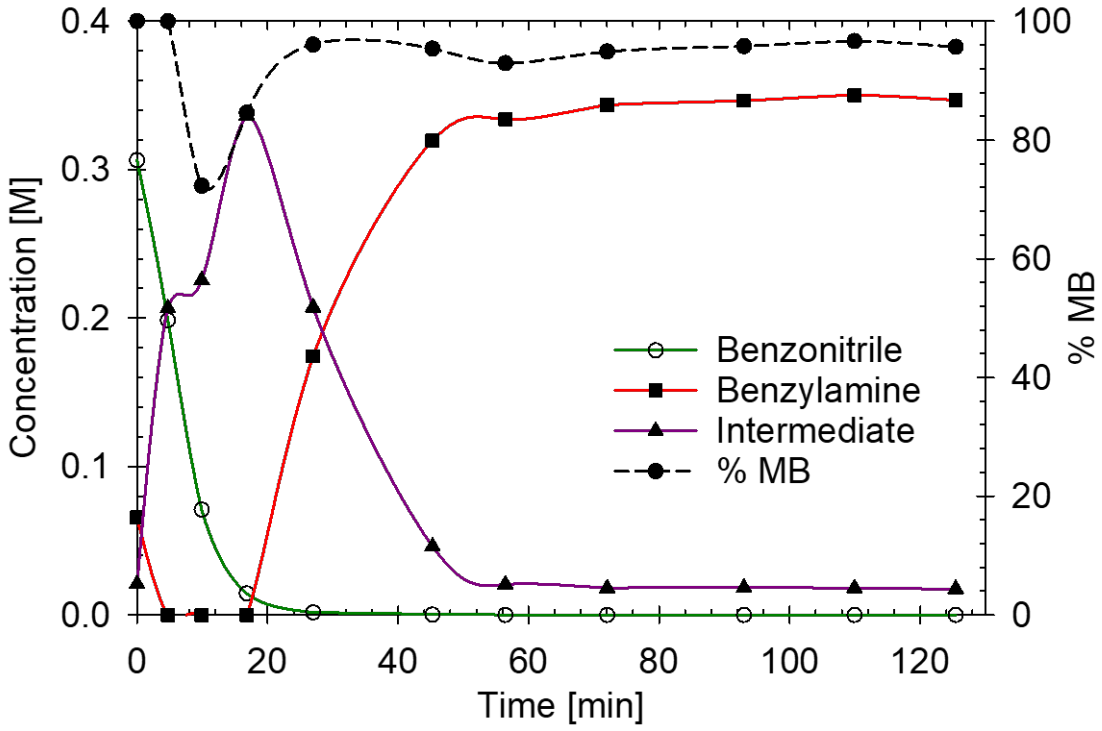

Figure 3.9: Reaction implementing sub-stoichiometric amounts of benzylamine at initial conditions.

Chemical processes that would allow for control over the selectivity of producing **11**, **13**, or **4**

would be of great value. Compound **11** has been used in the synthesis of an equivalent synthon to Ningnanmycin, an agrochemical used to treat tobacco mosaic virus (TMV).[249] Additionally, **11** has been used in the synthesis of substituted imidazoles, which have pharmaceutical relevance as antitumor agents, and inhibitors of p38 MAPK receptors, among others.[70] Continuous process options are anticipated to offer such control. Plug flow reactors facilitate control over conversion and associated selectivity in cascade chemistries but are challenged by mass transfer limitations in meso-scale continuous, low residence time distribution (RTD) reactors. Our future work will explore these strategies through custom reactor design.

3.4 Conclusion

The mechanism of benzonitrile hydrogenation to benzylamine with PNP-$Fe^{II}(H)_2CO$ catalyst **1** has been characterized by a combination of hydrogen uptake measurements, SC-XRD and in-situ high pressure NMR studies. For the first time, the intermediacy of oligomeric intermediates arising from imine self-condensation have been identified in the mechanism of nitrile hydrogenation. The crystal structure of derivative, **11** cannot result from amine imine condensation, supporting the mechanistic proposal. This investigation implicates aminal species as the transient form of intermediates in two completely reversible cascades en route to excellent yield of benzylamine. The nature of the oligomeric cascades can be controlled through hydrogen concentration or benzylamine loading in the reactor at initial conditions. Higher hydrogen pressures minimize the first oligomeric cascade, where benzylimine acts as the nucleophile, and promote selectivity to benzylamine. The opposite is also true, the trimeric species, **11**, is promoted at lower hydrogen pressures. An initial charge of benzylamine promotes the formation of the secondary cascade, where benzylamine acts as the nucleophile, to form a fleeting dimeric intermediate before forming benzylamine.

Protic solvents are preferred in the subject reaction. In the catalytic cycle, 2-propanol stabilizes the catalyst intermediates during hydrogen addition, which is mediated by proton shuttling. This occurs through a dissociative mechanism where the 2-propanol molecules are expelled from the

transition state as it regenerates complex **1**. These findings are consistent with regressed reaction energetics: $\Delta G^{\ddagger}_{298K}$ (79.6 $\pm$ 26.8 [kJ mol^{-1}]), enthalpy $\Delta H^{\ddagger}$ (90.7 $\pm$ 9.7 [kJ mol^{-1}]), and entropy $\Delta S^{\ddagger}$ (37 $\pm$ 28 [J mol^{-1} K^{-1}]). A high enthalpy value affirms the presence of a hydrogen bonding network, meanwhile a positive entropy is suggestive of a dissociative nature of the transition state. The rate of reaction exhibits a first order dependence on both hydrogen and catalyst concentrations. Meanwhile, benzonitrile does not influence the rate of reaction. Benzonitrile and/or benzylimine are partially reduced through an outer-sphere mechanism. The activation energy and pre-exponential factor were regressed through an Arrhenius plot and determined to be 93.6 $\pm$ 9.7 [kJ mol^{-1}] and $1.75{\cdot}10^{15} \pm 4.9{\cdot}10^{4}$ [M^{-1} s^{-1}], respectively.

Overall, this work advances the understanding of the PNP-Fe^{II}(H)$_2$CO complexes in nitrile hydrogenations to facilitate future catalyst optimization and design of continuous processes for industrial implementation in support of the U.N. sustainable development goals.

Chapter 4

A First Iteration at Enabling Continuous, Intensified, Modular Chemical Manufacturing

Abstract

Continuous flow reactors enable quality by design (QbD) strategies that minimize the risk of drug substance rejection during steady-state operations. Continuous flow reactors are categorized by their internal diameter (ID) into micro-, meso-, and macro-scale configurations. Traditionally, micro-scale reactors (ID $<$ 1 mm) produce gram quantities per day. Meso-scale reactors (1 mm $<$ ID $<$ 10 mm) can produce kilogram quantities per day. Macro-scale reactors (ID $>$ 10 mm) can produce tons of product per day. To take advantage of the high specific interfacial area and volumetric mass transfer coefficient of micro-scale reactors, but also the production capacity of a meso-scale reactor, a continuous flow hydrogenation on the low meso-scale regime is designed with an ID of 1.7 mm. A LabVIEW program integrates sensors to monitor reactor temperature, pressure, and control gas and liquid flow rates. Additionally, the science of residence time distribution analyses is advanced by providing the world with a robust off-line analyzer and tracer that approaches substrate identity.

4.1 Introduction

Continuous flow reactors are highly sensitive to mass transfer limitations, but are often desirable for their well-defined residence time distributions during steady-state operations that enable reliable quality by design (QbD) strategies. From a pharmaceutical perspective, reliable quality

control strategies[106] and Green Chemistry and Engineering (GC&E)[228] principles are fueling the search for reactors capable of efficacious mass transfer to meet kg and ton product quantities per day, Figure 4.1.[23,47]

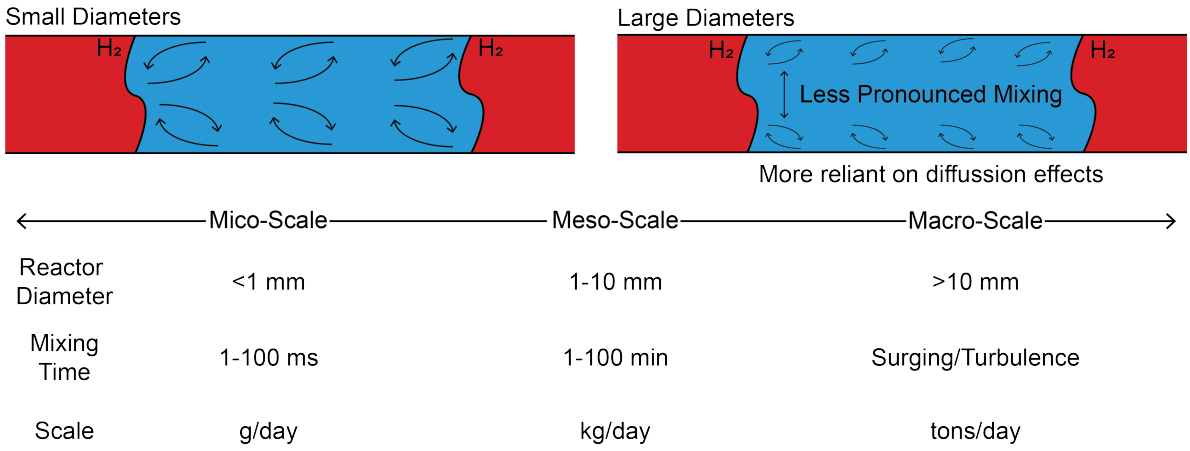

Figure 4.1: A depiction of the three continuous flow reactors by internal diameters (ID) and their transport and production capabilities.

Micro-scale reactors (ID $<$ 1 mm) have their place in early process development, with highly hazardous chemistries, or with highly potent drug substances that require less than a gram per day production capacity. Micro-scale reactors have gigantic specific interfacial area (SIA), a, and the volumetric mass transfer coefficient (VMC), $K_L a$, Table 4.1, arising from their small transport length and high mixing within fluid elements mandated by the proximity of the no-slip boundary condition at the reactor wall and the maximum linear velocity profile at the reactor's center, Figure 4.1. This behavior provides millisecond (ms) mixing times that make these reactors highly efficient. To increase production capacity with micro-scale reactor performance, one must adopt a numbering-up strategy rather than a scale-up of reactor dimensions, e.g., internal diameter. When trying to develop a flexible manufacturing supply chain, having numerous reactors that need to be changed between syntheses is not ideal; especially if one acknowledges that one facility is used to produce a large variety of drugs within a year. As a result, the ideal manufacturing platform would have one reactor with micro-scale regime performance that is easy to swap when different chemical transformations are required.

Table 4.1: Comparison of reactor type by specific interfacial area (SIA), a, and volumetric mass transfer coefficient (VMC), $K_L a$.

Reactor Type	**SIA** $\frac{m^2}{m^3}$	**VMC** (10^2 s^{-1})	**Source**
Bubble Column	50-600	0.5-24	147,169,192
Packed Column (concurrent)	10-1700	0.04-102	147,192
Spray Column	75-170	1.5-2.2	147,169
Static Mixers	100-1000	10-250	147
Stirred Tank	100-2000	3-40	147
Tubular Reactor (Horizontal)	50-700	0.5-70	147
Tubular Reactor (Vertical)	100-2000	2-100	147
Micro-channel Reactor	3400-18,000	30-2100	147,169
Corning Flow Reactor	160-1300	20-300	169
Falling Film Reactor	20,000	N/A	169
Tube-in-tube Reactor	3000-10,000	10-100	192

Meso-scale reactors (1 mm < ID < 10 mm) share properties of both micro- and macro-scale reactors in that at lower ID (ca. 5 mm or less) they behave as ideal plug flow reactors with gas-liquid slugs and at higher ID (above ca. 5 mm) bubbles surge through the liquid, promoting turbulence. In the former, the mass transfer interface is associated with the cross-sectional area of the reactor, while the latter is dependent on the number and size of gas bubbles. However, the primary drawback with meso-scale reactors is that most commercial static mixers that boost mass transfer efficiencies are not available in the lower meso-scale spectrum. As a result, there is a need for implementing additive manufacturing in the production of customizable meso-scale reactors that feature static mixer-type internal architecture.

Macro-scale reactors (ID $>$ 10 mm) are of great interest in the commodity chemical sector as they can meet tonnage production capacities while being compatible with static mixers, as well as heterogeneous catalyst and their porous supports. Chapter 8 describes the physics of x-ray

tomography and its applications in the in-situ investigation of heterogeneous catalyst activation and reactions. The interested reader is referred to Section 8.6.5 for details on this matter.

Here, a blueprint for developing continuous flow reactor platforms, characterizing the residence time distribution, and testing the reaction performance of a (ca. 2 mm ID) meso-scale flow hydrogenation reactor with a LabVIEW control and data acquisition platform is presented.

4.2 Reactor Design, Safety Attributes, and LabVIEW Program

The continuous flow reactor, Figure 4.2, was designed to have a low residence time distribution to enable intrinsic high quality profiles based on the reaction mechanism and reactive intermediates elucidated in Chapter 3. The identity of a valuable trimeric intermediate utilized in the formation of tri-substituted imidazoles, which make valuable agrochemicals and pharmaceuticals, is determined. Additionally, for the formation of primary amines, secondary imines, and oligomeric intermediates, a narrow residence time distribution is required.

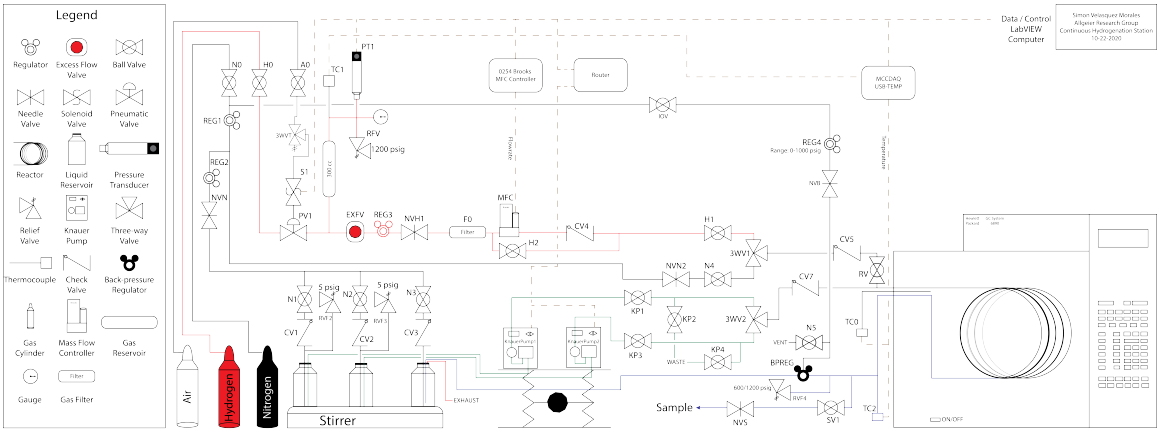

Figure 4.2: Process flow diagram (PFD) and data flows for the continuous flow hydrogenation reactor.

A GC (HP 6890) was utilized as a heating source due to its great insulating properties. No fittings were present inside the GC oven, as any hydrogen leak could lead to an explosion based on all the exposed motors and heating elements. The temperature was controlled through the oven's robust control system. A panel was mounted on the side of the GC oven to reduce footprint and

minimize heat losses through exposed tubing. Any exposed tubing was insulated through a heating tape control independently through its own control box, whose output was limited through a Variac transformer. Downstream of the reactor, an Equilibar back-pressure (Diaphragm) regulator was set at the desired reactor pressure using nitrogen gas. Upstream of the reactor, the liquids were supplied through Knauer 4.1S pumps, capable of performing between 1 μL to 10 mL per minute. Additionally, hydrogen gas flow was controlled through a high-pressure Brooks mass flow controller (MFC). All electronics were connected to the computer running LabVIEW with Ethernet, RS-232, and USB cables (vide-infra).

4.2.1 Hydrogen Safety

Continuous supply of hydrogen from a purchased cylinder was not permitted for continuous operations due to the risk of exceeding the hydrogen lower flammability limit (LFL) of 4 %. As a result, a 300 mL stainless-steel Swagelok reservoir to supply hydrogen throughout the course of the reaction was implemented. The reservoir would be resupplied when the pressure fell within 100 psig of the reactor's pressure to allow for the appropriate driving force required by the MFC between the reactor and the reservoir. This intermittent supply would limit the amount of hydrogen to the volume of the reservoir. The following calculation was performed to appropriately size the hydrogen reservoir, Equation 4.1.

$$
\begin{aligned}
V_{air} &= 1,161,300 \text{ mL} \\
V_{H_2} &= \frac{(0.834 \text{ mol}) \times (82.1 \frac{\text{mL atm}}{\text{mol K}}) \times (298K)}{(1 \text{ atm})} = 20,394 \text{ mL} \\
V\% &= \frac{20,394}{20,394 + 1,161,300} = 1.73\%
\end{aligned}
\tag{4.1}
$$

The stagnant volume of air inside a 5 feet long fume hood is denominated by V_{air}. V_{H_2} represents the volume of hydrogen at atmospheric conditions if the reservoir was filled with 68 atm of hydrogen and release its contents into the hood (at 1 atm). If the contents of the reservoir vent into

the hood, the volume percent of hydrogen in the stagnant air of the hood would equate to 1.73 %, which is roughly less than half the LFL value for hydrogen.

Additionally, the fume hood is designed to cut hydrogen supply in case of rupture, through excess flow valves at the tank and at the fumehood, and in case of ventilation failure by closing the pneumatic valve that pulses when the reservoir needs to be refilled.

4.2.2 Material Preparation

The reactor requires hydrogen gas (UHP from Matheson Tri Gas), and an inert supply of benzonitrile, PNP-$Fe^{II}(H)_2CO$ catalyst, and 2-propanol to prevent decomposition of the catalyst complex into phosphine and iron oxides that are inactive during the homogeneous hydrogenation of benzonitrile to benzylamine. As a result, the reactants were prepared inside a nitrogen glovebox and transferred to the reactor station, where they were immediately placed under nitrogen flow that was vented through a relief device at 5 psig. The back-pressure generated by the relief device should force nitrogen out of any unsealed point in the container while still maintaining the structural integrity of the flask. A typical reaction medium is composed of 1 g of benzonitrile, 13 mg of catalyst (0.3 mol%), and 78.5 g of 2-propanol.

4.2.3 Reactor Configuration and Standard Operations

To operate the reactor, the system has to be inert to prevent flammable mixtures. To inert the system, nitrogen flows through the reagent station, the reactor, and effluent collection vessel. 2-propanol is pumped into the reaction medium and the GC oven is set to the desired temperature. Once the reactor is full, the nitrogen gas is swapped for hydrogen and the Equilibar back-pressure regulator is set to the desired pressure. At this point, the pure 2-propanol stream is switched to pump the reagents into the reactor. LabVIEW has been used up to this point to set the pump and MFC set points and assess the stability of process variables while achieving steady-state operations.

4.2.4 LabVIEW User Interface and Programming

The labVIEW program user interface describe the overall features of the code without going into all detail, Figure 4.3.

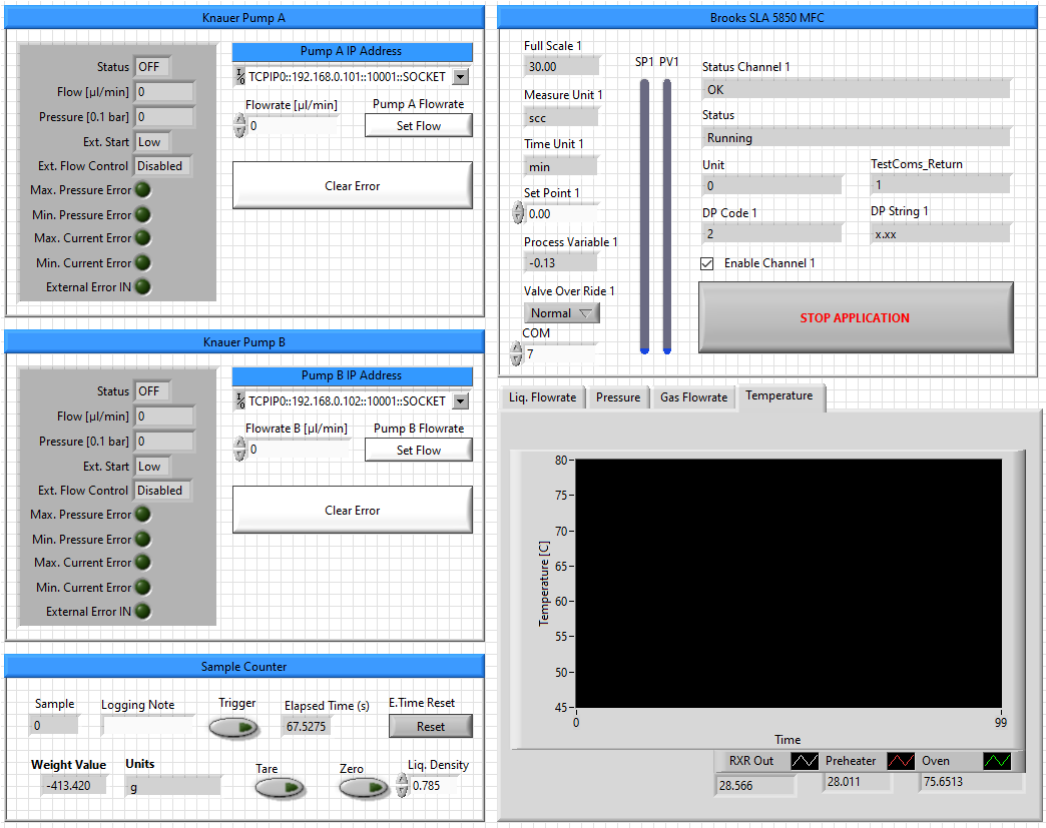

Figure 4.3: LabVIEW program user interface controlling and monitoring the continuous flow hydrogenation reactor.

First, as with all labVIEW documents described in this dissertation, the data file where all data will be stored is created. This is done by activating the program and its connections behind the scenes. The primary while loop running the labVIEW program is associated with the Brooks SLA 5850 MFC. As a result, the labVIEW program is dependent on this connection to work properly. Otherwise, an error will be prompted. The MFC controller is connected to a control box (Brooks 0254) capable of independently controlling 4 MFC. The LabVIEW code presented here has been simplified to run one MFC. The MFC is capable of operating 0.16 to 30 standard cubic centimeters per minute (sccm).

Second, there are two Knauer pumps connected to the system via Ethernet cables; Pump A (TCIP0::192.168.0.101::1001::SOCKET) and B (TCIP0::192.168.0.102::1001::SOCKET) can be identified by its IP addresses. The labVIEW program is independent of the Knauer pump connection, meaning that it can operate with only one pump or with both at a time. The IP addresses are automatically assigned by a router that connects the pumps to the computer. The router is connected through an Ethernet cable to the computer. The Knauer pumps are capable of flowing 1 μL to 10 mL per minute. The pump is capable of monitoring the pressure; these measurements provide insights into the reactor pressure. The pumps have safety features that prevent them from running in dry conditions or if there is a plug in the reactor, causing the system pressure to increase.

Third, to manage the data collection system, sample logging capabilities are incorporated into the data file on a time-dependent basis. Additionally, we have added the capability of measuring the weight of the effluent as a function of time to calculate the liquid flowrate of the system in case there is a need to check the flowrate calibrations. This is best done in the absence of hydrogen flow for accuracy.

Lastly, process variables, e.g., liquid and gas flowrates, reactor pressure, and inlet, outlet and reactor temperatures, can be monitored as a function of time.

4.3 Residence Time Distributions

With the continuous flow reactor operating properly and recording all data sets through LabVIEW, the characterization of the average residence time and degree of plug flow behavior exhibited by the reactor is assessed.

A residence time distribution requires a tracer, a detector, and an input that elicits a specific response moments later. For example, by implementing a unit-step input a break-through curve would be observed; while a pulse input would result in Gaussian distribution behavior. Both curves are related; they are used to interpret the residence time between the input and the response and the distribution associated with the reactor configuration. A plug flow behavior exhibits the narrowest distribution possible.

Berard *et al.* defines a good tracer as one that is easy to detect, is inert, and is absent of interactions with walls or other species. He then adds, that often a compromise is reached between a good tracer and detection.[24] Table 4.2 contains a list of tracer and detector pairs and the phase under which residence time distribution analyses that are typically conducted.

Table 4.2: Tracer-Detector pairings for residence time distributions (RTD). Adopted from Berard *et al.*[24]

Phase	Tracer	Detector
Water	Eriochrome black T	UV-Vis
Water	NaCl	Conductivity
Water	NaCl	Conductivity
Air	Helium	Thermal Conductivity
Water	Uranine	UV-Vis
Water	Carbon Ink	Camera
Water	NaCl	Conductivity

Based on Table 4.2, there are very limited options in the literature to conduct residence time distributions, and mostly all require an aqueous medium. It seems to be common to use dyes and electrolytes in combination with UV-Vis and conductivity detectors, respectively. In the step-input approach implemented here, the concentration of the tracer is normalized to 1. As a result, a break-through type behavior is expected, and the data can be fitted to Equation 4.2. Berard *et al.* share more details on derivations of these equations.[24]

$$F(\theta) = \int E(\theta) d\theta = \int \frac{1}{\sqrt{4\pi/Pe}} \exp\left[-\frac{Pe(1-\theta)^2}{4}\right] d\theta \tag{4.2}$$

The Peclet number (Pe) is a dimensionless quantity that is equivalent to $\frac{uL}{D}$. A Peclet number below 10 represents a back mixed reactor, and a Peclet number above 20 represents a plug flow behavior. First, methylene blue is utilized as the tracer in combination with an online UV-Vis spectrophotometer for detection, Figure 4.4 correlates the inverse Peclet number against flowarate

at which the online UV-Vis residence time distributions were conducted.

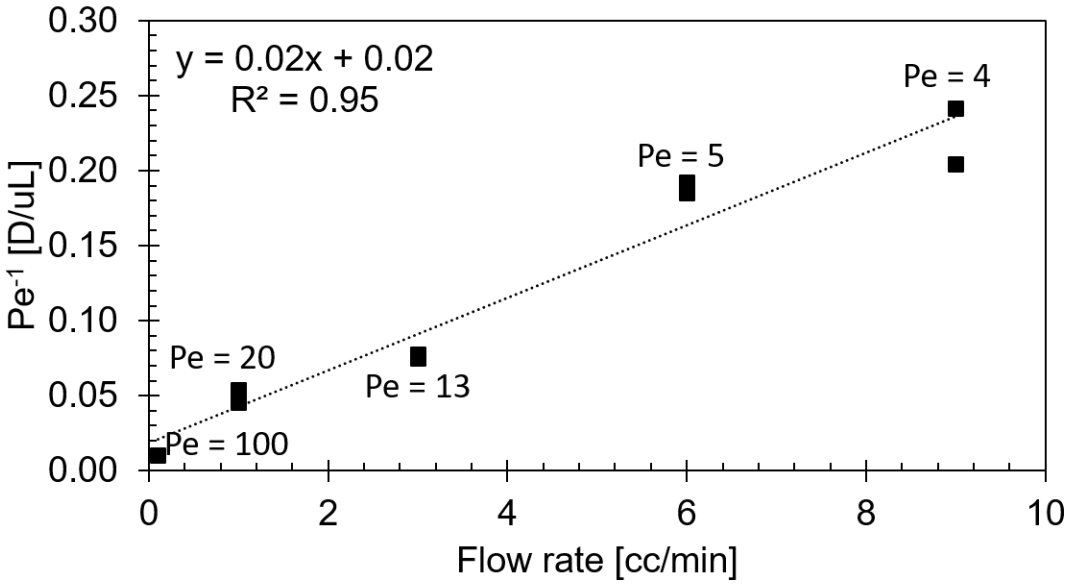

Figure 4.4: Inverse Peclet number versus flow rate. Where $y = Pe^{-1}$ and $x =$ flow rate.

According to Figure 4.4, the reactor is no longer operating under plug flow behavior when flowrates are above 0.5 mL per minute. Even a Reynold's number reveals laminar flow under the fastest flowrates. Posed as a hypothesis, the online UV-Vis cell with a cell volume of 0.6 mL acts as a continuous stirred tank and obfuscates the true nature of the reactor upon analysis. To corroborate, a residence time distribution with LF-NMR while using iron chloride as the tracer was performed, Figure 4.5.

LF-NMR measures solvent relaxation time by using radio frequency pulses to knock protons out of alignment (90°) with the instrument's magnetic field. For these experiments, we measure the spin-spin relaxation, T_2, which measure the exponential decay of a population of protons as they return to alignment with the instrument's magnetic field.

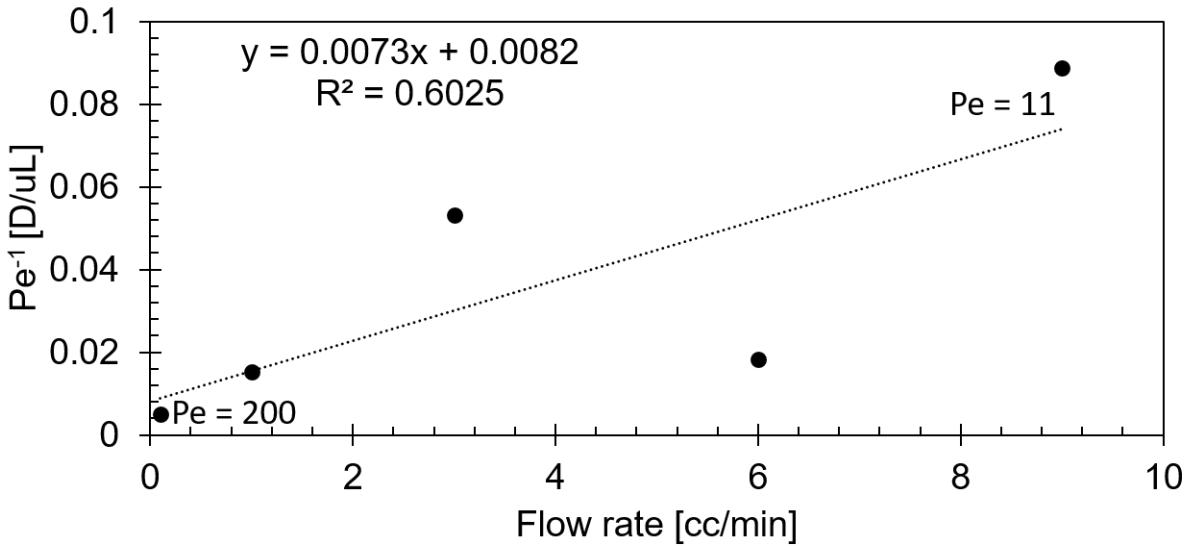

Figure 4.5: Mean residence time distribution versus flowrate under LF-NMR detection. Where $y = Pe^{-1}$ and $x =$ flow rate.

In comparing Figures 4.4 and 4.5 it is evident that the UV-Vis view cell had a drastic impact on dispersion as Figure 4.5 shows that even at 9 mL per minute the reactor does not enter the back mixed behavior, suggesting (near) plug flow behavior at all instances. This confirms that a continuous flow reactor with a narrow residence time distribution was designed and commissioned.

The use of LF-NMR in residence time distribution studies greatly expands the available capabilities in the literature to the point where new tracers with great levels of detection, that closely resemble substrates, can be implemented. Figure 4.6 utilizes 4-hydroxy-TEMPO, a radical, as a tracer in 2-propanol solvent. This radical is of similar size to benzonitrile, at least when contrasted against methylene blue. Additionally, deuterated solvents and their non-deuterated counterparts as tracer-solvent pairs can be utilized with LF-NMR; however, it is worth noting the deuterated solvents do not elicit as strong of a response as radicals do. Therefore, radicals like 4-hydroxy-TEMPO are preferred.

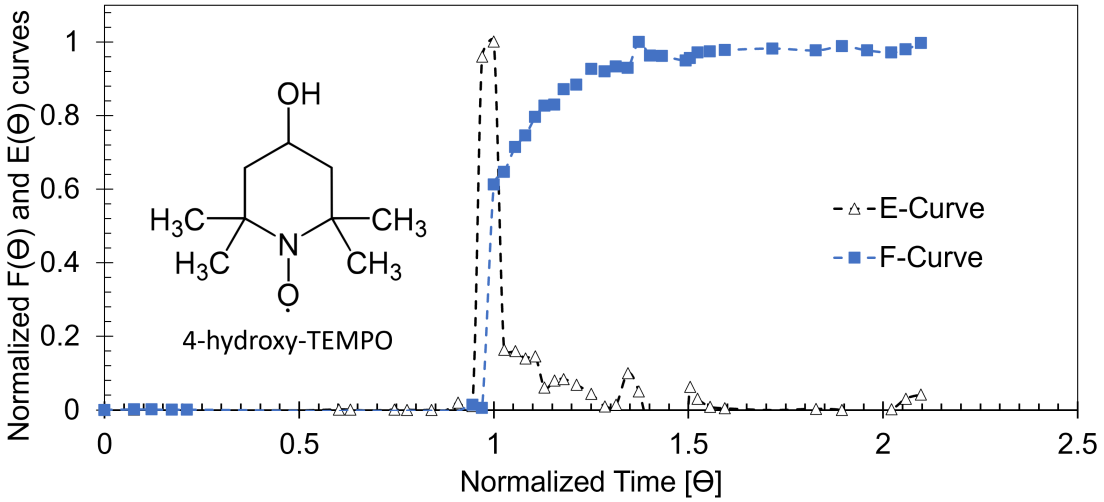

Figure 4.6: Mean residence time of 18.7 minutes. The F-curve, or breakthrough curve, is the response associated with the step input of 4-hydroxyg-TEMPO. The E-curve, or distribution of the analyte, is the derivative of the F-Curve.

Based on this analysis, an average residence time of 18.7 minutes with a narrow distribution that experiences tailing is characterized. Tailing can be explained by fittings, such as: tees, valves, back-pressure regulator, etc.

4.4 Reactor Performance

During initial studies, the reactor showed little to no performance. During the time course of the experiment, benzonitrile conversions stayed between 1-2 mol% for residence times ranging from 18.7 to 374 minutes. The continuous meso-scale flow hydrogenation reactor operates under laminar flow (Re $<$ 800), meaning that mass transfer is mostly governed by diffusion through the cross-sectional area of the reactor. To maximize reactor performance, a two prong approach was implemented. 1) A co-solvent with high hydrogen solubility profile at 50 w/w% is used. This would enable the liquid to intake a larger quantity of hydrogen while still promoting the proton shuttled hydrogen addition, as discussed in Chapter 3. 2) The liquid flowrate is decreased to reduce the diffusional length required for a molecule of hydrogen to travel to the center of the liquid slug. This approach is highly effective as the diffusion time is dependent on the square of

the length, thus a reduction in the diffusional length by an order of magnitude causes a two order of magnitude decrease in diffusion time. Leading to faster mass transfer rates in continuous flow hydrogenation reactors.

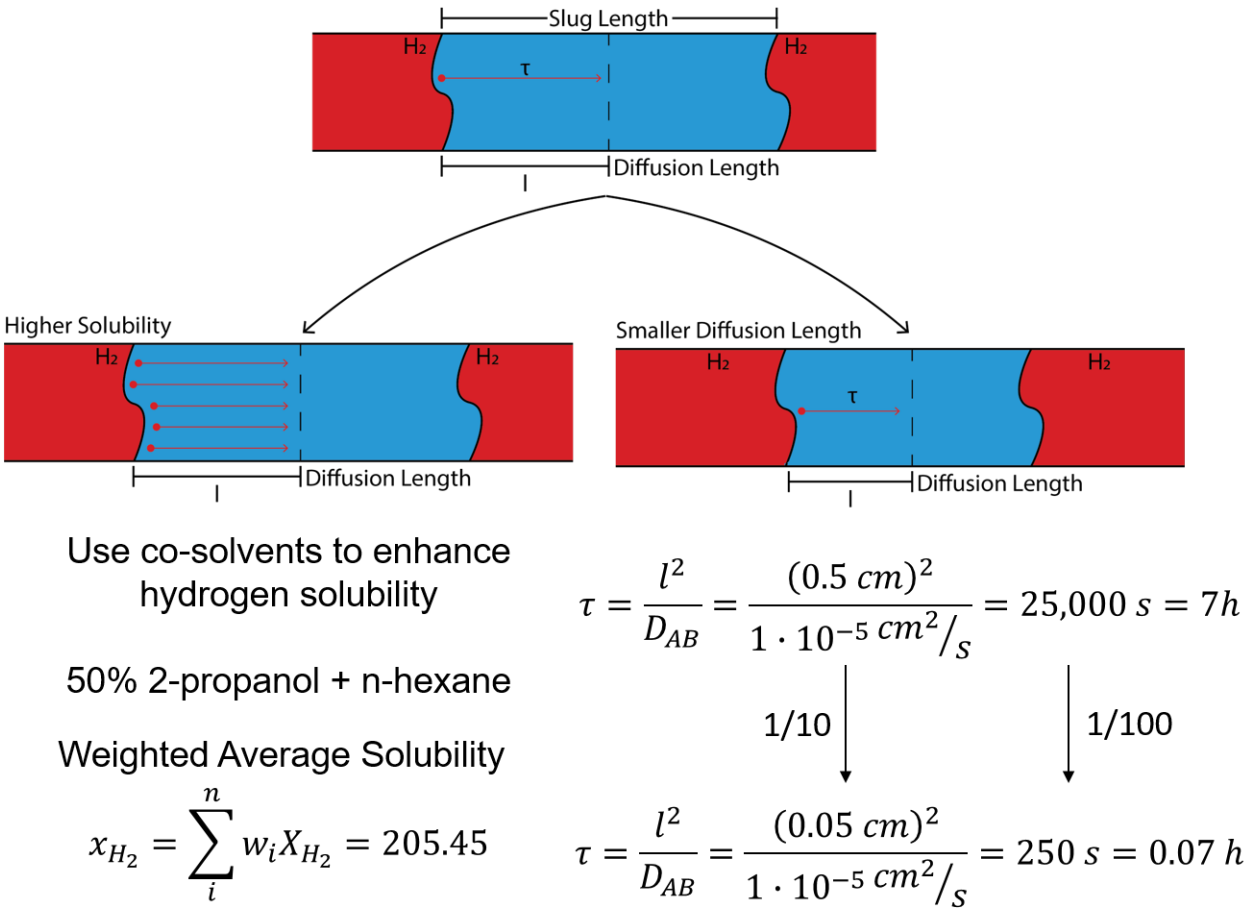

Figure 4.7: Two prong strategy to improve reactor meso-scale flow reactor.

Unfortunately, Figure 4.8 shows a momentary increase in conversion from 2 to ca. 5 mol% conversion when both strategies were implemented simultaneously. It is believed that at low liquid flowrates the small liquid slugs collapse and aggregate with previous material until larger slugs are formed, similar to those in the original studies of this reactor.

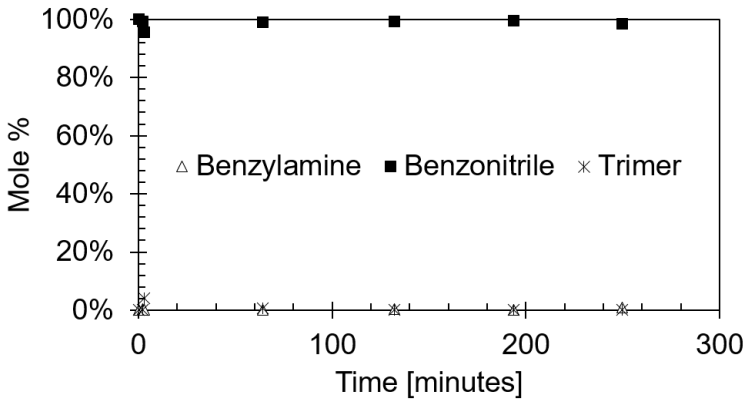

Figure 4.8: Continuous flow hydrogenation of benzonitrile to benzylamine using 50% hexane-2-propanol mixture and an PNP-$Fe^{II}(H)_2CO$ catalyst at 70°C and 30 bar H_2

As a result of the mass transfer inefficiencies and inability of this 2 mm meso-scale flow hydrogenation reactor to achieve decent conversion, this problem is better suited for a larger (ca. 7 mm) meso-scale hydrogenation reactor, which operates under different governing mass transport principles. Chapter 9 contains more details on the second iteration design for this continuous hydrogenation reactor station.

4.5 Conclusion

Enhancing gas-to-liquid (G-L) mass transfer rates in continuous processes is vital to the success of highly reactive systems. Mass transfer inefficiencies can affect residence time, conversion, and selectivity; three parameters critical to the overall productivity of any chemical process and its economic and environmental impacts.[7,93] Paying for reactor inefficiencies in terms of capital and utility costs is not acceptable for commercialization. As a result, different reactor configurations are explored so that higher mass transfer rates, great reaction performance, and a low residence time distribution can be achieved. Here, a new method and instrumentation for residence time distribution analysis relying on radicals and LF-NMR are developed.

Chapter 5

A Blueprint to Enable Smart Manufacturing through Conductivity: a Process Analytical Technology (PAT) Under Conditions of Use

Abstract

Quality by Control (QbC) is the next modality in pharmaceutical manufacturing that will enable optimized process conditions that satisfy complex criteria, i.e., economics, energy expenditure, etc., while guaranteeing product quality even in the presence of external event that threaten steady-state operations. Model predictive control (MPC) helps achieve this goal by going beyond PID controls that correct the difference between a set point and process variable through proportional, integral, and derivative action. MPC relies on process models, e.g., kinetics, to predict the future output of the system. These tools can correct for changes in the system and optimize processing conditions to improve upon energy consumption, process economics, and responsible resource utilization.

Conductivity, a process analytical technique for the monitoring of electrolytes, is deployed to garner concentration profiles of dibenzylamine hydrobromide. LabVIEW simulation and control environment is used to build the modelling capabilities required for MPC.

5.1 Introduction

In Chapter 3, a semi-batch Parr reactor was used in an in-depth kinetic and mechanistic characterization that provided insights for developing a continuous flow process. During batch operations, quality of the product was assured through testing with an off-line analytical technique, i.e., gas chromatography. In Chapter 4, a continuous flow reactor was designed, built, and commissioned with a low residence time distribution and a LabVIEW programming for data acquisition and control. A design with low axial mixing that minimizes the risk of an underperforming system, but the system had to rely on off-line analytical tools to monitor product quality. In Chapter 5, a smart manufacturing paradigm is advanced by deploying conductivity as an on-line analytical technique capable of monitoring electrolytes at a variety of reaction conditions. Additionally, in an unprecedented approach (to the best of our knowledge) LabVIEW's control and simulation tools to develop model predictive control were used. The intent is to couple data acquisition and simulation modules to enable predictive control strategies that assure an excellent quality profile and process efficiency under unprecedented circumstances, Figure 5.1. The latter, however, is outside the scope of this dissertation and will be discussed further in Chapter 9.

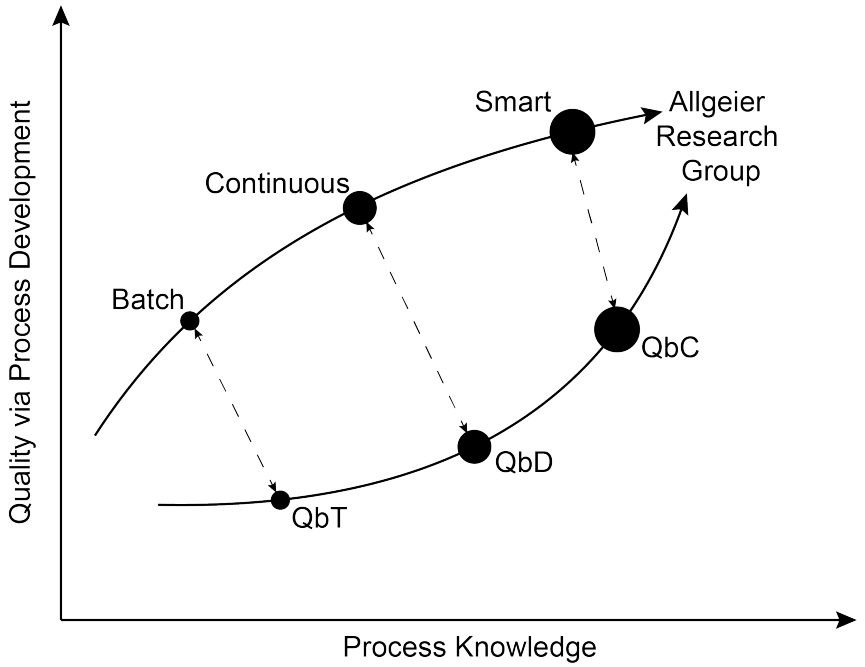

Figure 5.1: A depiction of product quality throughout development and knowledge of process.

In the specialty chemical modalities (including pharmaceuticals) product development begins in small batch reactors/flasks that suffer from batch-to-batch variability. Quality in this respect is assured through testing at the end of processing; thus implementing a quality-by-testing (QbT) approach. Batch manufacturing is dependent on following strict manufacturing procedures, similar to cooking, but is not flexible to external influences on the process. Batch reactors also suffer mass and heat transfer inefficiencies upon scale-up that make the reactors more susceptible to deviating conditions that can lead to rejected product or unsafe working conditions. As a result, hazardous chemistries, chemicals, and reactions conditions are often restricted from use in these reactors.

Continuous flow reactors have the ability to overcome these challenges. The continual pull of raw materials and push of products out of the reactor introduces time as a processing variable. Here, a batch or lot is defined as a specific product volume per unit time; depending on the reactor size, different amounts of product can be achieved at any given time, Figure 4.1. In the pharmaceutical modality, where production volumes keep decreasing as more potent drugs come to market, lower volume reactors are feasible and make processing conditions inherently safer. Smaller dimension improve upon heat transfer properties that enable harsher processing conditions and chemistries.[112] However, to achieve the best quality profile during steady state operations, the right reactor and internal configurations have to be deployed. Here, quality-by-design (QbD) is deployed based on metrics and in-depth understanding of kinetics and reaction profile, among other critical processing parameters (temperature, pressure, etc.). Monitoring processing parameters and controlling deviations from their set points allows for out-of-specification materials to be removed from the manufacturing line until steady-state operations resume. Continuous flow reactors are designed to maintain a narrow residence time profile for these purposes.

To go beyond, the efficiencies set during the design stage of continuous flow reactors, model predictive control and decision-making strategies based on real-time analytics need to be implemented. In this manufacturing paradigm, the system can respond to unforeseen changes in processing conditions and raw materials specifications before they become an issue.[112]

Predictive control has been proven essential in advancing sustainable development. Solar pan-

els have increased efficiency by 50%, which translate to a 2% increase in energy output, by implementing predictive controls to best orient themselves to the sun.

5.2 Results and Discussion

Benzylamine, the product of interest in Chapters 3-4, is utilized in nucleophilic substitution with benzyl bromide (aryl halide) to produce dibenzylamine hydrobromide, Figure 5.2. In early production steps, nucleophilic substitutions are highly implemented in N-, O-, and S-containing moieties to couple different drug substance precursors together. However, due to their high toxicity, alkylating agents cannot be of the drug substance; this provides an excellent opportunity to deploy QbC strategies and model predictions.

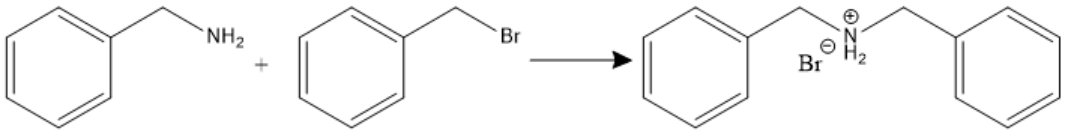

Figure 5.2: Reaction between benzylamine and benzyl bromide to form dibenzylamine hydrobromide salt.

In a batch reactor, 98.5 mM of benzylamine (BA) and 61.5 mM of benzyl bromide (BBr) in methanol solvent were mixed for ca. 2.5 hours at 25°C, Figure 5.3. A conductivity probe monitored the reaction progression through the concentration of dibenzylamine HBr, the product of the reaction, until a plateau, marking the end of the reaction, was reached.

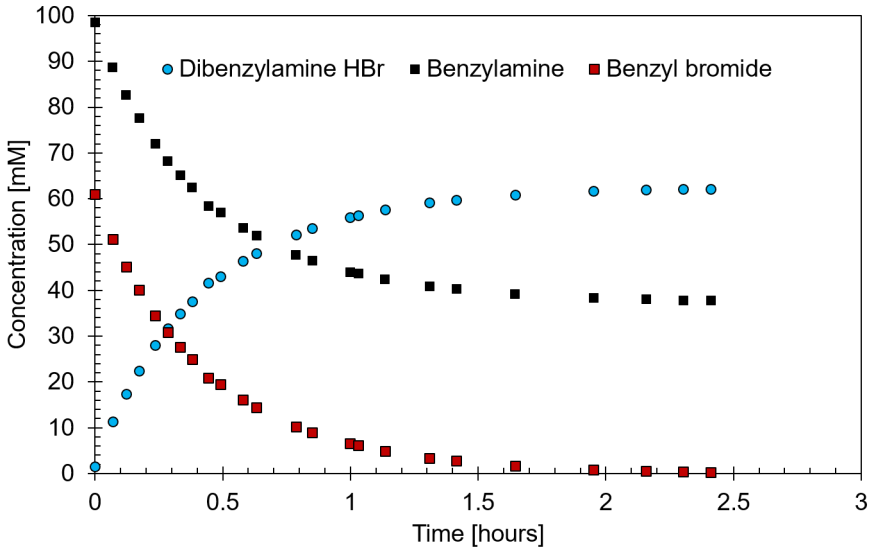

Figure 5.3: Reaction profile for the nucleophilic substitution of benzyl bromide and benzylamine.

Figure 5.3 plots the concentration of dibenzylamine HBr, benzylamine, and benzyl bromide, the limiting reagents. The concentrations for the substrates were calculated based on initial conditions and rate of consumption based on the production of the dibenzylamine HBr salt.

5.2.1 LabVIEW Programming for Data Acquisition

LabVIEW is a graphical programming environment commonly used in academic laboratories throughout the scientific communities. This is an easy coding language that allows virtually anyone to learn in a short amount of time the skills needed to integrate tools to collect data, and monitor and control laboratory equipment. Figure 5.4 shows the graphical coding language used in the implementation of conductivity as a PAT in the production of dibenzylamine hydrobromide. First, the data file where data will be stored is initiated and the columns where the data will be inserted are formatted according to the labels. Once the file has been initiated, the comma-delimited serial connection to the YSI 3200 conductivity meter is initiated through an RS-232 cable. Second, once the data file and connection to the instrument have been initiated and established, the code enters a while loop that terminates via a user generated command. In the meantime, LabVIEW reads the data from the conductivity meter in 5 second intervals. The data is read as a comma separated

string and was deconvoluted into its respective categories, i.e., compensation (%/°C), temperature (°C), conductivity (S cm^{-1}), and resistance (Ohms). Once the experiment was concluded, the while loop is terminated and the data file is closed and ready for analysis, Figure 5.3.

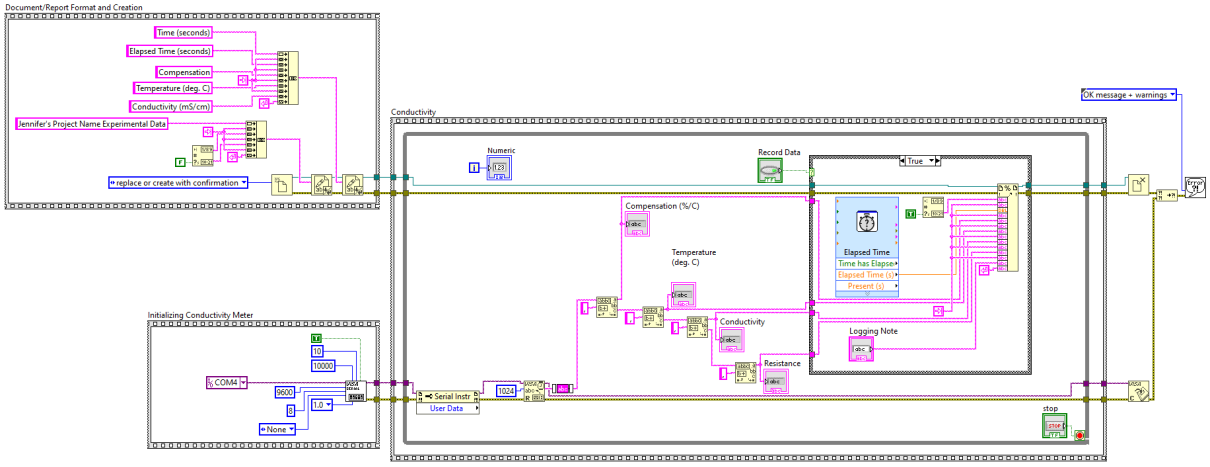

Figure 5.4: LabVIEW Code used to deploy YSI 3200 conductivity meter with a 3252 conductivity cell as a Process Analytical Technology (PAT).

The implications of this simple code goes well beyond allowing data collection and integration of process analytical technique to our reaction platforms. From an experimentalist perspective, this code reduced the work requirements of the scientist from 7-8 hours per reaction to about 30-45 minutes, which mostly comprise preparation time. When employing highly specialized, expensive scientist, automation becomes a way to achieve economic savings during process development.

5.2.2 Kinetic Modelling of the Nucleophilic Substitution Between Benzylamine and Benzylbromide

The reaction between benzyl bromide and benzylamine follows a first order dependence upon both benzyl bromide and benzylamine concentrations,[193] yielding a second order rate expression, Equation 5.1.

$$Rate = k_{obs}[\text{Benzylamine}]^1[\text{Benzyl bromide}]^1 \tag{5.1}$$

Based on the insights by Ravi *et al.* three differential equations, Equations 5.2-5.4, were solved using Runge-Kutta 45 in LabVIEW (vide-infra). The three equations exhibit first order dependence on benzylamine and benzyl bromide. The product, dibenzylamine HBr (DBAHBr) differs from the other two equations by having a positive sign associated with the change in concentration as a function of time as this material is being generated while the others are being consumed.

$$\text{Rate} = -\frac{dC_{BA}}{dt} = k[\text{BA}]^1[\text{BBr}]^1 \tag{5.2}$$

$$\text{Rate} = -\frac{dC_{BBr}}{dt} = k[\text{BA}]^1[\text{BBr}]^1 \tag{5.3}$$

$$\text{Rate} = \frac{dC_{DBAHBr}}{dt} = k[\text{BA}]^1[\text{BBr}]^1 \tag{5.4}$$

In Figure 5.5 a close relationship between the experimental data, plotted with symbols, and the kinetic model, plotted with dashed lines can be observed. Based on this kinetic modelling, a kinetic rate constant, k, of 0.075 $M^{-1}s^{-1}$ was regressed.

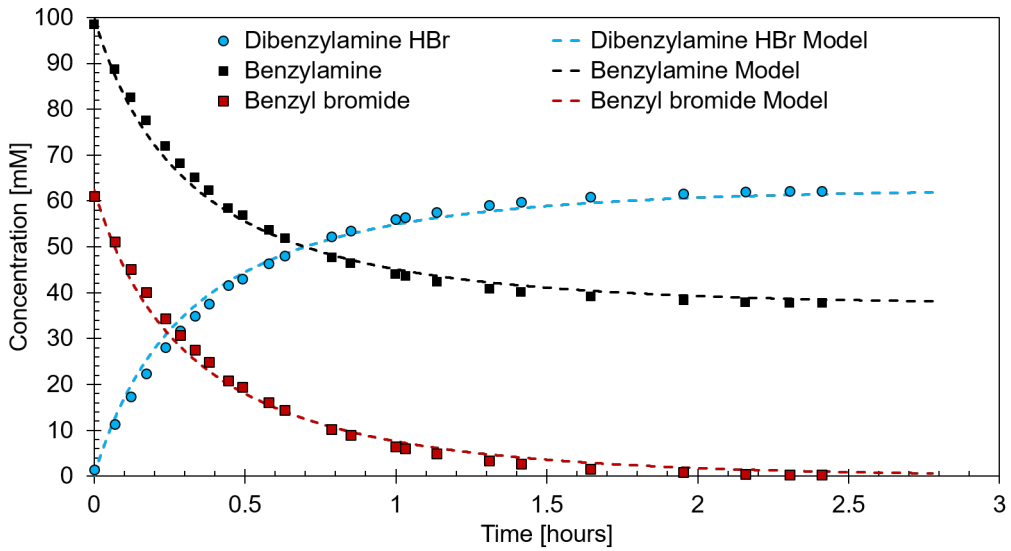

Figure 5.5: Reaction profile and LabVIEW generated kinetic model data fitted against each other.

The goodness of the fit was determined by minimizing the root-mean-square error (RMSE),

described by Equation 5.5, through an iterative process that altered the kinetic rate constant value. The resulting RMSE value was 0.0021.

$$\text{RMSE} = \sqrt{\sum_{i=1}^{n} \frac{(\text{Predicted}_i - \text{Actual}_i)^2}{n}} \tag{5.5}$$

The RMSE was the preferred optimization function, as it does not penalize the fit by having a high density data set. Optimizing with R^2 methodology does this by summing the residuals without normalizing for the number of data points.

5.2.3 LabVIEW Programming for Kinetic Modelling

A simple user interface has been designed so that the user can input reaction conditions, a guess for the kinetic rate constant, the duration of the simulation, and the type of ordinary differential equation (ODE) solver. For this work, Runge-Kutta 45, also known as ODE 45 was used, Figure 5.6.

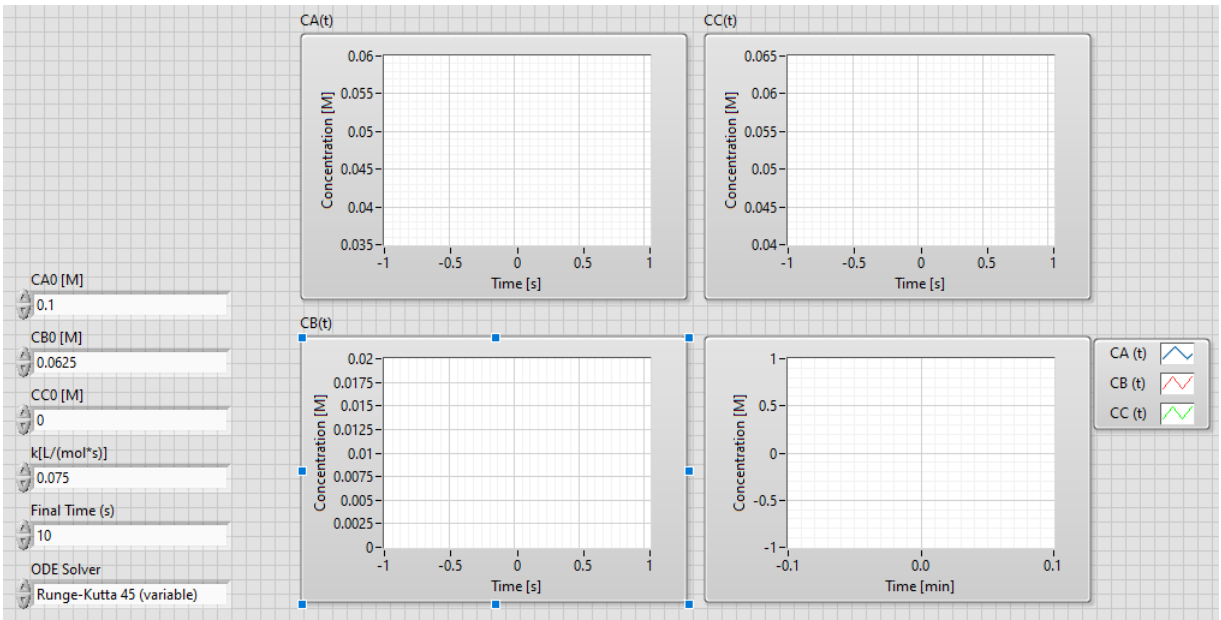

Figure 5.6: User interface for the kinetic modelling for the synthesis of dibenzylamine hydrobromide.

Similarly to the data acquisition LabVIEW program, the kinetic model begins by initiating a

text file for data storage where the concentrations and simulation time are stored after the end of the simulation, Figure 5.7.

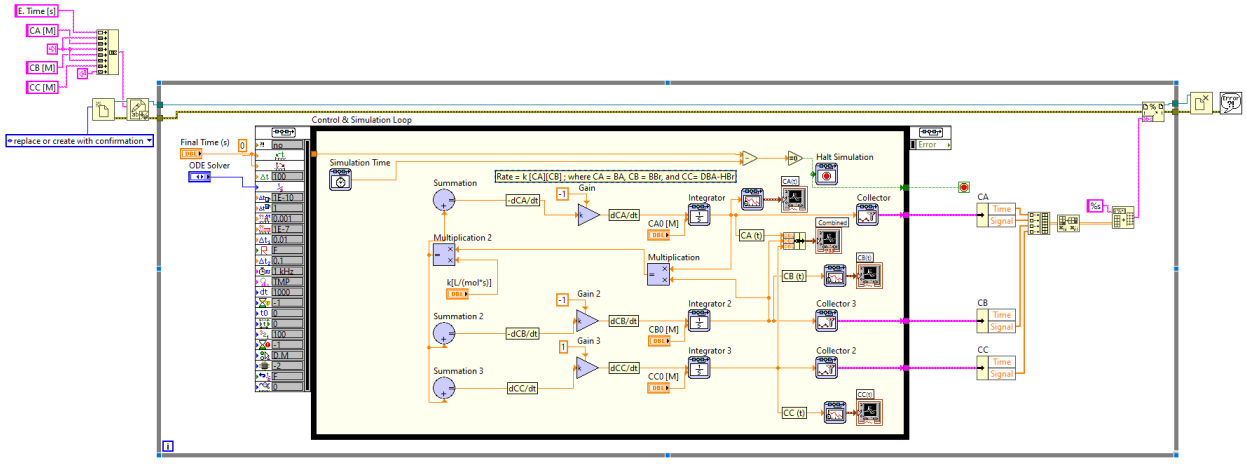

Figure 5.7: Graphical language code for the kinetic modelling of the synthesis of dibenzylamine hydrobromide.

To solve an ODE in LabVIEW, the summation, the gain, the multiplication, and the integral simulation tools are required, Figure 5.8.

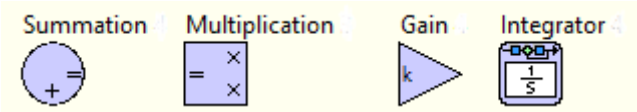

Figure 5.8: LabVIEW control and simulation block tools critical to kinetic modelling.

To solve Equation 5.2, a summation was set equal to the left-hand side of Equation 5.2, $-\frac{dC_{BA}}{dt}$. Then, a gain of negative one was multiplied by the summation to yield a positive output signal which was sent to an integrator to obtain the concentration of benzylamine, C_{BA}, as a function of time. Similarly, for Equations 5.3 and 5.4. Once a signal for benzylamine (C_{BA}) and benzyl bromide (C_{BA}) are obtained, these can be multiplied together by using a multiplication block, and sequentially the product can be combined with the kinetic rate constant, k. Once the right-hand side of the equation has been built, then the output signal can return to the summation under the appropriate sign. For a product this would be a positive signal and for a reactant a negative signal would be used. Once the code for all reacting species is built, the simulation will plot the signal and output the data after the simulation is terminated.

5.3 Conclusion

Here, conductivity and kinetic modelling of a nucleophilic substitution between benzylamine and benzyl bromide to yield dibenzylamine HBr is deployed. Conductivity is perfect to monitor electrolytes in solution. By providing automation, productivity of researchers is increased while also improving data density and quality. From the kinetic models, the data set is complemented by regressing kinetic parameters critical to furthering process understanding.

Chapter 6

Compostable Food Packaging α-1,3-Glucan-Palmitate Thermoplastics: Synthesis and Characterization

Abstract

The environmental persistence of plastics prompts development of new plastic materials that balance performance in use with potential to degrade to benign products in the environment. Derivatized polysaccharides have gained attention for their inherent compostability, while imparting thermoplastic characteristics not attained in native polysaccharides. Here alpha-1,3-glucan has been derivatized with palmitate chains in processes with the lowest process mass intensity (PMI = 7) reported. The process has been developed to reduce solvent utilization supporting a solid to solute transition, while simultaneously limiting backbone degradation. The degree of substitution may be controlled in the range 0 - 2.7 per anhydrous glucose units, yielding materials with melting points in the range 140-260°C. Melt pressed brittle films have been prepared with maximum stress and strain of 2.7 MPa and 5.7%, respectively. Glucan palmitate films have a high permeability of oxygen and water (283.8×10^{-7} $\frac{cm^3_{STP}m}{m^2 dayPa}$ and 490 $\frac{gm}{m^2 sPa}$, respectively), in contrast to common non-renewable thermoplastics. The films are appealing for the replacement of plastics used in the sorting of tomatoes, berries, and grapes, among other items that are in constant exposure to atmospheric conditions while protecting them from insects and undesired microorganism.

6.1 Introduction

The permanence of plastics in the environment is an issue that impacts all of our lives.[9,191,213,234] In 2018, the United States generated 35.7 million tons of plastic. Approximately 75% (27 million tons) of those plastics made its way into landfills and/or oceans, where they are transformed into microplastics which contaminate our food and water supply. Furthermore, 16% (5.6 million tons) of the produced plastics were incinerated for energy supply, leaving 9% (3.1 million tons) of plastics for recycling.[1,151] Unfortunately, the demand for plastics will only increase; as it is expected to double in the next 20 years.[151]

Biodegradable plastic alternatives that aspire to solve the environmental persistence problem may be classified as oxo-degradable, industrially compostable, and at-home compostable. Oxo-degradable plastics are often deceitful to the consumer's intent; these materials are typically formed from petroleum based polymers and include metal and organic additives that promote fragmentation, but not degradation to renewable materials.[225,250] Industrially compostable plastics are a good alternative, if the appropriate local compositing infrastructure is in place.[61] These type of plastics require controlled conditions for extended periods of time. The European Union made significant investments in industrial composting infrastructure and set ambitious goals to achieve 55% of packaging recirculation by 2025 and recycling all plastics by 2030.[151] Allowing the EU to decouple resource depletion from economic growth.[77] At-home compostable plastics look to surpass technological and infrastructure scarcity by utilizing naturally occurring components that degrade with ease under atmospheric conditions and in the presence of local microbiota in a short period of time.[163]

Naturally derived polysaccharides are of interest for at-home compostable food-packaging plastics due to their benign and biocompatible nature.[5] α-1,3-glucan, a linear, water-insoluble biopolymer, is naturally produced by mouth bacteria (dental plaque) and fungi (cell wall).[99] For industrial scale purposes, the α-1,3-glucan has been produced in vitro through a bioengineered glucosyltransferases (Gtfs) enzyme in a completely aqueous synthesis with an average weight degree of polymerization (DPw) of 800.[22,181,188] The synthesis utilizes untreated sucrose as a starting ma-

terial that undergoes enzymatic cleavage to produce glucose and fructose units, sequentially, Gtfs creates glycosidic bonds to selectively yield α-1,3-glucan without the use of additives.[188]

To generate thermoplastics for packaging applications these materials may be modified with long-chain carboxylates but the low-solubility has led to use of very dilute conditions and use of salt additives to enhance solubility. Here, we present a greener modification of α-1,3-glucan with improved process mass intensity (PMI) and work-up protocols; in contrast to the best reported syntheses.[94] Additionally, we report the hot-press fabrication and mechanical, chemical, and transport characterization of the α-1,3-glucan-palmitate films, justifying their further development in practical applications.

6.2 Experimental

α-1,3-glucan was sourced from Industrial Flavors & Fragrances and pretreated in a vacuum oven at 100°C for a minimum of 3-4 hours. N,N-Dimethylacetamide (DMAc; SKU: 271012-1L), pyridine (PYR; SKU: 270970-1L), and palmitoyl chloride (Palm Cl; SKU: P78-500ML) were used as received from Sigma Aldrich. Nitrogen gas (N_2; SKU: NI UHP1L) was used as received from Matheson Tri Gas to promote an inert and dry reaction environment.

6.2.1 Synthesis of alpha-1,3-glucan-palmitate Thermoplastics

100.76 g of dried glucan and 201.16 g of DMAc were added to the 1L kettle reactor. The reactor was placed in the heating mantle, connected to the overhead stirrer motor, and set to 400 rpm. The reactor was inerted with N_2 and the temperature was set to 160°C. A slight coloration (brown) was observed as the reactor temperature increased to this set point. Using the distillation apparatus 63.18 g of distillate (31% of the loaded DMAc weight) was removed from the reactor. The distillate was captured using 6°C condenser temperature and a round bottom collection flask in an ice-bath. The distillate had 13% water via Karl Fischer titration. When ca. 35 wt. % of solvent was removed, the temperature was set to 70-80°C. The remaining reaction mixture

comprised 137.98 g of DMAc. Once the desired temperature was reached, 247.99 g of palmitoyl chloride and 104.97 g of pyridine were added over 30 minutes using an HPLC and syringe pump, respectively. The addition of palmitoyl chloride and pyridine is highly exothermic and led to a raise in temperature from 90°C to 118°C without supplemental heating. The components were added in 1.5 palmitoyl chloride to AGU and 1.5 pyridine to palmitoyl chloride mole ratios based on optimal conditions established in 1 g glucan scale. The reaction was removed from the heating mantle 30 minutes after the addition of materials concluded. Pale yellow solids were present on top of a highly viscous reaction solution.

6.2.2 Work-up of alpha-1,3-glcuan-palmitate Thermoplastics

Multiple cycles of methanol (MeOH) washes and filtration were conducted until the reaction media pH was neutralized. In these cycles, 500 mL of MeOH was added to the 1L kettle reactor at 80°C under inert, reflux conditions. The higher temperatures facilitated the extraction of pyridinium chloride (PyrH-Cl), hydrogen chloride (HCl), methyl palmitate, and palmitic acid from the reaction media. Initial pH of this mixture was ca. 4. Higher water content in the reactor decreases yield and produces palmitic acid, which further causes acidification of the reaction media. The liquid was decanted and passed through vacuum filtration with a 150 mm ID Büchner funnel and filter paper for particles greater than 20 μm. The collected solids were partially dried on the filter paper and reintroduced to the work-up vessel, where successive cycles were conducted. A dark brown color was removed with each wash to yield an off-white product. The cake was placed in a vacuum oven at 60°C and 25-30 mmHg vacuum overnight. The vacuum-oven treatment further removed impurities that help improve the color of the product. The mass of dry product was collected, and samples were taken for NMR (DS, impurities), melting point, and GPC/SEC (Mw) analysis.

6.3 Results and Discussion

In recent years, there has been an increasing interest to produce at-home compostable thermoplastics to alleviate the plastic permanence problem (in marine and soil environments) and remove transportation related pollution.[77] Polyhydroxybutyrate (PHB), thermoplastic starch (TPS), polycarolactone (PCL), a 80/20 blend of polylactic acid (PLA) and PCL, a 85/15 blend of PHB and polyhydroxyoctanoate (PHO), a 60/40 blend of PHB and PCL, a 50/50 blend of PHB and poly(butylene succinate) (PBS), a 85/15 blend of PCL and PHO, a 70/30 blend of PCL and TPS, and PCL have passed at-home composting standards.[163] However, only PHB and TPS demonstrated biodegradation in unmanaged marine and fresh water and soil environments.[163] These materials show incredible promise for the food packaging industries that are important stakeholders in the plastics problem.

Chemically, TPS and PHB are naturally present in the environment. α-1,4-glucan (starch) is commonly present in staple foods, i.e., potatoes, rice, sugar cane, etc., meanwhile PHB is produced and digested by microbiota for food and energy storage purposes.[216] PHB has ester (R-COOR) linkages and methyl groups (CH_3) that give the polymer thermoplastic behavior, hydrophobicity, high crystallinity, and brittle characteristics, Figure 6.1.[150]

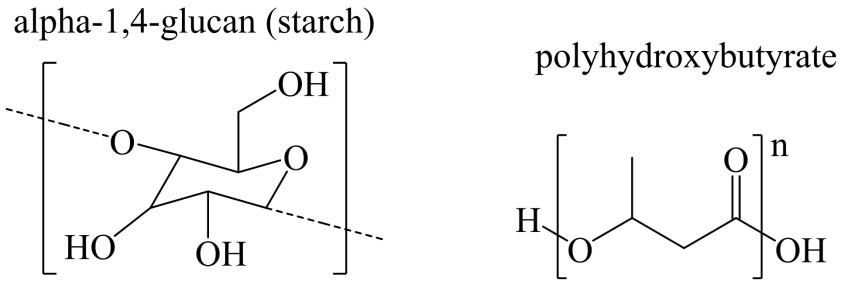

Figure 6.1: Structural depiction of starch and polyhydroxybutyrate (PHB).

Enomoto-Rogers, Heinze, and Porfyris & coworkers were among the first to take the initiative to create thermoplastic polysaccharides to meet the need for at-home composting, Table 6.1. Polysaccharides with ester linkages of different alkyl chains have become the standard for a greener generation of thermoplastics. Their synthesis, however, still needs to be improved.

Enomoto-Rogers & coworkers utilized ca. 5% LiCl/DMAc to improve the solubility of the α-1,3-glucan polymer and promote the reaction with the acetic anhydride in pyridine. The synthesis was conducted at 60°C for 48 hours. Unfortunately, the mass intensity upon purification was not reported and a PMI index could not be calculated, however, based on molar ratios and a degree of substitution (DS) of 3, the selectivity achieved was of 22%. The glucan-acetate resulting from this work achieved a glass transition temperature of 177°C, melting point temperature of 339°C, and a decomposition temperature of between 375-400°C.[188] Increasing the alkyl chain of the modifier, e.g., acetic anhydride to propionic anhydride, decreases the glass transition and melting point temperatures.[188,189]

Heinze & coworkers demonstrated the synthesis of glucan-laurate, glucan-palmitate, and glucan-stereate, through the use of p-toluenesulfonic acid chloride (TsCl), N, N'-carbonyldiimidazole (CDI), and the in-situ generated iminium chloride (ImCl) as activation agents. Iminium chloride is obtained through the reaction between N, N-dimethyl formamide and oxalyl chloride. Needless to say, these activation agents do not add to the final product and therefore lead to process inefficiencies and increased PMI. Additionally, the reaction conducted with CDI did not yield products with thermoplastic properties.[94] A thermoplastic should have a melting point temperature around 150°C to be compatible with industrial hot melt extrusion processes.

Porfyris & coworkers utilized $NaPO_2H_2 \cdot H_2O$ to catalyze the modification of α-1,3-glucan with succinic anhydride in a solventless synthesis. Through this protocol, they were able to minimize PMI up to 1.2, but were only able to achieve a DS value of 0.37. The glucan-succinate thermoplastic yielded a melting point temperature of ca. 175°C.[185] In our experience, increasing DS values alters a variety of properties, including but not limited to melting point temperatures. Therefore, a modification protocol that allows for higher DS is preferred over a completely solventless system. Additionally, based on initial molar loading of the succinic anhydride, this synthesis achieved 40% selectivity; an undesired attribute for sustainable development.

A thermoplastic polysaccharide that meets thermoplastic criteria and a flexible synthesis with improved PMI values at scales 50-100 fold greater than current literature precedent is presented in

Figure 6.2. Additionally, films are fabricated and their chemical, structural, and transport properties are characterized. Table 6.1 contrasts the current work to that which is present in the literature.

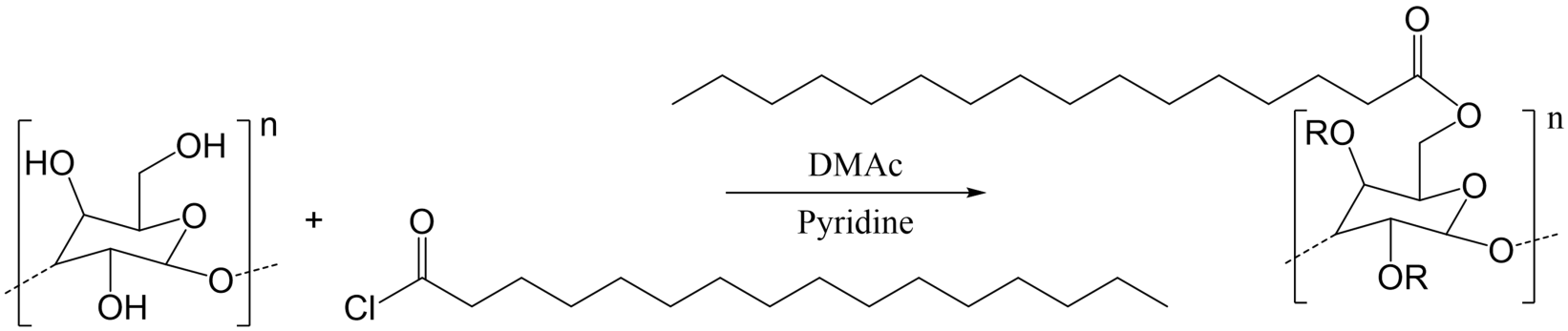

Figure 6.2: Reaction between α-1,3-glucan and palmitoyl chloride DMAc solution. Pyridine acts as a base to form reactive alkoxide sites.

Table 6.1: Polysaccharide based thermoplastics synthesis and PMI indices.

Mass of Reactants [g]										Wokr-up [g]		Product		Process				Citation
Substrate	Type	Solvent	Type	AA	Type	Additive	Type	Reagent	Type	Solvent	Type	Yield [g]	DS	Temperature [C]	Time [h]	PMI	% Selectivity	
0.50	α-1,3-glucan	9.37	DMAc	1.96	Pyridine	0.45	LiCl	2.16	AcAnh	N/A	MeOH	1.85 (73%)	3.00	60	48	N/A	22	[188]
2.00	α-1,3-glucan	46.85	DMAc	7.06	TsCl	3.66	LiCl	7.42	LA	868.12	EtOH	4.40	1.64	100	4	213	55	[94]
2.00	α-1,3-glucan	28.11	DMAc	6.01	CDI	3.66	LiCl	7.42	LA	868.12	EtOH	4.30	1.22	100	4	213	41	
2.00	α-1,3-glucan	47.03	DMAc/DMF	7.84	OxylCl	3.66	LiCl	17.56	SA	868.12	EtOH	7.10	1.90	100	4	133	38	
2.00	Maize Starch	56.22	DMAc	7.05	TsCl	0.6	LiCl	7.41	LA	1089.20	EtOH/Water	2.59	0.68	60	3	449	23	[30]
2.00	Maize Starch	56.22	DMAc	7.66	DCC/PP	0.6	LiCl	7.41	LA	789.20	MeOH	4.11	0.94	60	3	210	31	
2.00	Maize Starch	79.65	DMAc	6.00	CDI	0.6	LiCl	7.41	LA	863.50	iPrOH	3.43	0.74	60	3	280	25	
2.00	Maize Starch	75.17	DMAc/DMF	4.69	OxylCl	0.6	LiCl	7.41	LA	1200.66	EtOH/Water	5.18	1.67	60	3	249	56	
10.54	α-1,3-glucan	-	-	1.62	$NaPO_2H_2$	-	-	6.23	SuccAnh	-	-	15.10	0.37	-	-	1.2	77	[185]
1.00	α-1,3-glucan	2	DMAc	0.71	Pyridine	-	-	2.45	PC	157.84	MeOH	1.95	1.20	80	1	84.1	83	Current
100.76	α-1,3-glucan	137.98	DMAc	104.97	Pyridine	-	-	247.99	PC	2000	MeOH	309.55	2.30	80	1	7	89	Work

AA : Activation Agent
DS : Degree of Substitution
TsCl : 4-Toluenesulfonyl chloride
CDI : 1,1'-Carbonyldiimidazole
OxylCl : Oxalyl chloride
DCC/PP :
LA : Lauric Acid
SA : Stearic acid
SuccAnh : Succinic anhydride
PC : Palmitoyl Chloride

The α-1,3-glucan, with an anhydrous glucose unit (AGU) molecular weight (MW) of 162.15 g mol^{-1}, has a weight average degree of polymerization (DPw) of 800; making the molecular weight of the α-1,3-glucan utilized in this work 130 kDa. The MW of the modified glucan is expected to increase with increasing DS. For example, a glucan-palmitate thermoplastic with a DS value of ca. 2.2 should have an average MW of 576 kDa. Similar to all other reported synthesis, this method suffers from MW degradation promoted by acid hydrolysis of the glycosidic bonds. The acidic degradation of the polymer molecular weight is one of the attributes of these materials that favor atmospheric decomposition, but during synthesis this outcome should be minimized. For some glucan-palmitate products obtained in this work, an average MW of 214 kDa was obtained.

TGA and DSC characterization of α-1,3-glucan revealed an 8% moisture content accompanied by a large endotherm peak below 125°C associated with the evaporation of water. The glucan structure is maintained upon heating until a decomposition temperature of ca. 300°C is achieved, Figure 6.3. Decomposition of the unmodified α-1,3-glucan is represented by a sharp drop in the weight % curve and a single peak heat flow.

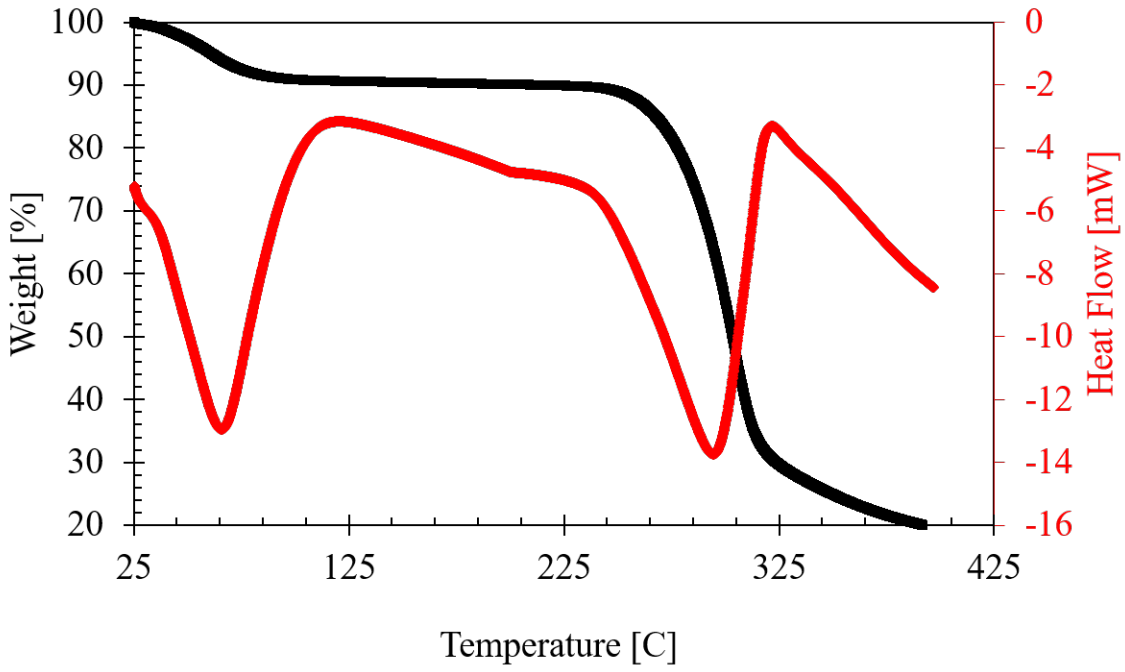

Figure 6.3: TGA/DSC characterization of native α-1,3-glucan polysaccharide.

For a 100 g glucan scale synthesis, the α-1,3-glucan would bring 8 g of water into the reactor. Based on Karl Fischer analysis of DMAc and pyridine, the solvents contain 139 and 58 ppm, respectively. The 200 g of DMAc loaded into the reactor prior to distillation contribute 2.78 g of water to the reaction media. The total water content prior to distillation is approximately 10.78 g. Through distillation, 68.13 g of a 13% water-DMAc mixture was obtained, accounting for 75% of water in the reactor. The distillate mass accounts for 31% of the total DMAc mass loaded. Figure 6.4 portrays that by increasing distillate mass, the percent recovery is increased drastically. The optimal distillate mass is approximately 37%. The 104 g of pyridine contribute 0.6 g of water to the reaction media after distillation, and therefore it is recommended to use anhydrous sources of pyridine that are stored in dried environments. The remaining 25% of water remaining in the reactor can lead to the formation of palmitic acid, decreasing the % selectivity of the synthesis. The palmitic acid is then removed through the reaction work-up (vide-infra).

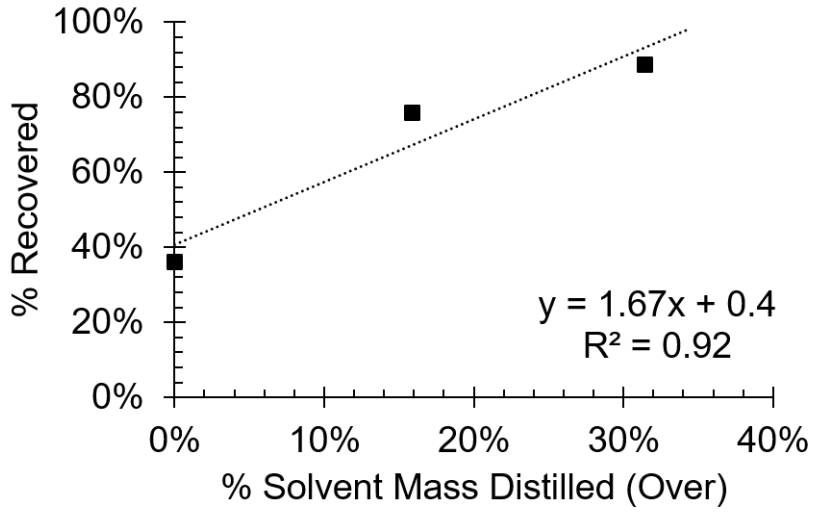

Figure 6.4: Correlation between percent recovery and percent DMAc mass distilled during reactor preparation.Where $y = \%$Recovery and $x = \%$Solvent Mass Distilled.

The pretreatment of the reaction media, especially at scale, is one of the most important requirements to achieving a low PMI value and high percent product recovery and selectivity. The PMI was lowered from ca. 80 to 7, the % Recovery was increased from 40 to 92%, and an 89% selectivity was obtained, Table 6.1.

The dry, isolated product was characterized through ^{1}H NMR at 55°C in deuterated chloroform, Figure 6.5. The ^{1}H NMR was used to determine the degree of substitution (DS) and impurity profile of the material.

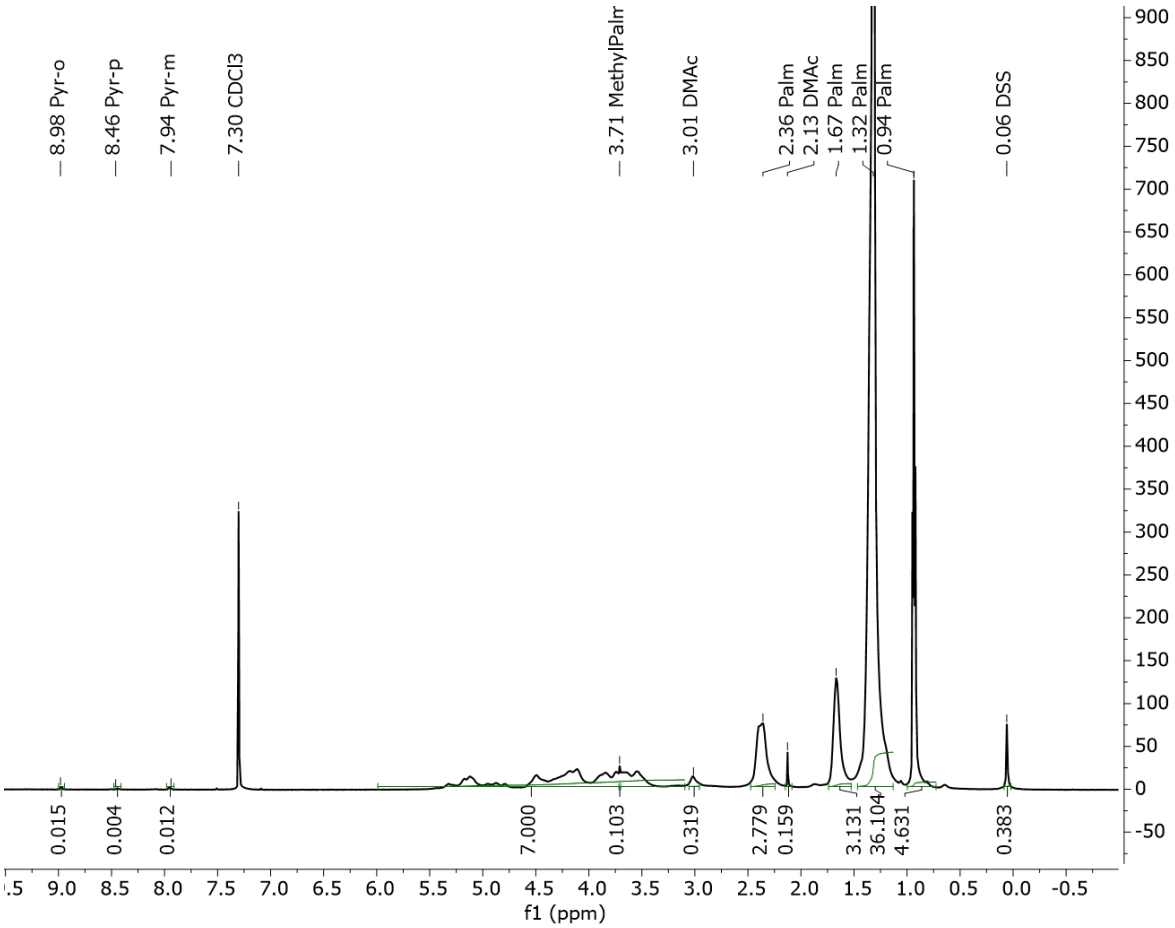

Figure 6.5: ^{1}H NMR of dry, isolated α-1,3-glucan-palmitate thermoplastic.

The DS was calculated from the ^{1}H NMR spectrum by taking the integral of the terminal methyl protons associated with the aliphatic palmitate chain (0.94 ppm) and the integral of the protons on the glucan backbone (3-6 ppm). The methyl protons of the palmitate were normalized by dividing the area by 3 and the glucan was normalized by dividing the area by 7, Equation 6.1

$$DS = \frac{7}{3} \cdot \frac{I_{0.94ppm}}{I_{3-6ppm}} \tag{6.1}$$

To accurately calculate DS with Equation 6.1, it is very important to remove any contributions

from methyl palmitate or DMAc that remain in the solid after purification and drying by subtracting its contribution to the area in the regions of interest away. The presence of pyridine can be seen in the aromatic region of the spectrum.

The modified α-1,3-glucan-palmitate (GP) material was characterized with TGA-DSC, Figure 6.6. The TGA (black) analysis revealed minimal loss of mass upon heating prior to decomposition. The DSC (red) analysis suggest there is a modest glass transition temperature at 135°C, followed by an endothermic peak associated with melting of the material around 220°C, and finally the decomposition is presented with two peaks rather than one arising from the palmitate and the glucan contributions of the GP material.

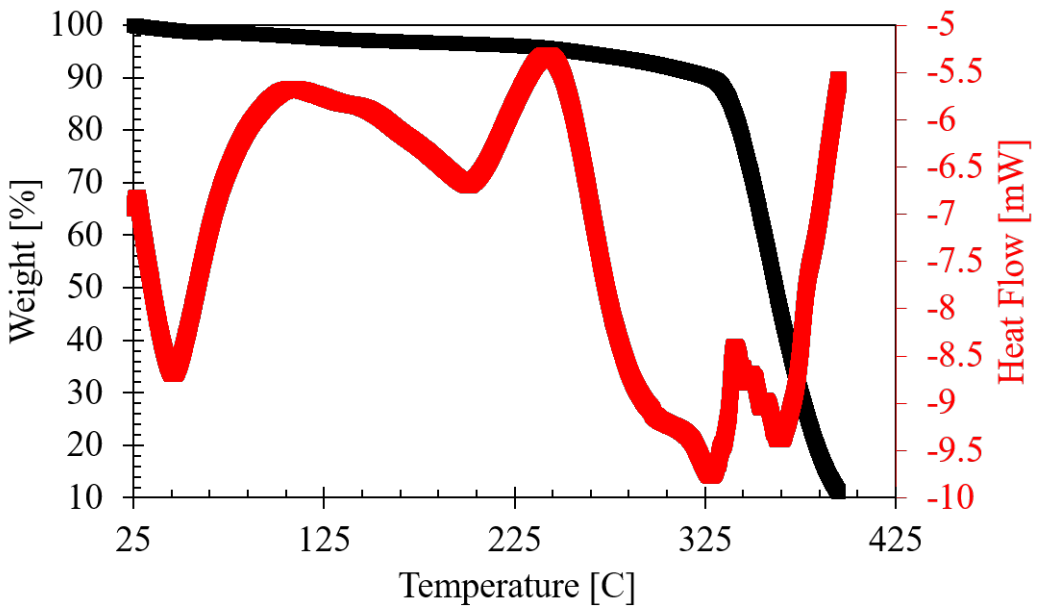

Figure 6.6: TGA/DSC characterization of the modified α-1,3-glucan-palmitate.

After thermal characterization, the glass and melting point temperatures were utilized in the development of a hot press fabrication method. However, due to material heterogeneity, the GP material was cryomilled and turned into a fine powder prior to hot pressing. Once cryogrinded, a 0.5 mm thick layer of material was placed between two Kapton (non-adhesive) films that evenly and quickly dissipate the heat through the material for an even melt. The material requires 100 lbs

per in^2 and a temperature of at least 140°C. The film had an average thickness of 786 μm, Figure 6.7.

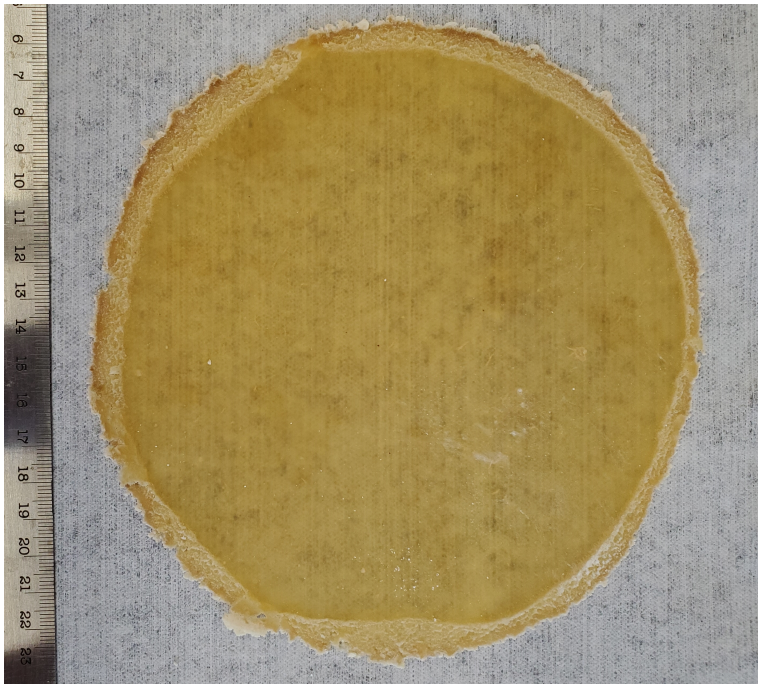

Figure 6.7: α-1,3-glucan-palmitate hot pressed films with a thickness of 786 μm.

After pressing, the films were characterized through a variety of techniques, including contact angle measurements with polar (water) and non-polar (hexadecane) components. The native α-1,3-glucan polymer, with an overall surface polarity of 39.9%, is rich with hydrogen bond donor/acceptors that promote highly energetic polar interactions. However, the dispersive components (32.1 mJ m^{-2}), rather than the polar components (21.3 mJ m^{-2}), are the main contributors to the overall surface energy of the native glucan (53.4 mJ m^{-2}), Figure 6.8.

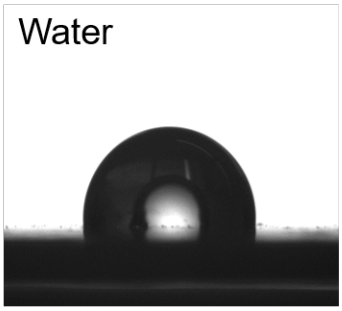

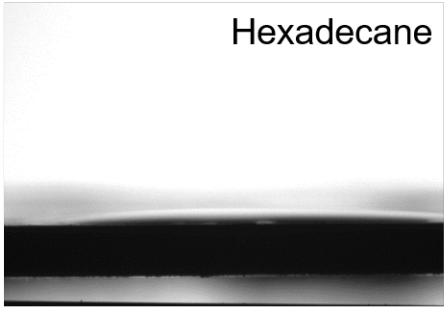

Material	Surface Energy [mJ/m^2]
Alpha-1,3-glucan	53.4
Glucan-palmitate	28.2

Figure 6.8: Surface energy of native and modified glucan polysaccharides obtained through the contact angle of water and hexadecane.

It is apparent from the surface energetics that the interactions with the solvents decrease with the palmitate substitution of the glucan. The contact angle for hexadecane and water were 9.3 and 97.8, respectively. Yielding a surface free energy for the dispersive and polar forces of 27.1 and 1.0 mJ m^{-2}. Suggesting that the overall surface polarity of the material is of 4%. This confirms the modification of the material by the palmitate.

The mechanical properties of the films were characterized with RSA III dynamic mechanical analyzer. The film showed a maximum stress of 2.7 MPa and strain 5.7%, with a Young's modulus of 0.47 MPa, Figure 6.9.

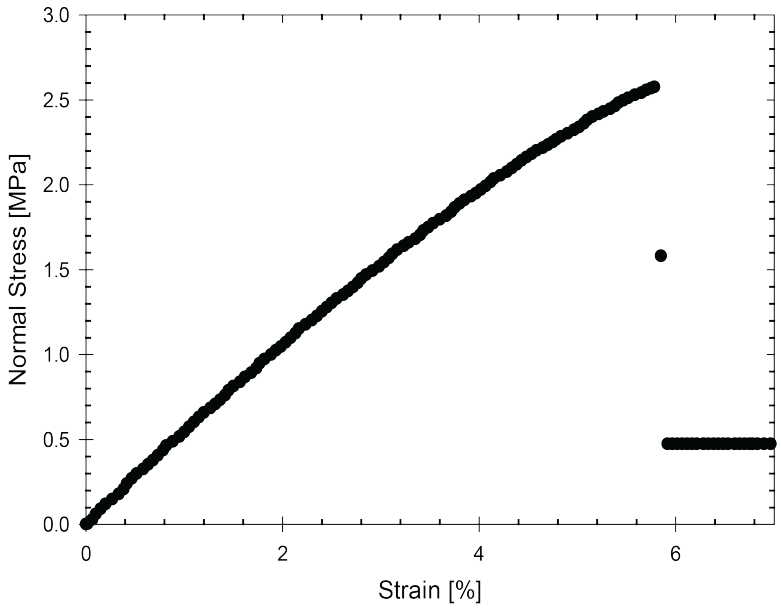

Figure 6.9: Tensile Strength of Sample A8-89.

Iwata & coworkers demonstrated that tensile stress and Young modulus have an inverse relationship with increasing alkyl chain of the modifier.[189] In their studies, α-1,3-glucan-acetate and α-1,3-glucan-octanoate had a tensile strength and Young's modulus of 41 MPa and 0.84 GPa, and 4.8 MPa and 0.07 GPa, respectively. Even thought the alkyl chain is doubled that of α-1,3-glucan-octanoate, the α-1,3-glucan-palmitate possess similar tensile strength, but does have a significantly lower Young's modulus. It is worth noting that Iwata & coworkers utilized a chloroform solution casting method to produce a large variety of films and properties that would be different through hot pressing methods.[175] For example, the α-1,3-glucan-acetate and -propionate have a melting point and decomposition temperatures of 339 and 299°C, and 350 and 355°C.[189] The proximity between these two values makes melting protocols tough to achieve without partial decomposition of the material.

The water vapor transmission rate (WVTR) and permeance (WVP) were characterized with a custom apparatus that tracked the loss of mass, room temperature, and relative humidity of the room throughout the course of 10-15 days, Figure 6.10.

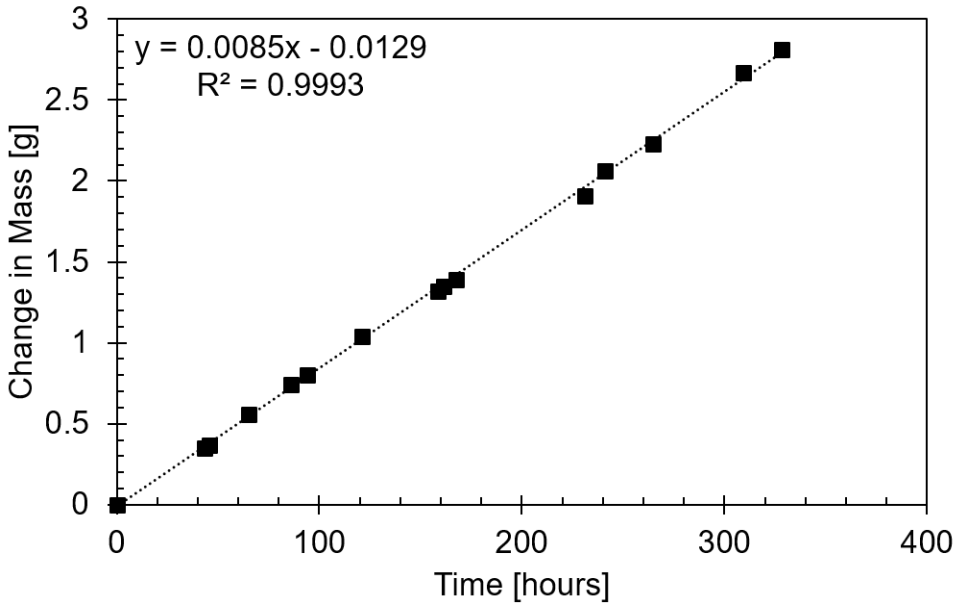

Figure 6.10: Water Vapor Transmission Rate Sample A8-89.Where $y =$ Change in Mass and $x =$ Time.

The oxygen permeability of an α-1,3-glucan-palmitate thermoplastic with a degree of substitution of 2.1 is reported in Table 6.2. Additionally, Table 6.2 also contains the water and oxygen permeance properties for polyvinyl alcohol (PVOH), polyvinylidene chloride (PVDC), polyamide (PA), polyethylene terephthalate (PET), polyvinyl chloride (PVC), high- and low- density polyethylene (HDPE or LDPE), polypropylene (PP), polystyrene (PS), ethylene-vinyl acetate (EVA), polyisobutylene (PIB), polydimethylsiloxane (PDMS), and polylactic acid (PLA). Steady-state permeability values of 27.3 ± 0.5 Barrer, or $1.8 \cdot 10^{-5}$ $\frac{cm^3_{STP}m}{m^2 dayPa}$, were obtained, Figure 6.11.

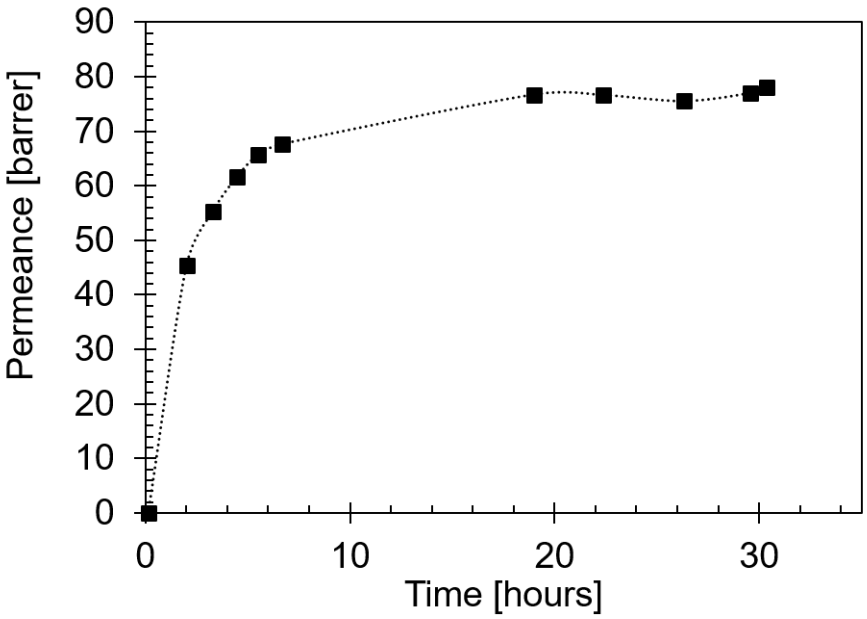

Figure 6.11: Steady-state permeance of glucan-palmitate films.

Table 6.2: Oxygen and water permeance properties for a variety of oil and bio-based thermoplastics commonly used in food packaging applications.

Plastic	OP $\cdot 10^{-7}$ $\frac{cm^3_{STP}m}{m^2 dayPa}$	WVP $\cdot 10^{-14}$ $\frac{gm}{m^2 sPa}$	Citation
PVOH	0.003	342.7	19
PVDC	0.001-0.030	1.2	
PA	0.01-0.10	5.8-114.3	
PET	0.1-0.5	5.8-22.9	
PVC	0.2-0.8	18.3	
HDPE	7.1	1.7-3.5	
PP	4.9-9.9	2.3-4.6	
PS	9.9-14.8	11.3-45.6	
EVA	21.2	6.7-17.1	
LDPE	44.8	6.7-8.7	
PIB	7.8		248
PDMS	3,888		
PLA	1.8	1290	222
GP (DS 2.1)	283.8	490	This Work

A proper oxygen barrier is critical to maintain the quality of the packaged food. Most vegetables are packed in an inert environment and require little to no permeance of oxygen. A material for this application is generally considered to have an adequate oxygen barrier if the oxygen permeability is less than $1 \cdot 10^{-8}$ $\frac{cm^3_{STP}m}{m^2 dayPa}$.[222] From Table 6.2, the GP film is an order of magnitude above this threshold. These preliminary results suggest that further modification to the structure of GP material could yield lower oxygen permeability. However, tomatoes, potatoes, among other food items, are often packaged in plastic and require direct contact with water and oxygen. These materials with a higher water and oxygen permeability would be great for these applications, while providing a seal to avoid flies and other contaminants from coming into contact with the produce.

6.4 Conclusion

Palmitate derivatization of alpha-1,3-glucan yields a thermoplastic material that may be melt cast to a film for packaging applications and which is anticipated to be compostable. The process has been optimized to reduce the process mass intensity (PMI) index from 213 to 7 further enhancing the attractiveness of this material for sustainable packaging applications. Based on the property and performance characterization provided herewith, the films generated from the modified GP material have potential for applications where a high water and oxygen permeance is needed, but also for applications that require little mechanical stress. An example being the sorting of tomatoes, berries, and grapes, among other fruits and vegetables into small quantities that one can buy at a supermarket.

The inherent susceptibility of the α-1,3-glucan for acid-catalyzed hydrolysis promotes degradation in natural environments, while microorganisms can decompose the modified material back to naturally occurring components. As shown, thermoplastic starch, a polysaccharide, is one of two materials that experiences degradation under all natural conditions and environments.

Chapter 7

Biodegradable non-ionic Glucan Benzoate Detergents

Abstract

Here, a completely aqueous synthesis of α-1,3-glucan-benzoate detergent at low temperatures (3-5°C) in a 1 L kettle reactor is reported. The synthesis achieves 94% selectivity, 96% recovery, and PMI indices as low as 10. An aqueous synthesis is preferred as it resembles the conditions of use; reducing purification intensity by eliminating organic hazardous organic solvents. Additionally, at low temperatures the benzoylation of glucan is preferred over the competitive hydrolysis of benzoyl chloride. Yielding adequate reaction performance for the synthesis of greener detergents.

Soaps and detergents represent an increasing threat to the health of aquatic life. Traditional detergents are made up of surfactants, fillers, foaming agents, stabilizers, perfume agents, soil-suspending agents, enzymes, dyes, optical brighteners, bactericide agents, etc., that negatively impact the ecosystems by promoting eutrophication, foaming, and changes in temperature, salinity, turbidity, pH, and dissolved oxygen concentrations.[159] Phosphates are largely responsible for eutrophication of rivers and oceans. Eutrophication leads to excessive algal growth that decreases dissolved oxygen and the transmission of light needed to sustain life below water. As a result, both fish and lake/ocean flora are threatened. Surfactants improve our health and well-being. Unfortunately, some surfactants decrease the operational efficiency of wastewater treatment facilities by compromising the health of microorganisms required aerobic and anaerobic processes. Surfactants that diminish aquatic life and the working conditions of wastewater treatment facilities that protect our water supply are in

need of replacement. In order to overcome these issues, a non-ionic α-1,3-glucan-benzoate (GB) detergent that can be broken down under atmospheric conditions where it can then be processed by microorganisms in nature, not just in wastewater treatment facilities, is made.

7.1 Introduction

Soaps and detergents are interchangeable words to describe cleaning agents, but differ in that soaps have traditionally employed naturally occurring components, while detergents are made from synthetic counterparts.Traditional detergents are made up of surfactants, fillers, foaming agents, stabilizers, perfume agents, soil-suspending agents, enzymes, dyes, optical brighteners, bactericide agents, etc., that negatively impact the ecosystems by promoting eutrophication, foaming, and changes in temperature, salinity, turbidity, pH, and dissolved oxygen concentrations.[159] Compounding ingredients are those that are non-surface-active, i.e., all components but surfactants.

Surfactants are the surface-active agents that reduce the surface tension of the solvent they are dissolved in, typically water.[74] There are four categories of surfactants utilized today: 1) amphoteric surfactants that contain both acidic and basic groups that allow them to switch between cationic or anionic properties based on pH changes. 2) Anionic surfactants have a negatively charged ion. 3) cationic surfactants have a positively charged ion. Anionic and cationic surfactants can be made of a variety of functional groups that ionize at different pH to match the desired application. 4) Non-ionic surfactants do not ionize in neutral aqueous environments, i.e., pH of approximately 7. In general, surfactants are made of a polar, ionic head and a non-polar, hydrophobic tail that break the hydrogen bonding network between water molecules, thus decreasing surface tension of a liquid.

Surfactants are essential to life! They reduce the surface tension in the liquid films surrounding lungs to help them easily expand in order to increase the transport of gases, e.g., oxygen, carbon dioxide, etc.[253] As detergents, surfactants help clean and decontaminate surfaces and clothes.[74,126] As a result of their use, better health and well-being is achieved, a U.N. sustainable development goal. During the SARS-COVID-19 pandemic, the utilization of detergents has drastically

increased. In spite of their consequences on the environment, surfactants are essential. Therefore, solutions to minimize their environmental impact need to be developed. These alternatives should not use phosphates, to prevent eutrophication. Even if the detergent formulations become less efficacious, especially in hard water environment. Nor should they be composed of surfactants that are resistant to microorganisms, so they can degrade in the environment, but also so that wastewater aerobic and anaerobic processes function properly and remove other toxic wastes.

To function properly as detergents, surfactants need to reach and go beyond the critical micelle concentration (CMC), Figure 7.1. At this concentration, the surface tension reaches a minimum, as the surface of the fluid is saturated with surface acting agents. To act as a detergent, the surfactant concentration has to go beyond this concentration so that the excess surfactants can form micelles. Micelles are the spherical arrangement of surfactants, where the oleophilic tails (non-polar) orient themselves towards the center of the sphere and the hydrophilic heads (polar) are on the outside of the sphere to interact with the hydrogen bond network. The interactions among surfactant molecules begin to dominate the medium and prompt structural organization into micelles.

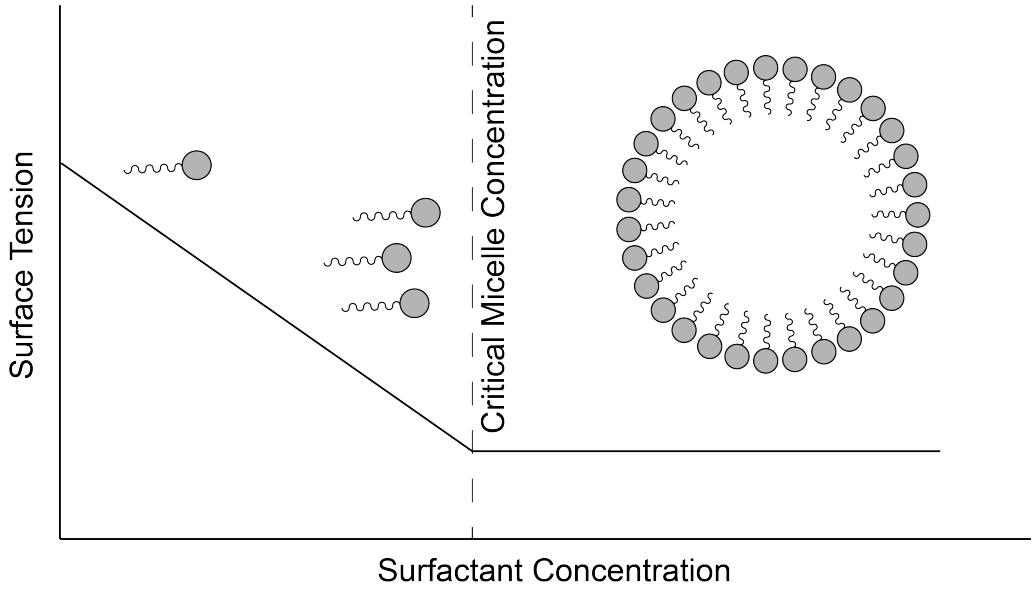

Figure 7.1: Surfactant and micelle arrangement of detergents in water.

Micelles sequester oleophilic components, e.g., dirt and grease, among other articles found in clothes/dishes/etc., inside the vesicles. These components are suspended in the fluid due to the

strong interactions between the ionized/polar group with water. The CMC is highly dependent on solvent polarity, structural configuration of surfactant and the ion concentrations in solution.[65] Most anionic surfactants become less effective in hard water as it contains different cationic species (Ca^{2+}, Mg^{2+}, Fe^{3+}) that detrimentally interact with the polar head and cause inefficiencies in micelle formation and therefore detergent properties.[115,126]

Here, a non-phosphate based non-ionic detergent made of a bioengineered polysaccharide, α-1,3-glucan, derivatized with benzoate moieties under completely aqueous conditions for synthesis and work-up is described.

7.2 Experimental

Samples of α-1,3-glucan were sourced from Industrial Flavors & Fragrances with degrees of polymerization (average number of repeated units) of 800, 165, and 50. The molecular weights of the polymer are 130, 27, and 8 kDa, respectively. Nitrogen gas (N_2; SKU: NI UHP1L) was used as received from Matheson Tri Gas. Reversed osmosis (RO) treated water was sourced in-house.

The experimental set-up for this system is described in detail in Section 2.8. However, a distillation apparatus was not utilized for this process.

7.2.1 Synthesis of alpha-1,3-glucan-benzoate.

A typical synthesis consists of loading 50.3 g α-1,3-glucan, 250.0 g of RO water, and 18.0 g of solid NaOH into the reactor. After 30 minutes of mixing at room temperature, the slurry becomes a solution while also transitioning in color from white to a light yellow. This transformation indicates the activation of the glucan polysaccharide. At this point, the solution was placed in an ice bath (3-5°C) prior to the addition of benzoyl chloride at 1 ml/min. The addition of benzoyl chloride led to precipitate formation and a color transition from yellow back to white. The solution was left stirring for an additional 30 minutes, totaling 2 hours of synthesis.

7.2.2 Work-up of alpha-1,3-glucan-benzoate.

The work-up for this synthesis consists of a series of washes and filtrations to remove unreacted materials, but also bring the pH of the reaction media to neutrality. A minimum of 3, 250-500 mL RO water washes were used to neutralize the reaction media from a pH of 14 to a pH of approximately 7. A large filter, approximately 15 cm in diameter for particles $>20\ \mu$m in size, was used to collect the α-1,3-glucan-benzoate non-ionic surfactant while allowing impurities dissolved in the water to be removed. Impurities consist of benzoic acid (or sodium benzoate), sodium chloride, and unreacted glucan. Once the pH is neutralized, the solid content was placed in a vacuum oven at 60°C.

7.3 Results and Discussion

The esterification of α-1,3-glcuan with benzoyl chloride (BC) has great atom economy, approximately 92%. The inefficiencies in terms of atom economy arise through the loss of the chloride species into the solution. The schematic in Figure 7.2 shows the general conditions under which this reaction is performed.

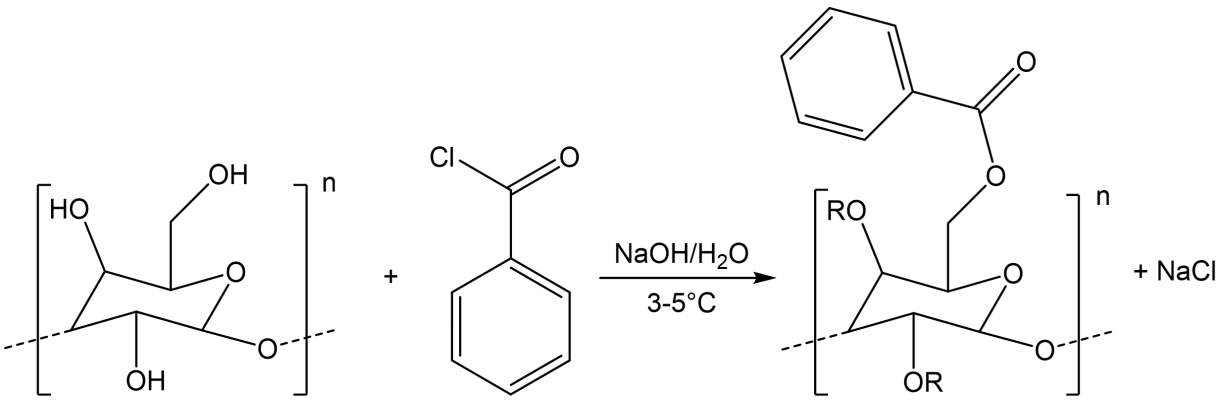

Figure 7.2: Reaction between α-1,3-glucan and benzoyl chloride to yield a non-ionic detergent. R can either a proton or a benzoate group.

Appendix E contains a summary, Table E.1, of the most important reactions, their conditions, PMI index, recovered mass, degree of substitution (DS), and selectivity (Equation D.1). In terms

of PMI, a minimum value of 10 was achieved. This is a fairly low value but is even more attractive when noting that the waste materials are exclusively aqueous and more benign than wastes comprising the organic solvents and bases used in Chapter 6. In terms of recovery, the best synthesis and work-up yielded 74.4 grams which equates to 96% recovery of this reaction. In terms of degree of substitution, the primary target range supporting the detergent application is from 0.25 to 0.5; a variety of reactions met that criteria. However, in terms of selectivity, the best synthesis achieved 94%.

The relationship among these variables is highly complex and dependent on a variety of things, most importantly to the concentration of sodium hydroxide (NaOH). There is a strong relationship between % selectivity and the ratio between NaOH and BC, Figure 7.3.

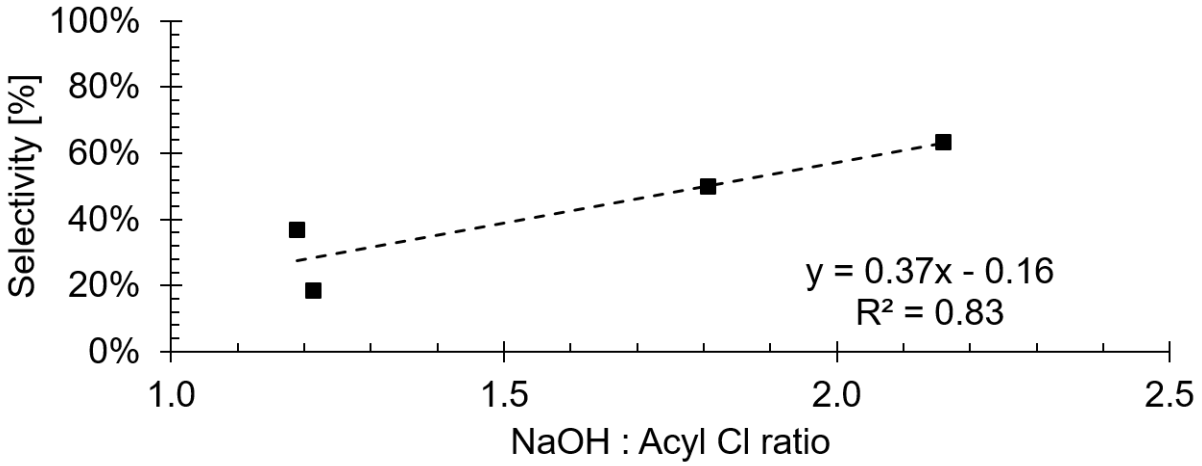

Figure 7.3: Trend describing the relationship between selectivity and NaOH to BC ratio in the synthesis of GB. Where $y = \%$Selectivity and $x =$ NaOH:Acyl Cl ratio.

Increasing the ratio of NaOH with respect to BC increases the selectivity by promoting higher activation of the α-1,3-glucan. There are 3 R-OH groups per anhydroglucose unit (AGU) along the polymer chain. Alcohols, e.g., ethanol and methanol, have a pKa of 16 and 15, respectively, which means that when the pH is 16, half of the -OH groups have been deprotonated to form alkoxides R-O$^-$. This statement is based on the Henderson-Hesselbalch equation, Equation 7.1.

$$pH = pKa + \log\left(\frac{[Base^-]}{[Acid]}\right) \tag{7.1}$$

When the pH is equivalent to the pKa, the concentration of the acid and conjugate base are equivalent. As pH moves further away from the pKa, the population of alkoxide ions changes, according to Equation 7.1. At a ratio of NaOH to BC of 2 is approached, the pH value can only be reported up to 14 due to equipment limitations. As an example, at a pH of 14, 1% of the ethanol and 10% of the methanol groups would be deprotonated, facilitating the reaction with BC.

As NaOH is increased, the alkoxide ions interact with the Na^+ to promote ionic-bond crosslinking between different polymer chains. At the end of the reaction, a high sodium content can lead to the formation of gels, that make the work-up of this synthesis resource and labor-intensive. A gel was observed when the sodium content reaches the vicinity of 6 w/w%, but not around 1 w/w% in isolated products.

Since a completely aqueous synthesis implemented, hydrogels crossed linked through Na^+ ions are formed. Crosslinking negatively impacts reaction work-up by promoting retention of water and dissolved impurities in the solid matrix. To alleviate the work-up intensity, guidance from the Hofmeister series (Table 7.1) was taken to select different cations that might show promising results in terms of reaction performance but also in decreasing purification intensity.

Hofmeister Series										
CO_3^{2-}	SO_4^{2-}	$S_2O_3^{2-}$	$H_2PO_4^-$	F^-	Cl^-	Br^-	NO_3^-	I^-	ClO_4^-	SCN^-
Native						Denatured				
$N(CH_3)_4^+$	NH_4^+	Cs^+	Rb^+	K^+	Na^+	Li^+	Ca^{2+}	Mg^{2+}	Zn^{2+}	Ba^{2+}

Table 7.1: Hofmeister series describing the influence of cation to protein/polymer folding and unfolding.[115]

Based on the Hofmeister series, it is expected that cations such as lithium, calcium, magnesium, zinc, and barium promote the activation and crosslinking of the polymer, while cations like potassium, rubidium, cesium, ammonium, and tetramethylammonium promote structural integrity, but not gelation. To try to reduce work-up intensity ammonium hydroxide (NH_4OH) and potassium hydroxide (KOH) were both used as substitutes for NaOH under the same reaction conditions,

Table 7.2.

Table 7.2: Performance evaluation of cation species in hydroxide bases.

Reaction	A8-141	A8-138	A8-135
Base	KOH	NaOH	NH_4OH
DS	0.39	0.27	0.02
% Selectivity	73	46	4
% Recovery	77	77	63
PMI	42	21	50

Potassium hydroxide showed an improvement in selectivity, and degree of substitution, while it matched the same performance of NaOH in terms of % recovery. PMI and % Recovery are both indicators of work-up intensity. Ammonium hydroxide showed enhanced performance in this category; however, it is worth mentioning that cation identity and concentration plays a crucial role in activating the glucan and in this case the concentration of ammonium hydroxide was lower. Both KOH and NaOH showed great performance, the former on reaction efficiency, the latter on reduced work-up intensity. The NH_4OH experiment likely suffered from reduced activation of alcoxides because of the reduced pH of the medium. As one seeks to improve the PMI of a process to improve sustainability, one cannot sacrifice product performance. Ultimately, the best synthesis is that which gives the best detergent attributes (vide-infra) at lowest PMI.

Once the product was isolated and dried, a ^{1}H NMR was collected at 55°C, Figure 7.4. The proton NMR has been referenced to DMSO (2.5 ppm). The glucan resonances (3-6 ppm) are broad from the anisotropy arising from the limited mobility of the polymeric matrix. Indeed spectra are collected at 55°C to enhance polymer motion and spectrum quality. The aromatic region (7-8 ppm) contains broad and sharp benzoate signatures.

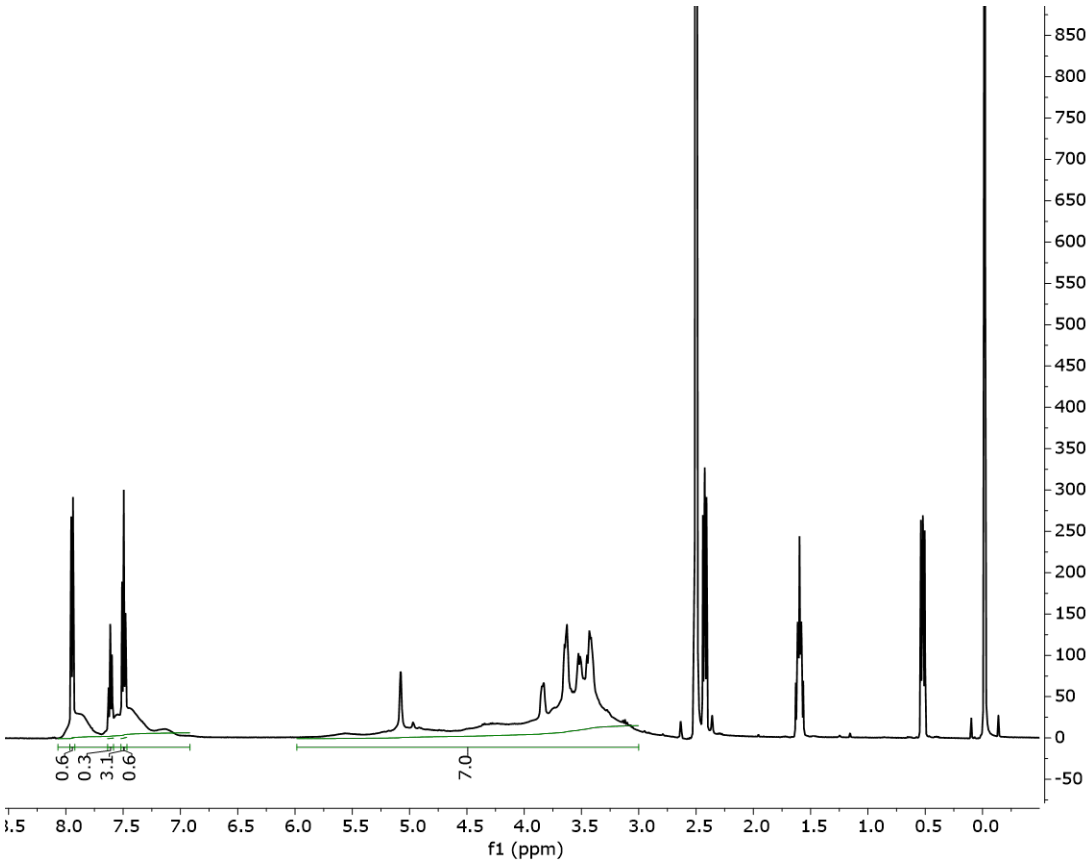

Figure 7.4: ^{1}H NMR of α-1,3-glucan benzoate (A8-119) at 55°C in DMSO-d_6.

To assess whether the sharp aromatics peaks were part of the glucan benzoate polymer or left-over by impurities, a diffusion-ordered spectroscopy NMR experiment was conducted, Figure 7.5. This experiment differentiates resonances based on the self-diffusivity of each moiety (polymers low; small molecules high).

Based on this analysis, it is clear that the signal (sharp peaks) associated with lower molecular weight species disappear before the polymer and the broad aromatic signatures. The signatures associated with the polymer are broad since they experience anisotropic interactions with the magnetic field. To determine the degree of substitution of the GB products, the sharp aromatic peaks from the aromatic region's integral are subtracted along with any impurities present in the glucan region, Figure 7.4.

In a quantitative NMR (qNMR), sodium trimethylsilylpropanesulfonate (DSS) is used as an internal standard to measure the concentration of benzoic acid (or sodium benzoate) in solution.

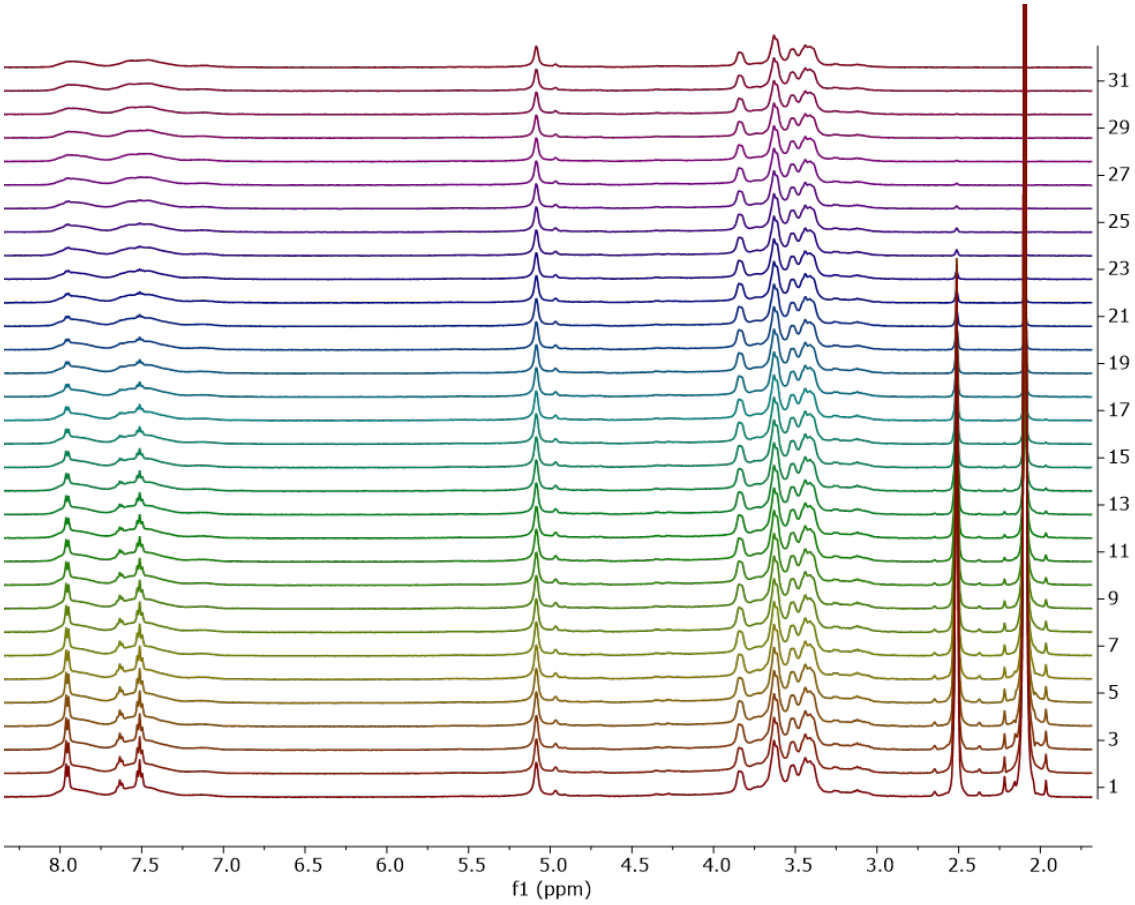

Figure 7.5: DOSY NMR spectroscopy experiment of sample A8-119

For reaction A8-130, a mass balance on the benzoyl chloride was performed, Table 7.3.

Table 7.3: Mass balance of benzyl chloride extracted from work-up protocol in reaction A8-130.

BC Loaded [g]	BC Reacted [g]	BC Removed [g]	BC Remaining [g]
23.5	11.7	11.4	0.4

The reaction exhibited a 50% selectivity for incorporation of benzoate moieties. Out of the 23.5 g of benzoyl chloride loaded into the reactor, 11.7 g were incorporated into the final product. Based on qNMR data, 11.4 g were removed through the reaction work-up, while the product maintained 0.4 g, presumably as benzoic acid and visible in the NMR as sharp aromatic peaks. This raises the point that benzoylation in a NaOH solution involves competing kinetics for glucan modification and BC hydrolysis to benzoic acid. While mass loss to this hydrolysis product is undesired, the

very fact that a large percent of BC reacts with glucan instead of directly hydrolyzing is itself pleasantly surprising and the utilization of completely aqueous conditions engenders sustainability advantages compared to organic solvents. Complete characterization of the kinetics of the desired and undesired competing reactions of BC remains a goal of research.

In an orthogonal approach, FTIR in KBr pellets was performed as described in Section 2.17. In this approach information is collected on the α-1,3-glucan (A8-D104657-814), and reactions 127, 128, and 129.

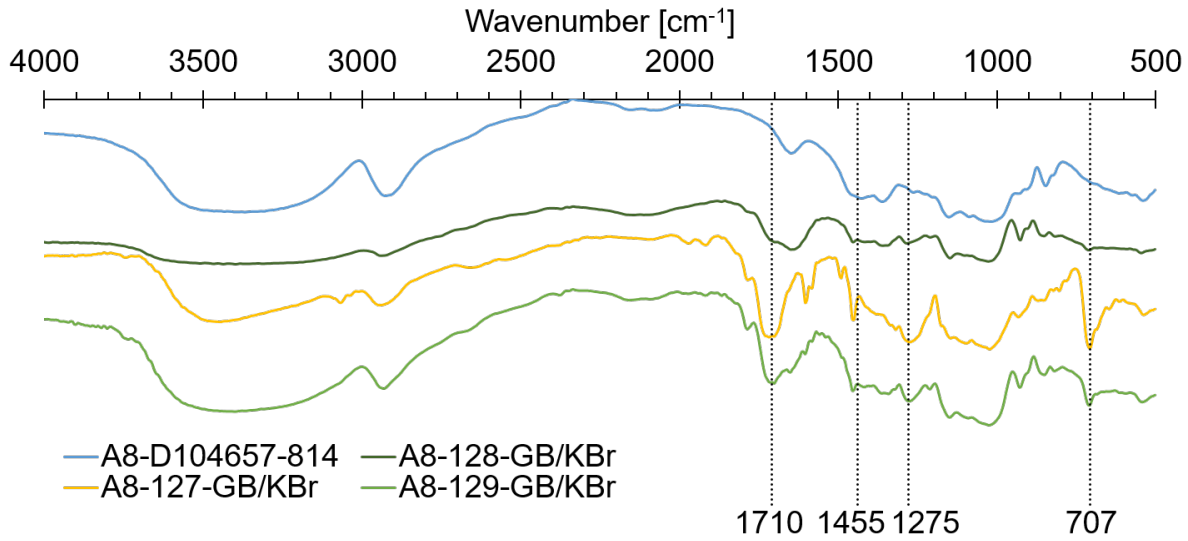

Figure 7.6: FTIR experimental data of GB products in contrast to native α-1,3-glucan.

From Figure 7.6 and Table 7.4 signature peaks unique to the modified materials can be observed. These are carboxylic acid, aromatic ester, and C-Cl. Through the signature of aromatic ester (C-O) between 1310-1250 cm^{-1}, we confirm the presence of modified glucan with benzoate. As determined through qNMR, there is unreacted benzoyl chloride (C-Cl; 800-600 cm^{-1}) and impurities such as benzoic acid (C=O; 1720-1706 and O-H; 1440-1395).

Table 7.4: Relevant FTIR peaks for the glucan-benzoate detergent synthesis.

Functional Group	O-H Alcohol	C-H Alkane	C=O Carboxylic Acid	O-H Carboxylic Acid	C-O Aromatic Ester	C-Cl
Wavenumber [cm^{-1}]	3500-3200	3000-2850	1720-1706	1440-1395	1310-1250	800-600
A8-D104657-814	3385	2923	"N/A"	"N/A"	"N/A"	"N/A"
A8-127-GB/KBr	3459	2940	1712	1455	1278	707
A8-128-GB/KBr	3397	2929	1710	1347	1278	707
A8-129-GB/KBr	3385	2929	1707	1455	1273	707

In terms of applications testing, a high throughput solubility screening of these products was performed, Figure 7.7. Ideally, a solubility of 10 mg mL^{-1} and a parabolic behavior would be obtained as a function of isopropanol concentration for the binary solvent mixtures of isopropanol and water. Attaining both of these criteria reflects homogeneity in substitution and the desired degree of substitution. In reaction A8-133, these criteria are achieved.

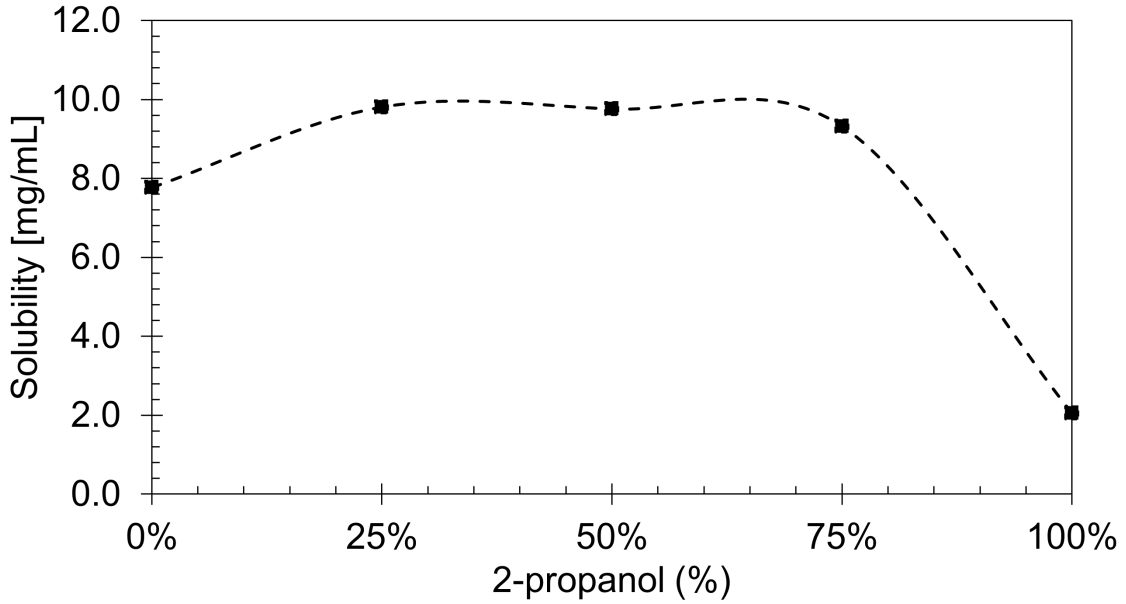

Figure 7.7: Solubility profile of reaction A8-133.

When the degree of substitution exceeds the desired range, the GB material has poor solubility, approximately 1- mg mL^{-1}. When the modification is heterogeneous different interactions of the

polymer and the solvent mixture are expected which lead to a sinusoidal or linear variation within the data. In reaction A8-133, sodium chloride (NaCl) was used as an additive in addition to NaOH. The additional sodium content could improve the stability of the active glucan and promote the reactivity across the polymer.

Additional details about the future of this investigation will be shared in Chapter 9.

7.4 Conclusions

The glucan benzoate synthesis was conducted in a fully aqueous, high pH environment at 5°C as a differentiated approach to a sustainable process. Gratifyingly, the rate of BC hydrolysis was lower than BC reaction with the glucan backbone. Here, an intensive process development investigation was conducted to get insight into optimal reactor loadings, reaction conditions, reaction performance (DS, selectivity, recovery), investigate impurity profiles through qNMR and test the solubility of the GB product. From solubility data, a 10 mg mL^{-1} and a parabolic behavior criteria were achieved, which suggest modification homogeneity along the length of the polymer. The DS was confirmed by ^{1}H NMR. DOSY NMR experiments corroborated the sharp aromatic peaks in the aromatic region are free benzoate impurities. FTIR corroborated the presence of benzoic acid and unreacted benzoyl chloride.

Chapter 8

Characterization of Porous Materials Under Conditions of Use: Time-Domain NMR and X-ray Tomography

Portions of this chapter have been previously published by the authors in the Handbook of Porous Materials: Characterization under Practical Conditions: Time-Domain NMR, X-ray Scattering and Tomography (Ch. 2).[233]

Abstract

The characterization of porous materials has traditionally been dominated by techniques which require sample preparation under vacuum, for example gas adsorption techniques, mercury intrusion and electron microscopy. These techniques are valuable, yet they have limits, because the conditions of characterization differ from the conditions of use. This chapter provides a tutorial on key techniques that can be applied for characterizing porous materials under conditions of use. Two broad classifications of characterization problems may be addressed: understanding material textural properties[141] and understanding interactions of surfaces with contacting fluids.[221,242] Textural properties, such as pore size distribution, total porosity and surface area are critical for evaluation of fluid transport and dictate performance of many industrial materials comprising catalysts,[56,140] thermal insulation,[166,226,238] adsorbents,[36,141] paper[157] and more. Understanding the interactions of surfaces with fluids, including reactive interactions, are essential in understanding mechanism in catalysis,[32,86,89,110,167,236] adsorption[31,221,245] and other reactive processes. Amidst a variety of potential applications and characterization methodologies of materials under conditions of

use, the current chapter focuses on two key technologies:

1. time-domain (TD) nuclear magnetic resonance (NMR) and
2. X-ray computed tomography (X-CT).

and provides illustrative examples of their applications, including application of time-domain nuclear magnetic resonance to polysaccharide materials discussed in Chapters 6 and 7. In essence, however, this chapter serves as a handbook aimed at researchers and students, many of whom are not experts in analytical techniques and instrumentation. For each method a detailed theory and background explanation is augmented by examples pertaining to porous materials. Within the realm of characterizing materials under conditions of use the terms in situ and operando characterization are frequently used. We adopt the definitions that in situ characterization implies examination of a sample under a controlled atmosphere, e.g., a reaction mixture, while operando further requires a simultaneous characterization of reaction progress and performance.[152] For the in situ characterization of textural properties samples may be classified as either structurally rigid or bearing meta-stable porosity. For structurally rigid samples characterization of textural properties by ex situ gas adsorption or other techniques is expected to be congruent with characterization under conditions of use. Meta-stable porous materials, on the other hand possess porosity, which may be perturbed by conditions of use, e.g., polymer swelling in the presence of solvent, structural collapse under vacuum, deformation at elevated temperatures. Care must be taken in concluding that a sample is structurally rigid versus meta-stable. For example, select metal-organic frameworks (MOF) are known to deform or breathe while absorbing gases[6,16,76,164,165,178,202] and even zeolite frameworks with their high bulk moduli are known to expand upon gas adsorption, in some cases correlated with cation mobility.[96,142,143,176,179] Multiple techniques can be used for in situ characterization, in some cases. Several MOF and zeolite studies rely on X-ray and neutron diffraction and X-ray absorption spectroscopy to assess structural changes to great effect.[6,31,143,179,196]

Structural changes may be assessed from lattice spacing from diffraction data, whereas X-ray absorption spectroscopy provides information at atomic spacing (one to two bond lengths) and changes in porosity and total surface area must be inferred from correlations to other data including selective gas adsorption or diffusion.[31] In limiting the scope of this work to TD-NMR and X-CT, this chapter explores techniques, which are amenable to in situ characterization and do not perturb the samples from their conditions of use. TD-NMR is useful for characterizing pore size distributions of porous media filled with fluids and a key example to be discussed in Section 8.1 is the adsorption of methane in nanoporous materials and indeed the separation of methane from carbon dioxide. Furthermore, in situ TD-NMR analysis of polymeric hydrogels characterizes the structures without having to remove water via vacuum. This is critical because vacuum operations are known to lead to structural changes in these materials. In Section 8.2, the fundamentals of X-ray generation and interactions with matter are discussed with focus on background is covered in Section 8.2.1. X-CT offers complementarity to TD-NMR and is described in Section 8.2.2. The technique has been deployed to investigate changes in catalyst structure under elevated temperatures and pressures and to characterize supercritical CO_2 movement in nanopores. Finally, published reports combining multiple complementary techniques are described along with a discussion of the outlook and opportunities for growth in these areas of research.

8.1 Time Domain Nuclear Magnetic Resonance (NMR) - Relaxometry & Diffusometry

8.1.1 Introduction & Overview

The application of time-domain nuclear magnetic resonance (TD-NMR) to the characterization of porous materials relevant to petroleum exploration has been established since the 1960s.[37]

The ability to characterize porosity in natural formations using only signals from hydrogen-bearing fluids filling the pores has been applied to great advantage.[62] NMR data collected in

petroleum wells provides information about the porosity of the rock formation, the quantity of oil versus water and the likely productivity of a well. The physical phenomena underpinning the petroleum applications have been adopted for a variety of laboratory studies of porous materials.[26,63,153,155,205] Here the primary focus is upon relaxometry. Diffusometry has been covered in a number of authoritative discussions.[121,153,207,218]

Any atom with an odd number of protons and/or an odd atomic mass will exhibit a non-zero nuclear spin angular momentum (m_I). Useful examples of such nuclei, that exhibit $\pm$ 1/2 nuclear magnetic spin, include: ^{1}H, ^{19}F, ^{31}P, ^{15}N and ^{13}C. When an ensemble of these nuclei is placed in an external magnetic field (B_0), a net alignment of magnetic spin states with the external field will occur, defined by a vector ($\vec{M}$), Figure 8.1. The magnitude of this vector is dictated by the relative population of spins in two quantized energy states (aligned with field and opposite to field) and is further dependent upon the external magnetic field strength. Here the energy separating the levels ($h\nu$) is the product of the gyromagnetic ratio of the nuclei of interest (γ), the reduced Plancks constant ($\hbar$) and the strength of the magnetic field (B_0).

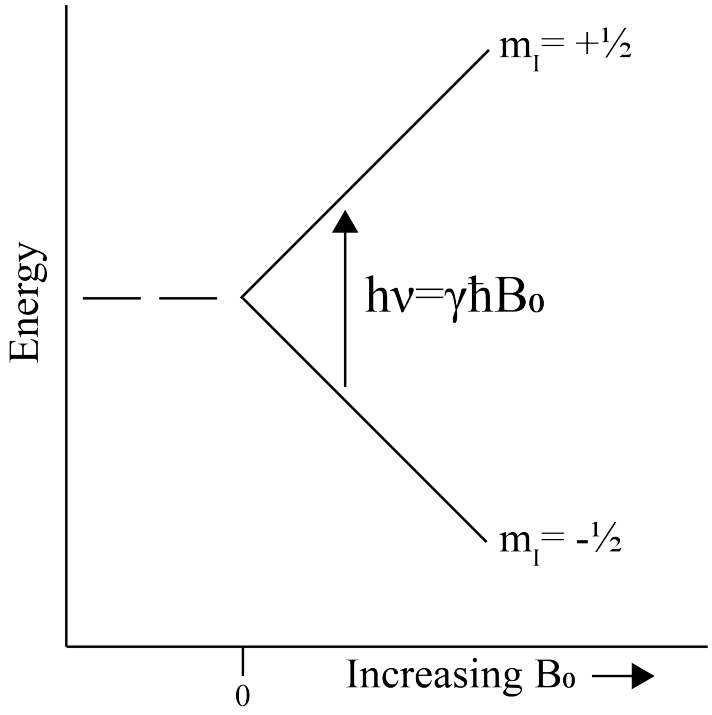

Figure 8.1: Dependence of energetic splitting of $m_I = \pm 1/2$ states in an external magnetic field (B_0).

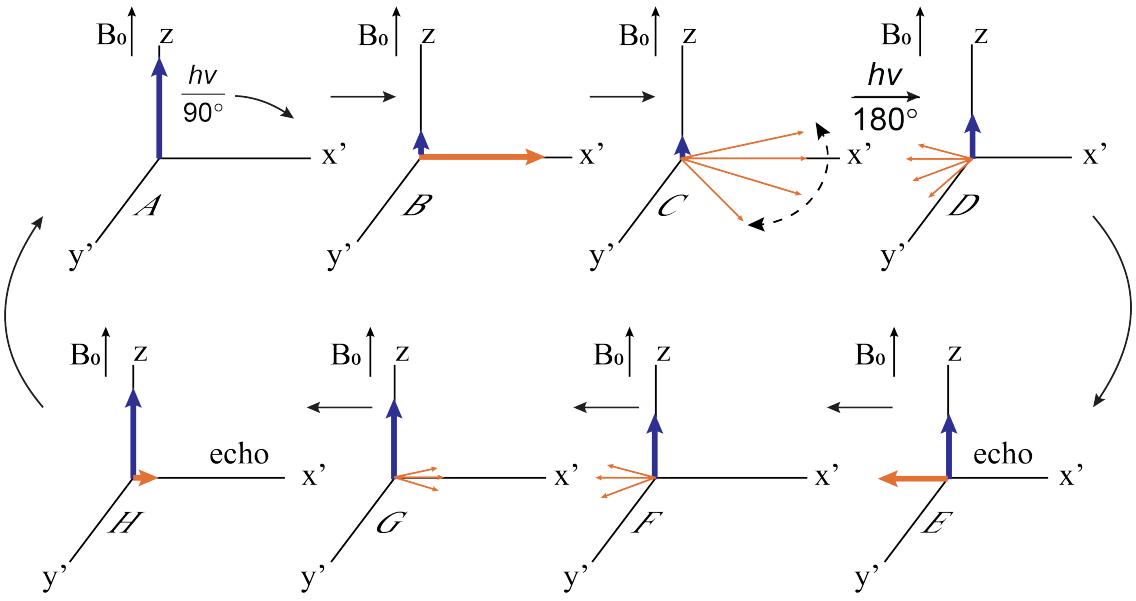

Figure 8.2: Nuclear magnetic relaxation phenomena.

Notably, the ratio of the population of spins is not large and, accordingly, NMR is not a sensitive technique. The population of magnetic moments precess about the external magnetic field vector with frequency, ω, termed the Larmor frequency. The alignment of the magnetic moment may be perturbed by application of an appropriate radio frequency over a specified time, leading to orthogonal perturbation (90°) or anti-parallel perturbation (180°), Figure 8.2. With an NMR instrument one can measure the rate of the spin system returning to equilibrium with the external magnetic field. Two relevant time constants are defined. The first, T_1 or spinlattice relaxation describes relaxation in the direction of the external magnetic field, seen in Equation 8.1. For the second a rotating frame of reference in the orthogonal plane is defined and rotates at the Larmor frequency. In this frame of reference (x', y'), the time constant, T_2 or spin-spin relaxation, describes loss of phase coherence as spins precess, Equation 8.2.

$$M_z(t) = M_z(0)\left[1 - e^{-\frac{t}{T_1}}\right] \tag{8.1}$$

$$M_{xy}(t) = M_{xy}(0)\left[e^{-\frac{t}{T_2}}\right] \tag{8.2}$$

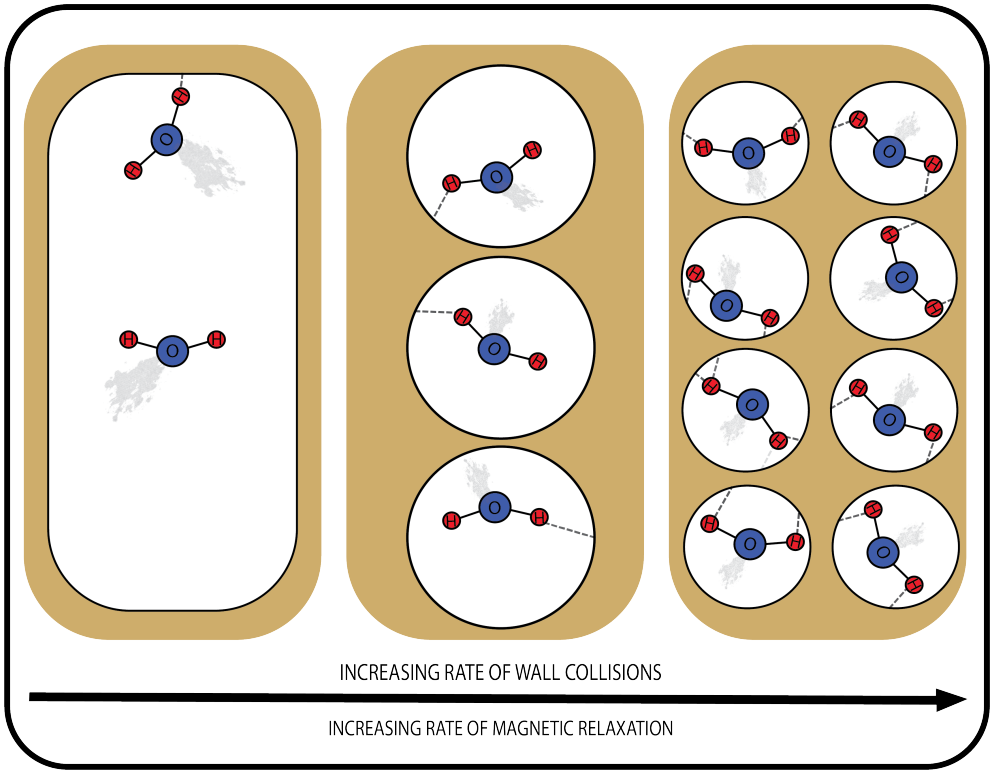

Figure 8.3: Pore size influences upon NMR relaxation rates.

It is important to recognize that following the brief application of a radio frequency, the magnitude of magnetization in the (x, y)-plane decays to zero and magnetization in the z-direction (coincident with the external field) increases exponentially.

Fluid molecules confined in a single pore are in the fast diffusion regime,[39] when all the molecules are diffusionally averaged, spending the same amount of time in contact with the pore surface on the timescale of the experiment. Such a population of molecules will exhibit a single decay rate and time-constant, consistent with Equations 8.1 and 8.2. The decay rate correlates to the size of the pore (Section 8.1.2), such that small pores lead to more rapid relaxation than large pores, Figure 8.3. For a multimodal porous material the population of fluid molecules in the fast-diffusion regime, will exhibit multiple unique relaxation time-constants, reflective of a population of pore sizes, in which the pore fluids do not rapidly exchange among the pores.[123] This is represented by Equation 8.3, with i distinct pore size modes, each with a unique T_2. A parallel expression may be generated for T_1, spin-lattice relaxation.

$$M_{xy}(t) = \sum M_{xy}(0)_i \left[e^{\frac{-t}{T_{2,i}}} \right] \tag{8.3}$$

Outside the fast diffusion regime, a population may experience very rapid surface-enhanced relaxation such that even within a single pore, sub-populations of fluid molecules relax at different rates (rapid relaxation near the surface and slower relaxation away from the surface). In this regime, care must be taken in evaluating relaxation data, as will be discussed in Section 8.1.2. Similarly, if surface enhanced relaxation is very slow compared to the rate of diffusion among pores then interpretation must acknowledge that the fluid is diffusionally averaged across the pore system and the observed rate reflects this averaging.

Before a description of physical bases and methods of data collection, an example of NMR relaxometry data is provided in Figure 8.4 along with a transformed data set typical of pore size distribution. The raw data comprise relaxation of multiple decay curves each with a unique T_2; the Inverse LaPlace Transform is applied typically with some regularization to constrain the derived distribution.

The Inverse LaPlace Transform addresses the ill-posed problem, in that no unique solution exists for deconvoluting multiexponential decay. Multiple approaches to the deconvolution have been discussed in the literature[186] and are addressed further in Section 8.1.2. Instrument manufacturers typically include software for this with their instruments. The data such as those in Figure 8.4 can be compared to pore size distribution data generated from other porous material characterization techniques such as X-ray computed tomography, mercury intrusion porosimetry or gas adsorption. NMR analyses are conveniently conducted in both laboratory and field studies and have been applied to a wide array of porous material types.

8.1.2 Physical basis of NMR relaxation

Recalling that an NMR experiment characterizes a population of nuclear spins, it is notable that individual spins are influenced by their neighbors, both within and external to a given molecule or

solid substance.[78] External spins interact with each other via diffusion. Each individual spin generates a small local magnetic field and contributes to the overall magnetization vector in alignment with the external field, Figure 8.5. A nuclear spin, A, aligned with B_0 may diffuse toward a spin B opposed to the field. The local field of A can promote alignment of B with the external field and transfer of energy in the form of translational and rotational energy, to A. The net effect is an increase in the population of spins aligned with the field. Here spin A and, indeed, all neighboring nuclear spins comprising solvents, solutes, and solid porous materials, etc. are referred to as the lattice and the process is labeled spin-lattice relaxation or longitudinal relaxation and described by the time constant, T_1. As noted above, individual nuclear magnetic moments precess about the external field. Upon excitation with energy in the radio-frequency spectrum, the spins precess in coherence but this coherence decays exponentially with T_2 time constant, resulting in zero net magnetization in the (x, y)-plane, Figure 8.2. Referring to Figure 8.5, as spin A interacts with B, they may exchange spin states, thus A goes from $m_I = +\frac{1}{2}$ to $-\frac{1}{2}$ and B does the opposite. While there is no net change in spin, the interaction of spins does lead to loss of phase coherence and is termed spin-spin relaxation or transverse relaxation.

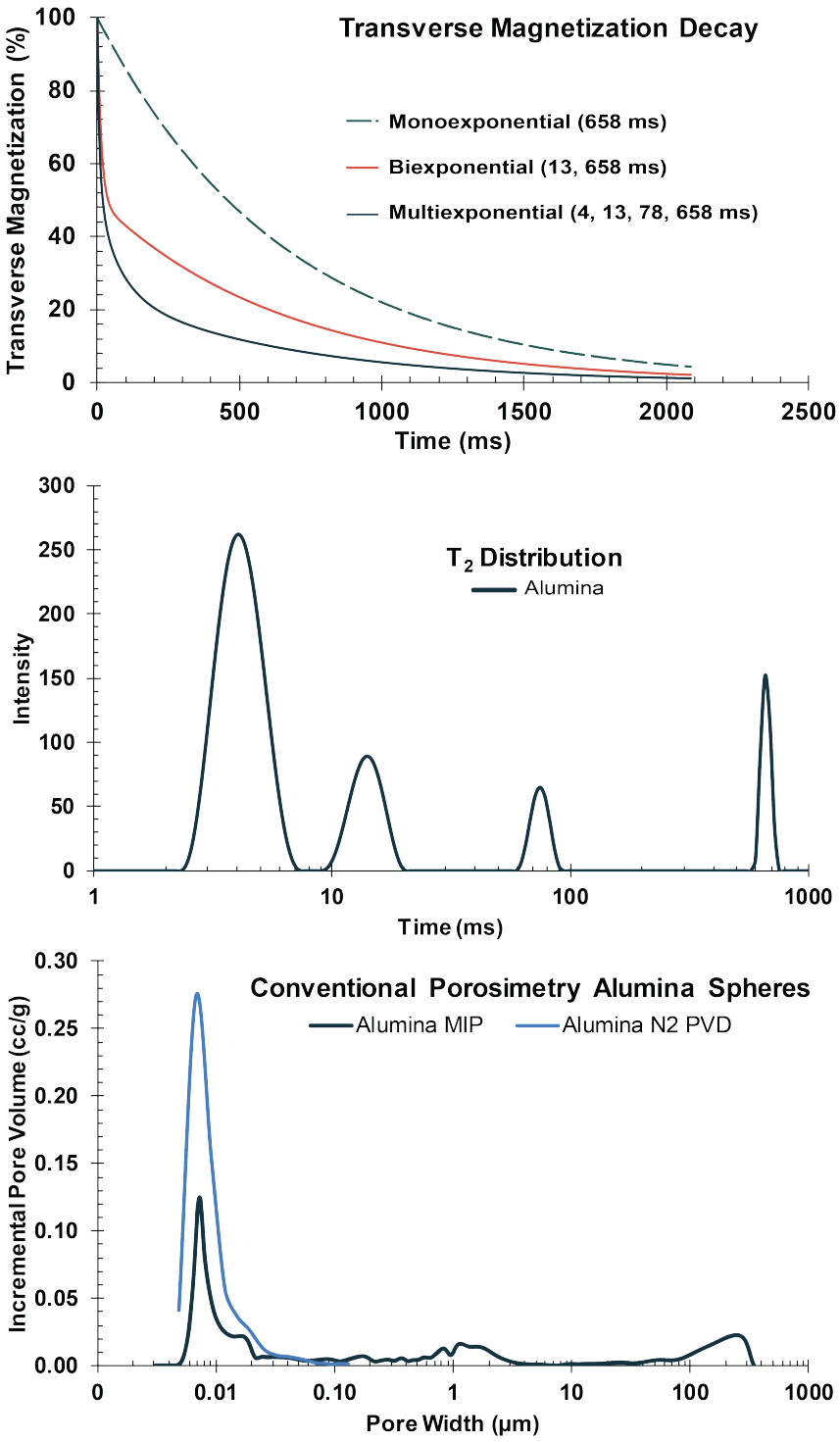

Figure 8.4: NMR relaxometry data for porous media. (a) Simulated multiexponential decay data, (b) Experimental data from the Inverse LaPlace Transform of relaxometry data for water filled alumina catalyst bed and (c) Corroborating data from nitrogen adsorption pore volume distribution (PVD) and mercury intrusion porosimetry (MIP).

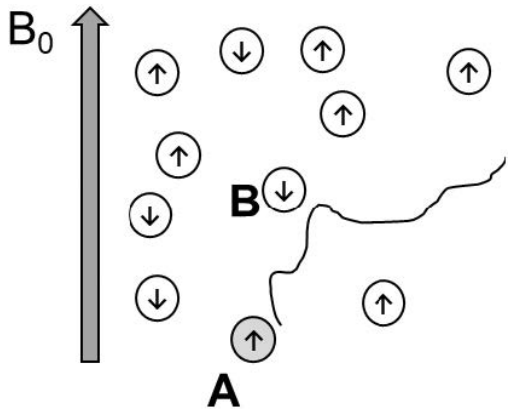

Figure 8.5: Relaxation of interacting nuclear magnetic spins.

The observed spin-spin relaxation decay rate (T_2^1) is attributable to multiple simultaneous mechanisms of relaxation, Equation 8.4.[239] The bulk fluid that fills the pore would experience relaxation rate T_{2B}^1, in the absence of perturbation; the surface of the porous medium promotes an enhanced rate of relaxation (T_{2S}^1), as will be described below, and as nuclear magnetic spins diffuse through internal gradients of magnetic field strength, an additional component of enhancement is produced (T_{2D}^1). Equation 8.4 can be expanded to Equation 8.5, where ρ_2 is the surface relaxivity, characteristic of a given fluid/surface pair; S is the solid surface area in contact with the fluid, V is the volume of fluid, D is the diffusivity of the fluid, γ is the gyromagnetic ratio, G is the average internal gradient of the nonuniform magnetic field, t_e is the echo time associated with the CPMG characterization method (vide infra). Magnetic field gradients, which contribute to T_{2D}^1 can arise from inhomogeneities in the external magnetic field or from paramagnetic impurities within the sample itself. It will be noted that the influence of the diffusion term is limited for low magnetic field (thus low G), for fluids with high D and for application of short echo time separation in the acquisition method. Often the term $\frac{D\gamma^2G^2t^2e}{12}$ is negligible and, accordingly the measured T_2^{-1} values are linearly related to the surface to volume ratio of a porous medium, which can be compared to other data characterizing porosity.

$$T_2^{-1} = T_{2B}^{-1} + T_{2S}^{-1} + T_{2D}^{-1} \tag{8.4}$$

$$T_2^{-1} = T_{2B}^{-1} + \rho_2 \frac{S}{V} + \frac{D\gamma^2 G^2 t^2 e}{12} \tag{8.5}$$

$$as \quad t_e \to 0 \qquad T_2^{-1} = T_{2B}^{-1} + \rho_2 \frac{S}{V} \tag{8.6}$$

The T_{2S}^1 term and, more specifically, ρ_2, capture the enhancement of relaxation rate due to surface fluid interactions. The significant mechanisms of surface enhanced relaxation comprise (1) dipole-dipole coupling and (2) interaction with paramagnetic centers.

8.1.3 Dipole-dipole coupling

The discussion of Figure 8.5 described the influence that individual spins (magnetic dipoles) may have on neighboring spins. This dipole-dipole coupling is a major mechanism of relaxation in pure fluids. In Figure 8.5, A could represent a spin in a fluid molecule and B could represent a spin on a solid surface. In such case, B would have much lower translational and rotational energy. Being constrained the spins within the solid lose coherence (i.e., relax) much more rapidly than those in liquids and gases. Indeed, their high fraction of aligned spins continue to influence fluid molecules with which they interact by diffusion. Accordingly, magnetic dipole-dipole coupling is a mechanism for enhanced fluid relaxation in the presence of a porous medium. The relaxation phenomenon has been modeled with a two-state function, i.e., one population of molecules interacts with the surface and has greatly enhanced relaxation rate (T_{1S}^1) and the remaining population has the relaxation rate of the pure bulk liquid (T_{1B}^1), Equation A.9.[139] In the equation, a represents the thickness of the surface layer and R represents the pore radius. In the model the surface layer relaxes more rapidly via dipole-dipole coupling than the spins of the bulk fluid. Equation 8.7 bears similarity to Equation 8.6 and, likewise provides insight to porous material structure. Studies by Korb and Jonas have explored the importance of surface interactions, adsorbent translation and confinement upon surface-enhancement of dipole-dipole coupling.[130,220]

$$T_1^{-1} = T_{1B}^{-1} + \frac{2a}{R}(T_{1S}^{-1} - T_{1B}^{-1}) \tag{8.7}$$

8.1.4 Paramagnetism

The presence of paramagnetic centers often dominates the surface relaxation term, since interaction of an NMR active nuclear spin (most commonly ^{1}H) and the electron spin of the paramagnetic ion leads to rapid relaxation of molecules in contact with the paramagnetic component.[124,131] The physical basis for enhanced relaxation in the presence of soluble paramagnetic species has been investigated since the middle twentieth century and is dependent upon multiple inputs including the spin quantum number of the unpaired electrons, the correlation times associated with molecular rotation and translation, and cube of distance from the unpaired spin, among others. The reader is referred to published work in the physics literature.[28,131,215] The implication of these phenomena has been significantly studied for porous media.[45,88,118,119,124,182] Bryar et al., observed that carefully controlled silica gel samples in the absence of paramagnetic impurities have a ρ_2 = 1.2 Œ 10^3 μm/s for water but substitution of just 0.01% of silica surface sites with Fe(III) increased the surface relaxivity by an order of magnitude.[45] Additionally they noted that many nominally pure sand and quartz samples published in the literature reported surface relaxivity values two orders of magnitude higher than pure silica gel, underscoring the role of trace paramagnetic impurities. It was noted by multiple authors that there is a linear relationship between Fe(III) impurity content and surface relaxivity over regions of interest, e.g., 01% w/w.[45,88] The application of Equation 8.6 to characterization of pore volume distribution thus has a sensitivity to surface bound paramagnetic centers and yet, Foley et al. noted that for a series of synthetic calcium silicates meant to mimic silica, the increase in ρ_2 was only a factor six between 85 ppm and 1% w/w concentration of Fe(III).[88] Accordingly, credible interpretation of NMR relaxometry data may be accomplished particularly when the concentration of paramagnetic impurities is characterized in advance. Indeed, Foley et al. present equations for determining ρ_2 as a function of iron and manganese content, e.g., ρ_2 = 3.96 μm/s + (0.00227 μm/s/ppm)[Fe]ppm, Figure 8.6.[88]

Notably the starting point for this correlation, $\rho_2 = 3.96\ \mu m\ s^{-1}$, is larger than Bryars value for silica and consistent with the presence of greater paramagnetic surface composition than Bryars synthetic silica gel.

Toward an independent determination of ρ_2 Washburn cleverly applied laser-induced breakdown spectroscopy (LIBS) coupled with inductively coupled plasma and optical emission spectroscopy to characterize the surface composition of porous geologic samples and derive a correlation for ρ_2.[240] The complexity of the mixture of metallic ions detected necessitated the use of multivariate analysis to derive correlations and the overall method seems to hold promise for facilitating the accurate interpretation of time-domain NMR data of natural and synthetic materials in the future.

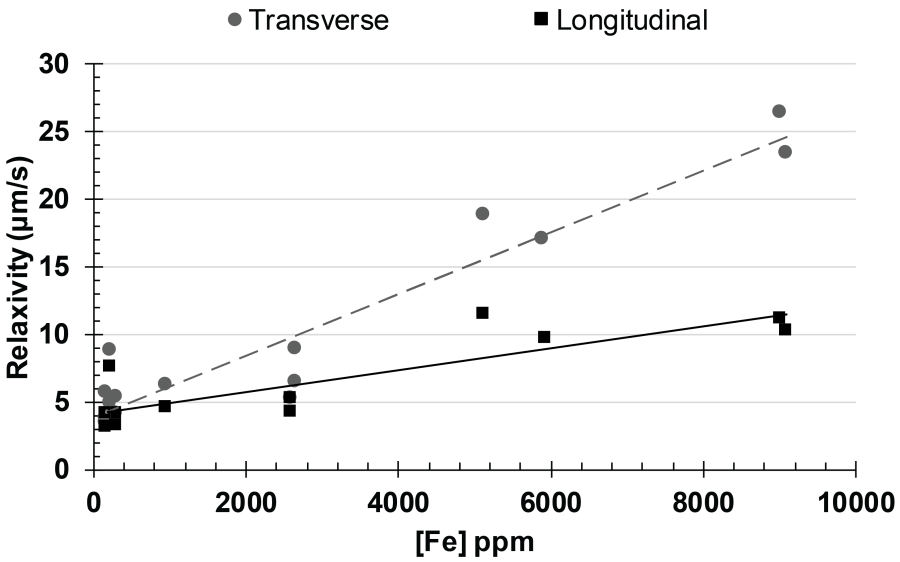

Figure 8.6: Correlation of surface relaxivity with Fe(III) content. Redrawn after Foley et al.[88]

8.1.5 Diffusion

The relative rate of diffusion versus relaxation is a critical component of interpreting NMR relaxation in terms of pore size distribution. In a complex pore system, multiple spin populations with different decay rates overlap to produce a single observed experimental response. Deconvolution of the experimental response is, preferably, interpreted assuming each sub-population is

a mode of the pore size distribution.[38,39,72,81,90,91,162] To satisfy this assumption the fluid within a pore should be diffusionally averaged, i.e., each molecule has equal probability of interacting with the surface. Brownstein and Tarr[39] defined three diffusion-based regimes for the interpretation of NMR relaxation data, where a is the radius of a spherical pore, ρ_2 is the surface relaxivity (symbolized M by Brownstein and Tarr) and D is the self-diffusivity of the fluid:

1. Slow diffusion regime (ρ_2a/D $>>$ 10) relaxation is very rapid compared to the substances diffusivity and fluid in a single pore will present a complex multi-exponential pattern, complicating analysis in terms of pore size distribution.

2. Intermediate diffusion regime ($1 < \rho_2$a/D < 10) the rate of relaxation is comparable to diffusivity and relaxation data cannot be interpreted in terms of pore size distribution.

3. Fast diffusion regime (ρ_2a/D < 1) the rate of relaxation is much slower than diffusivity. The molecules/spins in the pore produce an average signal proportional to the surface area to volume ratio of that pore, Equation 8.6. The fast diffusion regime is the most commonly applied regime in characterization of pore size distributions.

Beyond fluid diffusion within a single pore, diffusion among pores is an important consideration. If fluid molecules are not constrained to a single pore on the timescale of the experiment but rather explore the pore surface of more than one pore, an averaged value of surface area/pore volume (S/V) will be expressed, biased toward smaller pores, which have higher S/V ratios.[81] This is termed, diffusional averaging. The dimension of the volume element over which this averaging occurs is of similar magnitude to the diffusion length on the experiment timescale, $l = \sqrt{6D_R t}$. Here DR is the diffusion coefficient of the fluid confined in the porous medium and is typically 1050% lower than the diffusivity of the fluid in the absence of confinement. For water (DH_2O $10^9 m^2$ s^{-1} at room temperature) and an NMR timescale of $<$ 1 ms, the diffusion length is certainly less than 1 μm, perhaps double-digit nanometers but for longer relaxation processes the length scale can be much larger.

8.2 Instrumentation and Methods

8.2.1 Low-field Instrumentation

The characterization of porous media by NMR relaxometry is often conducted at low magnetic field strength (<0.5 T) to limit the influence of the diffusion term in Equation 8.5 and to take advantage of solid, permanent magnets, rather than electromagnets.[101] Such magnets are produced from cobalt samarium alloys or neodymium alloys,[69] limit the cost of instruments and are more easily deployed in field studies. Notable manufacturers include Bruker, Magritek, Niumag, Oxford Instruments and Xigo. As low field instruments these devices are generally situated on bench tops and occupy < 0.25 m^3. The cylindrical sample cell size (dictated by the probe dimensions) can range from 0.5 cm $\times$ 2.5 cm to 10.2 cm $\times$ 10.2 cm and is typically selected according to the field of study; analysis of geologic porous samples favor the larger instruments and research in novel nanoporous materials favor the small probe sizes. Some instruments are provided with temperature-controlled probes enabling additional experimental parameter space. While 5 to 60°C is common, temperature ranges as broad as 100 to 200°C are available.

8.2.2 High-field instrumentation

Characterization of fluid dynamics within a porous medium is commonly conducted via pulsed-field gradient NMR using high-field instruments comprising superconducting electromagnets.[117] These high-resolution instruments employ niobium or niobium-tin elements, which must be held at 4.2 K using liquid helium and accordingly have high capital cost and operating costs. The reader is referred to alternate relevant texts.[101,121]

8.2.3 Equipment for in situ time-domain NMR characterization

The examination of samples under conditions of use requires equipment appropriate for achieving relevant temperatures, liquid and gas compositions and pressures. The commercial availability

of NMR cells for variable temperature and high pressure operation in traditional 5 and 10 mm probes[59,66,134,237] as well as, solid-state NMR magic-angle spinning rotors[171] has increased the accessibility of many in situ NMR methods including time-domain methods. Materials of construction such as zirconia, sapphire, Vespel and polyether ether ketone (PEEK) have been utilized with varying pressure specifications dictated by material of construction and physical design. A custom-built low-field NMR pressure cell with 2 cm inner diameter and 4 cm outer diameter fabricated of PEEK has been used to study gas adsorption in nanoporous adsorbents and rock cores, Figure 8.7.[107,224]

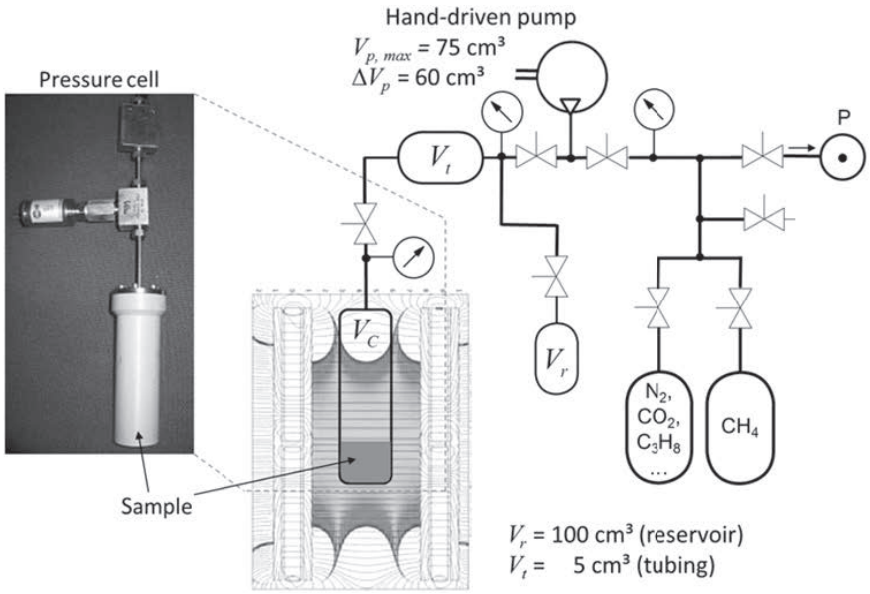

Figure 8.7: Low-field NMR apparatus for high-pressure gas adsorption from the University of Leipzig. Reprinted with permission.[107]

8.2.4 Data collection methods

It has been noted above that a population of nuclear magnetic moments at uniform temperature will align with an external magnetic field, B_0 at equilibrium. The magnitude of net magnetization (M_0) of such a system is given by Equation 8.8 in the direction of B_0, where N_0 is the number of magnetic moments per unit volume, μ is the individual nuclear magnetic moment, k is Boltzmanns constant, T is absolute temperature, I is the spin quantum number of the nucleus and B_0 is the field

strength.[78]

$$M_0 = \frac{N_0 \mu^2}{3kT} I(I+1) B_0 \tag{8.8}$$

The alignment may be perturbed by application of an oscillating field (B_1) perpendicular to B_0, causing the spins to precess initially with phase coherence about B_1. The oscillating field is induced by application of a radio frequency pulse. The angle of the perturbation (θ) is given by Equation 8.9, where γ is the gyromagnetic ratio and t is the time over which the oscillating field is applied.[62]

$$\theta = \gamma B_1 t \tag{8.9}$$

It is common to employ $\theta = \pi$ (180°) and $\frac{\pi}{2}$ (90°). Upon removal of the oscillating field the spin system will relax back to alignment with the external magnetic field B_0 via an exponential growth, with time constant, T_1, Equation 8.1. When magnetization is perturbed into the transverse plane, orthogonal to B_0 the initially coherent population of spins yield $M_{xy}(0)$ and gradually loses phase coherence in an exponential decay with time constant, T_2, Equation 8.2. This decay is labeled the free induction decay (FID) and may be analyzed via Fourier Transform for complex molecules to give a frequency spectrum that may be analyzed, especially at high field, to yield structural information of complex molecules, a topic beyond the present scope. The T_1 and T_2 time constants can be measured experimentally and analyzed in the characterization of porous media. Figure 8.8 displays pulse sequences that are used to determine T_1 and T_2.[26]

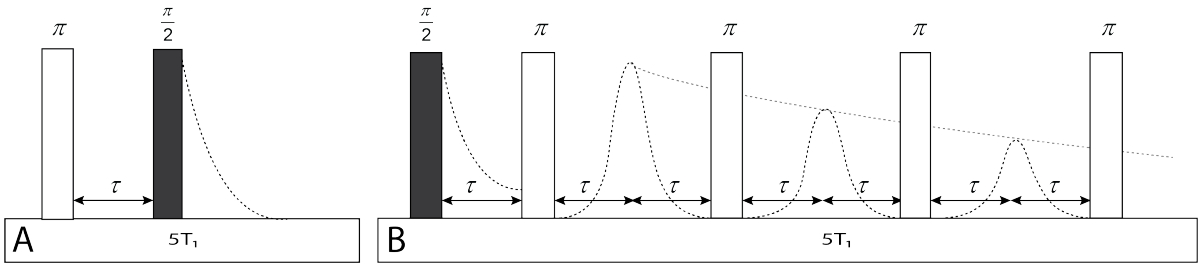

Figure 8.8: (a) Inversion recovery method to measure T_1 and (b) CarrPurcellMeiboonGill (CPMG) method to measure T_2. Redrawn after Besghini et al.[26]

The measurement of T_1 is often conducted via the inversion recovery method. An equilibrated population of NMR active nuclei/spins is exposed to a rapid radio frequency pulse sufficient to tip the spins 180°. After a hold time, τ, the system is exposed to a second pulse, which tip the spins 90° into the transverse plane and the degree of recovery of the initial magnetization is recorded with a detector that measures magnetization in the transverse direction. The system is given sufficient time to again reach equilibrium, M_0, after which the cycle is repeated multiple times with different hold times (τ), Figure 8.8. A series of M_z(t) values is thus measured as a function of time and fit to Equation 8.10, which differs slightly from Equation 8.1, since the spins are completely inverted 180° (negative magnetization) and require longer time to reach full alignment with the field.[121]

$$M_z(t) = M_z(0)\left[1 - 2e^{-\frac{t}{T_1}}\right] \tag{8.10}$$

The inversion recovery sequence works best with very homogeneous systems, e.g., simple molecules like water. In the case of complex systems, a series of 90° pulse sequences is substituted, as in the saturation recovery method.

In the Hahn echo and the Carr-Purcell-Meiboom-Gill (CPMG) pulse sequences an initial 90° pulse followed by FID is interrupted via one or more 180° pulses, which refocus the dephasing in the (x, y)-plane leading to periodic coherence and a spin echo, which is detected by the instrument, Figure 8.8. The amplitude of the sequential echoes decreases exponentially with a time-constant, T_2, Equation 8.2. As noted in Section 8.1.1, diffusion through magnetic field inhomogeneities leads to enhanced rates of relaxation. These inhomogeneities could arise from the instruments magnetic field and/or inhomogeneities in a sample, e.g., the presence of paramagnetic centers, and leads to an accelerated relaxation defined by time constant, T_2. In the CPMG pulse sequence, application of small echo time separations (see Equation 8.5) reduces the influence of inhomogeneities and the resulting T_2 is reflective of transversal relaxation processes.[26]

For fluid contacting a multimodal pore system, each mode in the pore size distribution contributes a unique relaxation rate to the observable signal in the CPMG pulse sequence, Equation 8.2, resulting in a multi-exponential decay. These data can be deconstructed into a multimodal

relaxation time distribution through a number of methods described in the literature, generally comprising regularization and Inverse LaPlace Transform.[80,102,186,243] The techniques have been reviewed[80] and continue to be a topic of emerging research.[102,194] As an ill-posed problem with no unique solution the deconvolution of multiexponential data presents complications but has been invaluable in numerous scientific problems and can be validated by reference to complementary characterization techniques, Figure 8.4.

8.3 Applications of Time Domain NMR for Characterizing Porous Materials under Conditions of Use

A comprehensive review of investigations pertaining to solvent NMR relaxation in colloidal and porous material suspensions describes numerous applications characterizing materials under conditions of use.[63] Fairhurst et al. demonstrated that the CPMG method for T_2 determination conveniently characterizes nanostructured carbon material suspensions, in situ, providing a measure of particle specific surface area that correlates very well to other methods, including transmission electron microscopy, which cannot be executed as an in situ method.[85] In one case, differences in the method of milling and conditions of preparing particle suspensions led to differences in wetted specific surface area for a series of nanographite suspensions all at 2% w/w loading. The ability to conveniently measure surface areas with a relatively low cost, low-field NMR instrument will continue to be exploited in both fundamental and industrially applied investigations.[180]

The ability to characterize fluids in the presence of a porous medium is a strength of time domain NMR.[128] The physical bases for enhanced relaxation rates under fluid confinement have been reviewed in the literature[122] and continue to be a topic of study.[87,129,139,154] Seminal applications aimed at correlations of NMR relaxation rate of confined water and the diameter of controlled porous glass[8] and were extended to mesoporous silica characterization and valuable studies elucidating the evolution of silica porosity as a function of processing parameters.[72,73,73,90]

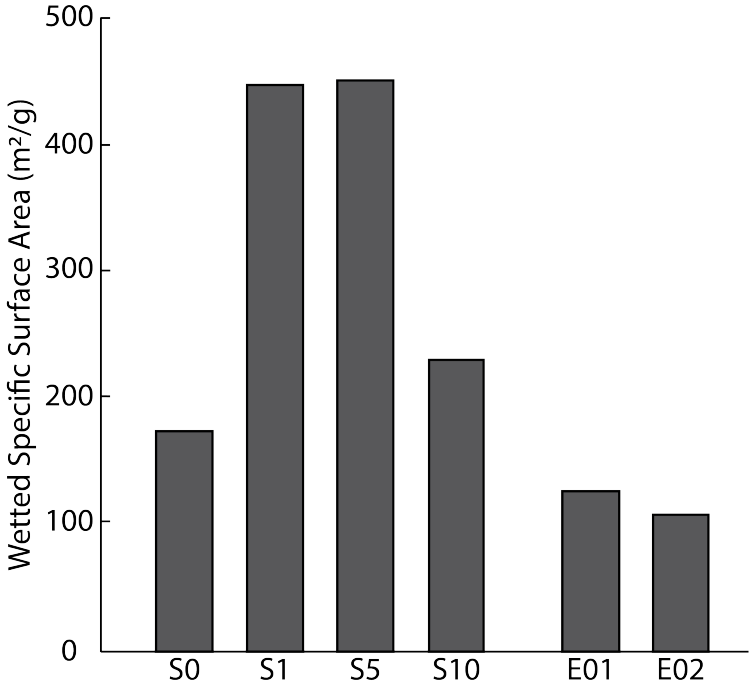

Figure 8.9: Wetted specific surface area via NMR CPMG T_2 determination for a series of nanographite particle suspensions, all at 2% w/w loading. Series S0S10 utilize different concentrations of surfactant and Series E01E02 use a different milling method and suspension method.[85]

Porous polymeric systems stabilized by interactions with water (so-called hydrogels) are well-suited to characterization via NMR relaxometry and diffusometry.[3,4,58,60,75,87,97,149,231] While there may be debate over the terms pore volume versus free-volume in the polymer community, applications ranging from food to drug delivery to tissue engineering, all rely on the structure of the polymer interacting with water and the diffusion of species into and out of the porous framework. Inexpensive low-field NMR instruments have been used to extract mesh (pore) size in these materials and the modeling of the data has been the subject of on-going research.[3] Central to the modeling is defining a relevant fiber radius that separates pores within the mesh structure. The model of Scherer[204] has been adopted with the assumption that one fiber comprises one polymer chain. Experimental studies relying on this model provide reasonable mesh sizes in comparison to values determined by mechanical property characterization, Figure 8.10.[4,149] Others have used alternate models assuming three states of water (surface bound, pore and bulk fluid) to model the multiexponential decay data.[58] NMR measurements of diffusion coefficients of the water under

confinement have been featured in further characterization.[10,58,97,98] TD-NMR characterization of hydrogels is of growing importance[3,75] by the very nature that it is an in situ measurement and does not require sample preparation techniques that may alter the structure. Indeed, it has been established that drying of hydrogels, even freeze-drying leads to structural changes that impact the quality of data and conclusions derived from freeze-dried samples.[230]

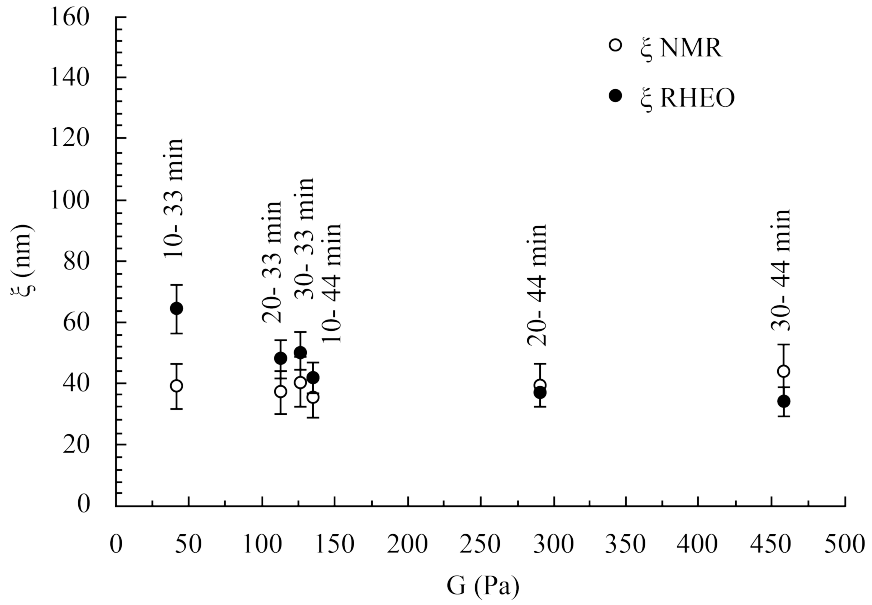

Figure 8.10: A comparison of hydrogel mesh/pore size determined from NMR transverse relaxation rates and modeling of rheological data. Data from Marizza et al.[149]

In addition to applications of NMR relaxometry for the characterization of pore volume distributions, the techniques are exploited for characterizing fluid/solid interactions. Reference to Equation 8.6 suggests that when the surface area to volume ratio of a pore system is known, the surface relaxivity, ρ_2, can be determined. As a reflection of strength of fluid interactions with the surface, ρ_2, provides insight relevant to a variety of adsorption processes and catalysis.

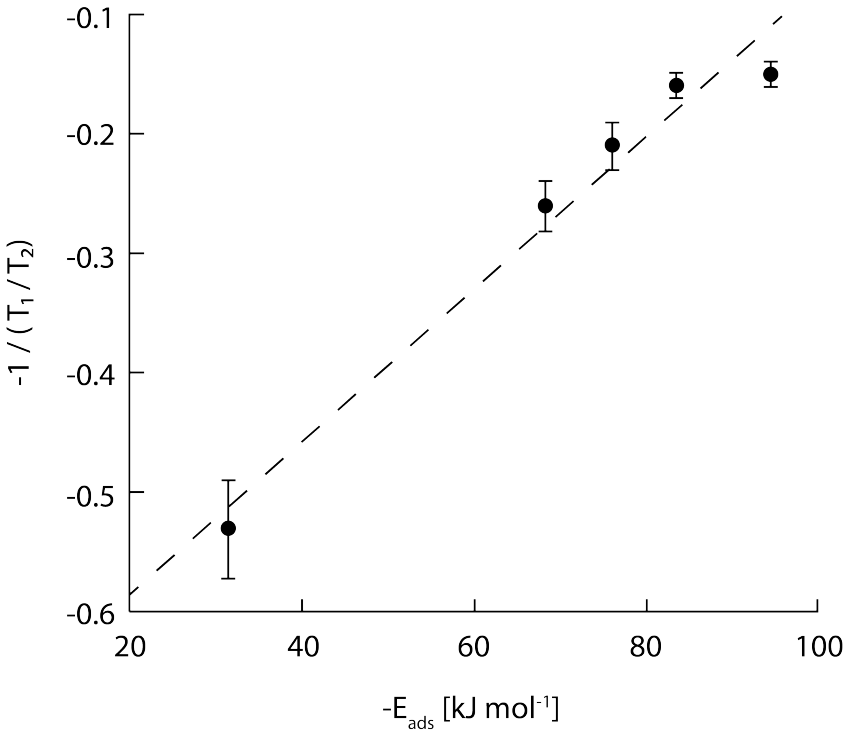

Figure 8.11: Comparison of the inverse NMR relaxation time ratio with adsorption energy as obtained from DFT calculations. From left to right the data points represent cyclohexane, methanol, ethanol, 1-propanol and 1-butanol. Redrawn from DAgonstino.[198]

Robinson et al. elucidated correlations between a solvents energy of adsorption on mesoporous silica and functions of T_1 and T_2, Figure 8.11.[198] These correlations can be utilized in modeling surface dynamics and optimization of catalytic materials for desired reactions. Indeed, the influence of water concentration on suppressing the rate of oxidation of diols over Au/TiO_2 in methanol solvent has been studied via time-domain NMR.[67] Both relaxometry and diffusometry have been applied to demonstrate that water suppresses adsorption of dissolved diols on the catalyst surface and the diffusivity of these molecules in the pore system. Furthermore, it was observed that T_1/T_2 was strongly correlated with conversion data, Figure 8.12. This is a promising area of study given the ease with which the experiments can be conducted and the utility of the data for optimization of the liquid phase composition.

In an era of increasing supply of natural gas from new developments in extraction technology, methods to purify methane from impurity gases are a focus of active research. NMR relaxome-

try has been applied to the characterization of microporous media for methane purification.[107,224] Adsorption isotherms for binary mixtures of CH_4/CO_2 in contact with metal-organic-framework Cu-BTC were conveniently characterized from T_2 distributions, Figure 8.13.[107] The method cleverly relied on the characteristic that only protons contributed to the signal, i.e., only CH_4 was directly observed, while CO_2 was silent. The influence of the CO_2, including displacement of CH_4 from a pore system method was inferred by changes in the CH_4 signal. Such a promising method of characterizing gas adsorption and adsorbents is expected to be increasingly utilized in the research community. Indeed, additional studies examining propane adsorption in porous carbons clearly elucidate nanoporous regimes from interparticle spacing and characterize adsorption isotherms in the same.[224] The transport behaviors of proton and methanol in layered double hydroxide catalysts for direct methanol fuel cells have also been characterized by NMR.[168]

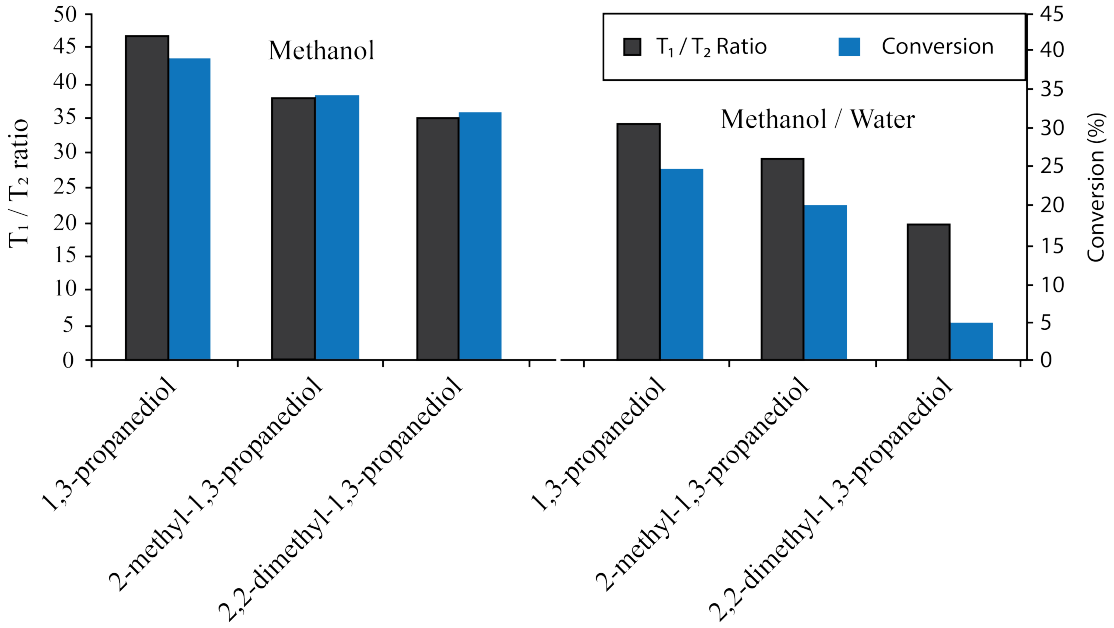

Figure 8.12: Time-domain NMR reveals a correlation of substrate adsorption strength (T_1/T_2) to conversion in the oxidation of diols. Redrawn after DAgostino et al.[67]

An advantage of NMR relaxometry techniques is the wide range of pore spaces accessible. In contrast to microporous media described above, NMR relaxometry in the form of magnetic resonance imaging (MRI) has been used to characterize the porosity of packed beds of catalyst particles in both loose packing and consolidated packing, Figure 8.14.[205] Here the spaces between

particles appear as light shades and the pore system within a particle appears dark, consistent with the vastly different relaxation rates associated with fluid confined in the spaces. MRI offers the advantage of generating images with three-dimensional rendering, but more importantly providing pore volume distributions to inform hydrodynamic studies for catalyst bed liquid flow profiles.

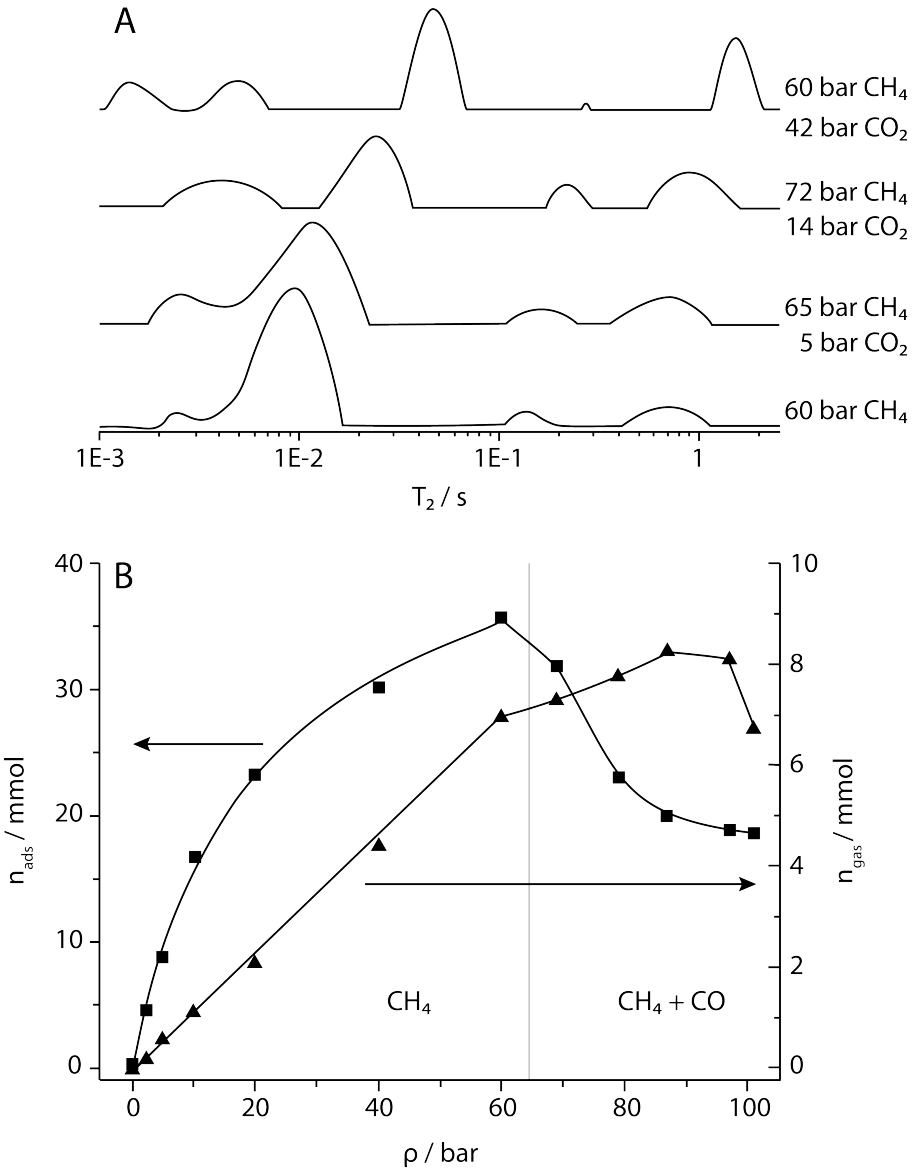

Figure 8.13: T_2 relaxation time distributions of CH_4 in MOF CuBTC as a function of pressure and carbon dioxide composition. (b) Adsorption isotherm points for CH_4 and CH_4/CO_2 mixtures, derived from calibrated NMR data. Redrawn after Horch et al.[107]

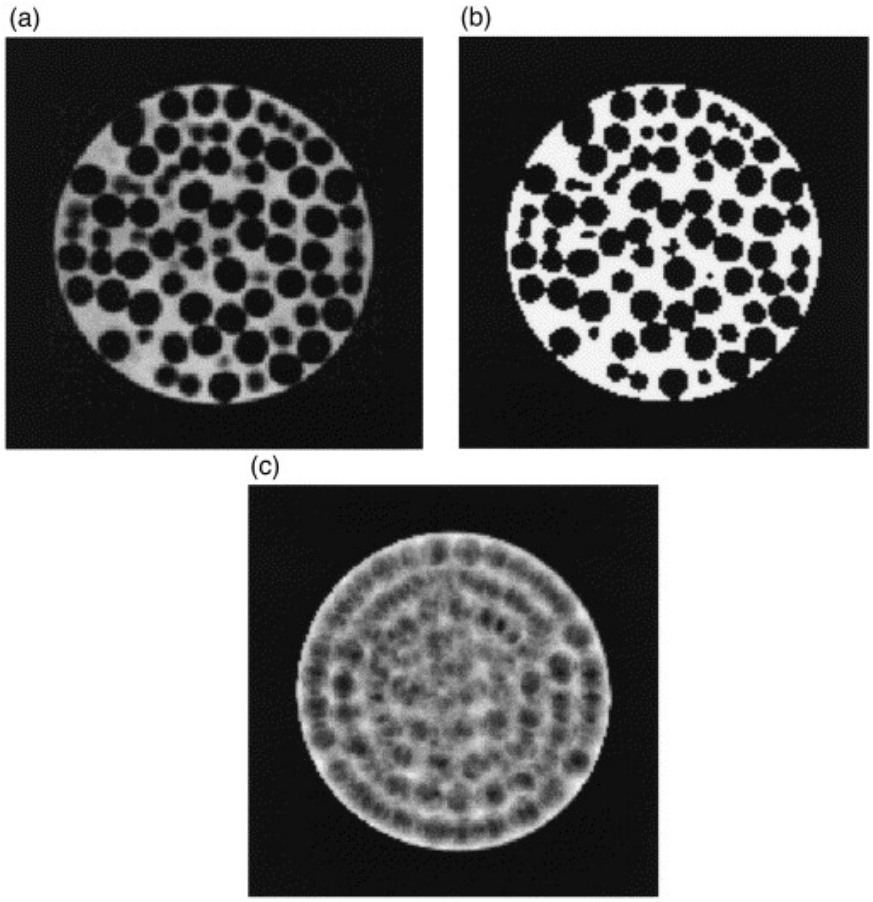

Figure 8.14: Magnetic resonance imaging of a packed bed of catalyst particles. Three stages in the analysis illustrated for a single plane through a 3D image volume. (a) raw data; (b) binary-gated data for the image slice; (c) projection of image along the axial direction of the bed to form an image of mean porosity perpendicular to the axis of the bed. Data are shown for a bed of D/d ratio = 9. Reprinted with permission.[205]

8.4 Applications of Time Domain NMR for Characterizing Bioengineered Glucan Polysaccharide

NMR relaxometry is greatly valued in the characterization of polysaccharides under conditions of use. The α-1,3-glucan, both microcrystalline glucan (McG) and wet-cake (WC - the filtered α-1,3-glucan that has not undergone drying operations), with degree of polymerization of 50 and 800, respectively, are utilized under aqueous condition in Chapter 7. Meanwhile, dried WC glucan, has been implemented under organic media in Chapter 6. McG is a crystalline material with a

mean particle size of approximately 2-5 μm, while WC is a semi-crystalline material with an approximate particle size 5-10 μm.

Here, we seek a better understanding of McG and WC's specific surface area (SSA) under their conditions of use, i.e., an aqueous environment. First, we look at the dried SSA obtained from gas adsorption measurements (Section 2.18). Table 8.1 shows the SSA obtained through a 5-point BET method.[140]

Table 8.1: Specific surface area (SSA) determined through gas adsorption.

Sample Name	BET SSA [m^2 g^{-1}]
McG	28.60 ± 0.23
WC	2.02 ± 0.20

The McG has a specific surface area an order of magnitude greater than the WC. As a crystalline material, the pretreat degassing step in gas adsorption experiments does not severely alter the matrix of the material. A small particle size should provide a higher SSA than one with a greater particle size. A semi-crystalline material, can be altered through the degassing pretreatment of gas adsorption techniques by promoting the collapse of the pore architecture or aggregation of primary particles, which lead to inaccessible sites that are not accounted for in the SSA measurements.

As a complementary method, we utilize LF-NMR to elucidate the SSA of these materials by measuring the interaction of the fluid with the surface of the materials according to Equation 8.11.[122,219]

$$\frac{1}{T_2} = \frac{1}{T_{2b}} + (\rho_2 \times SSA_{BET}) \frac{\text{Mass of Solid}}{\text{Mass of Water}} \tag{8.11}$$

Under the assumption that no surface chemistry (ρ_2) alteration has occurred under heating of the sample, we can deduce from Equation 8.11 that any change in slope is attributed to a change in the SSA. Figures 8.15 and 8.16 portray the difference between the native polymer and that affected by the drying condition of gas adsorption, respectively.

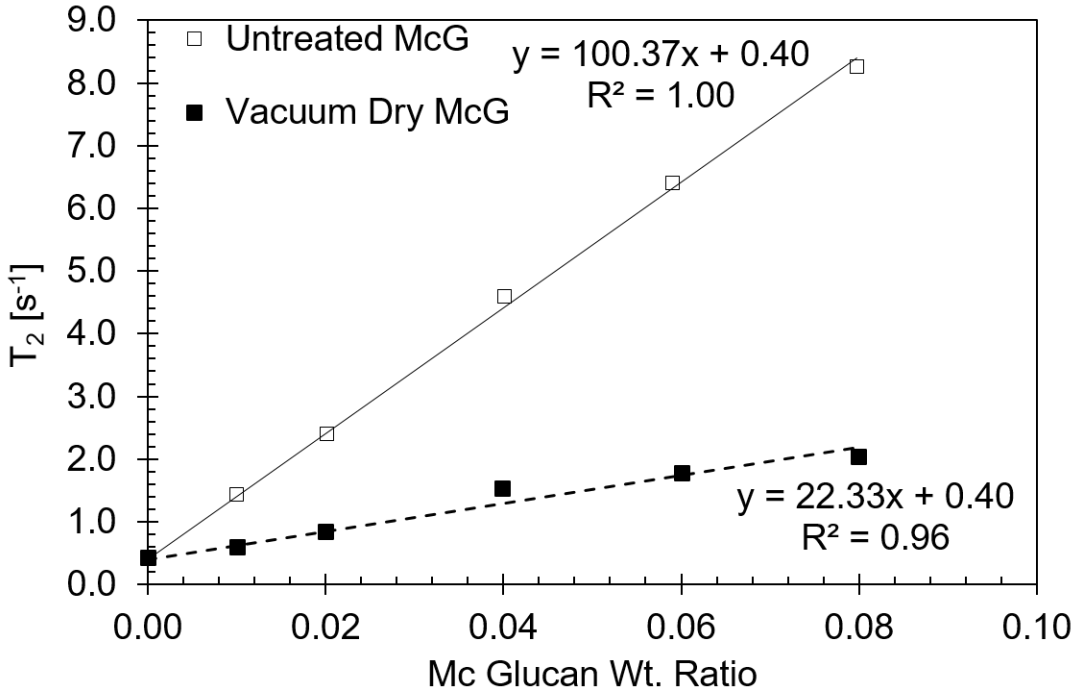

Figure 8.15: LF-NMR characterization of microcrystalline glucan (McG). Where $y = T_2^{-1}$ and $x =$ Wt. ratio of McG.

For McG, the vacuum dried polymeric material has 22% of the SSA accessible when contrasted to the native α-1,3-glucan polysaccharide. This would suggest that the SSA for the untreated McG would approximately be of 128.55 $m^2\ g^{-1}$.

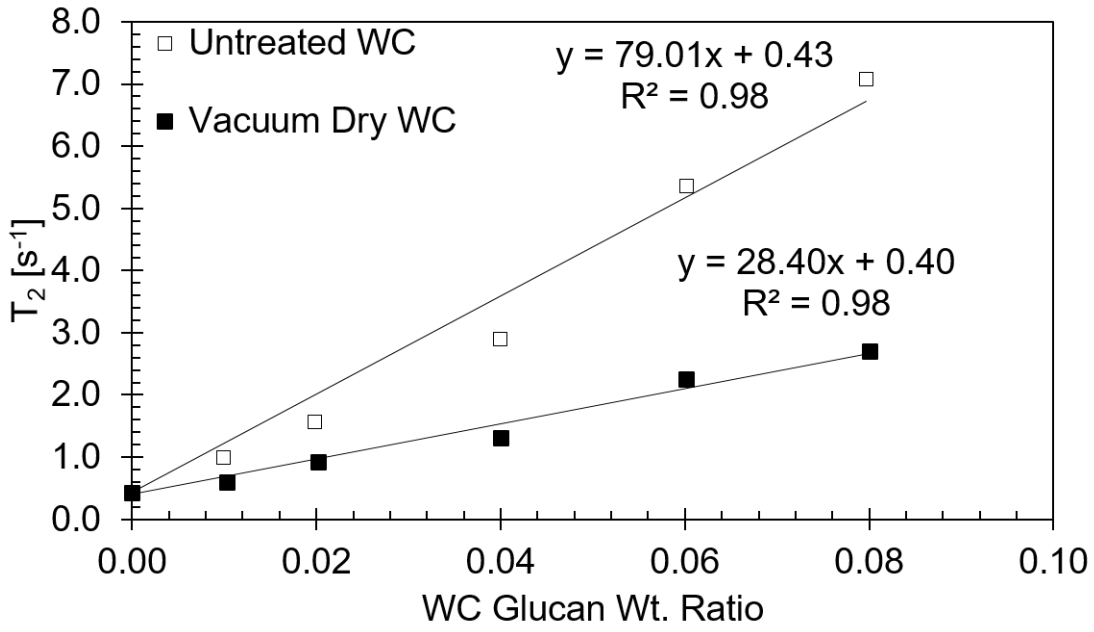

Figure 8.16: LF-NMR characterization of wet-cake glucan (WC). Where $y = T_2^{-1}$ and $x =$ Wt. ratio of WG.

For WC, the vacuum dried polymeric material has 36% of the SSA accessible when contrasted to the native α-1,3-glucan polysaccharide. This would suggest that the SSA for the untreated McG would approximately be of 5.62 m^2 g^{-1}.

8.5 X-ray illuminated characterization

X-ray illuminated characterization techniques span all scales, revealing information from the atomic structures to the macroporous networks. This section describes the fundamentals of X-ray illuminated techniques and selected applications operating under conditions of use.

X-ray radiation is utilized in laboratories across the world; whether the laboratory has a bench-top instrument or whether the instrument is connected to a synchrotron makes no difference to the operational basis of the technique. However, an X-ray tube and a synchrotron differ in that synchrotron illuminated X-rays give access to a broader distribution including an increased flux at higher energies, enhancing the quality of the image and allowing for finer spatial-temporal details from the analyte. The brightness of a synchrotron source may be up to 15 orders of magnitude

higher than that of an X-ray tube and the source may be highly tunable and monochromatic, as in the case of insertion devices. The high brightness shortens the time to < 10 ms, during which a usable integrated signal can be measured, or reduces the volume of a sample to <10 μL. Moreover, the tuning ability of an insertion device allows for radiation absorption to be reduced when the sample is contained within thick walls of heavy materials of construction, like pressure cells or reaction vessels. These attributes make synchrotron radiation very useful for in situ and operando scattering and imaging studies.

The operation of a conventional X-ray tube source is schematically represented in Figure 8.17. Electrons are produced by thermionic emission from a hot cathode at ground potential. The electrons are accelerated towards a target held at a high relatively positive potential of several tens of kV. The spectrum produced by such a source is shown in Figure 8.18. As the electrons approach the anode, they feel a decelerating potential from the electrons in the anode (repelling forces). The energy lost in deceleration is converted to radiation, and produces the broad continuum component of the spectrum, bremsstrahlung (braking radiation), which extends from very low energies up to a well-defined upper energy maximum given by the accelerating potential of the tube.

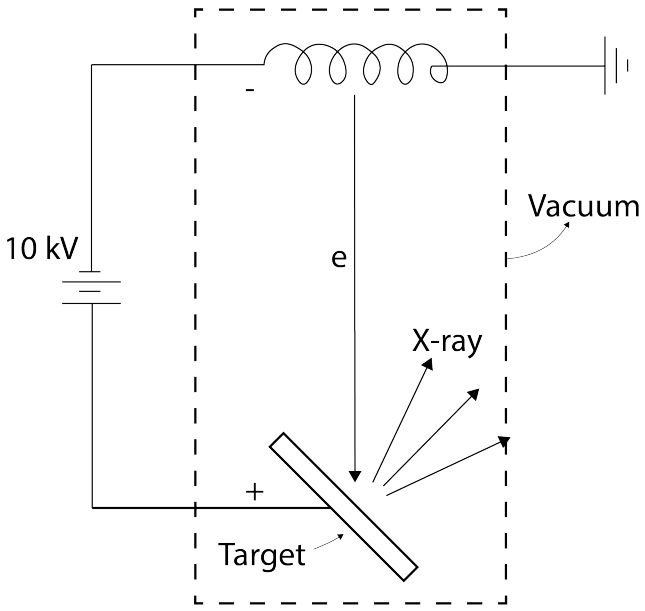

Figure 8.17: A conventional X-ray tube schematic.

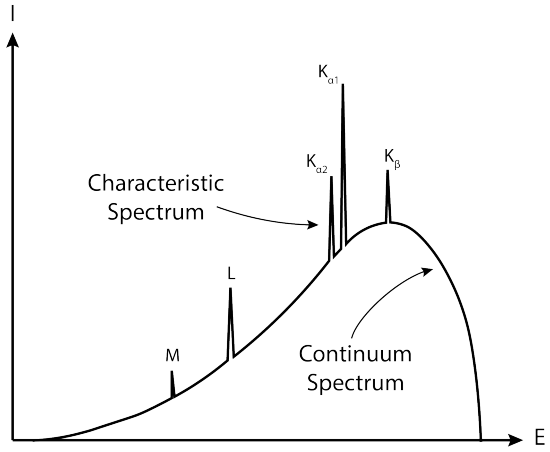

Figure 8.18: Spectrum produced by a conventional X-ray tube source.

In addition, the impinging electrons knock out some inner shell electrons in the atomic electron cloud of the anode (target) atoms. As a result, a vacancy is created in an inner shell, which is then filled by a cascading electron from a higher energy level in the atom. The process is shown schematically in Figure 8.19. Such a process produces several characteristic lines, which are very sharp and intense, occurring at well-defined energies. These characteristic lines are superimposed on the bremsstrahlung radiation, as shown in Figure 8.18. The origin of the various lines is shown in Figure 8.19.

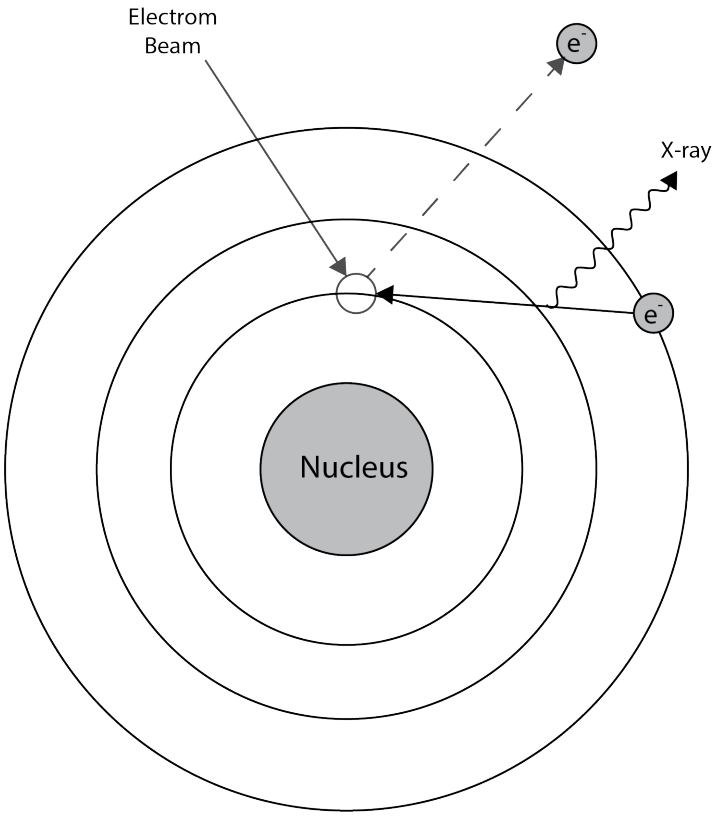

Figure 8.19: Electron beam knocks out an inner shell electron from an atom, which prompts a cascade of other electrons to fill inner shell vacancies.

Several refinements have been introduced to the basic principle shown in the schematic of Figure 8.17, resulting in stronger laboratory X-ray sources. However, the heat produced during electron bombardment is removed by water cooling to prevent the melting of the target, so there is a practical limit to the X-ray intensity, which depends on the current at a constant accelerating voltage. Synchrotron X-rays are produced by electrons that are accelerated to high energies, moving at nearly the speed of light in a circular storage ring. In a typical second or third generation synchrotron, 1.9 to 7GeV electrons circulate in a storage ring, which consists of bending magnets (producing polychromatic divergent radiation), and insertion devices (producing monochromatic, highly collimated and tunable radiation) in straight sections between bending magnets. Experimental end stations use the X-rays emitted from the storage ring for tomography, scattering, among other techniques used to investigate the structure and chemistry of matter across a broad spectrum of time and energy scales.106 Figure 8.21 displays the typical arrangement of a synchrotron facil-

ity.

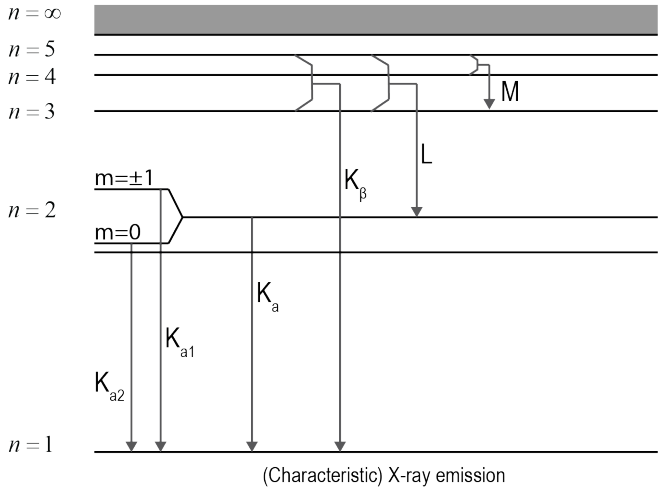

Figure 8.20: The origin of the various X-ray characteristic lines.

For the purposes of this text we will talk about X-ray radiation in terms of energy. If needed, the following relationship, Equation 8.12, can be used to convert between wavelength and energy, where h is Planks constant, c is the speed of light, and λ is the wavelength.

$$E = \frac{hc}{\lambda} = \frac{1.2398x10^3}{\lambda} \frac{eV \cdot nm}{nm} \tag{8.12}$$

X-rays are on the far end of the electromagnetic spectrum; they find their place between Gamma rays and Ultraviolet radiation. X-rays are high energy radiation, typically in the range from 103 to 105 eV, or in terms of wavelength they range from 1 to 0.01 nm, respectively. The greater the acceleration potential difference between the cathode and the anode the lower the wavelength range as seen in Equation 8.12, these variables are inversely proportional to one another.

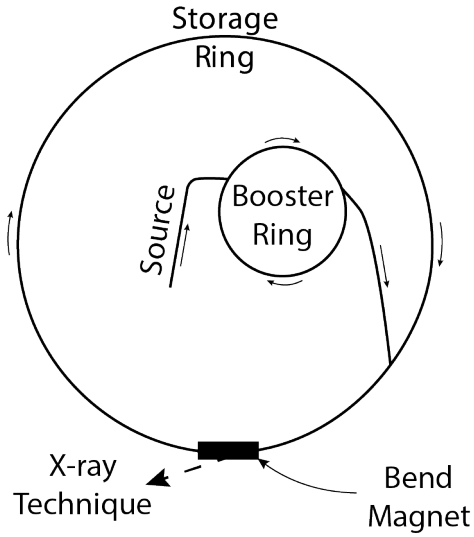

Figure 8.21: A synchrotron facility consists of an electron source, typically, a linear accelerator, a booster ring, a storage ring, bend magnets, and analytical equipment feeding off the radiation by the electrons as they are bent in a circular orbit.

X-ray radiation can be characterized as soft or hard; soft X-ray radiation is associated with energies below 10 keV and hard X-ray radiation is associated with energies above 10 keV. The distinction is that soft X-ray radiation enhances the resolution of an image while hard X-ray radiation penetrates through thicker objects. Typically, X-ray illuminated techniques utilize a distribution of both hard and soft X-rays, as seen in Figure 8.18

$$I = I_0 e^{\Sigma(-\mu_i x_i)} \tag{8.13}$$

Once an X-ray goes through the sample the radiation is attenuated and therefore the intensity decreases with increasing thickness of the sample, described by Equation 8.13. The degree of attenuation in a mono-energetic system is a function of the linear absorption coefficient, μ, the mass density, α, atomic number, z, and the thickness of the material, x. However, if the radiation that goes through the sample is not mono-energetic in nature or filtered, the degree of attenuation and the absorption coefficient become energy dependent, as seen in Equation 8.14.

$$I = \int I_0(E) e^{\Sigma(-\mu_i(E) x_i)} dE \tag{8.14}$$

Attenuation is one of the mechanisms affecting X-ray illumination as it penetrates through an analyte. Phase contrast imaging uses this principle to distinguish between elements or phases that possess a different absorption coefficient and thus attenuate the sample differently. This mechanism will be discussed in Section 8.2.2. Scattering is another mechanism affecting X-ray illumination as it goes through an analyte. Rather than measuring the intensity of the scattered illumination, attention is given to the diffraction patterns that radiate at different angles out of the sample.

8.6 X-ray Computed Tomography

8.6.1 Introduction

X-ray computed tomography (XCT) is a technique used extensively in the medical and material science fields to produce three-dimensional reconstruction, without compromising the specimens texture and structure during sample preparation.[17,170] In this regard, X-ray tomography is considered a non-invasive technique capable of elucidating the 3D (internal and external) pore networks of relatively dense materials. Equation 8.14 correlates the elemental density of the specimen to the degree of attenuation of the X-rays as they transverse through the specimen. In Figure 8.22[179], the behavior of the linear attenuation coefficient as a function of photon energy is plotted for different elements, common in cementitious materials.[35] The information found in Figure 8.22 can be obtained from the cited databases,[82,108] among others, for a variety of materials. As observed in Figure 8.22 there is a large difference between the degree of attenuation caused by water and iron, making the phase contrast between the two more distinct than that of water and portlandite. This information is helpful when planning an experiment and the necessary requirements to obtain enough contrast between the elements present in the specimen.

Compared to medical diagnostics[120] X-ray tomography in material science has permitted the exploitation of higher exposure time and energy X-rays to analyze denser materials. The high-intensity (high flux) X-rays obtained from synchrotron facilities and their monochromatic filtering have allowed for the advancement of the spatiotemporal resolution of tomography and thus cat-

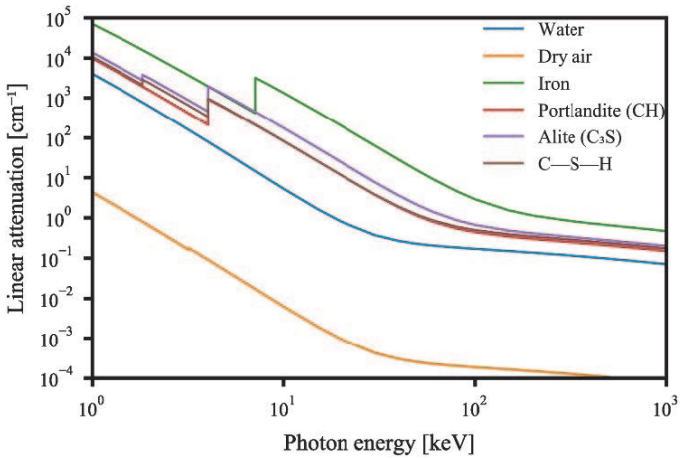

Figure 8.22: Linear attenuation coefficient of the phases present in cementitious materials as a function of photon energy. Reprinted with permission.[35]

alyzed the evolution of the technique over the years.

Future spatiotemporal improvements to this technique will not only improve image quality and understanding of time-dependent phenomena, but it will also unlock its potential to analyze materials under different conditions of use that are currently undetectable in the spatial or temporal domains of these experiments. Additionally, spatiotemporal improvements coupled with other non-invasive techniques, e.g., crystallography or time domain nuclear magnetic resonance (TD-NMR), can have a synergistic effect on materials characterization under conditions of use. Later in this section, we shall refer to a few examples of the former. As mentioned at the beginning of Section 8.2, X-ray sources play an important role in the implementation of tomography. The illumination produced by the source can differ in geometrical configuration, i.e., the illumination can come as a point source, fan projections, equiangular rays, among other configurations that dictate the mathematical approach of reconstruction algorithms. Kak and Slaney produced a comprehensive text, The Principles of Computerized Tomographic Imaging, which addresses the foundations of X-ray tomography reconstruction (e.g., Fourier Slice Transform, Filtered Back Projections, and Algebraic Reconstruction Techniques) with the different geometrical beam configurations.[114] It is worth mentioning that X-rays are not the only radiation available for this technique; electrons[13,127,158] and neutrons[148] are commonly used for tomographic purposes. Banharts Advanced Tomographic Methods in Materials Research & Engineering gives insight into other tomographic techniques not

covered in this chapter.[18] Others have reviewed the use of tomography in cementitious materials and included an overview of the technique and valuable examples.[35]

The description that follows is a high-level discussion of the mathematical basis behind the different reconstruction methods in X-ray tomography.

8.6.2 The Fourier slice theorem

The mass attenuation coefficient of the cross-section of an object placed inside a Cartesian coordinate system can be described by a continuous function composed of coordinate pairs (x, y), such that the complete shape of the cross-section is represented as μ(x, y), in terms of the mass attenuation coefficient. In Figure 8.23, a hexagon, described by μ(x, y), is bombarded by parallel X-ray beams at an angle, θ. Each X-ray, denominated by t_i, is located a certain distance from the origin of the (x, y)-plane; Equation 8.15 defines the relationship between the ray, t_i, and the (x, y)-plane when the two are perpendicular to one another. As the illumination is attenuated, according to Equation 8.14, while passing through the hexagon, a projection, P(t), is recorded by the detector.

$$t = \mathrm{x}\ cos\theta + \mathrm{y}\ sin\theta \tag{8.15}$$

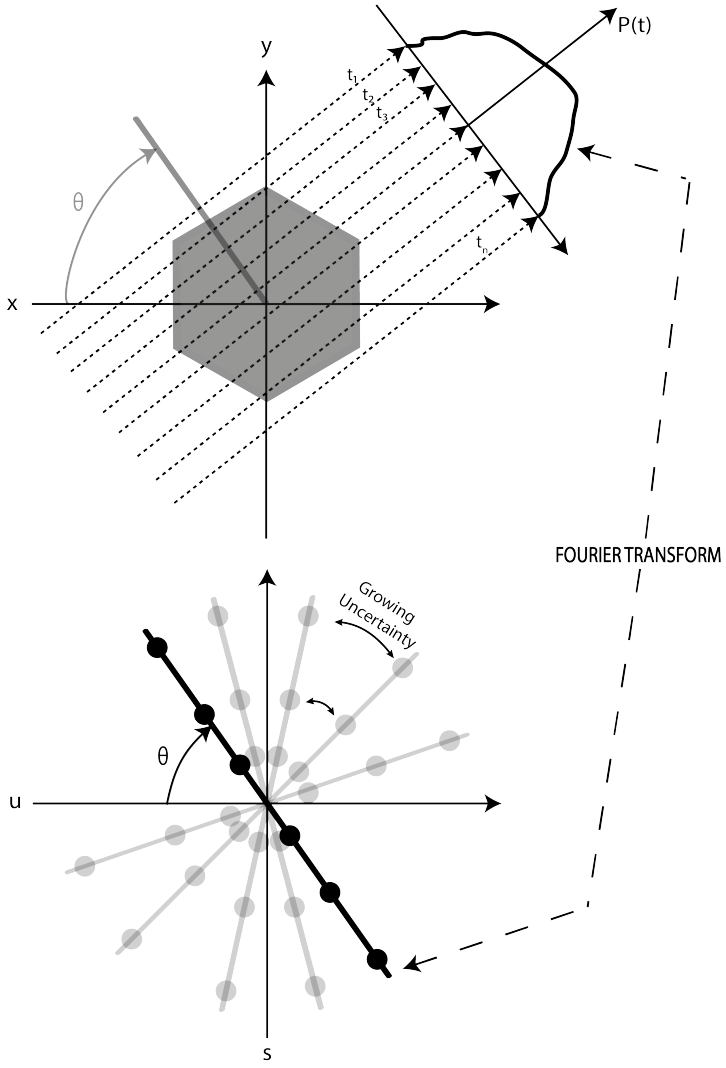

Figure 8.23: Depiction of the process required for computed tomography reconstructions. Each projection is manipulated by the Radon transform and both the forward and inverse Fourier transforms before obtaining a 3D representation of the analyte.

Each projection, at any given angle, maps the degree of attenuation of the X-rays based on the specimens attenuation coefficient(s). Mathematically this is described by the set of line integrals portrayed in Equation 8.16. This equation is named after Johann Radon who pioneered this type of transformation in 1917.[190]

$$P_{\theta=0}(t) = \int_{\infty}^{-\infty} \mu(x,y)dy \tag{8.16}$$

Sequentially, $P_{\theta}(t)$ is transformed from the Cartesian coordinate system to the frequency (u, s)

domain via the Fourier transform, Equation 8.17. The Fourier transform can be applied to transform the projection into the frequency domain, while the inverse Fourier transform (not shown) can be applied to transform back to the Cartesian coordinate system.

$$\begin{aligned} F(u,0) &= \int_{-\infty}^{\infty} P_{\theta=0}(x) e^{-j2} dx \\ &= \int_{-\infty}^{\infty} \left[\int_{-\infty}^{\infty} \mu(x,y) dy \right] e^{-j2\pi ux} dx \end{aligned} \tag{8.17}$$

Collecting projections at different angles and transforming them into the frequency domain populates the plane with radial lines that contain information about the projection of the specimen at each angle, θ. Increasing the number of projections, to infinity, would render the true image of the specimens cross-section once the inverse Fourier transform is applied. However, due to the limited number of projections that can be acquired and processed with reasonable computational costs, the use of interpolation between the nodes is necessary. In Figure 8.23, the spacing between the lines in the frequency domain increases radially, which makes the bounds for interpolation further from the point under investigation. As a result, there is a higher degree of error associated with these calculations, increasing as the frequency increases. This yields a degradation of the image based on the error associated with the interpolation between higher frequency components of the projection. The reader interested in exploring the computational aspects of computed tomography can find valuable information in the literature.[187]

8.6.3 The Filtered Back-Projection (FBP) algorithm

The FBP algorithm implements a similar approach to the Fourier Slice technique. First, a projection is measured. Then, that projection is transformed into the frequency domain by the Fourier transform, Equation 8.17, to get a map similar to that seen in Figure 8.23. However, at this stage, a weighting function is applied to filter each slice so that the map would look as the average between one projection and an infinite number of projections. This weighting function

is similar to interpolation. Lastly, the FBP algorithm utilizes the inverse Fourier transform of the filtered projections to reconstruct the image. The uncertainty in this process is decreased with an increasing number of projections. Figure 8.24 exemplifies the effects of increasing the number of projections with regards to image quality. In this case, 9 projections are all that is needed to identify the image as a circle, however, for more complex specimens, a higher number of projections are needed to elucidate the internal and external textural features.

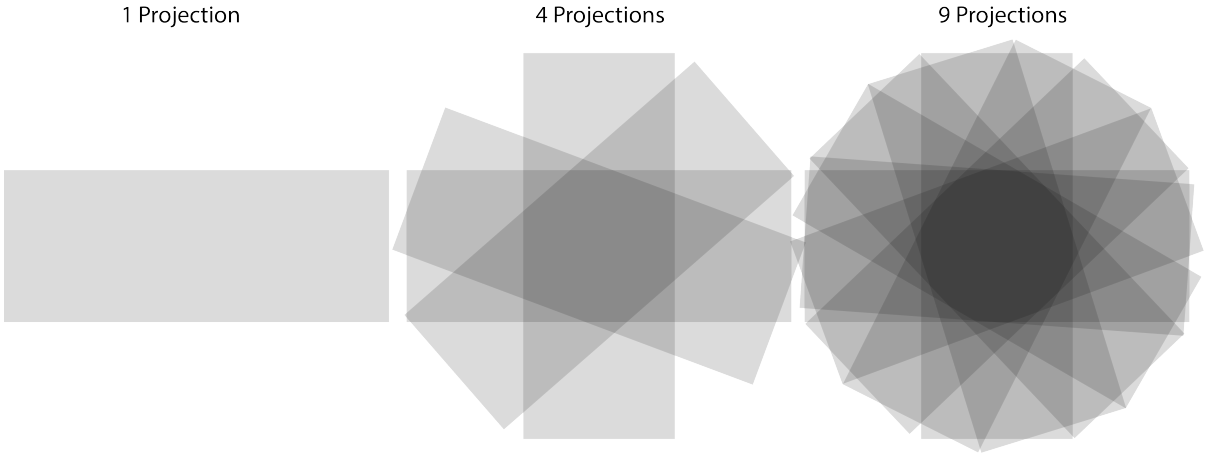

Figure 8.24: Reconstructions are with FBP algorithms are enhanced by the increasing number of projections. Symbolically, one projection of a cylinder does not render the object's true form, however, increasing the number of projections to 4, to 9, and beyond, render a closer approximation of the objects true form.

8.6.4 Algebraic reconstruction techniques

Algebraic Reconstruction Techniques (ART) are more computationally demanding than the commonly FBP algorithm to reconstruct images, rendering this reconstruction technique unfeasible for everyday use.[187] However, this method can bring benefits to X-ray tomography, especially, when there are not enough projections to make a good rendition of the specimen.[160] Figure 8.24 exemplifies the importance that the number of projection has on developing high quality reconstructions. Figure 8.25 contains a hexagon that sits in a Cartesian coordinate plane, similarly to Figure 8.23, where μ(x, y) describes the linear attenuation coefficient of the hexagon at any location in the 2D plane. The primary difference is that this Cartesian coordinate plane is composed of

small elements (pixels), f_j, with an area of δ^2.Within each pixel the linear attenuation coefficient is assumed constant.[18,114] This assumption is important since each projection is described by the summation of the product between the weight factor and the attenuation value contributing to each pixel in the grid. As seen in Figure 8.25, the weight factor links the contribution of each pixel to the area that is touched by the ray. In this method, a ray is not described by a thin line, but rather by a broad brushstroke that touches the area of certain pixels as it penetrates through the specimen. Equation 8.18 mathematically describes the contributions of each pixel to each projection and is analogous to Equation 8.16 from the FBP algorithm.

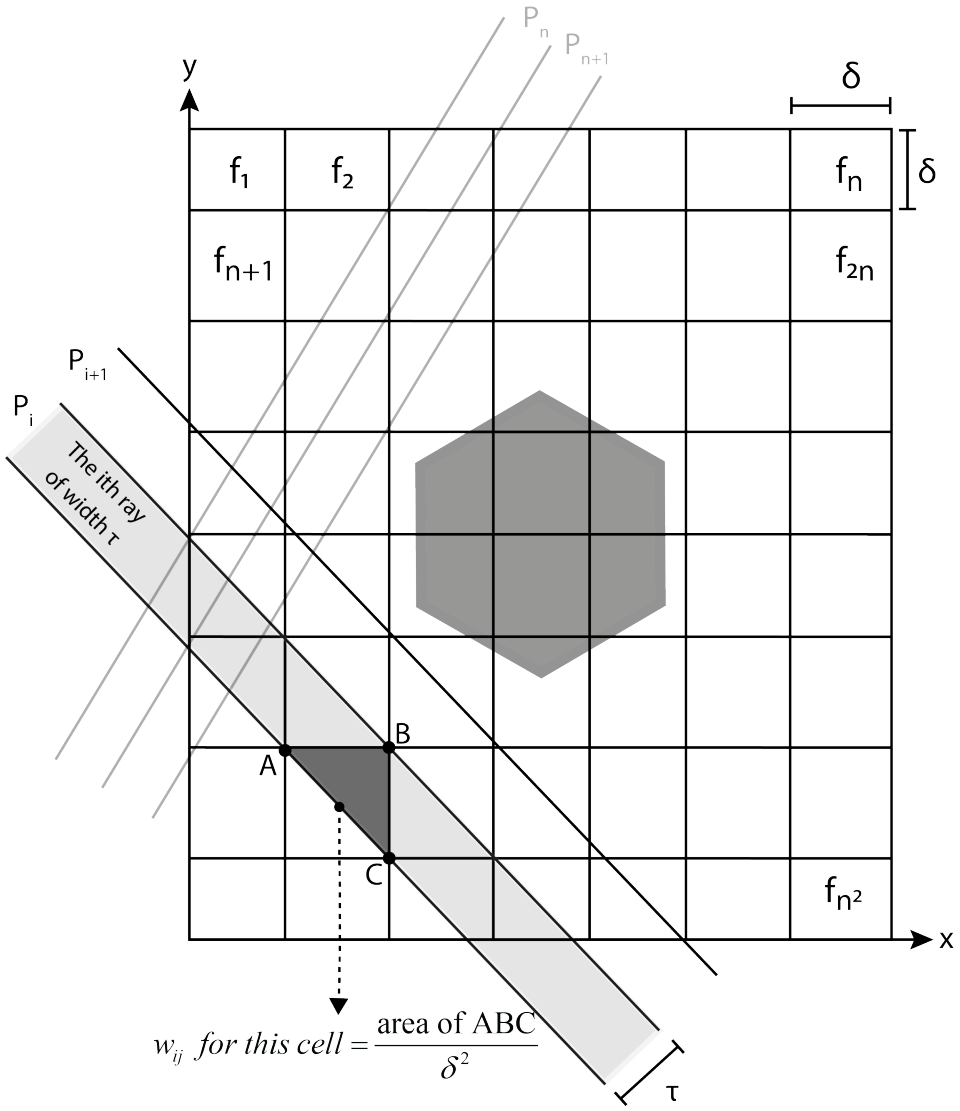

Figure 8.25: Top view of a specimen under parallel X-ray investigation. The grid represents pixels in a 2D view that make up the object in the (x, y)-directions, however, in 3D, the grid extends in the (x, y, z)-directions and is represented by voxels rather than pixels.

$$\sum_{j=1}^{N} \omega_{i,j} f_i = p_i, \qquad i = 1,2,...,M \tag{8.18}$$

Equation 8.19 combines all the equations for M number of X-rays and N number of elements associated with the unknown object during each projection. With a large number of M rays and N elements, the matrix grows to the point where iterative methods are needed to find a solution. For example, if the object to be reconstructed is composed of 2500 by 2500 pixels then, there

are 6.25 Œ 10^6 elements (N) contributing to each projection. Additionally, if each projection has 1000 measurements and there are a total of 1000 projections, then, there will be 1×10^6 X-rays containing information about the specimen. The product of the number of elements and X-rays results in the overall matrix size, which is 6.25×10^{12} under the conditions stated above. Fortunately, this matrix is sparse; meaning that most of the entries to Equation 8.19 are zeros.

$$\begin{aligned} w_{11}f_1 + w_{12} + f_2 + w_{13}f_3 + ... + w_{1N}f_N &= p_1 \\ w_{21}f_1 + w_{22} + f_2 + w_{23}f_3 + ... + w_{2N}f_N &= p_2 \\ &. \\ &. \\ &. \\ w_{M1}f_1 + w_{M2} + f_2 + w_{M3}f_3 + ... + w_{MN}f_N &= p_M \end{aligned} \tag{8.19}$$

Solving this problem is computationally expensive, however, the literature possesses some examples of iterative methods that use modern graphical processing units (GPUs) to accelerate ART algorithms through parallel computing.[177,246]

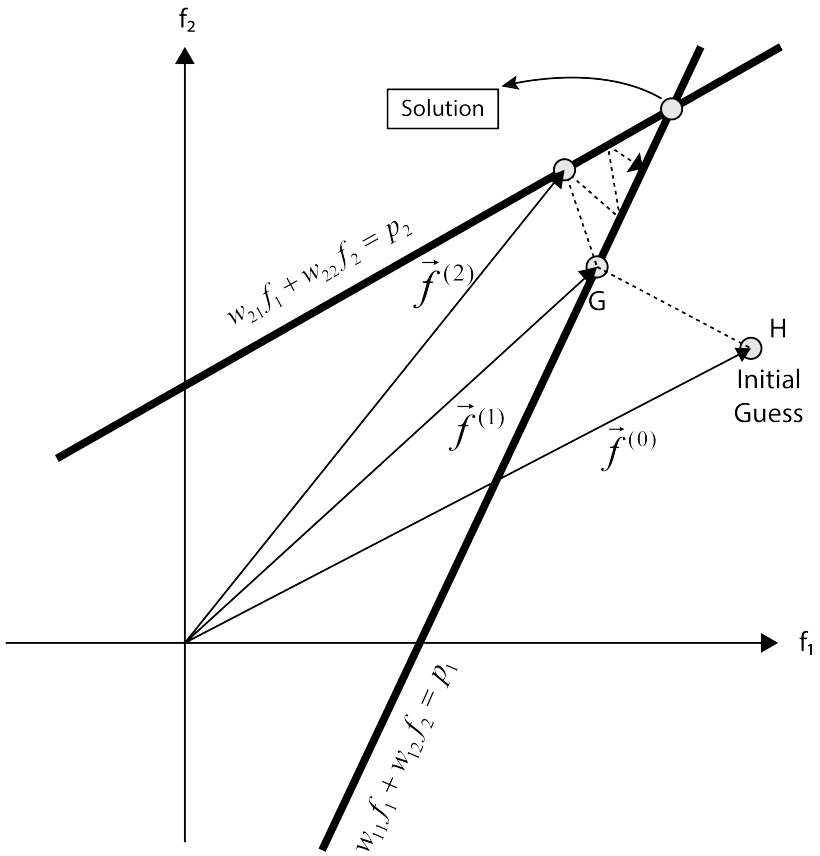

Figure 8.26: Graphical representation of the Kaczmarz method for solving algebraic equations. An initial guess is projected back and forth between p1 and p2 until a solution is obtained.

Alternatively, the Kaczmarz method, visualized in Figure 8.26, is an example of a method that would be utilized to solve linear equations by using an iterative approach based on an initial guess. A derivation of this method is presented in the works of Kak and Slaney.[114] The method consists of two intercepting X-rays from two different projections. The reconstruction is solved when the intercept of these two rays is obtained. To do so, the Kaczmarz methods utilizes an initial guess $\vec{f}^{(i1)}$, that is projected onto an X-ray, p_i, to obtain the first iterative solution. The solution becomes the next initial guess and the point is then projected to the second ray. The process is an iterative procedure that is repeated by utilizing the obtained solution and projecting back and forth between pi and p_{i+1} until the method converges onto a solution.

$$\vec{f}^{(i)} = \vec{f}^{(i-1)} - \frac{(\vec{f}^{(i-1)} \cdot \vec{\omega}_i - \vec{p}_i}{\vec{\omega}_i \cdot \vec{\omega}_i} \vec{\omega}_i \tag{8.20}$$

For ease of computation, ART simplifies Equation 8.20 to Equation 8.21 and assumes that the weighting fraction, w_{ik}, has a binary value of 1 or 0. The approximation reduces the quality of the reconstruction, but helps expedite the computational process.

$$\Delta f_j^{(i)} = f_j^{(i)} - f_j^{(i-1)} = \frac{p_i - q_i}{\sum_{k=1}^{N} \omega_{ik}^2} \omega_{ij} \tag{8.21}$$

The works of Kak and Slaney[114] and Banhart[18] provide a more in-depth description of the ART methods.

8.6.5 X-ray computed tomography in heterogeneous catalysis

A supported metal heterogeneous catalyst consists of a metal (e.g., platinum, palladium, nickel, etc.) that is deposited onto the surface of a material (e.g. TiO_2, SiO_2 , γ-Al_2O_3, etc.) often via incipient wetness impregnation and often reduced at high temperatures to create a composite that effectively transforms a substrate into a desired product. However, a heterogeneous catalyst can increase in complexity with the use of two or three metals, promoters, and mixed metal oxide supports. The complexity and the overall performance of these systems has been elucidated by ex situ characterization techniques, e.g., gas adsorption, temperature-programmed chemistry, and crystallography. Typically, these analyses are conducted before and after the reduction or use of the catalyst. Together, these techniques provide information on surface area, (exposed) pore volume, metal dispersion and active sites, and the phases of the composite in ex situ conditions. High-temperature environments and atmospheric compositional changes have led to phase changes and nucleation or crystal growth of the metals used for catalysis. Synchrotron X-CT and XRD can be coupled to provide non-invasive, in situ operando information on surface area, pore-volume, and metal phase dispersion as a function of space and time. This technique utilizes a pencil beam to raster through a layer of the material as it spins. The scattered X-ray intensities are recorded and correlated to a particular phase as a function of space, temperature, and time.[15]

Metal dispersion within the catalyst support can be of concern with regards to the activity of a

heterogeneous catalyst. Prior to the impregnation of the catalyst, ligands are added to generate a higher degree of dispersion once the catalyst is reduced and activated. Jacques & co-workers have implemented μ-XRD-CT to perform in situ characterization of the developing metal phases during the impregnation and activation of a Ni/γ-Al_2O_3 catalyst, typically used for hydrogenation.[111] Their study revealed that this technique could be used to observe a catalyst active metal phase as a function of temperature, space, and time.

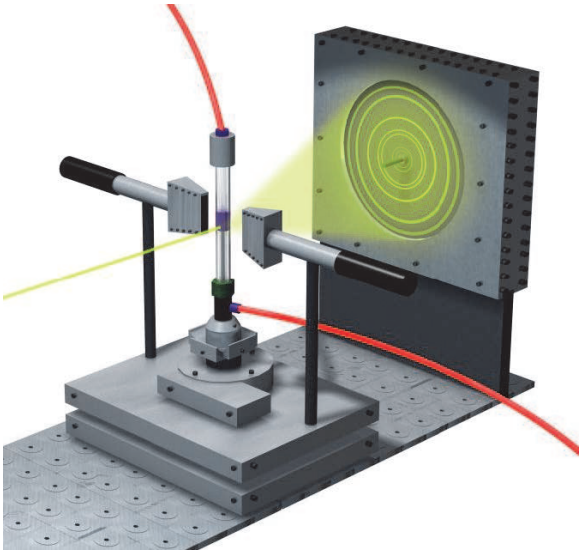

Figure 8.27: Customized experimental set-up for the in situ study of the activation of a Ni/γ-Al_2O_3 with μ-XRD-CT. Reprinted with permission.[111]

Jacques et al. utilized an experimental set-up, as seen in Figure 8.27, where a sample holder was mounted on a movable stage along with two heat sources. Additionally, the sample holder allowed for gases to flow from the bottom to the top of the cell during thermal treatment.[111] Figure 8.28 contains a visual representation of the Ni/γ-Al_2O_3 phase progression at a given slice during thermal treatment. The composite made of a Ni metal conjugated with an ethylenediamine (en) ligand was impregnated onto a γ-Al_2O_3 support and underwent decomposition, under nitrogen, upon thermal treatment. At the beginning, between 100-125°C, Ni(en)xCO_3 (green) and Ni(en)(CO_3)xCl_2(1x) ůxH_2O (cyan) reigned over the cross-section, where the former covered the exterior (egg-shell) of the material while the latter had an even (egg-white) distribution throughout. At 325°C the former decomposed into the active face center cubic (FCC) Ni phase (blue), while the latter underwent

dehydration at 175°C, among other transitions, to yield the active FCC Ni phase above 400°C.[111]

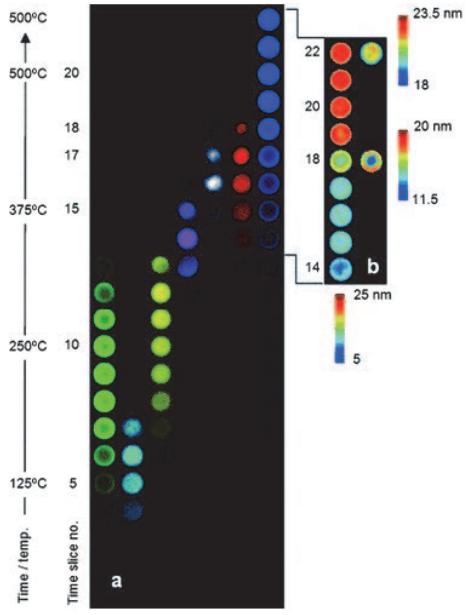

Figure 8.28: Temporal and thermal μ-XRD-CT scans of a single slice of a Ni/γ-Al_2O_3 catalyst particle during activation. (a) Solid-state phases: Ni(en)xCO_3(green), Ni(en)(CO_3)xCl_2(1x) ů xH_2O (cyan), Ni(en)(CO_3)xCl_2(1x) (yellow), Ni(en)0.5(O)xCl_2(1x) (magenta), Ni(en)Cl_2 (white), HCP Ni (red), and FCC Ni (blue). (b) Color maps showing the variation of crystalline size (between 525 nm). Reprinted with permissions.[111]

Jacques et al. demonstrated the capabilities of synchrotron CT coupled with XRD to investigate the in situ activation of a Ni/γ-Al_2O_3 catalyst with an active FCC Ni phase. The customizable stage provided key aspects to this analysis in replicating the conditions of use and demonstrates the need for innovative thinking when trying to replicate in situ conditions regardless of the analytical technique.

OBrien et al., furthered Jacquess work with μ-XRD-CT/ μ-absorption-CT to provide operando characterization of the Ni/γ- Al_2O_3 catalyst under activation and carbon monoxide (CO) methanation conditions.[173] CO methanation is described by Equation 8.22; CO reacts with three molecules of hydrogen (H_2) to form methane (CH_4) and water (H_2O).

$$CO + 3H_2 \rightarrow CH_4 + H_2O \tag{8.22}$$

At first, OBrien et al. conducted operando experiments under activation conditions, where they

sequentially flow nitrogen, a mixture of nitrogen and oxygen, oxygen, and hydrogen, to investigate the effects of temperature and gas atmosphere on the active metal phase. Figure 8.29 depicts the internal and external distributions of Ni as it develops to the active face-centered cubic (FCC) Ni phase under the aforementioned conditions. During the initial stage of the experiment, at low temperatures and under a nitrogen atmosphere, the $[Ni(en)_3](NO_3)_2$ phase dominated the exterior of the particle meanwhile the trans-$[Ni(en)_2(H_2O)_2](NO_3)_2$ dominated the interior of the particle. The increasing temperature allowed for the ligand to decompose and increase the distribution of the metal. Then, the increasing temperature and oxygen content promoted the diffraction silent (small or amorphous) Ni to sinter at the exterior of the γ-Al_2O_3 particle. Afterward, with hydrogen flowing through the bed, both the interior and exterior of the particle were activated to FCC Ni phase, where the exterior exhibits a slightly larger average particle size due to particle sintering during calcination.[173]

After activation, the 10 wt.% FCC Ni/γ-Al_2O_3 catalyst was utilized under a mixture of hydrogen and carbon monoxide at 450°C.[173] The dynamic progression of the reaction and steady-state values were tracked via mass spectrometer. Figure 8.30 portrays the results from the mass spectrometer, the μ-XRD-CT, and the μ-absorption-CT for the FCC Ni/γ-Al_2O_3 catalyst under operando methanation conditions. This analysis yielded that the FCC Ni phase was not altered by the reaction conditions, and it was stable for two hours, represented by the unchanged intensity from the μ-XRD-CT colored mapped slice.

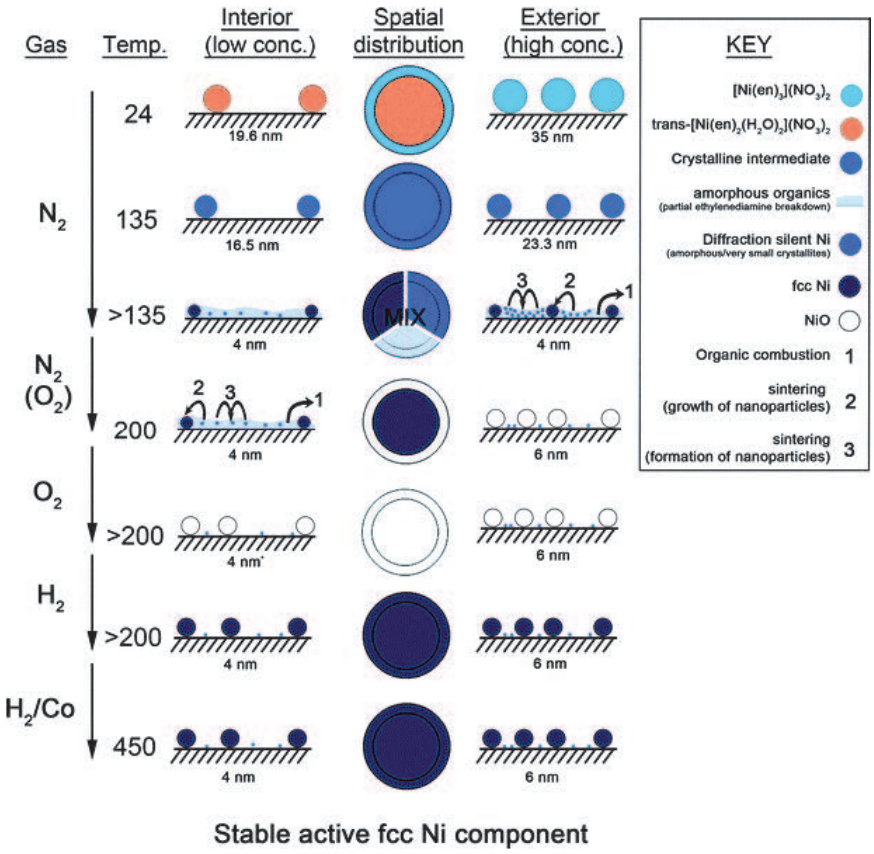

Figure 8.29: A representation of the catalyst metal phase evolution as a function of gas and temperature. Reprinted with permission.[173]

Heterogeneous catalysis implements many types of porous supports that enhance the performance of the catalyst metals. Porous materials have many properties; outside of catalysis, porous materials are used with separations, purifications, and storage of gases. The following section discusses the applications of tomography to the in situ analysis of carbon dioxide sequestration in anthracite reservoirs.

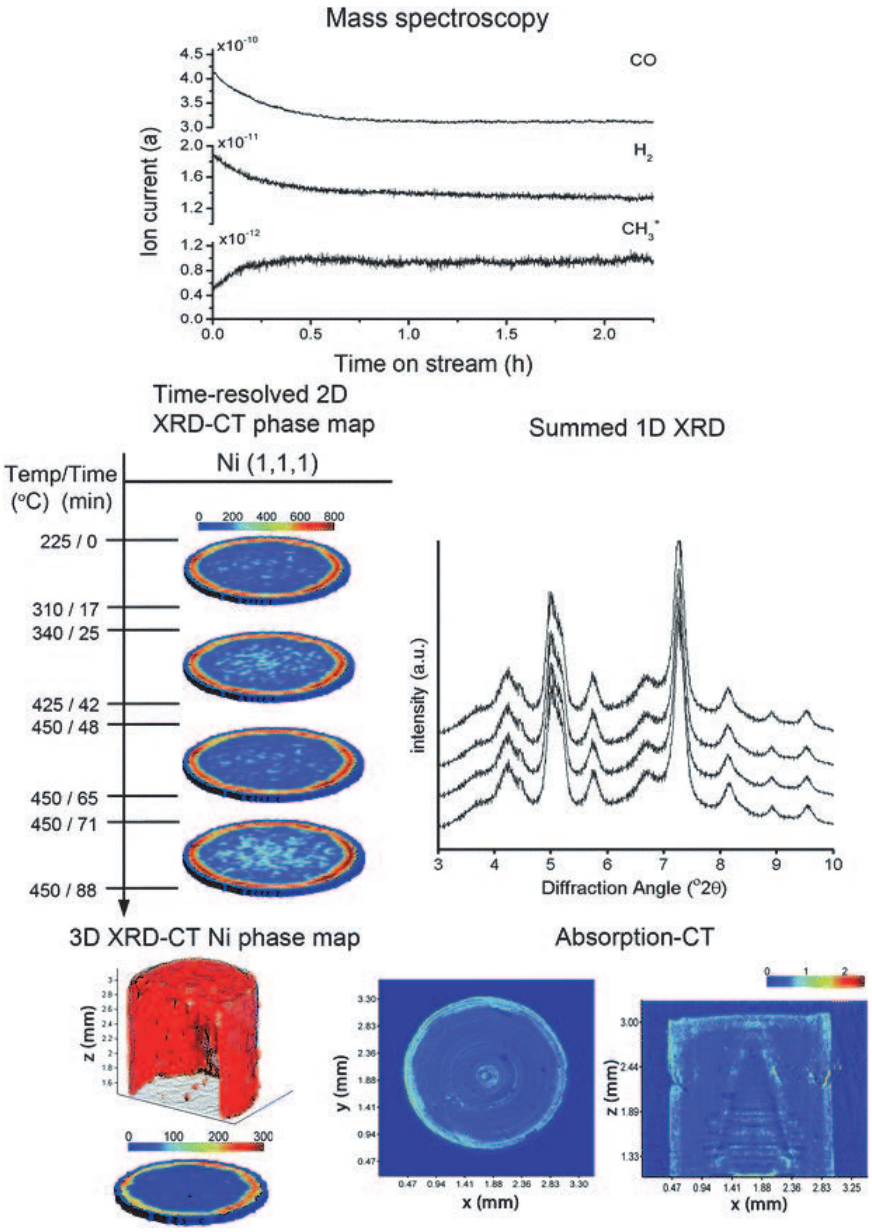

Figure 8.30: Operando 2D μ-XRD-CT characterization of Ni catalyst slice during methanation followed by mass spectrometer. Additionally, before and after 3D μ-XRD-CT scans of the entire specimen provided a Ni phase map and the absorption spectra of the specimen. Reprinted with permission.[173]

8.6.6 X-ray computed tomography in geological samples

Coal has been an important resource since before the beginning of the first industrial revolution. Anthracite, bituminous, subbituminous, and lignite are the types of coal, respectively decreasing

in quality, that support the electrical grid and the heating of homes. Anthracite is the highest quality coal type because of its high carbon content and low impurity levels. Outside of coal, methane, among other fuels are utilized for this purpose. The burning of such fuels produces carbon dioxide, a gas that has been linked to climate change. As a result, there is an increasing need for carbon capture and sequestration (CCS) into underground reservoirs to mitigate climate effects. The deepest underground reservoirs are perfect for this task; their depth renders these reservoirs technologically or economically unfeasible, however, by implementing CCS it has been shown that methane can be extracted from these systems.[132] Deep anthracite reservoirs, with low impurity content, makes CCS and methane production more attractive.[252]

Zhang et al. have utilized synchrotron computed tomography to characterize anthracite deposits under CCS conditions of use. Anthracite targeted coal seams are located at a depth of 800 m or greater. At that depth, the in situ conditions would exhibit temperatures and pressures above 31.1°C and 73.9 bar, respectively.[252] Mimicking external conditions without compromising the quality of the reconstruction or the mobility of the stage is always challenging. Zhang & coworkers fabricated a high-pressure cell composed of aluminum an X-ray transparent material to analyze anthracite cores under conditions of use. Figure 8.31 shows an innovative sample holder utilized by Zhang et al. to mimic high-pressure environments on the coal core as supercritical carbon dioxide ($scCO_2$) is injected into the bed.

The coal sample was cut to 35 mm in diameter and 70 mm in length. The ends were polished by using a rock grinder to create a uniform fit inside the sample holder. Subsequently, the confining and axial pressures were increased to 100 bar and the temperature was increased to 40°C via an external jacket.

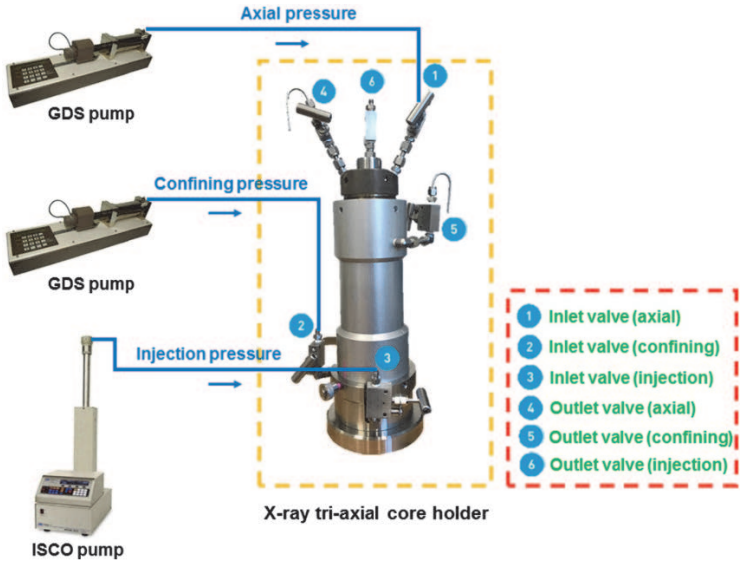

Figure 8.31: Pressure cell constructed out of X-ray invisible aluminum. The sample holder can accommodate for the pressure effects that are observed in a reservoir. Reprinted with permission.[252]

Figure 8.32 portrays the effects on permeability as a function of time during a 53-hour $scCO_2$ injection in an anthracite coal sample. The permeability of the core changed from 3 to 0.24 μD (micro-Darcy) within the first couple of hours. This behavior is caused by the molecular rearrangement that coal experiences in the presence of $scCO_2$. Supercritical carbon dioxide has fascinating properties, i.e., it can act as a solvent for organic molecules. An increase in permeability from 0.024 to 1.2 μD was observed over the course of the experiment. The solvent properties of $scCO_2$ allowed for organics (present in the coal sample) to travel through the core which created the channels for the CO_2 to permeate through the core. Figure 8.33 depicts the cracks produced by organic and mineral movement in the direction of carbon dioxide flow.

For other geologic materials the complementarity of TD-NMR and X-CT have proven valuable in the characterization of porosity and fluid flow. A challenge for correlating TD-NMR T_2 distribution measurements to pore size distributions is calibration of the signal using reference samples of known pore size distribution. Zhao et al. demonstrated a method for using X-CT data of reference materials to calibrate the NMR response and generate pore size distributions directly from TD-NMR, Figure 8.34.[255] Others have also studied correlations between X-CT and NMR.[14,144] For pore spaces less than 1 μm in diameter X-CT does not, generally, provide resolution, whereas

TD-NMR can resolve pore size. The full range of pore sizes accessible to TD-NMR is dependent upon the relative rates of diffusion and enhanced surface relaxation (vide supra) but may range from single digit nanometers to many micrometers and complements X-CT nicely.

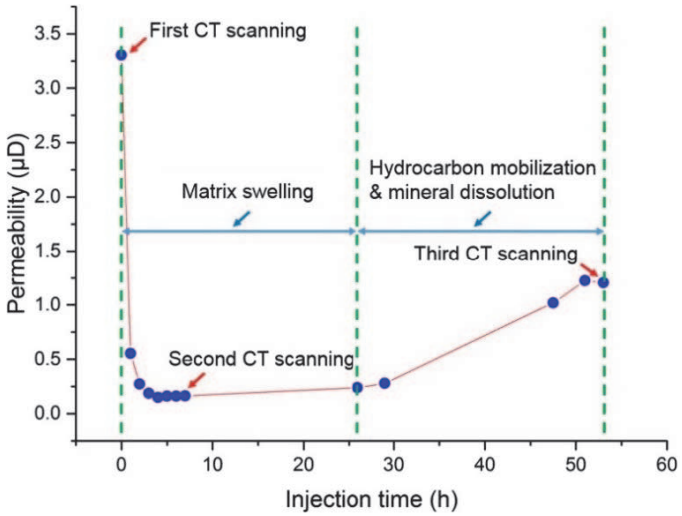

Figure 8.32: Permeability of carbon dioxide in anthracite coal as a function of injection time. Reprinted with permission.[252]

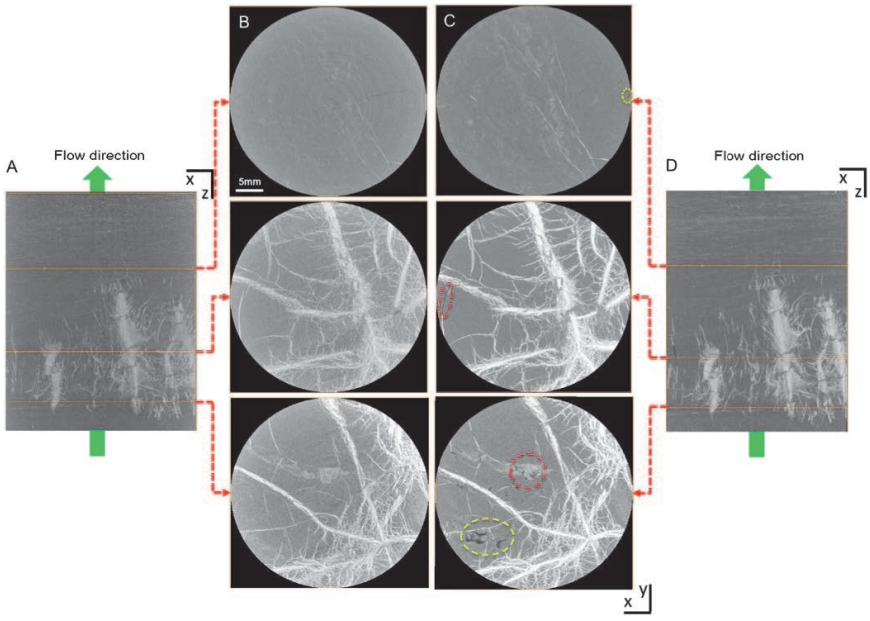

Figure 8.33: Migration of organics soluble in supercritical carbon dioxide through coal seam. Reprinted with permission.[252]

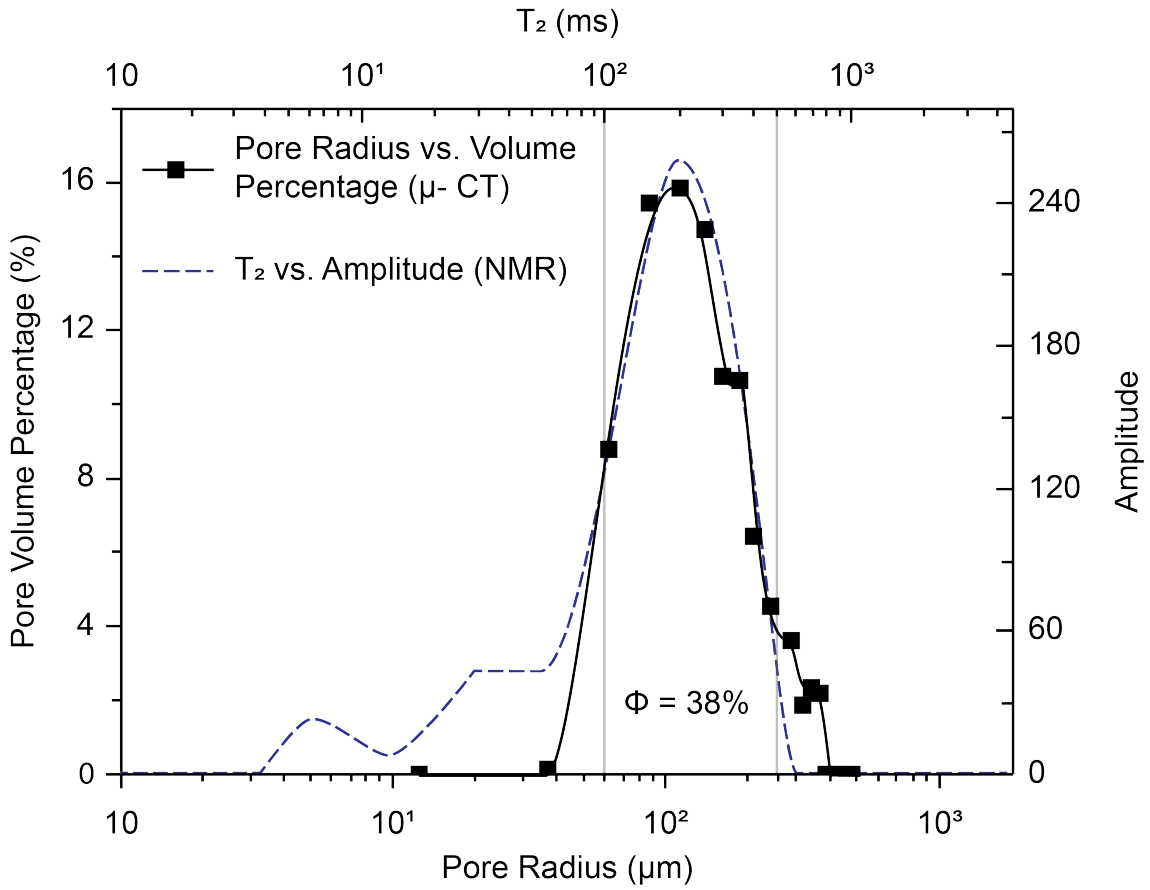

Figure 8.34: A comparison of pore size distribution from XCT and NMR of an artificial rock core reference material. Reprinted with permission.[255]

As mentioned above, the movement of $scCO_2$ in coal beds is crucial for the understanding of CCS and coal bed methane production. CCS coupled with coalbed methane production is an increasingly more attractive option to mitigate the climate change effects. However, there is an increasing interest in going completely emission-free through a hydrogen-energy infrastructure. Hydrogen is a fuel that has the capability of being CO_2 emission-free, basically, a clean fuel. Electrochemistry has made this a possibility for the automotive industry with hydrogel fuel cell cars.

8.6.7 X-ray computed tomography in electrochemistry

Hydrogen is one of the most abundant elements on earth; whether it is attached to a hydrocarbon or a water molecule, hydrogen can be converted into the fuel that is needed to power the transportation and electrical grids. Until now, our economy has mostly relied on combustion to access the chemically stored energy in hydrocarbons. Even though our energy system has become extremely efficient over the last century, it is not sustainable due to the carbon dioxide emissions that induce climate change.

$$\text{Fuel} + O_2 \rightarrow CO_2 + H_2O \tag{8.23}$$

However, with the boom of the hydrogen economy and decades of research in proton exchange membrane fuel cells (PEMFC), there are commercial vehicles that produce zero-emission at the tailpipe. To make this technology completely emission-free, there is a push to develop efficient mechanisms for solar-energy driven water electrolysis to produce greener hydrogen fuel. An electrolyzer utilizes electrochemistry to evolve hydrogen and oxygen from water. These reactions are known as the hydrogen and oxygen evolution reactions (HER & OER, respectively) and are shown in Equation 8.24.

$$\begin{aligned} &\text{HER:} \quad 2H_2 \leftrightarrow 4H^+ + 4e^- \\ &\text{OER:} \quad O_2 + 4e^- + 4H^+ \leftrightarrow 2H_2O \end{aligned} \tag{8.24}$$

Electrolyzers are composed of a membrane electrode assembly (MEA), flow fields, conducting plates, and external plates that sandwich the whole assembly together, just like a fuel cell. The conducting plates act as the positive and negative terminals, like a battery, and through them, the circuit is completed. The flow fields distribute water to the anode and oxygen and hydrogen away from the anode and cathode, respectively. The MEA contains the anode and the cathode adhered to either side of the proton exchange membrane. Typically, a Nafion^{TM} membrane is used for PEM

electrolyzers. Nafion^{TM} or PTFE membranes are sulfonated to facilitate proton transfer. Figure 8.35 portrays the electrolyzer assembly utilized by Leonard & co-workers at the Advanced Photon Source (APS) synchrotron facility.

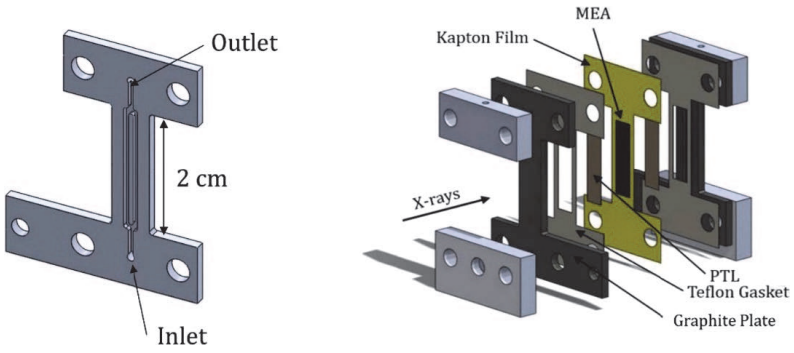

Figure 8.35: Experimental PEM electrolyzer assembly used for this analysis. (a) A CAD drawing of the flow fields used in the experimental setup. (b) A representation of the PEMFC assembly used by Leonard et al. Reprinted with permission.[137]

Leonard et al. utilize X-ray tomography and radiography to characterize the transport properties of the electrolyzer and the degradation of the electrode under in-situ conditions.[137] Here, time resolution is of high importance to monitor the formation, growth, and detachment of bubbles on either side of the MEA. Tomography provides extremely useful information with regards to morphology and permanent changes to the structure and texture of the electrodes as a function of space and time. On the other hand, radiographys sub-second acquisition time facilitates the monitoring of bubble formation and dynamics and their effects on the anode. Deciphering the in situ mass transfer (two-phase) regime can lead to further optimization of the electrolyzer and its components.

Leonard et al. utilized synchrotron X-CT to create a threedimensional map of the anode, cathode, and PEM. Within this reconstruction, there were dense water pockets rather than uniform distribution throughout the hydrophilic PTL layer (as seen in Figure 8.36) due to air bubbles or surface irregularities.[137] In addition to observing the water content, this reconstruction revealed spatiotemporal distributions of the iridium ruthenium oxide and platinum catalysts and their migration when operating between 50 mA/cm^2 and 200 mA/cm^2. The migration of the metal phases was promoted by the oxygen bubble forming near the catalyst particle and thus causing it to detach

and farther migrate towards the porous membrane.[137]

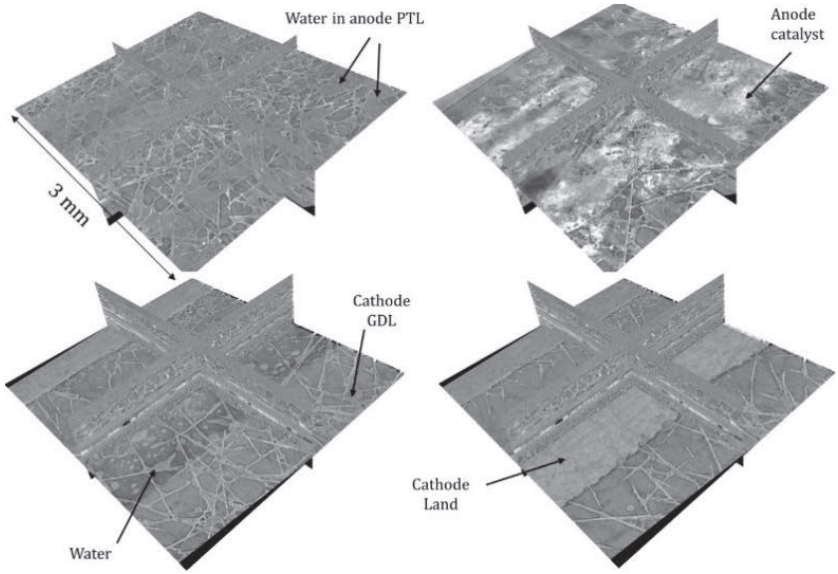

Figure 8.36: Three-dimensional reconstruction of an MEA. Reprinted with permission.[137]

Figure 8.37 contains radiographic images at different current densities. From this analysis, it is apparent that increasing current density increases the oxygen evolution, as seen by the transition from bubbles to slugs. The bubble formation is associated with the degradation of the electrode, and therefore understanding the mass transfer principles that govern this system can lead to improvements with regards to efficiency and lifetime of the electrolyzer.

The examples provided in this section highlight the recent spatiotemporal improvements of the technique and the novel applications researchers have found that couple complementary non-invasive characterization techniques, e.g., X-ray diffraction. Essentially, this approach elucidates different aspects of the specimen that would normally require a handful of ex situ techniques. For example, gas adsorption and transmission electron microscopy (TEM) would provide complementary data to the example provided in Section 8.6.7. Gas adsorption would provide surface area, pore volume, and pore size distributions, while TEM could provide particle size distribution for both the metal and the porous support. Additionally, based on the roughness of the particle and the overall spread of the metal, one could infer qualitative information about the crystalline phase and metal dispersion, respectively. However, to obtain quantitative measurements on the latter, another

ex situ technique, temperature programmed chemistry, would need to be implemented. Each ex situ technique brings its own sample preparation requirements and thus incrementing the chances for structural and textural changes that deviates from the specimens true nature under conditions of use.

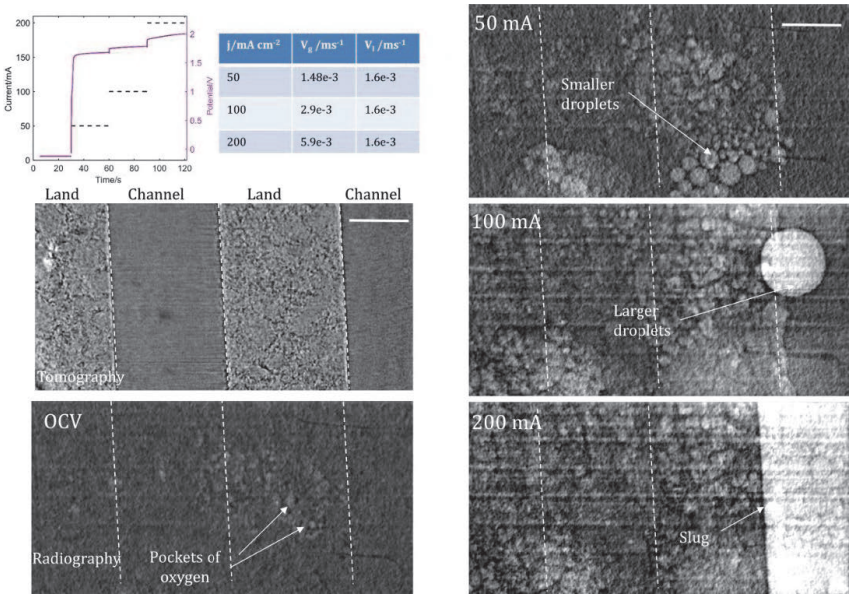

Figure 8.37: Current density versus bubble velocity. Reprinted with permission.146

Section 9.6 seeks to provide insight into the future of the characterization techniques discussed in this chapter, i.e., TD-NMR and X-CT, and their applications. Readers might find the following section as a source of inspiration to implement in situ characterization techniques in their research or guidance for developing future couplings of non-invasive complementary characterization techniques.

Chapter 9

Concluding Remarks and Future Recommendations

Abstract

Being the pioneering member of a research group is a very rewarding experience in the sense that all the work that you do, has no precedent in your laboratory, which forces you to continually explore new horizons to facilitate and promote different avenues for your research and that of the group. Here, are some concluding remarks on the work presented in this dissertation and future recommendations for those projects.

9.1 Chapter 3

The homogeneous iron complex under study in Chapter 3 has been broadly investigated for substrate compatibility in both hydrogenations and dehydrogenation reactions. An opportunity for an additional investigation, is to conduct a deep kinetic and mechanistic investigation for the remaining 7 substrates. Doing so will leverage the broad use of an earth-abudant catalyst and further the advancement of U.N. sustainable development goals by reducing our impact on terrestrial and aquatic life. In order to promote the usage of these complexes, it would be important to develop strategies for heterogenizing homogeneous complexes without compromising activity or develop isolation and redeployment scaffolds that transition this complex from a one-pass to a multi-pass process.

Additionally, from the investigation conducted at KU, we see the need to conduct density functional theory (DFT) studies that mimic reaction conditions in condensed phase. This would include

a full investigation into the reaction energetics through the proposed mechanism and reactive intermediates observed during the nitrile hydrogenation work. Additional DFT studies would be beneficial in understanding the true nature of the proton shuttles and their influence on the imine self-condensation cascade.

Additionally, the mechanistic study conducted in Chapter 3, conveys the important role that proton shuttles, e.g., 2-propanol, play in enabling faster reaction rates while experiencing the lowest hydrogen solubilities. In this regard, it would be advantageous to create a new generation of catalytic complexes that incorporates proton shuttles into the ligand backbone to enable the use of more efficient hydrogen carrying solvents. In parallel, the catalyst could be strengthened against oxidative decomposition by increasing denticity or the use of alternative earth-abundant elements, e.g., manganese.[241]

Due to the low toxicity of iron, and the high performance for this complex that allows the use of small amounts (under regulatory maxima) of this iron complex to be demanded for a particular reaction. It would be pertinent to conduct toxicity studies of the ligand, the dibromide precursor, the borohydride complex, the dihydride complex, and the bromide-hydride impurity.[46] If not toxic, this would reduce the burden of purification that requires excessive amount of solvents in pharmaceutical processes.

9.2 Chapter 4

The continuous flow hydrogenation reactor is highly sensitive to mass transport resistances and is not able to maintain small slugs throughout the course of the experiment in order to achieve excellent benzonitrile conversion. In order to improve upon the first iteration of this platform, it is recommended to engage the meso-scale regime on the upper end of the spectrum to enable surging and the use of static mixers to promote more efficient mixing while operating a mostly liquid full reactor. Based on the SIA and OMC data presented in Chapter 4, a bubble column and static mixer present some of the best opportunities for enhancing mass transfer rates. Based on recent data, the use of filter disks across tubular reactors promote the break of bubbles to enhance SIA and

therefore mass transfer, but also promotes agitation in the liquid phase.

Additionally, the fabrication of complex structures is limited by the resolution of the manufacturing methods. For this reason it is hard, not to say near impossible, to obtain commercial static mixer for low ID reactors. Additive manufacturing embodies a whole range of 3D printing techniques that could render structural features with enough resolution to use for reaction engineering. With the proximity to the additive manufacturing capabilities associated with Wichita State University's aerospace sector, this area of manufacturing could bring part of the pharmaceutical manufacturing sector to Kansas.

In Chapter 8, we discuss the fundamentals of x-ray computed tomography and investigations into catalysts and electrolytic cells under conditions of use. It would be interesting to probe the continuous reactor with x-ray illuminated radiography to investigate gas-liquid interfaces under conditions of use. Here, at KU we possess an X-ray microcomputed tomography device capable of taking images of this sort. Also, the tomographic capabilities could render high resolution 3D reconstructions of custom reactors for computer fluid dynamic (CFD) modelling and optimization.

9.3 Chapter 5

Smart manufacturing furthers the quality-by-design modality of continuous processing by instituting model predictive controls and optimization strategies for secondary variables, i.e., manufacturing goals other than a consistent, high quality profile. To advance the deployment of conductivity and model predictive control in the specialty chemical industries, there is a need to create an optimization model and decision-making strategies to meet the goals of the manufacturing campaign.

Additionally, to elevate the understanding and adoption of smart manufacturing paradigm by regulatory agencies, there is a need to develop resources, and blueprints of decision-making requirements to be followed by users so that quality is not compromised for the optimization of secondary variables. Often, the lack of understanding of regulatory agencies that slow progress when shifting to a new paradigm. This would be an effort to minimize such outcome.

9.4 Chapter 6

The synthesis of GP thermoplastics and the fabrication of films is a promising field with enough room for improvement and innovation.

To further the current work, there are opportunities in making films with improved mechanical and transport properties. Additional investigation into the nitrogen gas and multicomponent selectivity of these films would provide further insights into the food these materials would package. Also, there is a need to conduct composting of these materials with industrial and at-home conditions to validate the precedent in the literature and further the commercialization of these materials.

Currently, we are working towards implementing a molten imidazole synthesis of a glucan-acetate-palmitate thermoplastic. This synthesis provides a 'dry' synthesis medium and the opportunity to implement full recovery and recycle of imidazole. The products would be fully substituted with varying degrees of acetate and palmitate modifications. These features would reduce PMI significantly as no solvents are used and imidazole would be recycled. Additionally, by fully substituting the glucan we would minimize material variations that create heterogeneous melting profiles.

9.5 Chapter 7

The aqueous synthesis of the GB detergents with NaOH has shown promising results in terms of selectivity and the internal solubility criteria based on industrial product testing insights. The cation species, such as sodium, helps in stabilizing the alkoxide groups under basic conditions to activate the glucan. Potassium has also showed promising results in terms of reactivity, but based on solubility criteria, the modification for both ionic species is heterogeneous in nature. To improve upon this, we look toward implementing ions like calcium and zinc, which are better at reducing the interactions between different glucan strands. Preliminary results show promising data, but further optimization and understanding is required to find the right ionic paring.

Additionally, to move away from environmentally unhealthy components, e.g., phosphates, to remove cationic species in hard water, we can implement zeolites in the final formulation.[126] At KU, the institute for sustainable engineering (ISE) has a zeolite library with thousands of samples that we can leverage to find hard-water scavengers for detergent applications.

9.6 Chapter 8

Characterization of porous media under conditions of use has been advanced by developments in multiple techniques but notably this chapter has focused on time-domain NMR and X-ray computed tomography. Each of these is anticipated to be the subject of additional technological developments. Analysis of the raw experimental data requires algorithms and models in each case. A common need among the techniques is preparation of well-controlled reference samples of varying composition to assist in the definition of data reduction algorithms. Advances in material synthesis and preparation methodologies, including high-resolution 3D printing may yield advances in characterization science by filling the need for reference materials.

As discussed in Section 8.1, NMR relaxometry techniques that provide insight into porous media textural properties require calibration of experimentally determined relaxation rates to yield pore size distributions. Equation (6) expresses the relationship of relaxation rate to both surface area and surface relaxivity. It remains a challenge to provide a strong fundamental correlation between solid surface-chemistry and relaxation rate, which could be elucidated with well-controlled reference materials. Future investigations will surely address this need with both experimental studies and via computational modeling. Advances in instrumentation, particularly related to low-field, permanent magnet instruments, will surely provide access to more rapid sampling frequency, ultimately providing characterization of smaller pore size (<1 nm). Additionally, an expanding suite of pulse sequences and magnetic field gradients, even with low-field instruments, is under development to yield insights related to fluid flow through a pore system.

X-ray computed tomography is a technique that provides the ability to process a specimen without degrading its structural or textural properties. Future spatiotemporal improvements in this

technique will broaden the pore spectrum (spatial resolution) and decrease the need for ex situ characterization techniques that provide comparative information. Additionally, decreasing acquisition times (temporal resolution) will increase the dynamic phenomena accessible for investigation. However, these improvements are highly dependent on the technology behind the physical components of this technique, e.g., focusing mirrors, and brilliance behind the illumination, mostly requiring access to a synchrotron.

While these changes are important, especially in the field of catalysis where zeolites (materials with low pore size distributions) are commonly used, they are not the only area in need of refinement. Designing new sample holders to study dynamic behavior in porous media, while coupling other non-invasive techniques, would be highly beneficial. An example of this could be the use of TD-NMR-CT to quantitate the diffusion of drugs and dissolution of the tablets that house them.

Computational tools are used at many levels in the process of structural characterization via imaging. Certainly, a computer-driven data collection system is used during the collection of tomographic data, and a computer algorithm is used in the reconstruction process. Machine Learning algorithms are used widely in the process of image analysis, and a computer model may be used to simulate the experimental results for comparison with the observed images or the results from image analysis. Computation-driven processes of data collection, reduction and analysis improve the efficiency and accuracy of imaging techniques, including tomography.

References

[1] (2022). Plastics: Material-Specific Data.

[2] Abdur-Rashid, K., Clapham, S. E., Hadzovic, A., Harvey, J. N., Lough, A. J., & Morris, R. H. (2002). Mechanism of the hydrogenation of ketones catalyzed by trans-dihydrido(diamine)ruthenium(II) complexes. *Journal of the American Chemical Society*, 124(50), 15104–15118.

[3] Abrami, M., Chiarappa, G., Farra, R., Grassi, G., Marizza, P., & Grassi, M. (2018). Use of low field NMR for the characterization of gels and biological tissues. *ADMET and DMPK*, 6(1), 34–46.

[4] Abrami, M., D'Agostino, I., Milcovich, G., Fiorentino, S., Farra, R., Asaro, F., Lapasin, R., Grassi, G., & Grassi, M. (2014). Physical characterization of alginate-Pluronic F127 gel for endoluminal NABDs delivery. *Soft Matter*, 10(5), 729–737.

[5] Aduba, D. C. & Yang, H. (2017). Polysaccharide fabrication platforms and biocompatibility assessment as candidate wound dressing materials. *Bioengineering*, 4(1), 1–16.

[6] Alhamami, M., Doan, H., & Cheng, C. H. (2014). A review on breathing behaviors of metal-organic-frameworks (MOFs) for gas adsorption. *Materials*, 7(4), 3198–3250.

[7] Allgeier, A. M. & Sengupta, S. K. (2018). 5. Nitrile hydrogenation. In S. D. Jackson (Ed.), *Hydrogenation* (pp. 107–154). Berlin, Boston: De Gruyter.

[8] Almagor, E. & Belfort, G. (1978). Relaxation studies of adsorbed water on porous glass. *Journal of Colloid and Interface Science*, 66(1), 146–152.

[9] Amato-Lourenço, L. F., Carvalho-Oliveira, R., Júnior, G. R., dos Santos Galvão, L., Ando, R. A., & Mauad, T. (2021). Presence of airborne microplastics in human lung tissue. *Journal of Hazardous Materials*, 416(May).

[10] Amsden, B. (1998). Solute diffusion within hydrogels. Mechanisms and models. *Macromolecules*, 31(23), 8382–8395.

[11] Anastas, P. T. & Warner, J. C. (1998). Green Chemistry: Theory and Practice. *Green Chemistry: Theory and Practice, Oxford University Press, New York*.

[12] Anastas, P. T. & Zimmerman, J. B. (2007). Design through the 12 principles of green engineering. *IEEE Engineering Management Review*, 35(3), 16.

[13] Andrzejczuk, M., Roguska, A., Pisarek, M., Kdzierzawski, P., & Lewandowska, M. (2019). Effect of Pt Deposits on TiO2 Electrocatalytic Activity Highlighted by Electron Tomography. *ACS Applied Materials and Interfaces*, 11(20), 18841–18848.

[14] Arns, C. H. (2004). A comparison of pore size distributions derived by NMR and X-ray-CT techniques. *Physica A: Statistical Mechanics and its Applications*, 339(1-2), 159–165.

[15] Artioli, G., Cerulli, T., Cruciani, G., Dalconi, M. C., Ferrari, G., Parisatto, M., Rack, A., & Tucoulou, R. (2010). X-ray diffraction microtomography (XRD-CT), a novel tool for non-invasive mapping of phase development in cement materials. *Analytical and Bioanalytical Chemistry*, 397(6), 2131–2136.

[16] Bakhshian, S. & Sahimi, M. (2018). Theoretical Model and Numerical Simulation of Adsorption and Deformation in Flexible Metal-Organic Frameworks. *Journal of Physical Chemistry C*, 122(17), 9465–9473.

[17] Balwan, A. R. & Shinde, V. D. (2020). Development of patient specific knee joint implant. *Materials Today: Proceedings*, 27, 288–293.

[18] Banhart, J. (2008). *Advanced tomographic methods in materials research and engineering*, volume 66. OUP Oxford.

[19] Bastarrachea, L., Dhawan, S., & Sablani, S. S. (2011). Engineering Properties of Polymeric-Based Antimicrobial Films for Food Packaging. *Food Engineering Reviews*, 3(2), 79–93.

[20] Beatty, R. P. (1998). Homogeneous Catalytic Hydrogenation and Reductive Hydrolysis of Nitriles. In F. E. Herkes (Ed.), *Catalysis of Organic Reactions*, volume 75 (pp. 183). Marcel Dekker, Inc.

[21] Beatty, R. P. & Paciello, R. (1995). PROCESS FOR THE PREPARATION OF RUTHENIUM HYDROGENATION CATALYSTS AND PRODUCTS THEREOF.

[22] Behabtu, N. & Kralj, S. (2020). Enzymatic Polymerization Routes to Synthetic-Natural Materials: A Review. *ACS Sustainable Chemistry and Engineering*, 8(27), 9947–9954.

[23] Bennett, J. A., Campbell, Z. S., & Abolhasani, M. (2019). Role of continuous flow processes in green manufacturing of pharmaceuticals and specialty chemicals. *Current Opinion in Chemical Engineering*, 26, 9–19.

[24] Bérard, A., Blais, B., & Patience, G. S. (2020). Experimental methods in chemical engineering: Residence time distributionRTD. *The Canadian Journal of Chemical Engineering*, 98(4), 848–867.

[25] Bertoli, M., Choualeb, A., Lough, A. J., Moore, B., Spasyuk, D., & Gusev, D. G. (2011). Osmium and ruthenium catalysts for dehydrogenation of alcohols. *Organometallics*, 30(13), 3479–3482.

[26] Besghini, D., Mauri, M., & Simonutti, R. (2019). Time domain NMR in polymer science: From the laboratory to the industry. *Applied Sciences (Switzerland)*, 9(9).

[27] Bielinski, E. A., Lagaditis, P. O., Zhang, Y., Mercado, B. Q., Würtele, C., Bernskoetter, W. H., Hazari, N., & Schneider, S. (2014). Lewis acid-assisted formic acid dehydrogenation

using a pincer-supported iron catalyst. *Journal of the American Chemical Society*, 136(29), 10234–10237.

[28] Bloembergen, N. & Morgan, L. O. (1961). Proton Relaxation Times in Paramagnetic Solutions. Effects of Electron Spin Relaxation. *The Journal of Chemical Physics*, 34(3), 842–850.

[29] Blohm, S. & Heinze, T. (2019). Synthesis and properties of thermoplastic starch laurates. *Carbohydrate Research*, 486(October), 107833.

[30] Blohm, S. & Heinze, T. (2020). Mechanistic Considerations of Efficient Esterification of Starch with Propionic Anhydride/Lauric Acid in the Green Solvent Imidazole. *Macromolecular Chemistry and Physics*, 221(23), 2000264.

[31] Bonino, F., Lamberti, C., Chavan, S., Vitillo, J. G., & Bordiga*, S. (2013). Characterization of MOFs. 1. Combined Vibrational and Electronic Spectroscopies. In *Metal Organic Frameworks as Heterogeneous Catalysts* chapter 4, (pp. 76–142).

[32] Bordiga, S., Bonino, F., Lillerud, K. P., & Lamberti, C. (2010). X-ray absorption spectroscopies: useful tools to understand metallorganic frameworks structure and reactivity. *Chemical Society Reviews*, 39(12), 4885.

[33] Bornschein, C., Werkmeister, S., Wendt, B., Jiao, H., Alberico, E., Baumann, W., Junge, H., Junge, K., & Beller, M. (2014). Mild and selective hydrogenation of aromatic and aliphatic (di)nitriles with a well-defined iron pincer complex. *Nature Communications*, 5(May), 4111.

[34] Borys, A. (2022). The Schlenk Line Survival Guide.

[35] Brisard, S., Serdar, M., & Monteiro, P. J. (2020). Multiscale X-ray tomography of cementitious materials: A review. *Cement and Concrete Research*, 128(February 2019).

[36] Broom, D. (2018). Characterizing adsorbents for gas separations. *Chemical Engineering Progress*, 114(3), 30–37.

[37] Brown, R. J. S. & Gamson, B. W. (1960). Nuclear magnetism logging. *Transactions of the AIME*, 219(01), 201–209.

[38] Brownstein, K. & Tarr, C. (1977). Spin-lattice relaxation in a system governed by diffusion. *Journal of Magnetic Resonance (1969)*, 26(1), 17–24.

[39] Brownstein, K. R. & Tarr, C. E. (1979). Importance of classical diffusion in NMR studies of water in biological cells. *Physical Review A*, 19(6), 2446–2453.

[40] Bruker (2014a). Data Collection: SMART Software in APEX2 v2014.11-0 Suite. Bruker-AXS, 5465 E. Cheryl Parkway, Madison, WI 53711-5373 USA.

[41] Bruker (2014b). Data Reduction: SAINT Software in APEX2 v2014.11-0 Suite. Bruker-AXS, 5465 E. Cheryl Parkway, Madison, WI 53711-5373 USA.

[42] Bruker (2014c). Refinement: SHELXTL Software in APEX2 v2014.11-0 Suite. Bruker-AXS, 5465 E. Cheryl Parkway, Madison, WI 53711-5373 USA.

[43] Brunner, E. (1979). Solubility of Hydrogen in Alcohols. *Berichte der Bunsengesellschaft/-Physical Chemistry Chemical Physics*, 83(7), 715–721.

[44] Brunner, E. (1985). Solubility of Hydrogen in 10 Organic Solvents at 298.15, 323.15, and 373.15 K. *Journal of Chemical and Engineering Data*, 30(3), 269–273.

[45] Bryar, T. R., Daughney, C. J., & Knight, R. J. (2000). Paramagnetic Effects of Iron(III) Species on Nuclear Magnetic Relaxation of Fluid Protons in Porous Media. *Journal of Magnetic Resonance*, 142(1), 74–85.

[46] Bystrzanowska, M., Petkov, P., & Tobiszewski, M. (2019). Ranking of Heterogeneous Catalysts Metals by Their Greenness. *ACS Sustainable Chemistry and Engineering*, 7(22), 18434–18443.

[47] Carey, J. S., Laffan, D., Thomson, C., & Williams, M. T. (2006). Analysis of the reactions used for the preparation of drug candidate molecules. *Organic and Biomolecular Chemistry*, 4(12), 2337–2347.

[48] Chakraborty, S., Brennessel, W. W., & Jones, W. D. (2014a). A Molecular Iron Catalyst for the Acceptorless Dehydrogenation and Hydrogenation of N-Heterocycles. *Journal of the American Chemical Society*, 136(24), 8564–8567.

[49] Chakraborty, S., Dai, H., Bhattacharya, P., Fairweather, N. T., Gibson, M. S., Krause, J. A., & Guan, H. (2014b). Iron-Based Catalysts for the Hydrogenation of Esters to Alcohols. *Journal of the American Chemical Society*, 136(22), 7869–7872.

[50] Chakraborty, S., Lagaditis, P. O., Förster, M., Bielinski, E. A., Hazari, N., Holthausen, M. C., Jones, W. D., & Schneider, S. (2014c). Well-defined iron catalysts for the acceptorless reversible dehydrogenation-hydrogenation of alcohols and ketones. *ACS Catalysis*, 4(11), 3994–4003.

[51] Chakraborty, S., Leitus, G., & Milstein, D. (2016). Selective hydrogenation of nitriles to primary amines catalyzed by a novel iron complex. *Chemical Communications*, 52(9), 1812–1815.

[52] Chakraborty, S. & Milstein, D. (2017). Selective Hydrogenation of Nitriles to Secondary Imines Catalyzed by an Iron Pincer Complex. *ACS Catalysis*, 7(6), 3968–3972.

[53] Chandra, T. & Zebrowski, J. P. (2014). Reactivity control using a Schlenk line. *Journal of Chemical Health and Safety*, 21(3), 22–28.

[54] Chandra, T., Zebrowski, J. P., & Lenertz, L. Y. (2022). Safe Handling of Cannulas and Needles in Chemistry Laboratories. *ACS Chemical Health & Safety*, 29(2), 175–183.

[55] Chaudhari, R. V., Gholap, R. V., Emig, G., & Hofmann, H. (1987). Gas-liquid mass transfer in dead-end autoclave reactors. *The Canadian Journal of Chemical Engineering*, 65(5), 744–751.

[56] Chmelik, C. & Kärger, J. (2010). In situ study on molecular diffusion phenomena in nanoporous catalytic solids. *Chemical Society Reviews*, 39(12), 4864.

[57] Chou, C. H., Chu, L. T., Chiu, S. J., Lee, C. F., & She, Y. T. (2004). Synthesis of N,N-di(arylmethylidene)arylmethanediamines by flash vacuum pyrolysis of arylmethylazides. *Tetrahedron*, 60(31), 6581–6584.

[58] Chowdhury, M. A., Hill, D. J., & Whittaker, A. K. (2004). NMR imaging of the diffusion of water at 37 °C into poly(2-hydroxyethyl) methacrylate) containing aspirin or vitamin B12. *Biomacromolecules*, 5(3), 971–976.

[59] Christopher Roe, D. (1985). Sapphire NMR tube for high-resolution studies at elevated pressure. *Journal of Magnetic Resonance (1969)*, 63(2), 388–391.

[60] Chui, M. M., Phillips, R. J., & McCarthy, M. J. (1995). Measurement of the porous microstructure of hydrogels by nuclear magnetic resonance.

[61] Ciriminna, R. & Pagliaro, M. (2020). Biodegradable and Compostable Plastics: A Critical Perspective on the Dawn of their Global Adoption. *ChemistryOpen*, 9(1), 8–13.

[62] Coates, G. R., Xiao, L., & Prammer, M. G. (1999). *NMR logging: principles and applications*, volume 234. Haliburton Energy Services Houston.

[63] Cooper, C. L., Cosgrove, T., Van Duijneveldt, J. S., Murray, M., & Prescott, S. W. (2013). The use of solvent relaxation NMR to study colloidal suspensions. *Soft Matter*, 9(30), 7211–7228.

[64] Coq, B., Tichit, D., & Ribet, S. (2000). Co/Ni/Mg/Al Layered Double Hydroxides as Precursors of Catalysts for the Hydrogenation of Nitriles: Hydrogenation of Acetonitrile. *Journal of Catalysis*, 189(1), 117–128.

[65] Cserháti, T., Forgács, E., & Oros, G. (2002). Biological activity and environmental impact of anionic surfactants. *Environment International*, 28, 337–348.

[66] Daedalus (2020). Daedalus Innovations High Pressure NMR.

[67] D'Agostino, C., Kotionova, T., Mitchell, J., Miedziak, P. J., Knight, D. W., Taylor, S. H., Hutchings, G. J., Gladden, L. F., & Mantle, M. D. (2013). Solvent Effect and Reactivity Trend in the Aerobic Oxidation of 1,3-Propanediols over Gold Supported on Titania: NMR Diffusion and Relaxation Studies. *Chemistry - A European Journal*, 19(35), 11725–11732.

[68] Dai, H. & Guan, H. (2018). Switching the Selectivity of Cobalt-Catalyzed Hydrogenation of Nitriles. *ACS Catalysis*, 8(10), 9125–9130.

[69] Danieli, E., Mauler, J., Perlo, J., Blümich, B., & Casanova, F. (2009). Mobile sensor for high resolution NMR spectroscopy and imaging. *Journal of Magnetic Resonance*, 198(1), 80–87.

[70] Das Sharma, S., Hazarika, P., & Konwar, D. (2008). An efficient and one-pot synthesis of 2,4,5-trisubstituted and 1,2,4,5-tetrasubstituted imidazoles catalyzed by InCl3·3H2O. *Tetrahedron Letters*, 49(14), 2216–2220.

[71] Davis, C. M. & Curran, K. A. (2007). Manipulation of a Schlenk line: Preparation of tetrahydrofuran complexes of transition-metal chlorides. *Journal of Chemical Education*, 84(11), 1822–1823.

[72] Davis, P. J., Jeffrey Brinker, C., & Smith, D. M. (1992a). Pore structure evolution in silica gel during aging/drying I. Temporal and thermal aging. *Journal of Non-Crystalline Solids*, 142, 189–196.

[73] Davis, P. J., Jeffrey Brinker, C., Smith, D. M., & Assink, R. A. (1992b). Pore structure evolution in silica gel during aging/drying II. Effect of pore fluids. *Journal of Non-Crystalline Solids*, 142, 197–207.

[74] De, S., Malik, S., Ghosh, A., Saha, R., & Saha, B. (2015). A review on natural surfactants. *RSC Advances*, 5(81), 65757–65767.

[75] De'Nobili, M. D., Rojas, A. M., Abrami, M., Lapasin, R., & Grassi, M. (2015). Structure characterization by means of rheological and NMR experiments as a first necessary approach to study the l-(+)-ascorbic acid diffusion from pectin and pectin/alginate films to agar hydrogels that mimic food materials. *Journal of Food Engineering*, 165, 82–92.

[76] Deria, P., Gómez-Gualdrón, D. A., Bury, W., Schaef, H. T., Wang, T. C., Thallapally, P. K., Sarjeant, A. A., Snurr, R. Q., Hupp, J. T., & Farha, O. K. (2015). Ultraporous, water stable, and breathing zirconium-based metal-organic frameworks with ftw topology. *Journal of the American Chemical Society*, 137(40), 13183–13190.

[77] Di Bartolo, A., Infurna, G., & Dintcheva, N. T. (2021). A review of bioplastics and their adoption in the circular economy. *Polymers*, 13(8).

[78] Drago, R. S. (1992). *Physical methods for chemists*. New York: Harcourt Brace Jovanovich.

[79] Du Pisani, J. A. (2006). Sustainable Development Historical Roots of the Concept. *Environmental Sciences*, 3(2), 83–96.

[80] Dunn, K.-J., Bergman, D., & Latorraca, G. (2002). NMR data acquisition and inversion. In *Nuclear magnetic resonance petrophysical and logging applications* chapter 6, (pp. 165–196).

[81] DOrazio, F., Tarczon, J., Halperin, W. P., Eguchi, K., & Mizusaki, T. (1989). Application of nuclear magnetic resonance pore structure analysis to porous silica glass. *Journal of Applied Physics*, 65(2), 742–751.

[82] E. Gullikson (2022). X-ray Interactions With Matter.

[83] Elangovan, S., Topf, C., Fischer, S., Jiao, H., Spannenberg, A., Baumann, W., Ludwig, R., Junge, K., & Beller, M. (2016). Selective Catalytic Hydrogenations of Nitriles, Ketones, and Aldehydes by Well-Defined Manganese Pincer Complexes. *Journal of the American Chemical Society*, 138(28), 8809–8814.

[84] Evans, T. M., Bira, L., Gastelum, J. B., Weiss, L. T., & Vanderford, N. L. (2018). Evidence for a mental health crisis in graduate education. *Nature Biotechnology*, 36(3), 282–284.

[85] Fairhurst, D., Cosgrove, T., & Prescott, S. W. (2016). Relaxation NMR as a tool to study the dispersion and formulation behavior of nanostructured carbon materials. *Magnetic Resonance in Chemistry*, 54(6), 521–526.

[86] Fan, F., Feng, Z., & Li, C. (2010). UV Raman spectroscopic study on the synthesis mechanism and assembly of molecular sieves. *Chemical Society Reviews*, 39(12), 4794.

[87] Faux, D. A., Cachia, S.-H. P., McDonald, P. J., Bhatt, J. S., Howlett, N. C., & Churakov, S. V. (2015). Model for the interpretation of nuclear magnetic resonance relaxometry of hydrated porous silicate materials. *Physical Review E*, 91(3), 032311.

[88] Foley, I., Farooqui, S., & Kleinberg, R. (1996). Effect of Paramagnetic Ions on NMR Relaxation of Fluids at Solid Surfaces. *Journal of Magnetic Resonance, Series A*, 123(1), 95–104.

[89] Foster, A. J. & Lobo, R. F. (2010). Identifying reaction intermediates and catalytic active sites through in situ characterization techniques. *Chemical Society Reviews*, 39(12), 4783.

[90] Gallegos, D. P. & Smith, D. M. (1988). A NMR technique for the analysis of pore structure: Determination of continuous pore size distributions. *Journal of Colloid And Interface Science*, 122(1), 143–153.

[91] Gallegos, D. P., Smith, D. M., & Brinker, C. (1988). An NMR technique for the analysis of pore structure: Application to mesopores and micropores. *Journal of Colloid and Interface Science*, 124(1), 186–198.

[92] Garduño, J. A. & García, J. J. (2019). Non-Pincer Mn(I) Organometallics for the Selective Catalytic Hydrogenation of Nitriles to Primary Amines. *ACS Catalysis*, 9(1), 392–401.

[93] Gavriilidis, A., Constantinou, A., Hellgardt, K., Hii, K. K. M., Hutchings, G. J., Brett, G. L., Kuhn, S., & Marsden, S. P. (2016). Aerobic oxidations in flow: Opportunities for the fine

chemicals and pharmaceuticals industries. *Reaction Chemistry and Engineering*, 1(6), 595–612.

[94] Geitel, K., Koschella, A., Lenges, C., & Heinze, T. (2020). Meltable fatty acid esters of α-1,3-glucan as potential thermoplastics. *Advanced Industrial and Engineering Polymer Research*, 3(3), 111–119.

[95] Genoux, A., González, J. A., Merino, E., & Nevado, C. (2020). Mechanistic Insights into C(sp2)C(sp)N Reductive Elimination from Gold(III) Cyanide Complexes. *Angewandte Chemie - International Edition*, 59(41), 17881–17886.

[96] Georgieva, V. M., Bruce, E. L., Verbraeken, M. C., Scott, A. R., Casteel, W. J., Brandani, S., & Wright, P. A. (2019). Triggered Gate Opening and Breathing Effects during Selective CO2 Adsorption by Merlinoite Zeolite. *Journal of the American Chemical Society*, 141(32), 12744–12759.

[97] Ghi, P. Y., Hill, D. J., & Whittaker, A. K. (2002a). 1H NMR study of the states of water in equilibrium poly(HEMA-co-THFMA) hydrogels. *Biomacromolecules*, 3(5), 991–997.

[98] Ghi, P. Y., Hill, D. J., & Whittaker, A. K. (2002b). PFG-NMR measurements of the self-diffusion coefficients of water in equilibrium poly(HEMA-co-THFMA) hydrogels. *Biomacromolecules*, 3(3), 554–559.

[99] Giacomin, C. E., Kim, K., & Wagner, N. J. (2022). Rheological Behavior for α-1,3-Glucan Derived from Enzymatic Polymerization of Sucrose. *ACS Food Science and Technology*, 2(2), 240–248.

[100] Gomollon-Bel, F. (2021). A free online guide to master Schlenk lines.

[101] Gross, D., Zick, K., Oerther, T., Lehmann, V., Pampel, A., & Goetz, J. (2006). Hardware and Methods. In *NMR Imaging in Chemical Engineering* (pp. 47–77). Weinheim, FRG: Wiley-VCH Verlag GmbH & Co. KGaA.

[102] Guo, J., Xie, R., Zou, Y., Jin, G., Gao, L., & Xu, C. (2018). A new method for NMR data inversion based on double-parameter regularization. *GEOPHYSICS*, 83(5), JM39–JM49.

[103] Harders, A. N., Sturd, E. R., Vallier, J. E., Corbin, D. R., White, W. R., Junk, C. P., & Shiflett, M. B. (2022). Selective separation of HFC-32 from R-410A using poly(dimethylsiloxane) and a copolymer of perfluoro(butenyl vinyl ether) and perfluoro(2,2-dimethyl-1,3-dioxole). *Journal of Membrane Science*, 652(December 2021), 120467.

[104] Hasiuk, F. (2022). Kansas Geological Survey receives grant to study critical minerals mining potential in region | The University of Kansas.

[105] Heinze, T., Pfeifer, A., Koschella, A., Adelman, D., Howe, L., Behabtu, N., & Lenges, C. (2019). Engineered Polysaccharides: α-1,3-Glucan Acetates Showing Upper Critical Solution Temperature in Organic Solvents. *Macromolecular Chemistry and Physics*, 220(16).

[106] Hinz, D. C. (2006). Process analytical technologies in the pharmaceutical industry: The FDA's PAT initiative. *Analytical and Bioanalytical Chemistry*, 384(5), 1036–1042.

[107] Horch, C., Schlayer, S., & Stallmach, F. (2014). High-pressure low-field 1H NMR relaxometry in nanoporous materials. *Journal of Magnetic Resonance*, 240, 24–33.

[108] Hubbell, J. H. (2020). X-ray Mass Attenuation Coefficients.

[109] Huo, R. P., Zhang, X., Zhang, C. F., Qin, H. H., & Wang, R. X. (2021). A theoretical investigation of iron-catalyzed selective hydrogenation of nitriles to secondary imines. *Chemical Physics Letters*, 762(July 2020), 138130.

[110] Ivanova, I. I. & Kolyagin, Y. G. (2010). Impact of in situ MAS NMR techniques to the understanding of the mechanisms of zeolite catalyzed reactions. *Chemical Society Reviews*, 39(12), 5018.

[111] Jacques, S. D. M., Di Michiel, M., Beale, A. M., Sochi, T., O'Brien, M. G., Espinosa-Alonso, L., Weckhuysen, B. M., & Barnes, P. (2011). Dynamic X-Ray Diffraction Computed

Tomography Reveals Real-Time Insight into Catalyst Active Phase Evolution. *Angewandte Chemie International Edition*, 50(43), 10148–10152.

[112] Jelsch, M., Roggo, Y., Kleinebudde, P., & Krumme, M. (2021). Model predictive control in pharmaceutical continuous manufacturing: A review from a user's perspective. *European Journal of Pharmaceutics and Biopharmaceutics*, 159, 137–142.

[113] Johansen, M. B., Kondrup, J. C., Hinge, M., & Lindhardt, A. T. (2018). Improved Safety during Transfer of Pyrophoric tert-Butyllithium from Flasks with Protective Seals. *Organic Process Research and Development*, 22(7), 903–905.

[114] Kak, A. C. & Slaney, M. (1988). Principles of computerized tomographic imaging.

[115] Kang, B., Tang, H., Zhao, Z., & Song, S. (2020). Hofmeister Series: Insights of Ion Specificity from Amphiphilic Assembly and Interface Property. *ACS Omega*, 5(12), 6229–6239.

[116] Kang, J. G. (2014). *Schlenk Line Standard Operating Procedure*. Technical report.

[117] Kärger, J., Stallmach, F., Valiullin, R., & Vasenkov, S. (2006). Porous Materials. In *NMR Imaging in Chemical Engineering* (pp. 231–250). Weinheim, FRG: Wiley-VCH Verlag GmbH & Co. KGaA.

[118] Keating, K. (2014). A laboratory study to determine the effect of surface area and bead diameter on NMR relaxation rates of glass bead packs. *Near Surface Geophysics*, 12(2), 243–254.

[119] Keating, K. & Knight, R. (2010). A laboratory study of the effect of Fe(II)-bearing minerals on nuclear magnetic resonance (NMR) relaxation measurements. *GEOPHYSICS*, 75(3), F71–F82.

[120] Kemerink, M., Dierichs, T. J., Dierichs, J., Huynen, H. J., Wildberger, J. E., van Engelshoven, J. M. A., & Kemerink, G. J. (2011). Characteristics of a First-Generation X-Ray System. *Radiology*, 259(2), 534–539.

[121] Kimmich, R. (1997). Homonuclear Localized NMR. In *NMR* (pp. 340–359).: Springer.

[122] Kinn, B. E., Myers, T. R., & Allgeier, A. M. (2019). Surface enhanced nuclear magnetic resonance relaxation mechanisms and their significance in chemical engineering applications. *Current Opinion in Chemical Engineering*, 24, 115–121.

[123] Kleinberg, R. & Horsfield, M. (1990). Transverse relaxation processes in porous sedimentary rock. *Journal of Magnetic Resonance (1969)*, 88(1), 9–19.

[124] Kleinberg, R., Kenyon, W., & Mitra, P. (1994). Mechanism of NMR Relaxation of Fluids in Rock. *Journal of Magnetic Resonance, Series A*, 108(2), 206–214.

[125] Koehne, I., Schmeier, T. J., Bielinski, E. A., Pan, C. J., Lagaditis, P. O., Bernskoetter, W. H., Takase, M. K., Würtele, C., Hazari, N., & Schneider, S. (2014). Synthesis and structure of six-coordinate iron borohydride complexes supported by PNP ligands. *Inorganic Chemistry*, 53(4), 2133–2143.

[126] Kogawa, A. C., Cernic, B. G., do Couto, L. G. D., & Salgado, H. R. N. (2017). Synthetic detergents: 100 years of history. *Saudi Pharmaceutical Journal*, 25(6), 934–938.

[127] Koneti, S., Roiban, L., Dalmas, F., Langlois, C., Gay, A. S., Cabiac, A., Grenier, T., Banjak, H., Maxim, V., & Epicier, T. (2019). Fast electron tomography: Applications to beam sensitive samples and in situ TEM or operando environmental TEM studies. *Materials Characterization*, 151(February), 480–495.

[128] Korb, J.-P. (2011). Nuclear magnetic relaxation of liquids in porous media. *New Journal of Physics*, 13(3), 035016.

[129] Korb, J. P., Whaley-Hodges, M., & Bryant, R. G. (1997). Translational diffusion of liquids at surfaces of microporous materials: Theoretical analysis of field-cycling magnetic relaxation measurements. *Physical Review E - Statistical Physics, Plasmas, Fluids, and Related Interdisciplinary Topics*, 56(2), 1934–1945.

[130] Korb, J. P., Xu, S., & Jonas, J. (1993). Confinement effects on dipolar relaxation by translational dynamics of liquids in porous silica glasses. *The Journal of Chemical Physics*, 98(3), 2411–2422.

[131] Korringa, J., Seevers, D. O., & Torrey, H. C. (1962). Theory of Spin Pumping and Relaxation in Systems with a Low Concentration of Electron Spin Resonance Centers. *Physical Review*, 127(4), 1143–1150.

[132] Krooss, B. M., Van Bergen, F., Gensterblum, Y., Siemons, N., Pagnier, H. J., & David, P. (2002). High-pressure methane and carbon dioxide adsorption on dry and moisture-equilibrated Pennsylvanian coals. *International Journal of Coal Geology*, 51(2), 69–92.

[133] Kuhlman, T. & Farrington, J. (2010). What is sustainability? *Sustainability*, 2(11), 3436–3448.

[134] Laboratories, H. (2018). Green Imaging Technologies P5 Cell.

[135] Lange, S., Elangovan, S., Cordes, C., Spannenberg, A., Jiao, H., Junge, H., Bachmann, S., Scalone, M., Topf, C., Junge, K., & Beller, M. (2016). Selective catalytic hydrogenation of nitriles to primary amines using iron pincer complexes. *Catalysis Science & Technology*, 6(13), 4768–4772.

[136] Langin, K. (2022). Ph.D. students demand wage increases amid rising cost of living. *Science*.

[137] Leonard, E., Shum, A. D., Normile, S., Sabarirajan, D. C., Yared, D. G., Xiao, X., & Zenyuk, I. V. (2018). Operando X-ray tomography and sub-second radiography for characterizing transport in polymer electrolyte membrane electrolyzer. *Electrochimica Acta*, 276, 424–433.

[138] Li, T., Bergner, I., Haque, F. N., Iuliis, M. Z. D., Song, D., & Morris, R. H. (2007). Hydrogenation of benzonitrile to benzylamine catalyzed by ruthenium hydride complexes with

P-NH-NH-P tetradentate ligands: Evidence for a hydridic-protonic outer sphere mechanism. *Organometallics*, 26(24), 5940–5949.

[139] Liu, G., Li, Y., & Jonas, J. (1991). Confined geometry effects on reorientational dynamics of molecular liquids in porous silica glasses. *The Journal of Chemical Physics*, 95(9), 6892–6901.

[140] Llewellyn, P. L., Bloch, E., & Bourrelly, S. (2012). Surface Area/Porosity, Adsorption, Diffusion. In *Characterization of Solid Materials and Heterogeneous Catalysts* chapter 19, (pp. 853–879). Wiley.

[141] Lowell, S., Shields, J. E., Thomas, M. A., & Thommes, M. (2004). Pore Size and Surface Characteristics of Porous Solids by Mercury Porosimetry. In *Characterization of Porous Solids and Powders: Surface Area, Pore Size and Density* chapter 11, (pp. 189–212). Dordrecht: Springer Netherlands.

[142] Lozinska, M. M., Mangano, E., Mowat, J. P., Shepherd, A. M., Howe, R. F., Thompson, S. P., Parker, J. E., Brandani, S., & Wright, P. A. (2012). Understanding carbon dioxide adsorption on univalent cation forms of the flexible zeolite Rho at conditions relevant to carbon capture from flue gases. *Journal of the American Chemical Society*, 134(42), 17628–17642.

[143] Lozinska, M. M., Mowat, J. P., Wright, P. A., Thompson, S. P., Jorda, J. L., Palomino, M., Valencia, S., & Rey, F. (2014). Cation gating and relocation during the highly selective "trapdoor" adsorption of CO2 on univalent cation forms of zeolite Rho. *Chemistry of Materials*, 26(6), 2052–2061.

[144] Lucas-Oliveira, E., Araujo-Ferreira, A. G., Trevizan, W. A., Fortulan, C. A., & Bonagamba, T. J. (2018). Computational approach to integrate 3D X-ray microtomography and NMR data. *Journal of Magnetic Resonance*, 292, 16–24.

[145] Lundin, M., Bengtsson, M., & Molander, S. (2000). Life cycle assessment of wastewater systems: Influence of system boundaries and scale on calculated environmental loads. *Environmental Science and Technology*, 34(1), 180–186.

[146] Maharjan, A. (2018). *Hydrogel with Selective Absorption for Separation of Liquid Mixtures*. PhD thesis, University of Kansas.

[147] Mallia, C. J. & Baxendale, I. R. (2016). The Use of Gases in Flow Synthesis. *Organic Process Research & Development*, 20(2), 327–360.

[148] Manzi-Orezzoli, V., Mularczyk, A., Trtik, P., Halter, J., Eller, J., Schmidt, T. J., & Boillat, P. (2019). Coating Distribution Analysis on Gas Diffusion Layers for Polymer Electrolyte Fuel Cells by Neutron and X-ray High-Resolution Tomography. *ACS Omega*, 4(17), 17236–17243.

[149] Marizza, P., Abrami, M., Keller, S. S., Posocco, P., Laurini, E., Goswami, K., Skov, A. L., Boisen, A., Larobina, D., Grassi, G., & Grassi, M. (2016). Synthesis and characterization of UV photocrosslinkable hydrogels with poly(N-vinyl-2-pyrrolidone): Determination of the network mesh size distribution. *International Journal of Polymeric Materials and Polymeric Biomaterials*, 65(10), 516–525.

[150] McAdam, B., Fournet, M. B., McDonald, P., & Mojicevic, M. (2020). Production of polyhydroxybutyrate (PHB) and factors impacting its chemical and mechanical characteristics. *Polymers*, 12(12), 1–20.

[151] Mendes, A. C. & Pedersen, G. A. (2021). Perspectives on sustainable food packaging: is bio-based plastics a solution? *Trends in Food Science and Technology*, 112(April), 839–846.

[152] Meunier, F. C. (2010). The design and testing of kinetically-appropriate operando spectroscopic cells for investigating heterogeneous catalytic reactions. *Chemical Society Reviews*, 39(12), 4602.

[153] Mitchell, J. (2016). Industrial applications of magnetic resonance diffusion and relaxation time measurements. In *Diffusion NMR of Confined Systems* chapter 11, (pp. 353–389).

[154] Mitchell, J., Broche, L. M., Chandrasekera, T. C., Lurie, D. J., & Gladden, L. F. (2013).

Exploring surface interactions in catalysts using low-field nuclear magnetic resonance. *Journal of Physical Chemistry C*, 117(34), 17699–17706.

[155] Mitchell, J., Gladden, L. F., Chandrasekera, T. C., & Fordham, E. J. (2014). Low-field permanent magnets for industrial process and quality control. *Progress in Nuclear Magnetic Resonance Spectroscopy*, 76, 1–60.

[156] Monteith, E. R., Mampuys, P., Summerton, L., Clark, J. H., Maes, B. U., & McElroy, C. R. (2020). Why we might be misusing process mass intensity (PMI) and a methodology to apply it effectively as a discovery level metric. *Green Chemistry*, 22(1), 123–135.

[157] Moura, M. J., Ferreira, P. J., & Figueiredo, M. M. (2005). Mercury intrusion porosimetry in pulp and paper technology. *Powder Technology*, 160(2), 61–66.

[158] Mourdikoudis, S., Montes-García, V., Rodal-Cedeira, S., Winckelmans, N., Pérez-Juste, I., Wu, H., Bals, S., Pérez-Juste, J., & Pastoriza-Santos, I. (2019). Highly porous palladium nanodendrites: Wet-chemical synthesis, electron tomography and catalytic activity. *Dalton Transactions*, 48(11), 3758–3767.

[159] Mousavi, S. A. & Khodadoost, F. (2019). Effects of detergents on natural ecosystems and wastewater treatment processes: a review. *Environmental Science and Pollution Research*, 26(26), 26439–26448.

[160] Mueller, K. & Yagel, R. (2000). Rapid 3-D cone-beam reconstruction with the simultaneous algebraic reconstruction technique (SART) using 2-D texture mapping hardware. *IEEE Transactions on Medical Imaging*, 19(12), 1227–1237.

[161] Mukherjee, A., Srimani, D., Chakraborty, S., Ben-David, Y., & Milstein, D. (2015). Selective Hydrogenation of Nitriles to Primary Amines Catalyzed by a Cobalt Pincer Complex. *Journal of the American Chemical Society*, 137(28), 8888–8891.

[162] Munn, K. & Smith, D. M. (1987). A NMR technique for the analysis of pore structure: Numerical inversion of relaxation measurements. *Journal of Colloid And Interface Science*, 119(1), 117–126.

[163] Narancic, T., Verstichel, S., Reddy Chaganti, S., Morales-Gamez, L., Kenny, S. T., De Wilde, B., Babu Padamati, R., & O'Connor, K. E. (2018). Biodegradable Plastic Blends Create New Possibilities for End-of-Life Management of Plastics but They Are Not a Panacea for Plastic Pollution. *Environmental Science and Technology*, 52(18), 10441–10452.

[164] Neimark, A. V., Coudert, F. X., Boutin, A., & Fuchs, A. H. (2010). Stress-based model for the breathing of metal-organic frameworks. *Journal of Physical Chemistry Letters*, 1(1), 445–449.

[165] Neimark, A. V., Coudert, F. X., Triguero, C., Boutin, A., Fuchs, A. H., Beurroies, I., & Denoyel, R. (2011). Structural transitions in MIL-53 (Cr): View from outside and inside. *Langmuir*, 27(8), 4734–4741.

[166] Neugebauer, A., Chen, K., Tang, A., Allgeier, A., Glicksman, L., & Gibson, L. (2014). Thermal conductivity and characterization of compacted, granular silica aerogel. *Energy and Buildings*, 79, 47–57.

[167] Newton, M. A. & van Beek, W. (2010). Combining synchrotron-based X-ray techniques with vibrational spectroscopies for the in situ study of heterogeneous catalysts: a view from a bridge. *Chemical Society Reviews*, 39(12), 4845.

[168] Nicotera, I., Kosma, V., Simari, C., DUrso, C., Aricò, A. S., & Baglio, V. (2015). Methanol and proton transport in layered double hydroxide and smectite clay-based composites: influence on the electrochemical behavior of direct methanol fuel cells at intermediate temperatures. *Journal of Solid State Electrochemistry*, 19(7), 2053–2061.

[169] Nieves-Remacha, M. J., Kulkarni, A. A., & Jensen, K. F. (2013). Gas-liquid flow and mass

transfer in an advanced-flow reactor. *Industrial and Engineering Chemistry Research*, 52(26), 8996–9010.

[170] Nithin Kumar, K. C., Griya, N., Shaikh, A., Chaudhry, V., & Chavadaki, S. (2019). Structural analysis of femur bone to predict the suitable alternative material. *Materials Today: Proceedings*, 26, 364–368.

[171] NMR, R. (2022). Revolution NMR Products.

[172] Nuss, P. & Eckelman, M. J. (2014). Life Cycle Assessment of Metals: A Scientific Synthesis. *PLoS ONE*, 9(7), e101298.

[173] O'Brien, M. G., Jacques, S. D., Di Michiel, M., Barnes, P., Weckhuysen, B. M., & Beale, A. M. (2012). Active phase evolution in single Ni/Al 2O 3 methanation catalyst bodies studied in real time using combined μ-XRD-CT and μ-absorption-CT. *Chemical Science*, 3(2), 509–523.

[174] Olson, S. & Merrill, S. (2011). Impacts on the U.S. Economy and Quality of Life. In *Measuring Economic and Other Returns on Federal Research* chapter 3. Washington: The National Academies Press.

[175] Ortega-Toro, R., Collazo-Bigliardi, S., Talens Oliag, P., & Chiralt Boix, M. (2016). Thermoplastic Starch: Improving their Barrier Properties. *Agronomía Colombiana*, 34(1Supl.), S73–S75.

[176] Palomino, M., Corma, A., Jordà, J. L., Rey, F., & Valencia, S. (2012). Zeolite Rho: A highly selective adsorbent for CO2/CH4 separation induced by a structural phase modification. *Chemical Communications*, 48(2), 215–217.

[177] Pang, W. M., Qin, J., Lu, Y., Xie, Y., Chui, C. K., & Heng, P. A. (2011). Accelerating simultaneous algebraic reconstruction technique with motion compensation using CUDA-enabled GPU. *International Journal of Computer Assisted Radiology and Surgery*, 6(2), 187–199.

[178] Parent, L. R., Pham, C. H., Patterson, J. P., Denny, M. S., Cohen, S. M., Gianneschi, N. C., & Paesani, F. (2017). Pore Breathing of MetalOrganic Frameworks by Environmental Transmission Electron Microscopy. *Journal of the American Chemical Society*, 139(40), 13973–13976.

[179] Parise, J. B., Abrams, L., Gier, T. E., Corbin, D. R., Jorgensen, J. D., & Prince, E. (1984). Flexibility of the framework of zeolite Rho. Structural variation from 11 to 573 K. A study using neutron powder diffraction data. *Journal of Physical Chemistry*, 88(11), 2303–2307.

[180] Paruthi, A. & Misra, S. K. (2017). Relaxation time: a proton NMR-based approach as a metric to measure reactivity of engineered nanomaterials. *Journal of Nanoparticle Research*, 19(8), 292.

[181] Payne, M. S., Brun, Y., He, H., & Scholz, T. (2014). GLUCOSYLTRANSFERASE ENZYMES FOR PRODUCTION OF GLUCAN POLYMERS.

[182] Perepukhov, A., Kishenkov, O., Maximychev, A., Gudenko, S., Menshikov, L., & Alexandrov, D. (2015). Paramagnetic mechanism of NMR relaxation of fluids in silicates. *Microporous and Mesoporous Materials*, 205, 7–10.

[183] Pham, J., Jarczyk, C. E., Reynolds, E. F., Kelly, S. E., Kim, T., He, T., Keith, J. M., & Chianese, A. R. (2021). The key role of the latent N-H group in Milstein's catalyst for ester hydrogenation. *Chemical Science*, 12(24), 8477–8492.

[184] Piccinno, F., Hischier, R., Seeger, S., & Som, C. (2016). From laboratory to industrial scale: a scale-up framework for chemical processes in life cycle assessment studies. *Journal of Cleaner Production*, 135, 1085–1097.

[185] Porfyris, A., Papaspyrides, C. D., Behabtu, N., Lenges, C., & Kopatsis, A. (2021). High-solids, solvent-free modification of engineered polysaccharides. *Molecules*, 26(13).

[186] Prange, M. & Song, Y. Q. (2010). Understanding NMR T2 spectral uncertainty. *Journal of Magnetic Resonance*, 204(1), 118–123.

[187] Pratx, G. & Xing, L. (2011). GPU computing in medical physics: A review. *Medical Physics*, 38(5), 2685–2697.

[188] Puanglek, S., Kimura, S., Enomoto-Rogers, Y., Kabe, T., Yoshida, M., Wada, M., & Iwata, T. (2016). In vitro synthesis of linear α-1,3-glucan and chemical modification to ester derivatives exhibiting outstanding thermal properties. *Scientific Reports*, 6(January), 1–8.

[189] Puanglek, S., Kimura, S., & Iwata, T. (2017). Thermal and mechanical properties of tailor-made unbranched α-1,3-glucan esters with various carboxylic acid chain length. *Carbohydrate Polymers*, 169, 245–254.

[190] Radon, J. (1917). Uber die Bestimmung von Funktionen durch ihre Integralwerte langs gewisser Mannigfaltigkeiten, Berichte Verhandlunger Gesellschaft Wissenschaft. *Math.-Phys. Klasse*, 69, 262–271.

[191] Ragusa, A., Svelato, A., Santacroce, C., Catalano, P., Notarstefano, V., Carnevali, O., Papa, F., Rongioletti, M. C. A., Baiocco, F., Draghi, S., D'Amore, E., Rinaldo, D., Matta, M., & Giorgini, E. (2021). Plasticenta: First evidence of microplastics in human placenta. *Environment International*, 146, 106274.

[192] Ramezani, M., Kashfipour, M. A., & Abolhasani, M. (2020). Minireview: Flow chemistry studies of high-pressure gas-liquid reactions with carbon monoxide and hydrogen. *Journal of Flow Chemistry*, 10(1), 93–101.

[193] Ravi, R., Sanjeev, R., Jagannadham, V., & Skelton, A. A. (2015). Nucleophilic substitution reactions of meta- and para-substituted benzylamines with benzyl bromide in methanol medium. *International Journal of Chemical Kinetics*, 47(1), 36–41.

[194] Reci, A., Sederman, A. J., & Gladden, L. F. (2017). Retaining both discrete and smooth features in 1D and 2D NMR relaxation and diffusion experiments. *Journal of Magnetic Resonance*, 284, 39–47.

[195] Reguillo, R., Grellier, M., Vautravers, N., Vendier, L., & Sabo-Etienne, S. (2010). Ruthenium-Catalyzed Hydrogenation of Nitriles: Insights into the Mechanism. *Journal of the American Chemical Society*, 132(23), 7854–7855.

[196] Reisner, B. A., Lee, Y., Hanson, J. C., Jones, G. A., Parise, J. B., Corbin, D. R., Toby, B. H., Freitag, A., Larese, J. Z., & Kahlenberg, V. (2000). Understanding negative thermal expansion and 'trap door' cation relocations in zeolite rho. *Chemical Communications*, (22), 2221–2222.

[197] Rezayee, N. M., Samblanet, D. C., & Sanford, M. S. (2016). Iron-Catalyzed Hydrogenation of Amides to Alcohols and Amines. *ACS Catalysis*, 6(10), 6377–6383.

[198] Robinson, N., Robertson, C., Gladden, L. F., Jenkins, S. J., & D'Agostino, C. (2018). Direct Correlation between Adsorption Energetics and Nuclear Spin Relaxation in a Liquid-saturated Catalyst Material. *ChemPhysChem*, 19(19), 2472–2479.

[199] Rohmann, K., Hölscher, M., & Leitner, W. (2016). Can Contemporary Density Functional Theory Predict Energy Spans in Molecular Catalysis Accurately Enough to Be Applicable for in Silico Catalyst Design? A Computational/Experimental Case Study for the Ruthenium-Catalyzed Hydrogenation of Olefins. *Journal of the American Chemical Society*, 138(1), 433–443.

[200] Roughley, S. D. & Jordan, A. M. (2011). The medicinal chemist's toolbox: An analysis of reactions used in the pursuit of drug candidates. *Journal of Medicinal Chemistry*, 54(10), 3451–3479.

[201] Saito, Y., Ishitani, H., Ueno, M., & Kobayashi, S. (2017). Selective Hydrogenation of Nitriles to Primary Amines Catalyzed by a Polysilane/SiO 2 -Supported Palladium Catalyst under Continuous-Flow Conditions. *ChemistryOpen*, 6(2), 211–215.

[202] Salles, F., Ghoufi, A., Maurin, G., Bell, R. G., Mellot-Draznieks, C., & Férey, G. (2008). Molecular Dynamics Simulations of Breathing MOFs: Structural Transformations of MIL-

53(Cr) upon Thermal Activation and CO 2 Adsorption. *Angewandte Chemie International Edition*, 47(44), 8487–8491.

[203] Sarabipour, S., Khan, A., Seah, Y. F. S., Mwakilili, A. D., Mumoki, F. N., Sáez, P. J., Schwessinger, B., Debat, H. J., & Mestrovic, T. (2021). Changing scientific meetings for the better.

[204] Scherer, G. W. (1994). Hydraulic radius and mesh size of gels. *Journal of Sol-Gel Science and Technology*, 1(3), 285–291.

[205] Sederman, A. J., Alexander, P., & Gladden, L. F. (2001). Structure of packed beds probed by Magnetic Resonance Imaging. *Powder Technology*, 117(3), 255–269.

[206] Sella, A. (2007). Classic Kit: Schlenk apparatus.

[207] Sen, P. N. (2004). Time-dependent diffusion coefficient as a probe of geometry. *Concepts in Magnetic Resonance*, 23A(1), 1–21.

[208] Sharma, D. M. & Punji, B. (2019). Selective Synthesis of Secondary Amines from Nitriles by a User-Friendly Cobalt Catalyst. *Advanced Synthesis and Catalysis*, 361(17), 3930–3936.

[209] Sharninghausen, L. S., Mercado, B. Q., Crabtree, R. H., & Hazari, N. (2015). Selective conversion of glycerol to lactic acid with iron pincer precatalysts. *Chemical Communications*, 51(90), 16201–16204.

[210] Sheldon, R. A. (2007). The E Factor: fifteen years on. *Green Chemistry*, 9(12), 1273.

[211] Sieffert, N. & Bühl, M. (2009). Noncovalent interactions in a transition-metal triphenylphosphine complex: A density functional case study. *Inorganic Chemistry*, 48(11), 4622–4624.

[212] Smith, J. (1982). Chemical kinetics and reaction mechanisms. *The Chemical Engineering Journal*, 25(1), 122.

[213] Smith, M., Love, D. C., Rochman, C. M., & Neff, R. A. (2018). Microplastics in Seafood and the Implications for Human Health. *Current environmental health reports*, 5(3), 375–386.

[214] Smith, N. E., Bernskoetter, W. H., & Hazari, N. (2019). The Role of Proton Shuttles in the Reversible Activation of Hydrogen via MetalLigand Cooperation. *Journal of the American Chemical Society*, 141(43), 17350–17360.

[215] Solomon, I. (1955). Relaxation Processes in a System of Two Spins. *Physical Review*, 99(2), 559–565.

[216] Srivastava, R. K., Sushant, P., Sathvik, A., Kolluru, V. C., Ahamad, M. I., Alharthi, M. A., & Luqman, M. (2021). Sources and industrial applications of polysaccharides. In *Food, Medical, and Environmental Applications of Polysaccharides* (pp. 511–530). Elsevier.

[217] Staff (2022). What Is the Supply Chain? Why Is It Important?

[218] Stapf, S. & Han, S.-I. (2006). Introduction. In *NMR Imaging in Chemical Engineering*, Wiley Online Books (pp. 1–45). Weinheim, FRG: Wiley-VCH Verlag GmbH & Co. KGaA.

[219] Suekuni, M. T., Myers, T. R., McNeil, M. C., Prisco, A. J., Shelburne, S. S., Shepperson, W. A., & Allgeier, A. M. (2020). Surface Area Determination of Kevlar Particles in Suspensions Containing Iron Impurities Using Low-Field Nuclear Magnetic Resonance Relaxometry. *ACS Applied Polymer Materials*, 2(6), 2134–2141.

[220] Sullivan, V. S., Kim, Y. J., Xu, S., Jonas, J., & Korb, J.-P. (1999). Carbon-13 NMR Study of the Effect of Confinement on the Molecular Dynamics of 2-Ethylhexyl Benzoate. *Langmuir*, 15(13), 4664–4670.

[221] Sun, S.-G., Christensen, P. A., & Wieckowski, A. (2007). *In situ Spectroscopic Studies of Adsorption at the Electrode and Electrocatalysis*. Berlin: Elsevier.

[222] Svagan, A. J., Åkesson, A., Cárdenas, M., Bulut, S., Knudsen, J. C., Risbo, J., & Plackett,

D. (2012). Transparent films based on PLA and montmorillonite with tunable oxygen barrier properties. *Biomacromolecules*, 13(2), 397–405.

[223] Tannahill, M. (2019). Engineering students host GEAK5 race, promote mental and physical health.

[224] Thern, H., Horch, C., Stallmach, F., Li, B., Mezzatesta, A., Zhang, H., & Arro, R. (2018). Low-field NMR laboratory measurements of hydrocarbons confined in organic nanoporous media at various pressures. *Microporous and Mesoporous Materials*, 269(December 2016), 21–25.

[225] Thomas, N. L., Clarke, J., McLauchlin, A. R., & Patrick, S. G. (2012). Oxo-degradable plastics: Degradation, environmental impact and recycling. *Proceedings of Institution of Civil Engineers: Waste and Resource Management*, 165(3), 133–140.

[226] Tillmann, W., Khalil, O., & Abdulgader, M. (2019). Porosity Characterization and Its Effect on Thermal Properties of APS-Sprayed Alumina Coatings. *Coatings*, 9(10), 601.

[227] Tokmic, K., Jackson, B. J., Salazar, A., Woods, T. J., & Fout, A. R. (2017). Cobalt-Catalyzed and Lewis Acid-Assisted Nitrile Hydrogenation to Primary Amines: A Combined Effort. *Journal of the American Chemical Society*, 139(38), 13554–13561.

[228] Tucker, J. L. (2006). Green chemistry, a pharmaceutical perspective. *Organic Process Research and Development*, 10(2), 315–319.

[229] U.N. (2022). THE 17 GOALS | Sustainable Development.

[230] Van Vlierberghe, S., Cnudde, V., Dubruel, P., Masschaele, B., Cosijns, A., De Paepe, I., Jacobs, P. J., Van Hoorebeke, L., Remon, J. P., & Schacht, E. (2007). Porous gelatin hydrogels: 1. Cryogenic formation and structure analysis. *Biomacromolecules*, 8(2), 331–337.

[231] Varcoe, K. M., Blakey, I., Chirila, T. V., Hill, A. J., & Whittaker, A. K. (2007). The Effect of Synthetic Conditions on the Free Volume of Poly(2-hydroxyethyl methacrylate) as Studied

by 1 H NMR, 129 Xe NMR, and Position Annihilation Spectroscopy. In *New Approaches in Biomedical Spectroscopy* (pp. 391–409).

[232] Vardanyan, R. & Hruby, V. (2016). Adrenergic (Sympathomimetic) Drugs. In *Synthesis of Best-Seller Drugs* chapter 11, (pp. 189–199). Elsevier.

[233] Velasquez Morales, S., Londono, J. D., & Allgeier, A. M. (2021). Characterization under Practical Conditions: Time-Domain NMR, X-ray Scattering and Tomography. In *Handbook of Porous Materials*, volume Volume 16 of *Materials and Energy* (pp. 71–165). WORLD SCIENTIFIC.

[234] Vethaak, A. D. & Legler, J. (2021). Microplastics and human health. *Science*, 371(6530), 672–674.

[235] Volf, J. & Pasek, J. (1986). Hydrogenation of Nitriles. In L. Červený (Ed.), *Catalytic Hydrogenation* chapter 4, (pp. 105–144). Elsevier.

[236] Wachs, I. E. & Roberts, C. A. (2010). Monitoring surface metal oxide catalytic active sites with Raman spectroscopy. *Chemical Society Reviews*, 39(12), 5002.

[237] Wallen, S. L., Schoenbachler, L. K., Dawson, E. D., & Blatchford, M. A. (2000). A polymer NMR cell for the study of high-pressure and supercritical fluid solutions. *Analytical Chemistry*, 72(17), 4230–4234.

[238] Wang, Z., Kulkarni, A., Deshpande, S., Nakamura, T., & Herman, H. (2003). Effects of pores and interfaces on effective properties of plasma sprayed zirconia coatings. *Acta Materialia*, 51(18), 5319–5334.

[239] Washburn, K. E. (2014). Relaxation mechanisms and shales. *Concepts in Magnetic Resonance Part A: Bridging Education and Research*, 43A(3), 57–78.

[240] Washburn, K. E., Sandor, M., & Cheng, Y. (2017). Evaluation of sandstone surface relaxivity using laser-induced breakdown spectroscopy. *Journal of Magnetic Resonance*, 275, 80–89.

[241] Weber, S., Stöger, B., & Kirchner, K. (2018). Hydrogenation of Nitriles and Ketones Catalyzed by an Air-Stable Bisphosphine Mn(I) Complex. *Organic Letters*, 20(22), 7212–7215.

[242] Weckhuysen, B. M. (2010). Preface: recent advances in the in-situ characterization of heterogeneous catalysts. *Chemical Society Reviews*, 39(12), 4557.

[243] Whittall, K. P. & MacKay, A. L. (1989). Quantitative interpretation of NMR relaxation data. *Journal of Magnetic Resonance (1969)*, 84(1), 134–152.

[244] Wollein, U., Bauer, B., Habernegg, R., & Schramek, N. (2015). Potential metal impurities in active pharmaceutical substances and finished medicinal products A market surveillance study. *European Journal of Pharmaceutical Sciences*, 77, 100–105.

[245] Wong, Y. T. A., Martins, V., Lucier, B. E. G., & Huang, Y. (2019). SolidState NMR Spectroscopy: A Powerful Technique to Directly Study Small Gas Molecules Adsorbed in MetalOrganic Frameworks. *Chemistry A European Journal*, 25(8), 1848–1853.

[246] Xu, F. & Mueller, K. (2005). Accelerating popular tomographic reconstruction algorithms on commodity PC graphics hardware. *IEEE Transactions on Nuclear Science*, 52(3 I), 654–663.

[247] Xu, R., Chakraborty, S., Bellows, S. M., Yuan, H., Cundari, T. R., & Jones, W. D. (2016). Iron-Catalyzed Homogeneous Hydrogenation of Alkenes under Mild Conditions by a Stepwise, Bifunctional Mechanism. *ACS Catalysis*, 6(3), 2127–2135.

[248] Yampolskii, Y. (2012). Polymeric gas separation membranes. *Macromolecules*, 45(8), 3298–3311.

[249] Yan, Z., Cai, X., Yang, X., Song, B., Chen, Z., Bhadury, S. P., Hu, D., Jin, L., Xue, W., & Lu, P. (2009). Synthesis and antiviral activities of chiral thiourea derivatives. *Chinese Journal of Chemistry*, 27(3), 593–601.

[250] Yashchuk, O., Portillo, F., & Hermida, E. (2012). Degradation of Polyethylene Film Samples Containing Oxo-Degradable Additives. *Procedia Materials Science*, 1, 439–445.

[251] Zell, T. & Langer, R. (2018). From Ruthenium to Iron and ManganeseA Mechanistic View on Challenges and Design Principles of Base-Metal Hydrogenation Catalysts. *ChemCatChem*, 10(9), 1930–1940.

[252] Zhang, G., Ranjith, P. G., Wu, B., Perera, M. S., Haque, A., & Li, D. (2019). Synchrotron X-ray tomographic characterization of microstructural evolution in coal due to supercritical CO2 injection at in-situ conditions. *Fuel*, 255(July), 115696.

[253] Zhang, H., Wang, Y. E., Fan, Q., & Zuo, Y. Y. (2011). On the low surface tension of lung surfactant. *Langmuir*, 27(13), 8351–8358.

[254] Zhang, J., Leitus, G., Ben-David, Y., & Milstein, D. (2006). Efficient homogeneous catalytic hydrogenation of esters to alcohols. *Angewandte Chemie - International Edition*, 45(7), 1113–1115.

[255] Zhao, Y., Zhu, G., Dong, Y., Danesh, N. N., Chen, Z., & Zhang, T. (2017). Comparison of low-field NMR and microfocus X-ray computed tomography in fractal characterization of pores in artificial cores. *Fuel*, 210(March), 217–226.

[256] Ziegler, R. E., Desai, B. K., Jee, J.-A., Gupton, B. F., Roper, T. D., & Jamison, T. F. (2018). 7-Step Flow Synthesis of the HIV Integrase Inhibitor Dolutegravir. *Angewandte Chemie International Edition*, 57(24), 7181–7185.

Appendix A

Appendix A: Chapter 3

A.1 Catalyst NMR Characterization

Each PNP-Fe(H)(BH_4)CO batch was evaluated via ^{1}H and ^{31}P NMR for a purity $\geq$ 93% and via performance testing to achieve equivalent reaction rates to previous batches at the following conditions: 70°C, 0.1 mol% (2), 30 bar H_2, 1000 RPM. ^{1}H and ^{31}P NMR for both **1** (Figures A.1-A.2) and **2** (Figures A.3-A.4) were used to determine purity and identity of species.

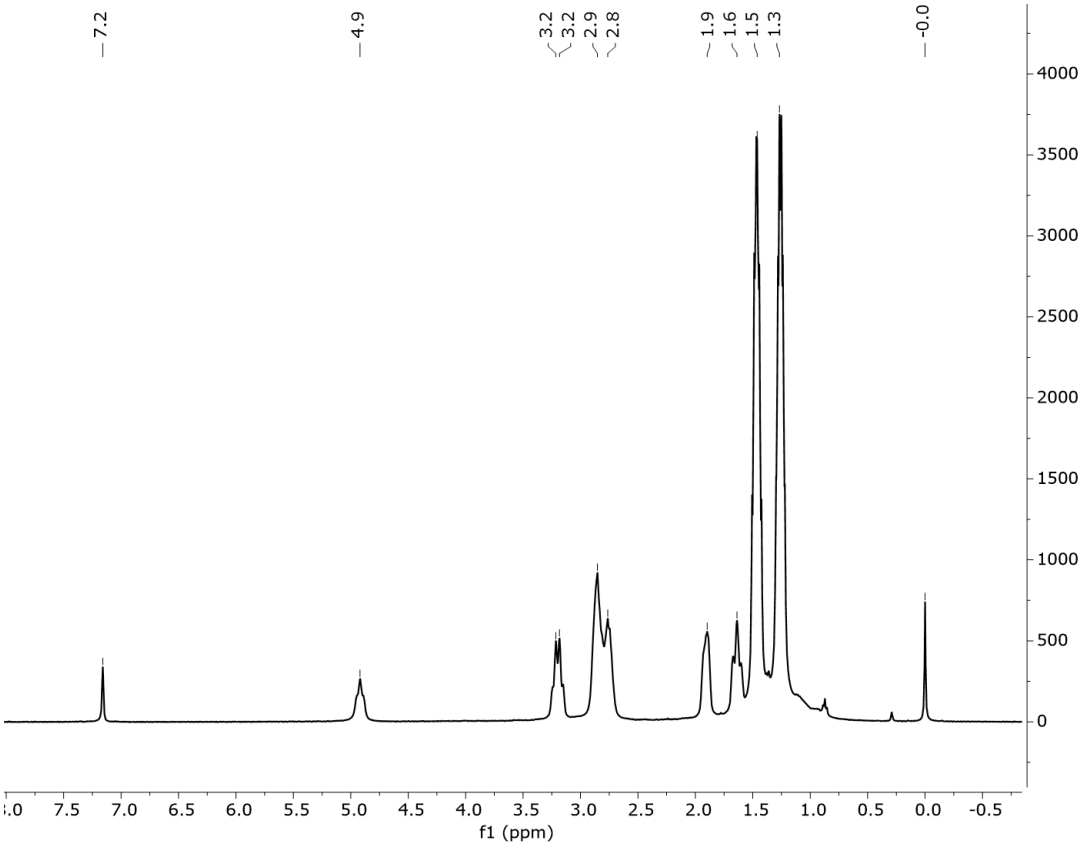

Figure A.1: ^{1}H NMR of PNP-Fe($Br)_2$CO complex (**14**)

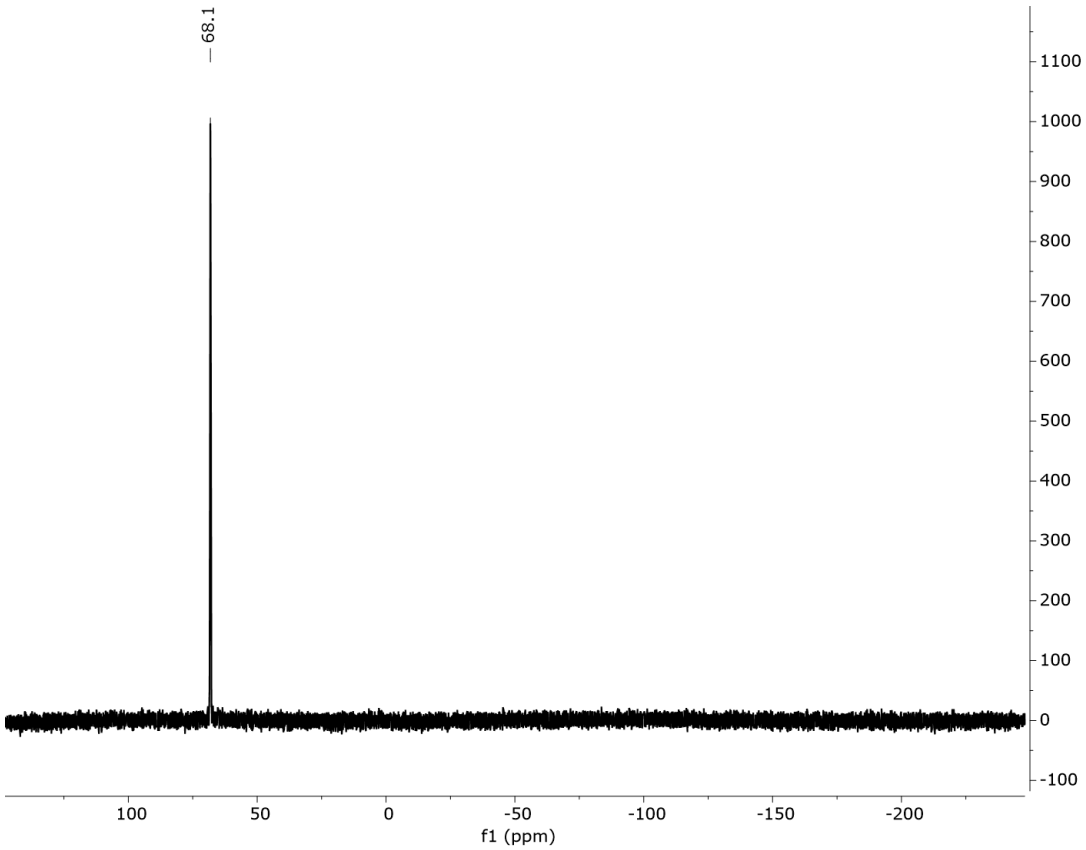

Figure A.2: ^{31}P NMR of PNP-Fe(Br)$_2$CO complex (**14**)

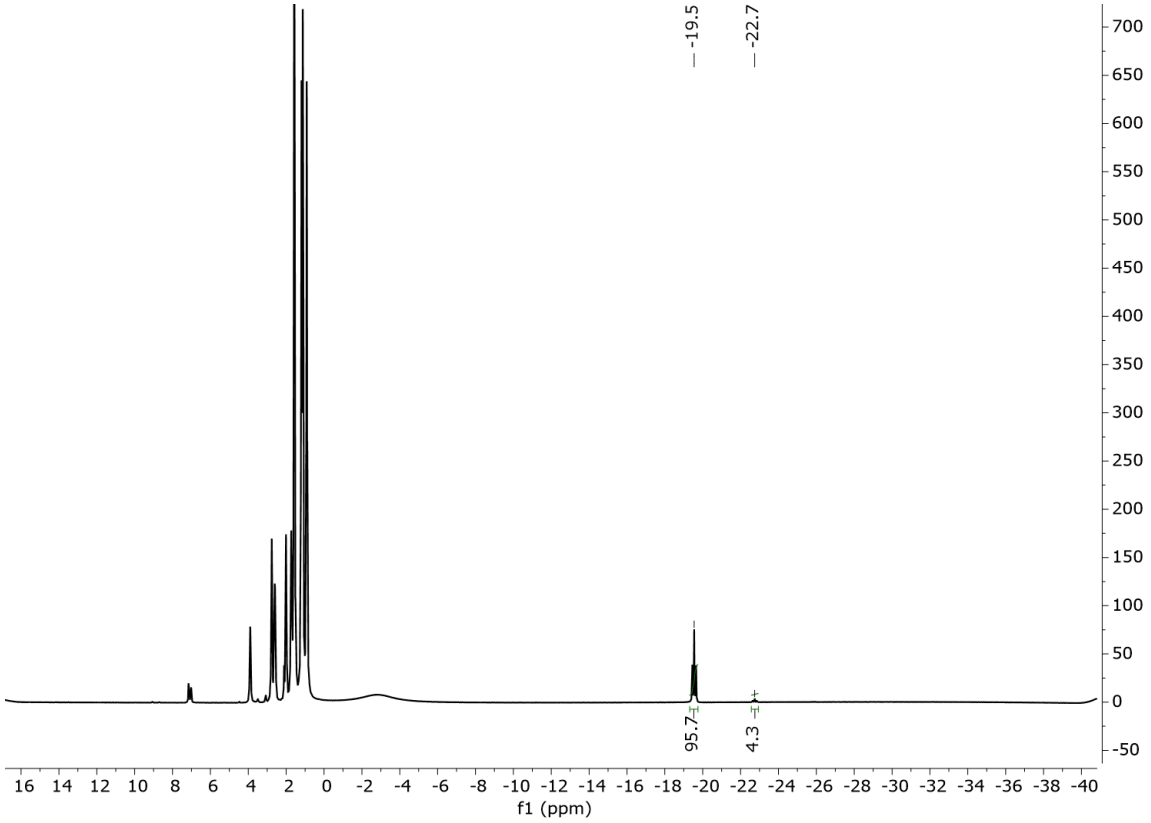

Figure A.3: ^{1}H NMR of catalyst complex (8) with its signature hydride shift at -19.5 ppm, while small impurity of 3 and its signature chemical shift at -22.7ppm

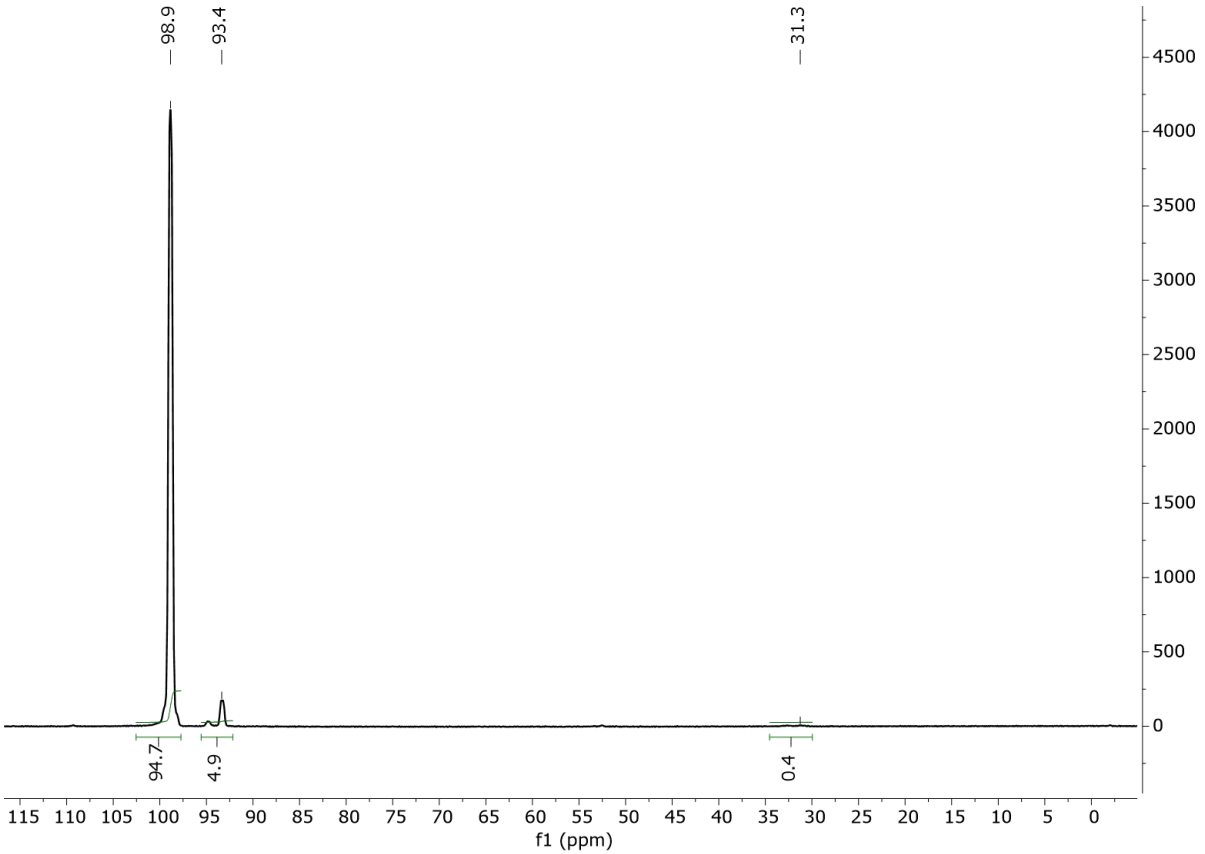

Figure A.4: ^{31}P NMR of catalyst complex (8) with chemical shift at 98.85 ppm, while small impurity of 3 identified by chemical shift at 93.36 ppm. At 31.25 ppm, there is small but noticeable presence of phosphine oxides.

A.2 Mass Transfer Coefficient and Limitations

Mathematically, the rate of mass transfer is a first order process described by Equation A.1, where $K_L a_B$ is the volumetric mass transfer coefficient, A^* is the equilibrium concentration of the gas in the liquid, and A_l is the bulk liquid concentration of the gas.

$$Rate = K_L a_B (A^* - A_l) \tag{A.1}$$

Conceptually, a two-film theory model can be used to describe the mass transfer process, Figure A.5. The bulk gas phase concentration, A_g, stretches towards the interface, A_{gi}. At high pressures, where the solvent has little to no contributions to the gas phase, A_g and A_{gi} are equivalent to

one another. Therefore, when at the interface the equilibrium concentration A* is equivalent to $\frac{A_{gi}}{H_A} = \frac{A_g}{H_A}$. Henry's constant ($H_A$) describes the interfacial discontinuity between the gas and liquid concentration of the gas. Substituting this equivalent expression into Equation A.1, we can describe the rate of mass transfer in terms of measurable quantities, i.e., pressure and liquid concentration, A_l, Equation A.2.

$$Rate = K_L a_B \left(\frac{A_g}{H_A} - A_l \right) \tag{A.2}$$

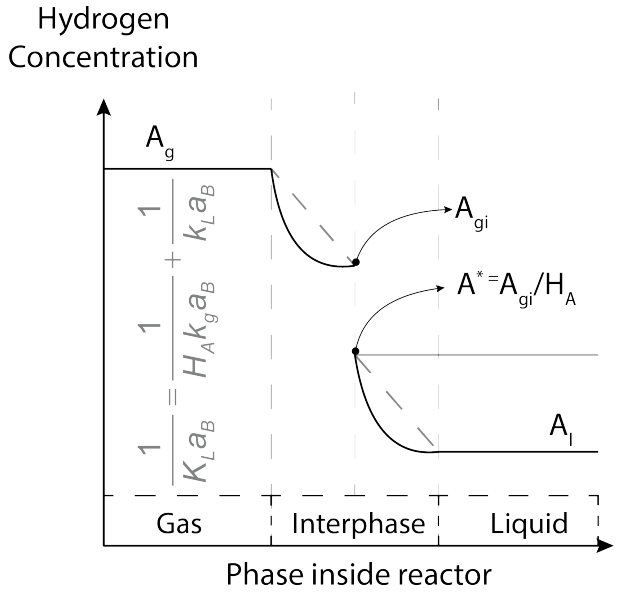

Figure A.5: Two film theory describing gas to liquid mass transfer model.

Gases with lower solubility would therefore have a greater Henry's constant. The lower the solubility would therefore render the gas side mass transfer resistance negligible in the overall mass transfer coefficient equation, Equation A.3.

$$\frac{1}{K_L a_B} = \frac{1}{H_A k_g a_B} + \frac{1}{k_L a_B} \tag{A.3}$$

The overall mass transfer equation is simplified to have only the liquid-side mass transfer resistance, Equation A.4.

$$\frac{1}{K_L a_B} \equiv \frac{1}{k_L a_B} \tag{A.4}$$

Chaudhari and coworkers characterized the liquid-side mass transfer resistance ($k_L a_B$) in high pressure autoclave Parr reactors. The experimental correlation is based on reactor parameters, i.e., impeller and vessel diameters, liquid and impeller height, volume occupied by the gas and the liquid, and agitation frequency.[55]

$$k_L a_B = 1.48X10^{-3}(N)^{2.18}\left(\frac{V_g}{V_L}\right)^{1.88}\left(\frac{d_I}{d_T}\right)^{2.16}\left(\frac{h_1}{h_2}\right)^{1.16} \tag{A.5}$$

To assess whether a reaction rate measurement is compromised by mass transfer, the Damköhler (D_α) criteria assess the ratio between the observed rate of reaction and the maximum rate of mass transfer, Equation A.6, was used. If the Dα number is <0.1 the reaction is not mass transfer limited; if the Dα number is between 0.1 and 1.0 the reaction could have mass transfer limitation and further study is recommended; else if the Dα number is above 1.0 then the reaction is severely limited by mass transfer further study is required.

$$Da = \frac{\text{Reaction Rate}}{\text{Max. Rate of Mass Transfer}} = \frac{\text{Uptake Rate}}{K_L a_B (A^*)} < 0.1 \tag{A.6}$$

The denominator, in Equation A.6, is a function of H_2 solubility (A^*); solvents with greater solubility are favored to minimize mass transfer limitations. Indirectly, greater H_2 solubility would reduce the need for high agitation frequencies in (semi-)batch stirred reactors, which would decrease energy demand and operational costs.

A.3 Assessing Intrinsic Kinetic Regime

Based on initial reaction screening data, which provided Dα numbers in the 0.1 - 1 range and the selection of a low hydrogen solubility solvent, i.e., 2-propanol, we decided to conduct and agitation rate study, Figure A.6.

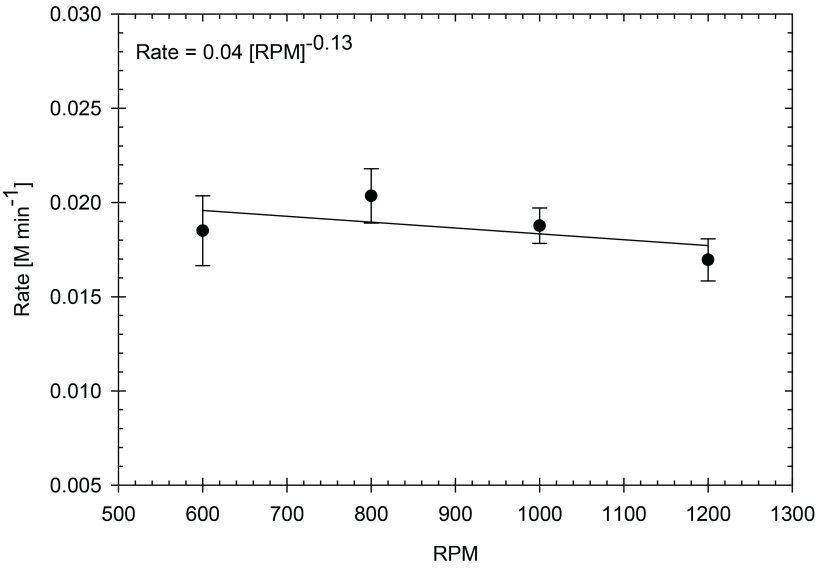

Figure A.6: The correlation of reaction versus agitation rates yields no significant change on reaction rate upon increasing agitation, above 600 RPM. Thus, 1000 RPM were used to assess intrinsic kinetic parameters.

An agitation rate range between 600 and 1200 rpm was investigated. The rates of reaction remained unchanged with increasing rate of agitation thus confirming that at these conditions there were no external mass transfer limitations impacting the rates of reaction.

A.4 Hydrogen Solubility and Solvent Screening

Solvent	Pressure [bar]	x_{H_2} x 10^4	Citation
1,2-ethanediol	39.4	25.0	[43]
2-methoxyethanol	30.0*	73.0	
1-propanol	30.0*	99.7	
2-propanol	30.9	120.1	
1-butanol	30.4	120.2	
2-butanol	30.0*	129.1	
1-pentanol	33.4	143	
1-Hexanol	32.6	155.2	
Toluene	30.0*	144.7	
Tetrahydrofuran	33.8	146.1	[44]
n-hexane	30.0*	290.8	
n-octane	30.5	286.0	
n-decane	30.0*	297.3	
HFIP	30.0*	297.3	

Table A.1: H_2 mole fraction (x_{H_2}) in numerous solvents at 100°C and approximately 30 bar; * values were obtained by interpolation of data.

The data in Table A.1 suggests that alcohol density decreases H_2 solubility. A clear example is presented with n-hexane and 1-hexanol where the mole fraction (x_{H_2}) drops from $290.8 \cdot 10^{-4}$ to $155.2 \cdot 10^{-4}$ with the addition of a terminal OH group, respectively. Additionally, decreasing the number of carbon atoms in the backbone of the terminal alcohol also decreases x_{H_2}. For example, 1-propanol has an x_{H_2} of $99.7 \cdot 10^{-4}$. H_2 solubility is reduced with the removal of 3 carbon atoms, from 1-pentanol to 1-propanol, by a factor of 1.55. Alcohol placement on the carbon backbone also changes solubility parameters, solubility in 2-propanol increases by a factor of 1.2 in contrast to 1-propanol.

Based on these data and literature precedent a range of solvents with different hydrogen solubilities were screened. 2-propanol with the lowest hydrogen solubility yielded the greatest conversion of benzonitrile and therefore was selected as the solvent for this investigation, Figure A.7.

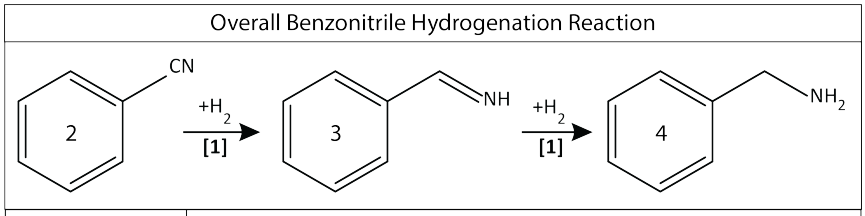

Properties	Solvent			
	TOL	iPrOH	tBuOH	HFIP
$X_{H2,liq.}$ [~30 bar]	0.019 (189°C)	0.0061 (123°C)	0.013 (100°C)	0.025 (100°C)
%Conversion	0%	94%	48%	0%

Figure A.7: Preliminary screening of toluene (TOL), 2-propanol (iPrOH), tert-butanol (tBuOH), and hexafluoro-2-propanol (HFIP) on the hydrogenation of benzonitrile with an iron-PNP catalyst.

A.5 Hydrogen Uptake

A.5.1 Reservoir calibration

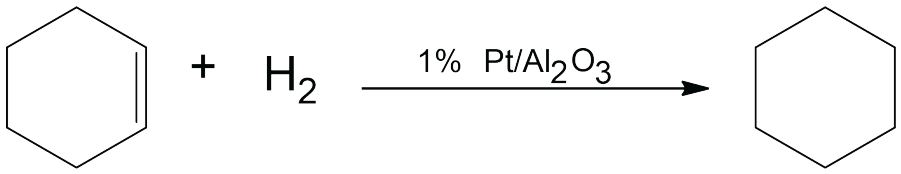

Figure A.8: The hydrogenation of cyclohexene to cyclohexane was used to calibrate H2 reservoir volume

A Swagelok pressure vessel was incorporated into our Parr reactor set up to monitor H_2 consumption rates via pressure-temperature measurements. To calibrate pressure-temperature data to moles of hydrogen, the gas reservoir and line volumes needed to be accounted for. The gas volume (V_g) was obtained by regressing cyclohexene conversion and H_2 pressure data. The V_g was determined to be 211 ± 9 mL.

A.5.2 Derivation Reaction Rates Based on Hydrogen Uptake Data

The following set of equations (5-13) are used in the derivation of the H_2 uptake data that equates the rate of reaction to pressure and temperature. We begin, with a general liquid mole balance for H_2, Equation A.7. The moles of hydrogen can be deconvoluted into the concentration of H_2 and volume contributions, Equation A.8. Assuming steady-state, we simplify Equation A.8 by eliminating the terms for changes in volume and concentration of hydrogen as a function of time and since there is no outflow of H_2 from the liquid we can eliminate ($F_{H_2,out}$). Equation A.8 is simplified to Equation A.9.

$$\frac{dN_{H_2}}{dt} = F_{H_2,in} - F_{H_2,out} + V_l R_{H_2} \tag{A.7}$$

$$A^* \frac{dV}{dt} + V \frac{dA^*}{dt} = F_{H_2,in} + V_l R_{H_2} \tag{A.8}$$

$$0 = F_{H_2,in} + V_l R_{H_2} \tag{A.9}$$

Similarly, a mole balance can be created for hydrogen in the gas phase, Equation A.10. The moles of H_2 can be substituted by the ideal-gas law. Since there is no reaction nor is there inflow of H_2 the $F_{H_2,in}$ and $V_l R_{H_2}$ terms can be eliminated to yield Equation A.11.

$$\frac{dN_{H_2}}{dt} = F_{H_2,in} - F_{H_2,out} + V_l R_{H_2} \tag{A.10}$$

$$\frac{dN_{H_2}}{dt} = \frac{d(\frac{PV_g}{RT})}{dt} = (\frac{V_g}{RT})\frac{dP}{dt} = -F_{H_2,out} \tag{A.11}$$

Equation A.9 and A.11 are related by the following expression, Equation A.12.

$$F_{H_2,in} = F_{H_2,out} \tag{A.12}$$

Combining Equations A.9 and A.11 yields an expression for changes in pressure as a function of time, which is dependent on the rate of reaction, Equation A.13.

$$\frac{dP}{dt} = \frac{V_l}{(\frac{v_g}{RT})} R_{H_2} \tag{A.13}$$

Further manipulation yields an equation for the rate of reaction based on pressure and temperature data.

$$R_{H_2} = \frac{V_g}{V_l} \frac{1}{RT} \frac{dP}{dt} \tag{A.14}$$

To plot hydrogen concentration we use a stoichiometry factor of 2 to account for the moles of hydrgoen consumed by converting benzonitrile to benzylamine, Equations A.15 and A.16.

$$R_{H_2} = \frac{1}{\alpha} \frac{dC_{H_2}}{dt} = \frac{V_g}{V_l} \frac{1}{RT} \frac{dP}{dt} \tag{A.15}$$

Where α=2

$$\frac{dC_{H_2}}{dt} = 2\frac{V_g}{V_l} \frac{1}{RT} \frac{dP}{dt} \tag{A.16}$$

A.5.3 Error Propagation in Reaction Rates

Propagation of error of the rate of reaction (Equation A.17 can be calculated by taking the partial derivatives of Equation A.14 with respect to V_l, V_g, T, and P. The error associated with each measurement: δV_g, δV_l, δT, and δP were regressed or obtained from the manufacturer.

$$U_{R_{H_2}} = \sqrt{\left[\left(\frac{dR_{H_2}}{dV_g}\right)(\delta V_g)\right]^2 + \left[\left(\frac{dR_{H_2}}{dV_l}\right)(\delta V_l)\right]^2 + \left[\left(\frac{dR_{H_2}}{dT}\right)(\delta T)\right]^2 + \left[\left(\frac{dR_{H_2}}{dP}\right)(\delta P)\right]^2} \tag{A.17}$$

$$\left(\frac{dR_{R_{H_2}}}{dV_g}\right) = \frac{1}{V_l RT} \frac{\delta P}{\delta t} \tag{A.18}$$

$$\left(\frac{dR_{R_{H_2}}}{dV_l}\right) = -\frac{V_g}{V_l^2 RT}\frac{\delta P}{\delta t} \tag{A.19}$$

$$\left(\frac{dR_{R_{H_2}}}{dT}\right) = -\frac{V_g}{V_l RT^2}\frac{\delta P}{\delta t} \tag{A.20}$$

$$\left(\frac{dR_{R_{H_2}}}{dP}\right) = \frac{V_g}{V_l RT}\frac{\delta^2 P}{\delta^2 t} = \frac{\left(\frac{dP}{dt}\right)_{x+1} - \left(\frac{dP}{dt}\right)_{x-1}}{t_{x+1} - t_{x-1}} \tag{A.21}$$

The following values were utilized in Equation 13 for the error associated with each variable in Equation 12.

$$\delta V_g = \pm 9 cm^3 \tag{A.22}$$

$$\delta V_l = \pm 0.26 cm^3 \tag{A.23}$$

$$\delta T = \pm 3.908^{\circ} C \tag{A.24}$$

$$\delta P = \pm 1.2 psi = \pm 0.083 bar \tag{A.25}$$

A.6 Arrhenius and Eyring Plot Equations and Theory

The basic premise from the transition state theory is that reactants exist in a quasi-equilibrium with the activated complex and have a characteristic frequency of passage over the potential-energy maximum or transition state.

Equation A.26 is the parent formulation that is used to assess the contribution of temperature upon the kinetic rate constant. C and U are constants that are regressed for three different theories, i.e., Arrhenius, collision, and Eyring (absolute rate) theories, where the temperature order, n, is 0, $\frac{1}{2}$, or 1, respectively. Collision theory will not be discussed furthered, but the interested reader is referred to Espenson as he provides a great overview of the theory.[212]

$$k = CT^n e^{\left(-\frac{U}{RT}\right)} \tag{A.26}$$

When $n = 0$, $C = A$ and $U = E_a$, Equation A.26 becomes Equation A.27; E_a has units of energy, i.e., J mol^{-1} , meanwhile, A has units of s^{-1} for a unimolecular reaction. For non-unimolecular reactions, A has units of M$^{-(m-1)}$s^{-1}, where m is the overall order of reaction.

$$k = Ae^{(-\frac{E_a}{RT})} \tag{A.27}$$

By taking the natural logarithm of both sides of Equation A.27 we obtain a linearized form, Equation A.28

$$\ln k = \ln A - \frac{E_a}{RT} \tag{A.28}$$

Similarly, while $n = 1$, $C = \frac{k_B T}{h}$ and $U = \Delta G^{\ddagger}$, Equation A.26 becomes Equation A.29. Where $\Delta G^{\ddagger}$ has units of J mol^{-1} and can be deconstructed into enthalpic and entropic contribution by substituting Equation A.30 into Equation A.29, resulting in Equation A.31.

$$k = \frac{k_B T}{h} e^{(\frac{\Delta G^{\ddagger}}{RT})} \tag{A.29}$$

$$\Delta G^{\ddagger} = \Delta H^{\ddagger} - T\Delta S^{\ddagger} \tag{A.30}$$

$$k = \frac{k_B T}{h} e^{(\frac{\Delta S^{\ddagger}}{R})} e^{(-\frac{\Delta H^{\ddagger}}{RT})} \tag{A.31}$$

By rearranging Equation A.31 and linearizing by taking the natural logarithm of both sides of the equation, we obtain, Equation A.32.

$$\ln \frac{k}{T} = \ln \frac{k_B T}{h} + \frac{\Delta S^{\ddagger}}{R} - \frac{\Delta H^{\ddagger}}{RT} \tag{A.32}$$

Contrasting Equation A.28 and A.32, there is similarity between the enthalpy of the transition state and the activation energy of the reaction; this can be represented by the formula $\Delta H^{\ddagger} =$

$E_a - RT$.

$\Delta H^{\ddagger}$ is a measure of the height of the energy barrier; it provides insight into the bond strength between reactants that needs to be overcome to achieve the transition state. The larger the value of, $\Delta H^{\ddagger}$ the slower the reaction becomes. If the $\Delta H^{\ddagger}$ is less than the dissociation energy of a particular group, one can conclude the reaction does not proceed.[212]

$\Delta S^{\ddagger}$ decreases with 'dilution' and therefore when regressing such parameters from DFT calculation it is important to incorporate confinement effects as to not underestimate the entropic contributions to the reaction energetics. $\Delta S^{\ddagger}$ tends to be positive if there are more products than reactants or if a dissociative mechanism is in place. The more negative the $\Delta S^{\ddagger}$ is, the lower the rate of reaction.[212] A unimolecular reaction has a $\Delta S^{\ddagger}$ near zero due to the lack of orientational factors.

A.7 GC Calibration

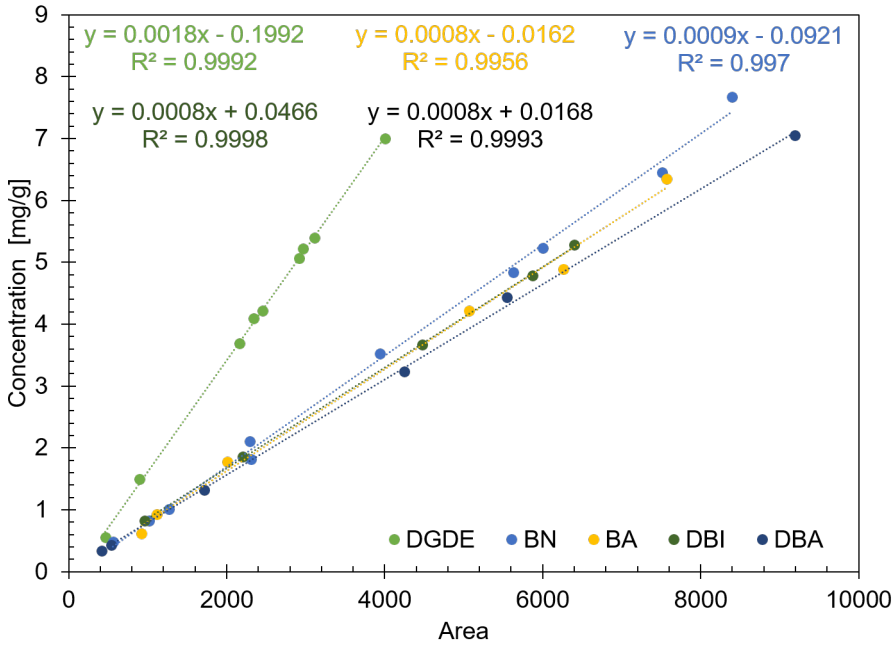

Figure A.9: Calibration of GC FID detector for benzonitrile, benzylamine, dibenzylimine, dibenzylamine, and diethylene glycol diethyl ether.

A.8 Mathematical models describing concentration changes of proposed reaction mechanism

Equations for catalytic species

$$r_8 = \frac{dC_8}{dt} = -k_{a,f}[8] + k_{a,b}[1][B_2H_6] \tag{A.33}$$

$$r_1 = \frac{dC_1}{dt} = -k_{a,b}[1][B_2H_6] - k_b[1][2] - k_c[1][3] + k_e[6][H_2] \tag{A.34}$$

$$r_5 = \frac{dC_5}{dt} = k_b[1][2] + k_c[1][3] - k_d[5][iPrOH] \tag{A.35}$$

$$r_6 = \frac{dC_6}{dt} = k_d[5][iPrOH] - k_e[6][H_2] \tag{A.36}$$

Equation for Reaction Mechanism

$$r_2 = \frac{dC_2}{dt} = -k_f[1][2] \tag{A.37}$$

$$\begin{aligned} r_3 = \frac{dC_3}{dt} = & -k_g[1][3] + k_f[1][2] - k_{h,f}[3] + k_{h,b}[9] - k_{i,f}[9][3] \\ & + k_{i,b}[10] - k_{k,f}[3][4] + k_{k,b}[12] \end{aligned} \tag{A.38}$$

$$r_4 = \frac{dC_4}{dt} = -k_{k,f}[3][4] + k_g[3][1] + k_{k,b}[12] \tag{A.39}$$

$$r_9 = \frac{dC_9}{dt} = -k_{h,b}[9] + k_{h,f}[3] - k_{i,f}[9][3] + k_{i,b}[10] \tag{A.40}$$

$$r_{10} = \frac{dC_{10}}{dt} = +k_{i,f}[9][3] + k_{j,b}[11][NH_3] - k_{i,b}[10] - k_{j,f}[10] \tag{A.41}$$

$$r_{11} = \frac{dC_{11}}{dt} = k_{j,f}[10] - k_{j,b}[11][NH_3] \tag{A.42}$$

$$r_{12} = \frac{dC_{12}}{dt} = k_{k,f}[3][4] + k_{l,b}[13][NH_3] - k_{k,b}[12] - k_{l,f}[12] \tag{A.43}$$

$$r_{13} = \frac{dC_{13}}{dt} = k_{l,f}[12] - kl,b[13][NH_3] \tag{A.44}$$

A.9 X-Ray Crystallographic Study for $C_{21}H_{18}N_2$ [q23l, (1)].

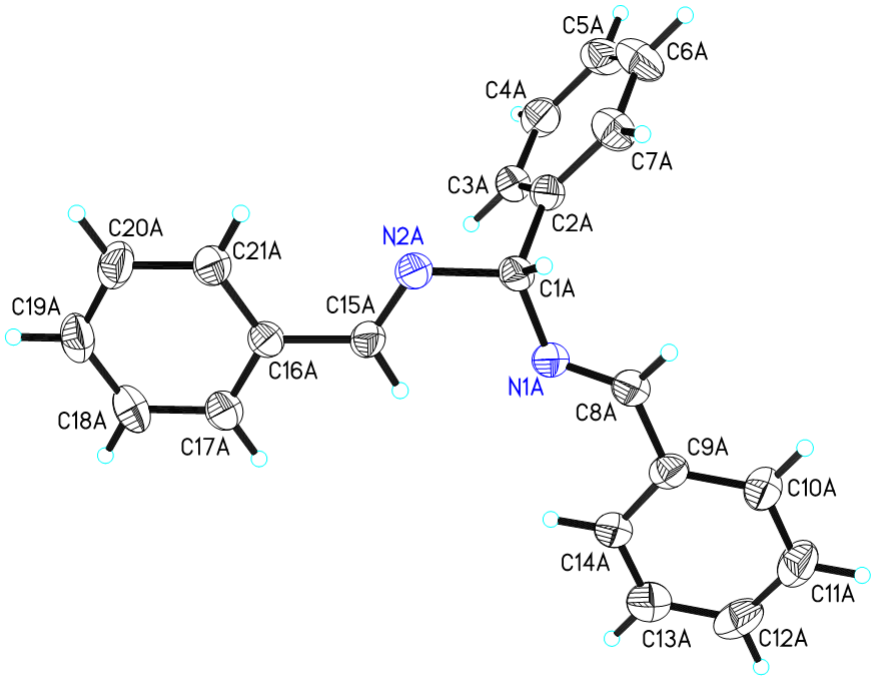

Figure A.10: ORTEP diagram of $C_{21}H_{18}N_2$

A complete set of unique reflections was collected with monochromated CuKα radiation for an 87/13 two-domain twinned crystal of 1. A total of 4906 1.0°-wide ω- or Φ-scan frames with counting times of 6-10 seconds were collected on a Bruker Apex II area detector. X-rays were provided by a Bruker MicroStar microfocus rotating anode operating at 45kV and 60 mA and equipped with Helios multilayer x-ray optics. Preliminary lattice constants were obtained with the Bruker program SMART.[40] Integrated reflection intensities were produced using the Bruker program SAINT.[41] The data set was corrected empirically for variable absorption effects using equivalent reflections. The Bruker software package SHELXTL was used to solve the structure using direct methods techniques. All stages of weighted full-matrix least-squares refinement were conducted using Fo2 data with the SHELXTL v2014 software package.[42] The final structural model incorporated anisotropic thermal parameters for all nonhydrogen atoms and isotropic thermal parameters for all hydrogen atoms. Hydrogen atoms were fixed at idealized riding-model sp^2- or sp^3-hybridized positions with C-H bond lengths of 0.95 - 1.00 Å. Isotropic thermal parameters of the idealized hydrogen atoms were fixed at values 1.2 times the equivalent isotropic thermal parameter of the carbon atom to which they are covalently bonded. The relevant crystallographic and structure refinement data are given in Table A.2.

Table A.2: Crystal Data and Structure Refinement for $C_{21}H_{18}N_2$.

Identification code	q23l	
Empirical formula	$C_{21}H_{18}N_2$	
Formula weight	298.37	
Temperature	200(2) K	
Wavelength	1.54178 Å	
Crystal system	Triclinic	
Space group	P-1 (Ci^1 - No. 2)	
Unit cell dimensions	a = 9.5293(5) Å	α= 92.340(3)°
	b = 9.7019(6) Å	β= 91.236(3)°
	c = 19.2087(11) Å	γ= 112.280(3)°
Volume	1640.6(2) $Å^3$	
Z	4	
Density (calculated)	1.208 g/cm3	
Absorption coefficient	0.55 mm^{-1}	
F(000)	632	
Crystal size	0.14 x 0.30 x 0.30 mm^3	
Theta range for data collection	2.30° to 70.24°	
Index ranges	$-11 \leq h \leq 11$, $-10 \leq k \leq 11$, $-22 \leq l \leq 22$	
Reflections collected	25678	
Independent reflections	5768 [R_{int} = 0.058]	
Completeness to theta = 66.00°	99.0 %	
Absorption correction	Multi-scan	
Max. and min. transmission	0.753 and 0.580	
Refinement method	Full-matrix least-squares on F^2	
Data / restraints / parameters	5768 / 0 / 417	
Goodness-of-fit on F2	1.088	
Final R indices [I>2sigma(I)]	R_1 = 0.094, wR_2 = 0.255	
R indices (all data)	R_1 = 0.106, wR_2 = 0.266	
Extinction coefficient	0.0020(6)	
Largest diff. peak and hole	0.44 and - 0.25 $e^-/Å^3$	

Table A.3: Atomic coordinate ($\times 10^4$) and equivalent isotropic displacement parameters (Å^2 $\times$ 10^3) for $C_{21}H_{18}N_2$. U(eq) is defined as one third of the trace of the orthogonalized U^{ij} tensor.

	x	y	z	U(eq)
N(1A)	3893(4)	-2101(4)	1551(2)	32(1)
N(2A)	2443(4)	-4783(4)	1545(2)	32(1)
C(1A)	2484(5)	-3294(5)	1742(2)	30(1)
C(2A)	1110(5)	-3124(5)	1386(2)	31(1)
C(3A)	858(5)	-3354(5)	673(2)	34(1)
C(4A)	-379(5)	-3173(5)	348(3)	40(1)
C(5A)	-1370(5)	-2762(6)	748(3)	44(1)
C(6A)	-1126(6)	-2539(7)	1456(3)	49(1)
C(7A)	120(5)	-2706(6)	1782(3)	40(1)
C(8A)	4346(5)	-887(5)	1911(2)	33(1)
C(9A)	5744(5)	371(5)	1765(2)	31(1)
C(10A)	6020(6)	1776(5)	2062(3)	40(1)
C(11A)	7320(6)	2986(6)	1910(3)	46(1)
C(12A)	8351(6)	2773(6)	1462(3)	49(1)
C(13A)	8085(6)	1382(6)	1173(3)	47(1)
C(14A)	6793(5)	183(5)	1321(2)	36(1)
C(15A)	3552(5)	-4924(5)	1229(2)	31(1)
C(16A)	3552(5)	-6395(5)	1005(2)	31(1)
C(17A)	4747(5)	-6467(5)	621(3)	38(1)
C(18A)	4725(6)	-7831(6)	366(3)	43(1)
C(19A)	3528(6)	-9126(6)	502(3)	43(1)
C(20A)	2348(6)	-9070(5)	896(3)	43(1)
C(21A)	2358(5)	-7705(5)	1144(3)	36(1)

Table A.4: Atomic coordinate ($\times 10^4$) and equivalent isotropic displacement parameters (Å^2 $\times$ 10^3) for $C_{21}H_{18}N_2$. U(eq) is defined as one third of the trace of the orthogonalized U^{ij} tensor.

	x	y	z	U(eq)
N(1B)	3598(4)	2517(4)	3412(2)	33(1)
N(2B)	2170(4)	-162(4)	3430(2)	33(1)
C(1B)	2150(5)	1272(5)	3238(2)	31(1)
C(2B)	866(5)	1525(5)	3608(2)	31(1)
C(3B)	806(5)	1502(5)	4331(2)	35(1)
C(4B)	-350(5)	1753(6)	4674(3)	40(1)
C(5B)	-1457(6)	2048(6)	4295(3)	45(1)
C(6B)	-1401(6)	2068(7)	3578(3)	52(1)
C(7B)	-244(6)	1808(6)	3232(3)	42(1)
C(8B)	3922(5)	3693(5)	3087(2)	32(1)
C(9B)	5364(5)	4982(5)	3223(2)	30(1)
C(10B)	5579(5)	6323(5)	2943(2)	36(1)
C(11B)	6927(6)	7564(6)	3089(3)	44(1)
C(12B)	8051(6)	7420(6)	3504(3)	50(1)
C(13B)	7852(6)	6078(6)	3775(3)	50(1)
C(14B)	6520(5)	4862(6)	3640(3)	38(1)
C(15B)	3323(5)	-223(5)	3756(2)	33(1)
C(16B)	3366(5)	-1630(5)	3991(2)	32(1)
C(17B)	4610(5)	-1621(5)	4383(3)	38(1)
C(18B)	4651(6)	-2905(6)	4651(3)	42(1)
C(19B)	3415(6)	-4242(6)	4519(3)	45(1)
C(20B)	2189(6)	-4281(6)	4115(3)	44(1)
C(21B)	2150(5)	-2988(5)	3854(2)	36(1)

Table A.5: Bond lengths [Å] for $C_{21}H_{18}N_2$.

Bond	Length	Bond	Length
N(1A)-C(8A)	1.259(6)	N(1B)-C(8B)	1.259(6)
N(1A)-C(1A)	1.468(5)	N(1B)-C(1B)	1.468(5)
N(2A)-C(15A)	1.279(6)	N(2B)-C(15B)	1.275(6)
N(2A)-C(1A)	1.463(6)	N(2B)-C(1B)	1.461(6)
C(1A)-C(2A)	1.531(6)	C(1B)-C(2B)	1.521(6)
C(1A)-H(1A)	1.0000	C(1B)-H(1B)	1.0000
C(2A)-C(3A)	1.380(6)	C(2B)-C(7B)	1.386(6)
C(2A)-C(7A)	1.388(6)	C(2B)-C(3B)	1.391(6)
C(3A)-C(4A)	1.394(6)	C(3B)-C(4B)	1.388(7)
C(3A)-H(3A)	0.9500	C(3B)-H(3B)	0.9500
C(4A)-C(5A)	1.390(7)	C(4B)-C(5B)	1.392(7)
C(4A)-H(4A)	0.9500	C(4B)-H(4B)	0.9500
C(5A)-C(6A)	1.369(8)	C(5B)-C(6B)	1.380(8)
C(5A)-H(5A)	0.9500	C(5B)-H(5B)	0.9500
C(6A)-C(7A)	1.397(7)	C(6B)-C(7B)	1.396(7)
C(6A)-H(6A)	0.9500	C(6B)-H(6B)	0.9500
C(7A)-H(7A)	0.9500	C(7B)-H(7B)	0.9500
C(8A)-C(9A)	1.467(6)	C(8B)-C(9B)	1.475(6)
C(8A)-H(8A)	0.9500	C(8B)-H(8B)	0.9500
C(9A)-C(10A)	1.382(7)	C(9B)-C(10B)	1.372(6)
C(9A)-C(14A)	1.387(6)	C(9B)-C(14B)	1.392(6)
C(10A)-C(11A)	1.392(7)	C(10B)-C(11B)	1.401(6)
C(10A)-H(10A)	0.9500	C(10B)-H(10B)	0.9500
C(11A)-C(12A)	1.388(8)	C(11B)-C(12B)	1.374(8)
C(11A)-H(11A)	0.9500	C(11B)-H(11B)	0.9500
C(12A)-C(13A)	1.366(8)	C(12B)-C(13B)	1.369(8)
C(12A)-H(12A)	0.9500	C(12B)-H(12B)	0.9500
C(13A)-C(14A)	1.381(7)	C(13B)-C(14B)	1.376(7)
C(13A)-H(13A)	0.9500	C(13B)-H(13B)	0.9500
C(14A)-H(14A)	0.9500	C(14B)-H(14B)	0.9500
C(15A)-C(16A)	1.473(6)	C(15B)-C(16B)	1.471(6)
C(15A)-H(15A)	0.9500	C(15B)-H(15B)	0.9500
C(16A)-C(21A)	1.388(6)	C(16B)-C(17B)	1.388(7)
C(16A)-C(17A)	1.393(7)	C(16B)-C(21B)	1.396(6)
C(17A)-C(18A)	1.384(7)	C(17B)-C(18B)	1.380(7)
C(17A)-H(17A)	0.9500	C(17B)-H(17B)	0.9500
C(18A)-C(19A)	1.378(8)	C(18B)-C(19B)	1.391(7)
C(18A)-H(18A)	0.9500	C(18B)-H(18B)	0.9500
C(19A)-C(20A)	1.386(7)	C(19B)-C(20B)	1.376(7)
C(19A)-H(19A)	0.9500	C(19B)-H(19B)	0.9500
C(20A)-C(21A)	1.385(7)	C(20B)-C(21B)	1.382(7)
C(20A)-H(20A)	0.9500	C(20B)-H(20B)	0.9500
C(21A)-H(21A)	0.9500	C(21B)-H(21B)	0.9500

Table A.6: Bond angles [°] for $C_{21}H_{18}N_2$.

Bonds	Angle	Bonds	Angle
C(8A)-N(1A)-C(1A)	118.0(4)	C(11A)-C(10A)-H(10A)	119.7
C(15A)-N(2A)-C(1A)	119.9(4)	C(12A)-C(11A)-C(10A)	119.5(5)
N(2A)-C(1A)-N(1A)	112.6(3)	C(12A)-C(11A)-H(11A)	120.3
N(2A)-C(1A)-C(2A)	108.0(3)	C(10A)-C(11A)-H(11A)	120.3
N(1A)-C(1A)-C(2A)	110.4(3)	C(13A)-C(12A)-C(11A)	119.9(5)
N(2A)-C(1A)-H(1A)	108.6	C(13A)-C(12A)-H(12A)	120.0
N(1A)-C(1A)-H(1A)	108.6	C(11A)-C(12A)-H(12A)	120.0
C(2A)-C(1A)-H(1A)	108.6	C(12A)-C(13A)-C(14A)	120.6(5)
C(3A)-C(2A)-C(7A)	119.5(4)	C(12A)-C(13A)-H(13A)	119.7
C(3A)-C(2A)-C(1A)	120.7(4)	C(14A)-C(13A)-H(13A)	119.7
C(7A)-C(2A)-C(1A)	119.8(4)	C(13A)-C(14A)-C(9A)	120.5(5)
C(2A)-C(3A)-C(4A)	120.7(4)	C(13A)-C(14A)-H(14A)	119.7
C(2A)-C(3A)-H(3A)	119.7	C(9A)-C(14A)-H(14A)	119.7
C(4A)-C(3A)-H(3A)	119.7	N(2A)-C(15A)-C(16A)	122.1(4)
C(5A)-C(4A)-C(3A)	119.5(5)	N(2A)-C(15A)-H(15A)	119.0
C(5A)-C(4A)-H(4A)	120.2	C(16A)-C(15A)-H(15A)	119.0
C(3A)-C(4A)-H(4A)	120.2	C(21A)-C(16A)-C(17A)	119.4(4)
C(6A)-C(5A)-C(4A)	119.9(4)	C(21A)-C(16A)-C(15A)	121.4(4)
C(6A)-C(5A)-H(5A)	120.0	C(17A)-C(16A)-C(15A)	119.2(4)
C(4A)-C(5A)-H(5A)	120.0	C(18A)-C(17A)-C(16A)	120.2(5)
C(5A)-C(6A)-C(7A)	120.7(5)	C(18A)-C(17A)-H(17A)	119.9
C(5A)-C(6A)-H(6A)	119.7	C(16A)-C(17A)-H(17A)	119.9
C(7A)-C(6A)-H(6A)	119.7	C(19A)-C(18A)-C(17A)	120.0(5)
C(2A)-C(7A)-C(6A)	119.7(5)	C(19A)-C(18A)-H(18A)	120.0
C(2A)-C(7A)-H(7A)	120.1	C(17A)-C(18A)-H(18A)	120.0
C(6A)-C(7A)-H(7A)	120.1	C(18A)-C(19A)-C(20A)	120.3(5)
N(1A)-C(8A)-C(9A)	122.3(4)	C(18A)-C(19A)-H(19A)	119.9
N(1A)-C(8A)-H(8A)	118.9	C(20A)-C(19A)-H(19A)	119.9
C(9A)-C(8A)-H(8A)	118.9	C(21A)-C(20A)-C(19A)	119.9(5)
C(10A)-C(9A)-C(14A)	118.9(4)	C(21A)-C(20A)-H(20A)	120.1
C(10A)-C(9A)-C(8A)	120.1(4)	C(19A)-C(20A)-H(20A)	120.1
C(14A)-C(9A)-C(8A)	121.0(4)	C(20A)-C(21A)-C(16A)	120.3(5)
C(9A)-C(10A)-C(11A)	120.6(5)	C(20A)-C(21A)-H(21A)	119.9
C(9A)-C(10A)-H(10A)	119.7	C(16A)-C(21A)-H(21A)	119.9

Table A.7: Bond angles [°] for $C_{21}H_{18}N_2$.

C(8B)-N(1B)-C(1B)	118.7(4)	C(11B)-C(10B)-H(10B)	119.7
C(15B)-N(2B)-C(1B)	120.4(4)	C(12B)-C(11B)-C(10B)	119.3(5)
N(2B)-C(1B)-N(1B)	112.5(3)	C(12B)-C(11B)-H(11B)	120.3
N(2B)-C(1B)-C(2B)	108.5(3)	C(10B)-C(11B)-H(11B)	120.3
N(1B)-C(1B)-C(2B)	110.3(4)	C(13B)-C(12B)-C(11B)	120.3(5)
N(2B)-C(1B)-H(1B)	108.5	C(13B)-C(12B)-H(12B)	119.9
N(1B)-C(1B)-H(1B)	108.5	C(11B)-C(12B)-H(12B)	119.9
C(2B)-C(1B)-H(1B)	108.5	C(12B)-C(13B)-C(14B)	120.5(5)
C(7B)-C(2B)-C(3B)	119.1(4)	C(12B)-C(13B)-H(13B)	119.8
C(7B)-C(2B)-C(1B)	120.5(4)	C(14B)-C(13B)-H(13B)	119.8
C(3B)-C(2B)-C(1B)	120.4(4)	C(13B)-C(14B)-H(14B)	119.9
C(4B)-C(3B)-C(2B)	120.8(4)	C(9B)-C(14B)-H(14B)	119.9
C(4B)-C(3B)-H(3B)	119.6	N(2B)-C(15B)-C(16B)	122.3(4)
C(2B)-C(3B)-H(3B)	119.6	N(2B)-C(15B)-H(15B)	118.8
C(3B)-C(4B)-C(5B)	120.0(5)	C(16B)-C(15B)-H(15B)	118.8
C(3B)-C(4B)-H(4B)	120.0	C(17B)-C(16B)-C(21B)	118.4(4)
C(5B)-C(4B)-H(4B)	120.0	C(17B)-C(16B)-C(15B)	120.0(4)
C(6B)-C(5B)-C(4B)	119.3(5)	C(21B)-C(16B)-C(15B)	121.6(4)
C(6B)-C(5B)-H(5B)	120.4	C(18B)-C(17B)-C(16B)	121.7(5)
C(4B)-C(5B)-H(5B)	120.4	C(18B)-C(17B)-H(17B)	119.2
C(5B)-C(6B)-C(7B)	120.8(5)	C(16B)-C(17B)-H(17B)	119.2
C(5B)-C(6B)-H(6B)	119.6	C(17B)-C(18B)-C(19B)	119.0(5)
C(7B)-C(6B)-H(6B)	119.6	C(17B)-C(18B)-H(18B)	120.5
C(2B)-C(7B)-C(6B)	120.1(5)	C(19B)-C(18B)-H(18B)	120.5
C(2B)-C(7B)-H(7B)	120.0	C(20B)-C(19B)-C(18B)	120.2(5)
C(6B)-C(7B)-H(7B)	120.0	C(20B)-C(19B)-H(19B)	119.9
N(1B)-C(8B)-C(9B)	122.0(4)	C(18B)-C(19B)-H(19B)	119.9
N(1B)-C(8B)-H(8B)	119.0	C(19B)-C(20B)-C(21B)	120.5(5)
C(9B)-C(8B)-H(8B)	119.0	C(19B)-C(20B)-H(20B)	119.8
C(10B)-C(9B)-C(14B)	119.0(4)	C(21B)-C(20B)-H(20B)	119.8
C(10B)-C(9B)-C(8B)	120.3(4)	C(20B)-C(21B)-C(16B)	120.3(4)
C(14B)-C(9B)-C(8B)	120.7(4)	C(20B)-C(21B)-H(21B)	119.9
C(9B)-C(10B)-C(11B)	120.6(4)	C(16B)-C(21B)-H(21B)	119.9
C(9B)-C(10B)-H(10B)	119.7		

A.10 Reference Spectra for In-Situ NMR Characterization

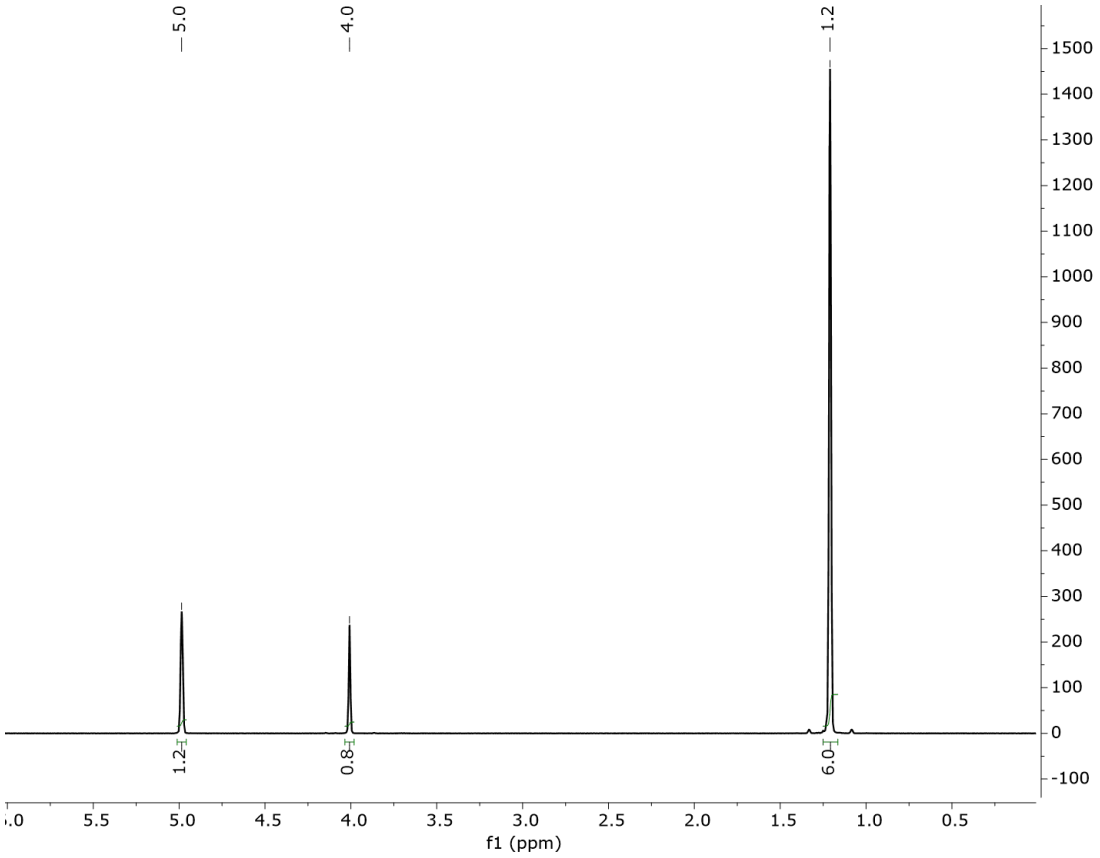

Figure A.11: ^{1}H NMR of deuterated 2-propanol referenced at 1.2 ppm.

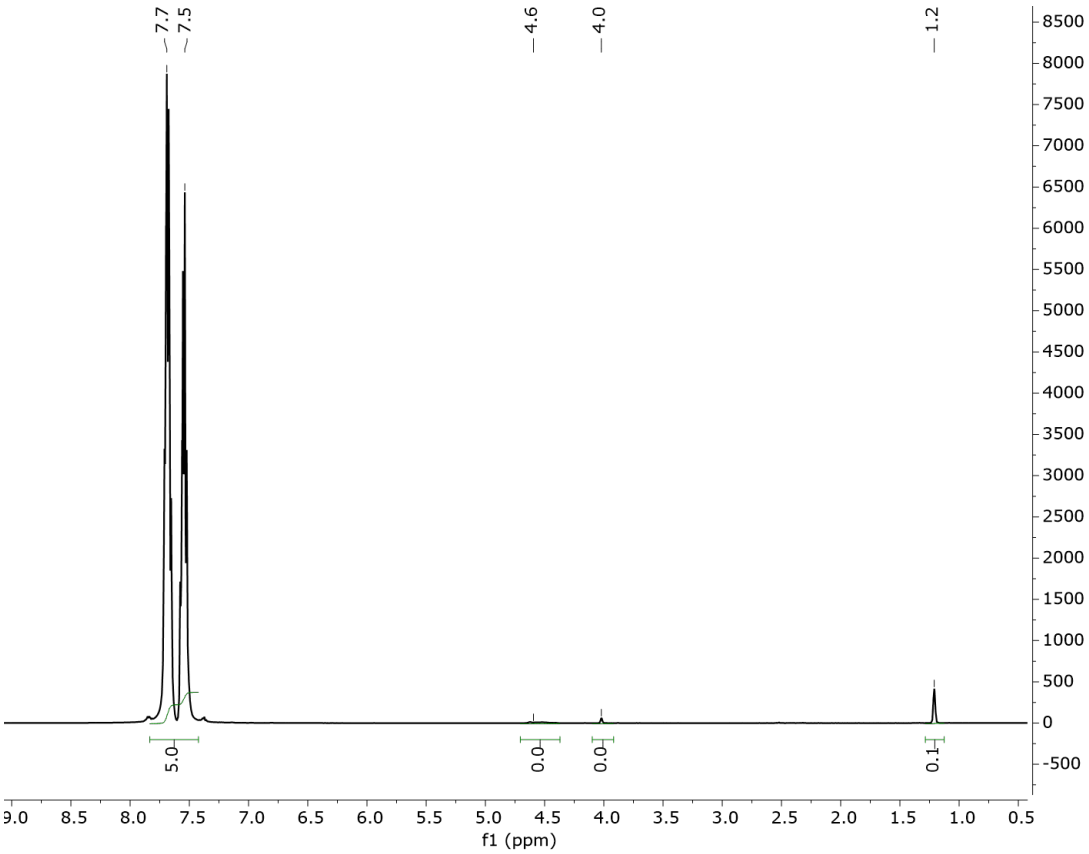

Figure A.12: ^{1}H NMR of benzonitrile in deuterated 2-propanol (referenced at 1.2 ppm).

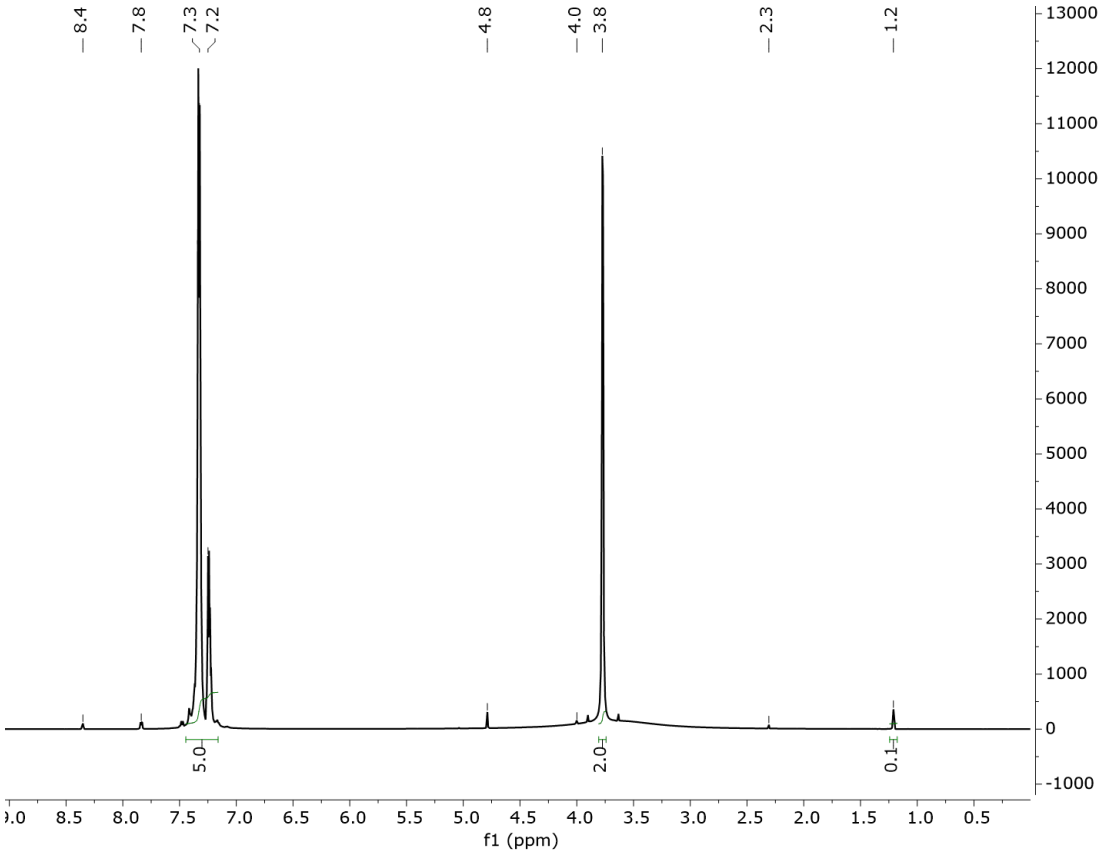

Figure A.13: ^{1}H NMR of benzylamine in deuterated 2-propanol (referenced at 1.2 ppm).

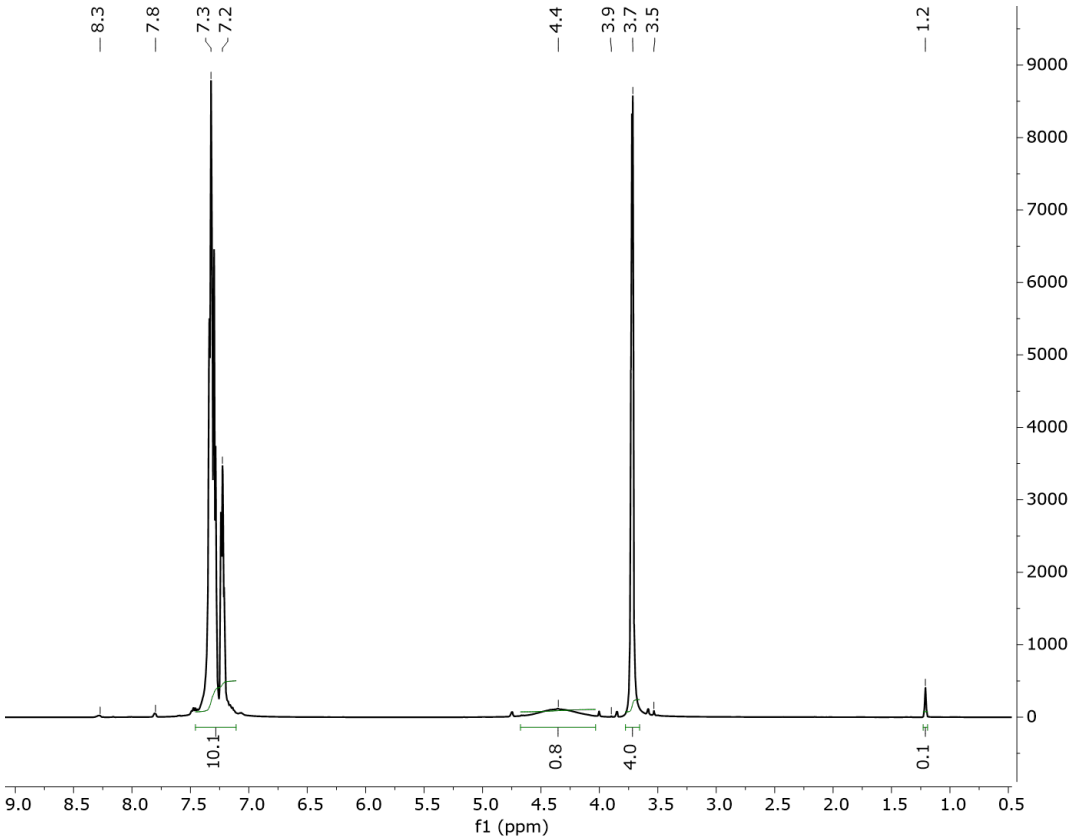

Figure A.14: ^{1}H NMR of dibenzylamine

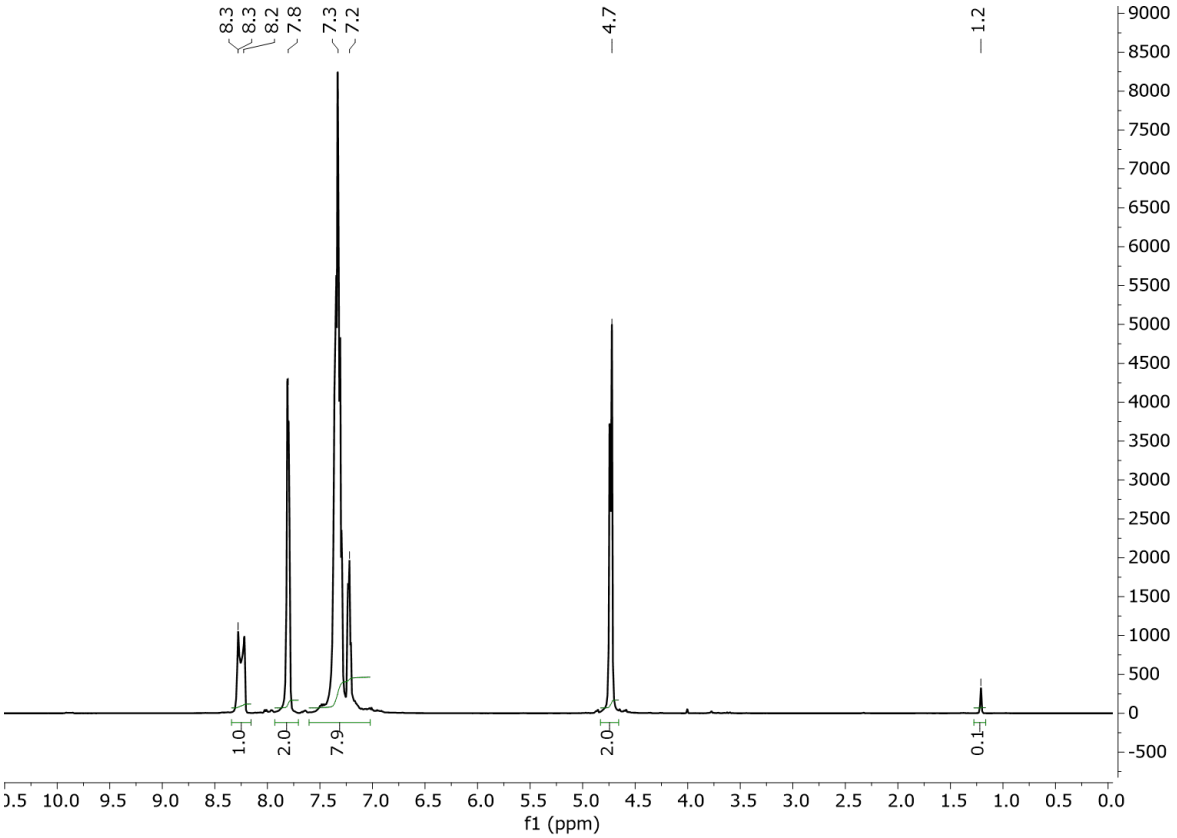

Figure A.15: ^{1}H NMR of dibenzylimine in deuterated 2-propanol (referenced at 1.2 ppm).

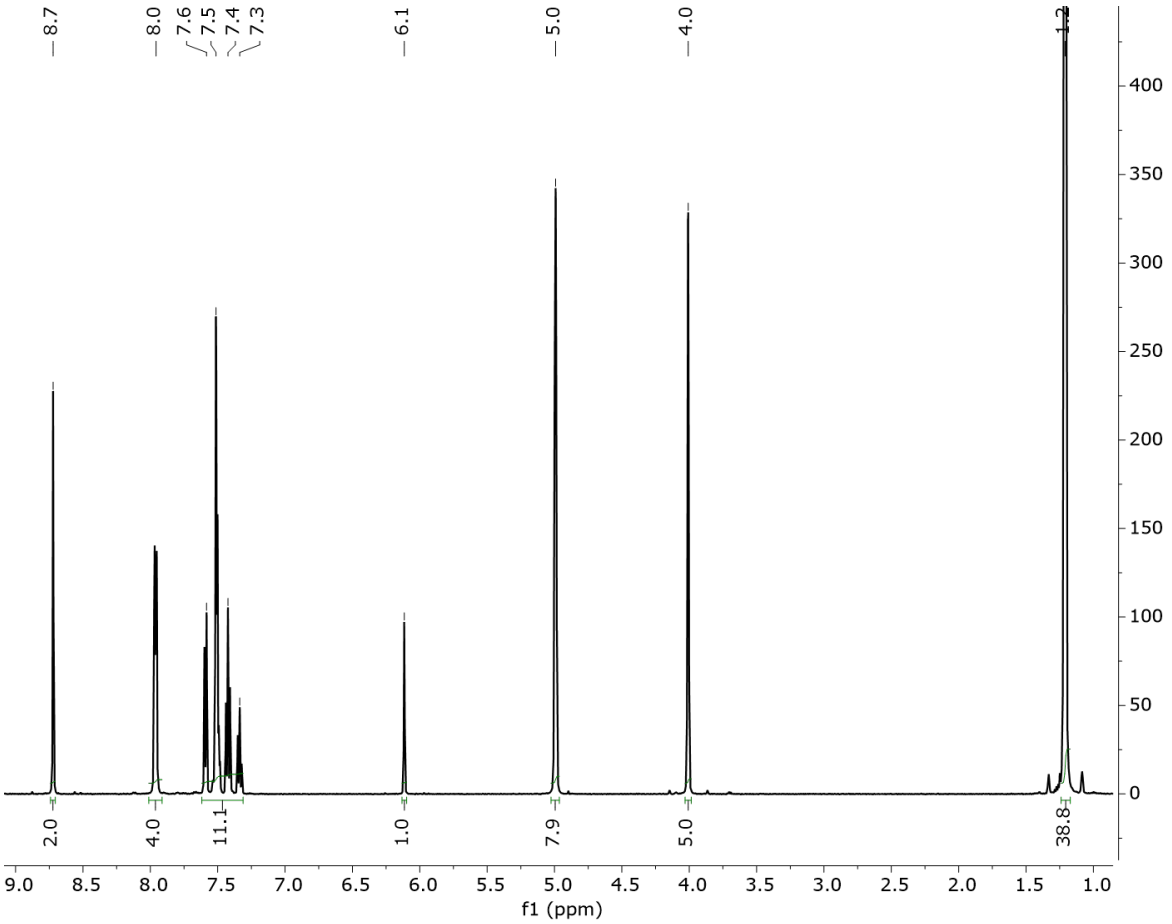

Figure A.16: ^{1}H NMR of N,N-(phenylmethylene)bis(1-phenylmethanimine) in deuterated 2-propanol (referenced at 1.2 ppm).

Appendix B

Appendix B: Chapter 4

B.1 Thermocouple Calibration Data

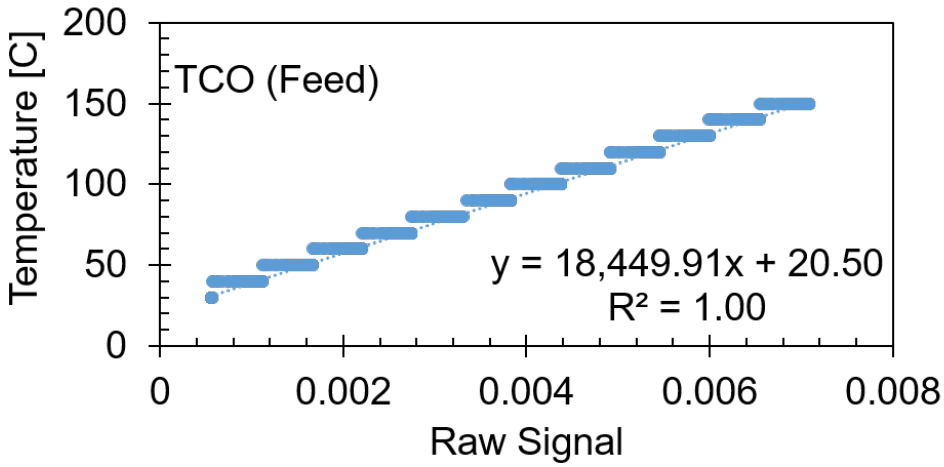

Figure B.1: Temperature calibration for the inlet thermocouple in the continuous flow reactor.

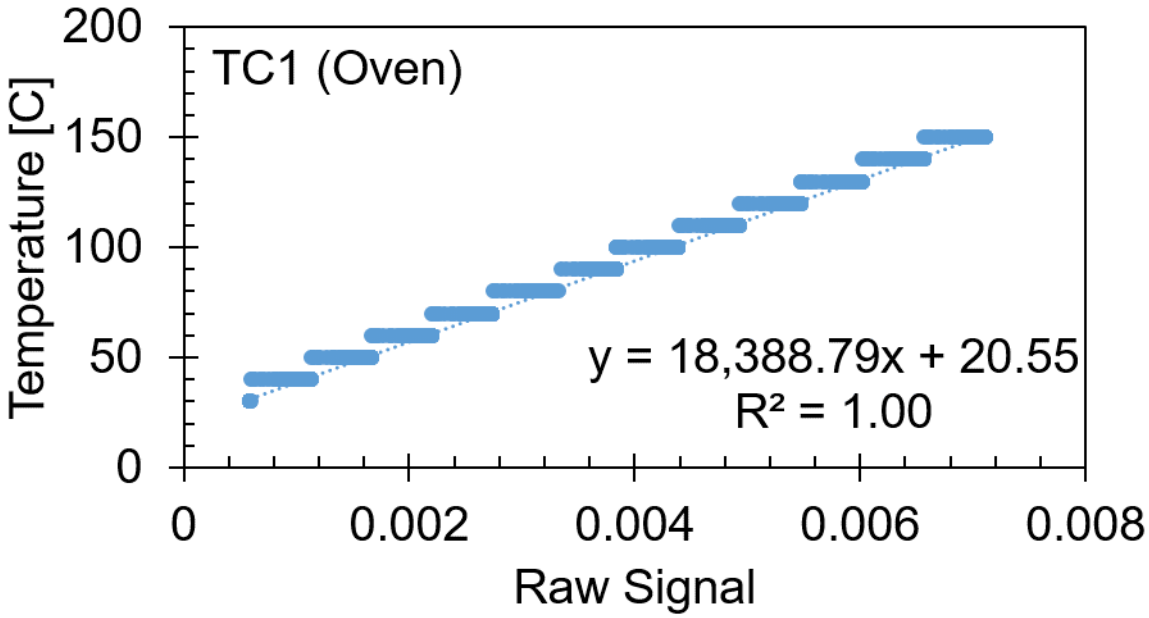

Figure B.2: Temperature calibration for the oven thermocouple in the continuous flow reactor.

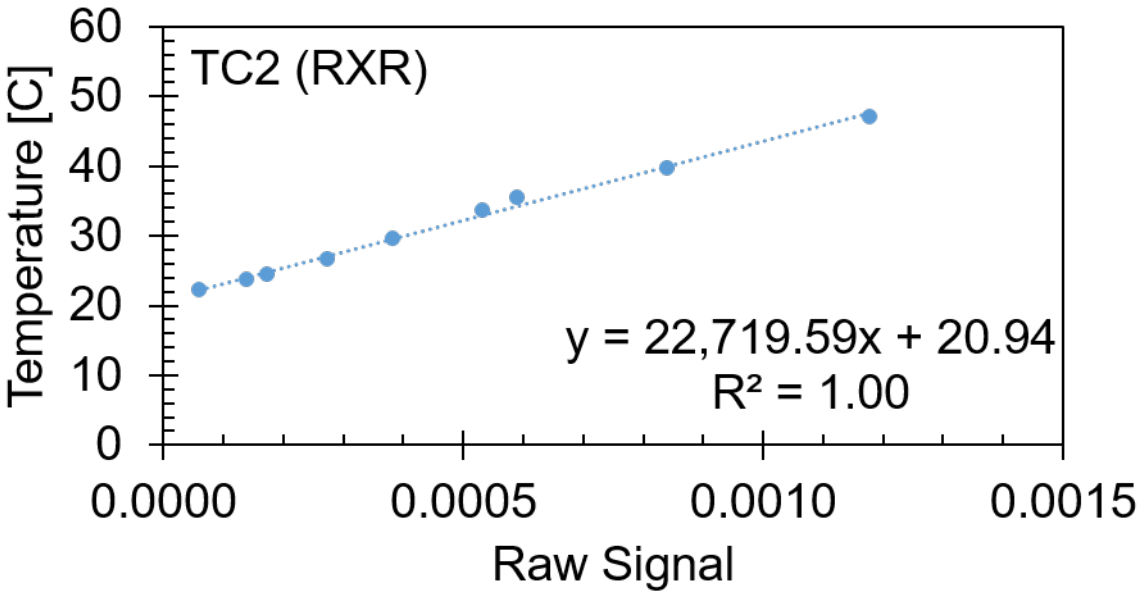

Figure B.3: Temperature calibration for the reactor thermocouple in the continuous flow system.

Appendix C

Appendix C: Chapter 5

C.1 Conductivity, Temperature, Concentration Calibrations

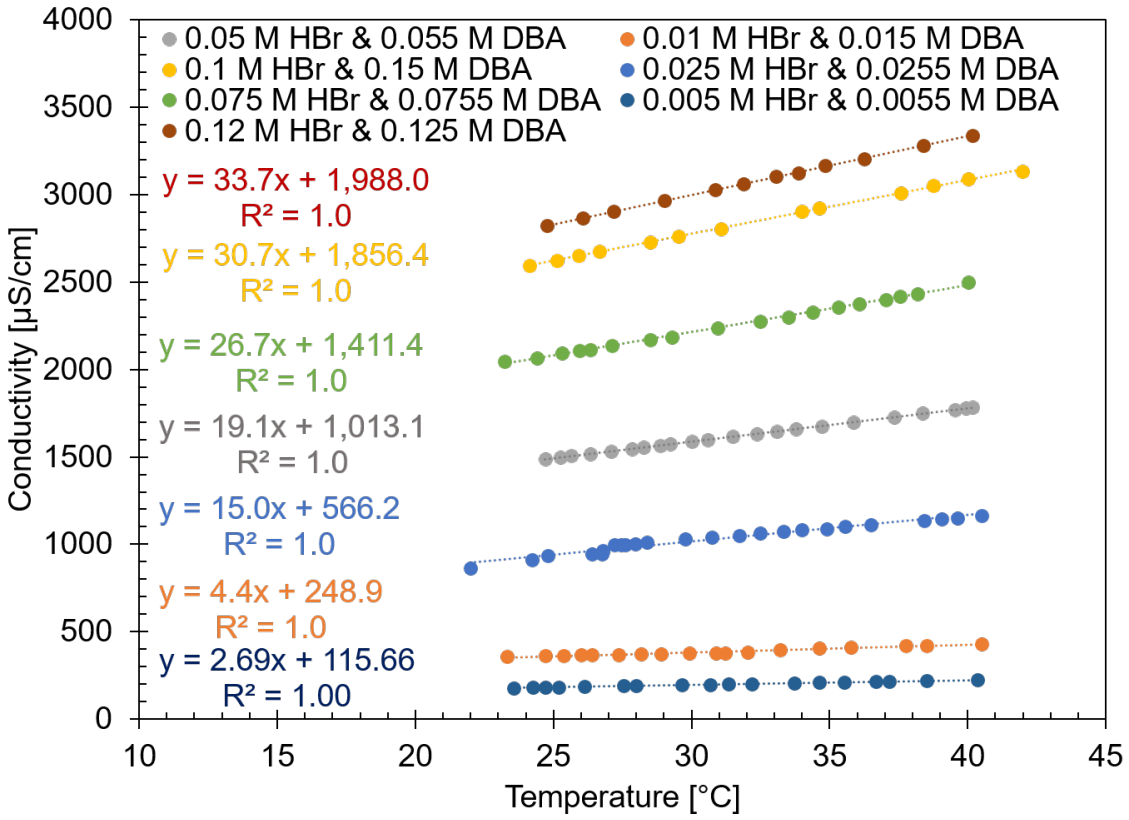

Figure C.1: Conductivity versus temperature for a variety of dibenzylamine HBr concentrations in methanol.

Concentration[M]	α_{25} [%/C]	α_{30} [%/C]	α_{35} [%/C]	α_{40} [%/C]
1.00	1.6	1.5	0.7	0.8
0.50	1.8	1.5	1.5	1.4
0.10	1.3	1.2	1.2	1.1
0.05	1.1	1.2	1.3	1.0
0.01	1.1	1.0	1.0	1.0

Table C.1: Conductivity temperature coefficient, α, for dibenzylamine HBr at different concentrations and temperature.

Appendix D

Appendix D: Chapter 6

The definition of selectivity utilized for Chapters 6 and 7 differ from that commonly used in chemistry. Here is its definitions:

$$\%\text{Selectivity} = \frac{\text{Degree of Substitution}}{\text{Mole Ratio of Acyl Cl to AGU}} \tag{D.1}$$

D.1 GP Summary Table of Reaction Conditions and Performance

Table D.1: Polysaccharide based detergent synthesis and PMI indices.

Rxn #	Mass of Reactants [g]							Work-up [g]		Product		Process					
	Substrate	Solvent	Type	AA	Type	Reagent	Type	Type	Solvent	Type	Mass [g]	Mass Distilled	% Distilled	DS	Temperature [C]	Time [h]	PMI
86	100	114	DMAc	247	PC	102	PYR	1582	MeOH	GP	126	0.0	0	2.40	90	0.7	18
89	100	183	DMAc	249	PC	104	PYR	2373	MeOH	GP	265	34.6	16	2.10	90	0.6	11
91	101	138	DMAc	248	PC	105	PYR	1582	MeOH	GP	310	63.2	31	2.30	80	0.6	7
98	100	139	DMAc	173	PC	76	PYR	2452	MeOH	GP	210	81.7	37	1.60	80	0.7	14
102	2	6	DMAc	5	PC	3	LUT	198	MeOH	GP	4	0.7	10	1.78	80	0.7	50
103	2	3	Sulfolane	5	PC	3	LUT	158	MeOH	GP	2	0.4	13	2.61	80	0.5	81

Appendix E

Appendix E: Chapter 7

E.1 GB Summary Table of Reaction Conditions and Performance

Table E.1: Polysaccharide based detergent synthesis and PMI indices.

Rxn #	Mass of Reactants [g]									Work-up [g]		Product		Process				% Selectivity
	Substrate	Solvent	Type	AA	Type	Additive	Type	Reagent	Type	Type	Solvent	Type	Mass [g]	DS	Temperature [C]	Time [h]	PMI	
119	50.0	250.0	Water	22.5	BC	-	-	12.9	NaOH	Water	500	GB	67.5	0.3	3	1.0	25	52
120	50.3	250.2	Water	22.5	BC	-	-	12.9	NaOH	Water	800	GB	25.0	0.4	22	1.0	46	79
121	50.0	250.4	Water	22.5	BC	-	-	12.9	NaOH	Water	900	GB	41.0	0.1	43	1.0	35	21
123	50.5	250.3	Water	22.5	BC	-	-	25.6	NaOH	Water	1100	GB	50.9	0.3	5	1.0	47	64
124	50.1	250.1	Water	22.5	BC	-	-	19.3	NaOH	Water	1200	GB	27.4	0.5	5	1.0	56	94
127	50.0	253.6	Water	26.7	BC	-	-	16.4	NaOH	Water	3000	GB	63.9	0.4	5	1.0	53	63
128	50.4	251.6	Water	23.3	BC	-	-	8.0	NaOH	Water	3000	GB	104.6	0.1	5	1.0	64	19
129	51.5	253.2	Water	24.1	BC	18.7	NaCl	8.1	NaOH	Water	3000	GB	75.3	0.2	5	1.0	57	37
130	50.3	252.0	Water	23.5	BC	18.6	NaCl	12.1	NaOH	Water	2100	GB	58.1	0.3	4	1.0	45	50
133	50.2	251.3	Water	25.5	BC	18.5	NaCl	21.8	NaOH	Water	-	GB	78.4	0.2	4	1.0	10	36
135	50.2	258.1	Water	22.6	BC	-	-	10.8	NH_4OH	Water	1963	GB	46.6	0.0	4	1.0	50	4
138	50.1	250.3	Water	25.3	BC	-	-	12.0	NaOH	Water	875	GB	58.3	0.3	3	1.0	21	46
139	50.0	250.0	Water	25.0	BC	-	-	12.0	NaOH	Water	683	GB	74.4	0.3	3	1.0	14	50
140	50.1	190.4	Water	22.5	BC	-	-	23.4	NH_4OH	Water	2038	GB	58.3	0.0	3	1.0	51	0
141	38.9	200.1	Water	18.0	BC	-	-	12.0	KOH	Water	1591	GB	44.1	0.4	3	1.0	42	73
153	50.0	450.0	Water	22.1	BC	-	-	12.0	NaOH	Water	500	GB	25.7	0.3	5	1.0	43	51
154	50.0	250.1	Water	23.5	BC	-	-	12.0	NaOH	Water	900	GB	28.8	0.3	5	1.0	44	59
161	25.1	276.0	Water	23.2	BC	-	-	21.0	NaOH	Water	1676	GB	8.9	1.0	4	1.0	227	94
164	25.2	277.3	Water	22.7	BC	-	-	27.3	KOH	Water	1514	GB	12.7	0.5	5	1.0	147	52
175	26.2	289.5	Water	31.4	BC	-	-	17.1	NaOH	Water	1200	GB	33.3	0.3	4	1.5	47	25
176	25.0	278.1	Water	33.2	BC	-	-	14.3	NaOH	Water	1000	GB	41.0	0.2	4	2	33	16
180	25.0	252.2	Water	33.0	BC	-	-	19.0	NaOH	Water	1656	GB	17.9	1.0	3	2	111	65
181	50.1	250.2	Water	33.5	BC	-	-	19.0	NaOH	Water	1703	GB	59.7	0.5	3	2	34	65
187	25.1	250.5	Water	33.8	BC	-	-	19.2	NaOH	Water	2643	GB	34.3	0.9	3	2	87	57

Abbreviations

AE	Atom Economy
ART	Algebraic Reconstruction Techniques
BET	Brunauer Emmett Teller
BC	Benzoyl Chloride
CCS	Carbon Capture and Sequestration
CMC	Critical Micelle Concentration
CPMG	Carr Purcell Meiboon Gill
CPS	Cycles Per Second
DFT	Density Functional Theory
DOSY	Diffusion Order Spectroscopy
DMA	Dynamic Mechanical Analyzer
DMAc	Dimethyl acetamide
DMSO	Dimethyl sulfoxide
DS	Degree of Substitution
DSC	Differential Scanning Calorimeter
DSS	Sodium Trimethylsilylpropanesulfonate
DPw	Weighted Degree of Polymerization
EU	European Union
FBP	Filtered Back-Projection
FDA	Food and Drug Administration
FID	Flame Ionization Detector
FID	Free Induction Decay
FTIR	Fourier Transform Infrared
GB	α-1,3-glucan-benzoate

GEAK5	Graduate Engineering Association Kilometer 5
GC	Gas Chromatography
G-L	Gas-to-Liquid
GP	α-1,3-glucan-palmitate
GPC	Gel Permeation Chromatography
GPU	Graphical Processing Unit
Gtfs	Glucosyltransferases
GWP	Global Warming Potential
HER	Hydrogen Evolution Reaction
HFIP	Hexafluoro-2-propanol
HIV	Human Immunodeficiency Virus
ID	Inner Diameter
iPROH	2-propanol
LCIA	Life Cycle Inventory and Assessment
LFL	Lower Flammability Limit
LIBS	Laser Induced Breakdown Spectroscopy
MB	Mass Balance
McG	Microcrystalline Glucan
MEA	Membrane Electrode Assembly
MFC	Mass Flow Controller
MIP	Mercury Intrusion Porosimetry
MOF	Metal-Organic Framework
MPC	Model Predictive Control
MRI	Magnetic Resonance Imaging
MW	Molecular Weight

NMR	Nuclear Magnetic Resonance
ODE	Ordinary Differential Equation
OER	Oxygen Evolution Reaction
OP	Oxygen Permeability
ORTEP	Oak Ridge Thermal Ellipsoid Plot
QbC	Quality by Control
QbD	Quality by Design
QbT	Quality by Testing
PAT	Process Analytical Technique
PEEK	Polyether ether ketone
PEM	Proton Exchange Membrane
PFD	Process Flow Diagram
PID	Proportional Integral Derivative
PMI	Process Mass Intensity
PPE	Personal Protective Equipment
PVD	Pore Volume Distribution
P-Ox	Phosphine Oxide
R&D	Research and Development
qNMR	Quantitative NMR
RMSE	Root Mean Square Error
RTD	Residence Time Distribution
SC-XRD	Single Crystal X-ray Diffraction
SDG	Sustainable Development Goals
SE	Surface Energy
SIA	Specific Interfacial Area

SSA	Specific Surface Area
SSE	Solid Surface Energy
tBuOH	tert-butanol
TEM	Transmission Electron Microscopy
TD	Time Domain
TGA	Thermogravimetric Analysis
THF	Tetrahydrofuran
TMV	Tobacco Mosaic Virus
TOF	Turnover Frequency
TOL	Toluene
UHP	Ultra High Purity
U.N.	United Nations
UV-Vis	Ultraviolet and Visible light
VMC	Volumetric Mass Transfer Coefficient
WC	Wet-cake Glucan
WCED	World Commission on Environment and Development
WVP	Water Vapor Permeance
WVTR	Water Vapor Transmission Rate
XCT	X-ray Computed Tomography
XRD	X-ray Diffraction